論文 / 著書情報
Article / Book Information

題目(和文)	
Title(English)	Study of One-body 2-D Beam-switching Butler Matrix with Short-slot 2-plane Couplers
著者(和文)	金東勲
Author(English)	Dong-Hun Kim
出典(和文)	学位:博士(工学), 学位授与機関:東京工業大学, 報告番号:甲第10638号, 授与年月日:2017年9月20日, 学位の種別:課程博士, 審査員:廣川 二郎,水本 哲弥,阪口 啓,西方 敦博,青柳 貴洋,小西 善彦
Citation(English)	Degree:Doctor (Engineering), Conferring organization: Tokyo Institute of Technology, Report number:甲第10638号, Conferred date:2017/9/20, Degree Type:Course doctor, Examiner:,,,,,
学位種別(和文)	博士論文
Type(English)	Doctoral Thesis

Doctoral Dissertation

Study of One-body 2-D Beam-switching Butler Matrix with Short-slot 2-plane Couplers

September, 2017

Under the Supervision of

Professor Jiro Hirokawa

Presented by

Dong-Hun Kim
Department of Electrical and Electronic Engineering
Tokyo Institute of Technology

Table of contents

Chapter 1

Introduction

1.1 Background of the research

The present and the future of wireless communication

Since Nikola Tesla pronounced on the possibility of radio communication in 1893 [1.1], the wireless communication has been proliferating and developing to satisfy demands in a variety of area. Now, 4G (4th generation wireless systems) service is operated in the mostly countries. Under the well-controlled circumstance, existing commercial mobile devices supported LTE-A (3GPP Long Term Evolution-Advanced) UE (User Equipment) category 12 can provide 603 Mbps download and 102 Mbps upload [1.2]. Although many subscribers think that these download and upload data rates are enough to use recent data contents such as the streaming service and SNS (Social Network Service), the industry and the academia plan and prepare a higher data rate communication for following four mega trends. First, increases of the numbers of mobile-connected and IoT (Internet of Things) devices. Those are expected 11.1 billion and 50 billion in 2020 as shown in Fig. 1.1 and 1.2, respectively [1.3]-[1.4]. The use of these devices is not only restricted handheld mobile communication, but also various applications such as V2V (Vehicle to Vehicle) and V2I (Vehicle to Infrastructure) for connected car, M2M (Machine to Machine) for industrial automation (Industry 4.0), and monitoring sensors for healthcare and infrastructure maintenance, etc. Through the proliferation of these applications, unexpected applications will be appeared to satisfy additional needs. It makes to increase the number of devices. Second, increase of mobile data traffic. It is forecasted 30.6 Exabyte per month in 2020 as shown in Fig. 1.3 [1.3]. The increment of data traffic is contributed not only by the increment of the number of devices, but also by the increment of usage per device listed in Table 1.1 [1.3]. Among the contents, video contents such as the streaming and VOD (Video On Demand) occupy mostly data traffic. Eager to display images same as human eye’s view, broadcasting providers and display makers are planed official 8K (resolution 7680×4320) service in 2018 [1.5]. It makes to increase data traffic per content. Third, the movement of the processing and the storage functions from the device to the cloud service. The cloud-based data traffic is reached to 70% of data traffic in 2020 [1.6]. Finally, mobile services are converged such as AR (Augment Reality), VR (Virtual Reality), LBS (Location Based Service), and hologram, etc. [1.7]. These converged services are required stable and seamless wireless connection. Satisfying these mega trends, the next generation communication should be prepared for needs such as large data traffic, devices for various applications, high QoE (Quality of user Experience), and low energy consumption and cost for the operation.

5G communication

5G (5th generation wireless systems) communication should be designed on the consideration of previous mentioned four mega trends. ITU-R (International Telecommunication Union-Radiocommunication) WP (Working Party) 5D plans and schedules IMT (International Mobile Telecommunications)-2020 for the framework of standards of 5G communication [1.8]. In recommendation ITU-R M.2083-0, eight parameters are considered to be key capabilities of IMT-2020 as shown in Fig. 1.4 [1.9]. The spectrum efficiency is the most important capability within these parameters, because it affects the selection of the frequency band (candidates 11, 15, 28, 44, 60, 70 and 80 GHz) for 5G communication. There are two approaches to improve the spectrum efficiency. First, advanced waveforms, modulation and coding, and multiple access schemes such as FOFDM (Filtered Orthogonal Frequency-Division Multiplexing), FBMC (Filter Bank Multi-Carrier modulation), PDMA (Pattern Division Multiple Access), SCMA (Sparse Code Multiple Access), IDMA (Interleave Division Multiple Access) and LDS (Low Density Spreading), etc. Second, advanced antenna technologies such as 3D-BF (3D-BeamForming), AAS (Active Antenna System), massive MIMO (Multiple-Input and Multiple-Output), and network MIMO, etc. Within previously mentioned technologies, this dissertation focuses on beam-switching network which is one of 3D-BF techniques.

Radar

Radar is an abbreviation word of “RAdio Detection And Ranging” [1.10]. Like the origin of a word, radar was basically developed for detecting and ranging of target using electromagnetic waves for the surveillance and the reconnaissance in the military. Like many advanced military technologies, radar was transferred from the exclusive military-industry-academic complex to civilian areas after World War II ended. Radar was applied the remote sensing such as air traffic control, ship navigator, and altimeter, etc. In radar, the most required capability is how to discriminate a target signal from receiving signals with clutter signals. A target signal indicates the position of target in the specified space by the detection ability. The position of a target is divided into the range and the direction of a target. By increasing the output power of radar, exactly say that the arrived power at a target, the detection range of radar can be increased. The precision of the direction estimation of a target is not related the output power of radar, however it is deeply related the beam-width of antenna. Because not only increased the amplitude of reflected signal from a target, but also increased the amplitude of reflected signals from clutters as same ratio when the output power of radar is increased. That makes to maintain TCR (Target to Clutter Ratio), there is no the improvement of the direction estimation of a target. Even there are signal processing techniques to improve TCR, the fundamental solution is the reduction of the beam-width of antenna. It means that concentrate radiation power to the specified direction where seems to exist a target. An antenna has the intrinsic radiation pattern depended the variation of the electric current distribution on its aperture. Radiation pattern can discriminate the space by the irradiated intensity, and its directionality is expressed as a beam. Simple method to reduction of the beam-width of antenna is the increase of aperture area of antenna. Because the radiation pattern is acquired from electric current distribution on the aperture by Fourier transform. However if a target is not put on the straightforward of the aperture, it is difficult to discriminate a target signal from clutters signals. To turn the direction of a beam, mechanical and electrical methods are existed. The mechanical ways are the change of the physical movement or the physical configuration of an antenna using the rotator or the actuator, respectively. The electrical ways are based on the change of the electric current distribution of the antenna aperture using feeding methods. However previous mentioned methods have restriction in views of the reliability and the efficiency. At those reasons, beamforming techniques are adapted versatilely for detecting and tracking.

Beamforming

Beamforming is a beam-generation technique using the arrangement of antenna elements. Varying phases and amplitudes of signals fed antenna elements, a beam can be created with an arbitrary form. Generated beams have the orthogonality in the time, the frequency and the space. First, the time orthogonality is achieved by the arrangement of active components such as switch circuits, amplifiers and attenuators, and active phase shifters as shown in Fig. 1.5(a). Precise controls of beam direction and gain can be achieved without complex computation. However the selected single direction can be accessible or detectable in the specified time, because the antenna design structure of the time orthogonality is SPNT (Single Pole N Throw). Sometimes the scanning algorithm is required to cover the access or the detection areas. And active phase shifters have high insertion loss and active components are expensive. Second, the frequency orthogonality is realized by the frequency dependency of the physical structure as shown in Fig. 1.5(b). Like the leaky wave antenna, electrical length is varied by frequency variation in the given physical length. Orthogonal multiple beams can be generated simultaneously in the simple structure, but the spectrum efficiency is decreased. Third, the spatial orthogonality is acquired by the arrangement of passive components such as hybrid and cross couplers, and passive phase shifters as shown in Fig. 1.5(c). It can operate multiple transmitting and multiple receiving simultaneously, however the number of components is larger than others. In 5G communication, one of candidate topology is that fixed large areas for moderate-rate data connections are covered by the existing network, but adaptive spot areas for high-rate data connections are covered by the beamforming network as shown in Fig. 1.6.

Beam-switching network

Beam-switching network is a discretized technique of the beamforming. When a specified input port is excited, the amplitude and the phase of the output ports is an orthogonal set to the outputs of other inputs. It makes the spatial orthogonality between generated beams. There are many topologies to design the beam-switching network such as Rotman lens, Blass matrix, Nolen matrix, and Butler matrix, etc. Rotman lens is designed that each propagation path has a different physical length to other propagation paths, and its difference is depended the position of input port and the distance between propagation paths on the aperture as shown in Fig. 1.7(a). Because the difference between physical lengths is not changed, therefore the interval between electrical lengths is maintained by frequency variation [1.11]. At that reason, Rotman lens has wide operating bandwidth, however it is restricted by the spillover unwanted propagation paths and increases SLL (Side Lobe Level). So the absorber or the mated load are surrounded or placed between the focal surface and the inner surface of the lens to dissipate the spillover. When the input port moves from the center to the boundary on the focal surface, the spillover is increased because of its spatial dependency. It makes to increase the insertion loss and the discrepancy of the realized gain. Blass matrix consists of hybrid couplers with different coupling coefficients for the power dividing and transmission lines with different electrical lengths for the phase shifting [1.12]. Because hybrid couplers and transmission lines are arranged like a mesh, Blass matrix can be simply designed and fabricated as shown in Fig. 1.7(b). However, it has relatively large insertion loss because of the existence of matched load, and the multiple reflections are happened because of the existence of detour paths. And there are many the numbers of hybrid couplers and transmission lines. Nolen matrix is an improved topology of Blass matrix [1.13]. In comparison with Blass matrix, it has no matched load when $M=N$ and the number of hybrid couplers reduces from MN to $(N-1)(M-1)-(N-1)(N-2)/2$ when $M>N$ or $(N-1)(M-1)-(M-1)(M-2)/2$ when $M<N$ as shown in Fig. 1.7(c). It makes to decrease the insertion loss and the multiple reflections. However it still should be considered adaptive coupling coefficients and phase delays. Butler matrix is a multi-port symmetric beam-switching network [1.14]. Butler matrix consists of quadrature hybrid couplers, cross couplers, and phase shifters as shown in Fig. 1.7(d). The number of the orthogonal beams is corresponded to the number of the input ports given as $N=2^n$ where n is an integer. Ideal Butler matrix is lossless and the number of hybrid couplers is reduced to $N\log_2^N$. As mentioned previously, the radiation pattern is related the spatial Fourier transform. So the beam-switching network can be expressed as Fourier transform. When the numbers of the input ports and the output ports are same and $N=2^n$, Blass matrix and Butler matrix are worked as DFT (Discrete Fourier Transform, the complexity $\Theta(N^2)$) and FFT (Fast Fourier Transform, the complexity $\Theta(N\log_2^N)$), respectively [1.15]-[1.16].

2-D Beam-switching network

Because actual coverage and scanning area for communication and radar applications are placed on 2-dimensional space, the beam-switching network is required to work on the same space. Basically, 2-D beam-switching network is formed as the connections between horizontally and vertically stacked 1-D beam-switching networks as shown in Fig. 1.8. Each stacked 1-D beam-switching network is in charge of the orthogonal functionality of beam-switching, and occupies the orthogonal volume to the other [1.17]-[1.18]. Another method is the reconfiguration of the component arrangement of the beam-switching matrix [1.19]. On the other hand, one-body 2-D beam-switching Rotman lens is designed by the insertion of a dimension and focal points as shown in Fig. 1.9 [1.20]. Because one-body 2-D beam-switching Rotman lens shares the orthogonal volumes with the orthogonal functionalities, it has less a volume and an insertion loss than the stacked and the connected 1-D beam-switching Rotman lenses. However its fabrication difficulty is increased because of its 3-D structure with a space curvature. The beam-switching matrix has a fractal-like structure, so easily expanding and fabricating. Unfortunately, there was no the one-body 2-D beam-switching matrix before the author proposed, fabricated, and evaluated of one-body 2-D beam-switching Butler matrix [1.21].

Short-slot coupler

The performance of the beam-switching matrix is depended on the performance of the hybrid coupler which combines and divides the input signal(s). There are several types of the hybrid coupler such as coupled-line coupler, branch-line coupler, Lange coupler, hybrid ring coupler, magic-Tee, Bethe-hole coupler, Schwinger reversed-phase coupler, Moreno crossed-guide coupler, and Riblet short-slot coupler, etc. [1.22]. These hybrid couplers can be divided into two types which are the transmission line and the waveguide. The transmission line type hybrid couplers propagate waves a form of quasi-TEM mode in the transmission line. These propagated waves are attenuated by losses due to electrical conductivities metal and dielectric material, dielectric loss tangent, and radiation. On the other hand, the waveguide type hybrid couplers propagate wave forms of non-TEM modes in the waveguide, except with coaxial waveguide. In the hollow waveguide, the propagated waves have only the conduction loss. In view of the large-scaled beam-switching matrix, the important design considerations are the insertion loss and the volume. At that reason, the author selected the hollow waveguide short-slot coupler. The short-slot coupler was proposed by Riblet in 1952 [1.23]. It has a waveguide structure with two input and two output ports as shown in Fig. 1.10. In the coupled region, two propagating modes (E-plane: TE10, TE11, H-plane: TE10, TE20) are generated with the orthogonal polarity of electric field [1.24]. A width and a length of the coupled region determine the coupling coefficients and the propagation constants of propagating modes, respectively. As a quadrature hybrid coupler, two output ports have -3 dB amplitude, and 90° phase difference between output ports. When the length of the coupled region of the short-slot coupler is a twice of short-slot hybrid coupler's, it works as the cross coupler. These short-slot couplers are inserted as the fundamental component into several microwave circuits such as high power circuit [1.25], directional filter and multiplexer [1.26], and beam-switching network [1.27]. Satisfying the design specification of microwave circuits, the short-slot couplers are devised to reduce its volume and loss [1.28]-[1.30], or increase its operating bandwidth [1.31], [1.32]. Basically, the length of the coupled region (≈the volume) and the operating frequency bandwidth are trade-off relationship. However the existing short-slot couplers did not meet the requirement equipped four input and four output ports for the one-body 2-D beam-switching Butler matrix.

1.2 Objectives of the research

Compact and low loss 2-D beam-switching matrix is required in communication and radar. One-body 2-D beam-switching Rotman lens has a small volume, but its spillover loss makes large the insertion loss. Hollow waveguide 2-D beam-switching matrix has a small the insertion loss, but it requires a large volume because of the absence of the one-body structure. This research activity is concentrated on the development of 2-D beam-switching network and its components. The author devised the short-slot 2-plane coupler and the one-body 2-D beam-switching Butler matrix to catch low insertion loss and small volume together for communication, radar, and other application.

The objectives of the research are as follows:

- To analyze and utilize the characteristic of propagating and evanescent modes.
- To design, fabricate, and evaluate short-slot 2-plane coupler and one-body 2-D beam-switching Butler matrix.
- To suggest the design guideline of 2-D beam-switching network based on the performance limitation.
- To investigate the feasibility of other applications using short-slot 2-plane coupler.

1.3 Contents of dissertation

The structure of dissertation is shown in Fig. 1.11. The remained chapters are briefed as follows.

Chapter 2 presents the design procedures of short-slot 2-plane coupler based on the orthogonality of electric field. Four orthogonal output signal sets are derived from the combinations of four orthogonal propagating modes in the coupled region. The roles of the short-slot 2-plane coupler as hybrid and cross couplers are determined by the length of the coupled region. Chapter 3 presents the improving method of the bandwidth of the short-slot 2-plane coupler using the relationship between four propagating modes and three complementary modes. Chapter 4 presents the design, the simulation and the measurement, and the evaluation of one-body 2-D beam-switching waveguide Butler matrix with short-slot 2-plane couplers. Chapter 5 presents the wideband and the large-scaled one-body 2-D beam-switching waveguide Butler matrix. Chapter 6 presents the summary and the future works of the research.

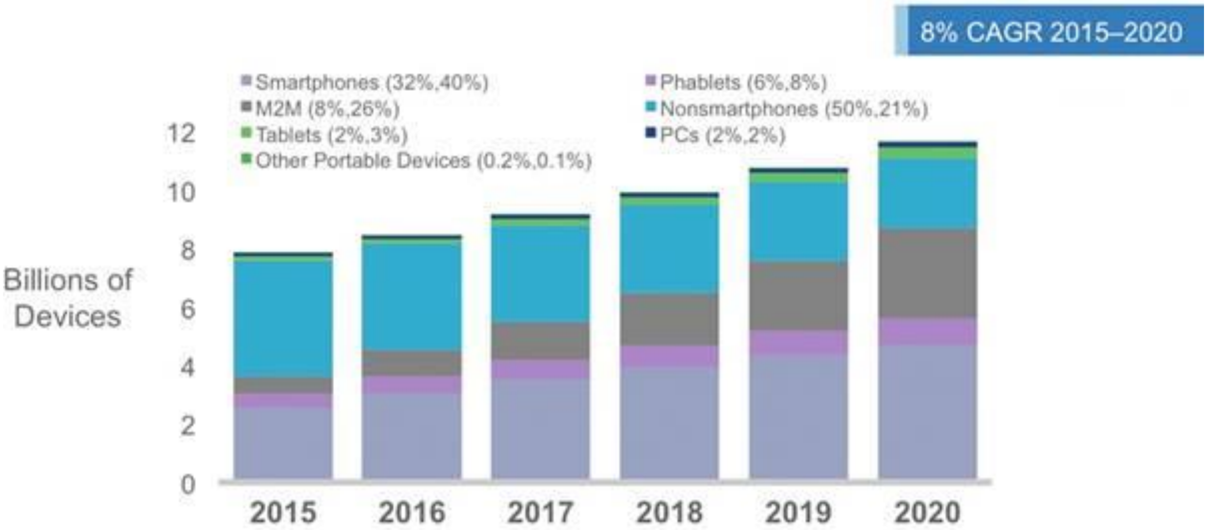

Fig. 1.1 Global Mobile Devices and Connections Growth. (Source: Cisco VNI Mobile, 2016)

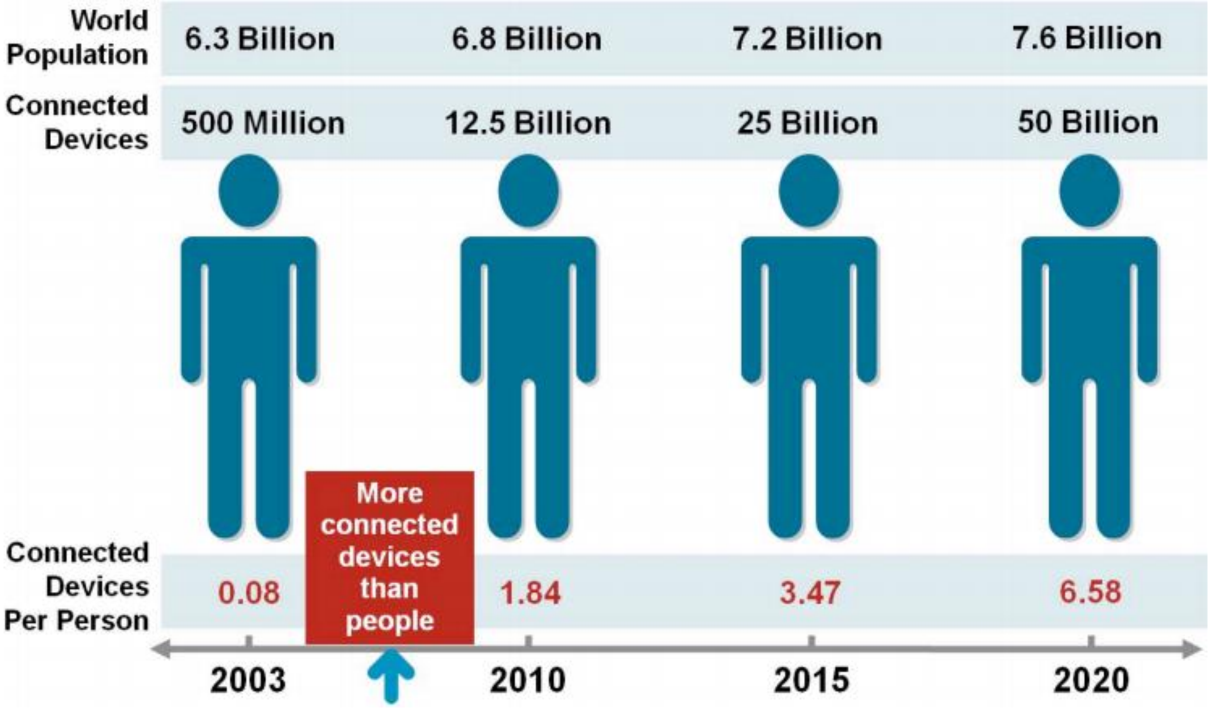

Fig. 1.2 The Internet of Things Was "Born" Between 2008 and 2009.

(Source: Cisco IBSG, Apr. 2011)

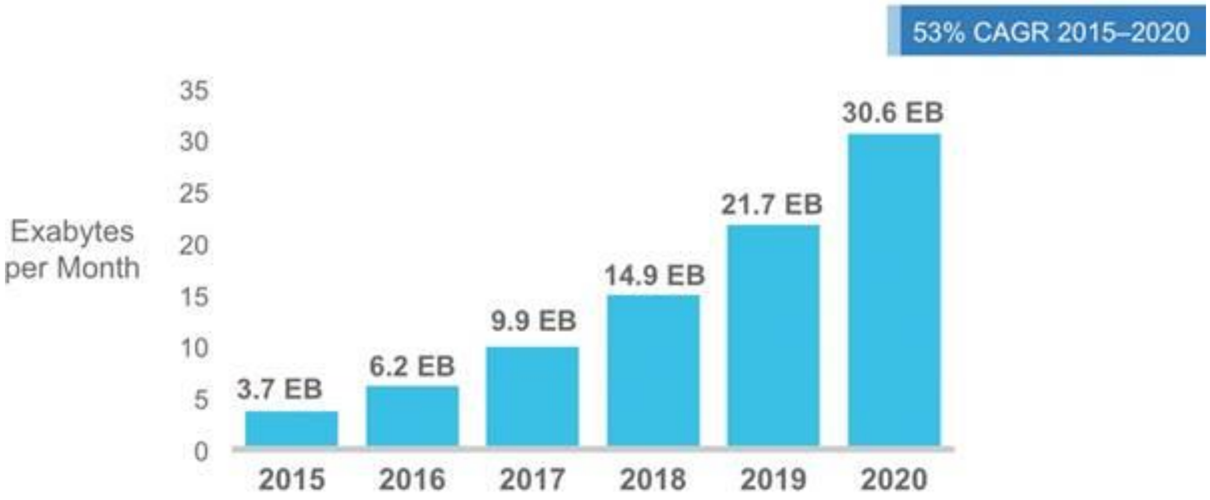

Fig. 1.3 Cisco Forecasts 30.6 Exabyte per Month of Mobile Data Traffic by 2020.

(Source: Cisco VNI Mobile, 2016)

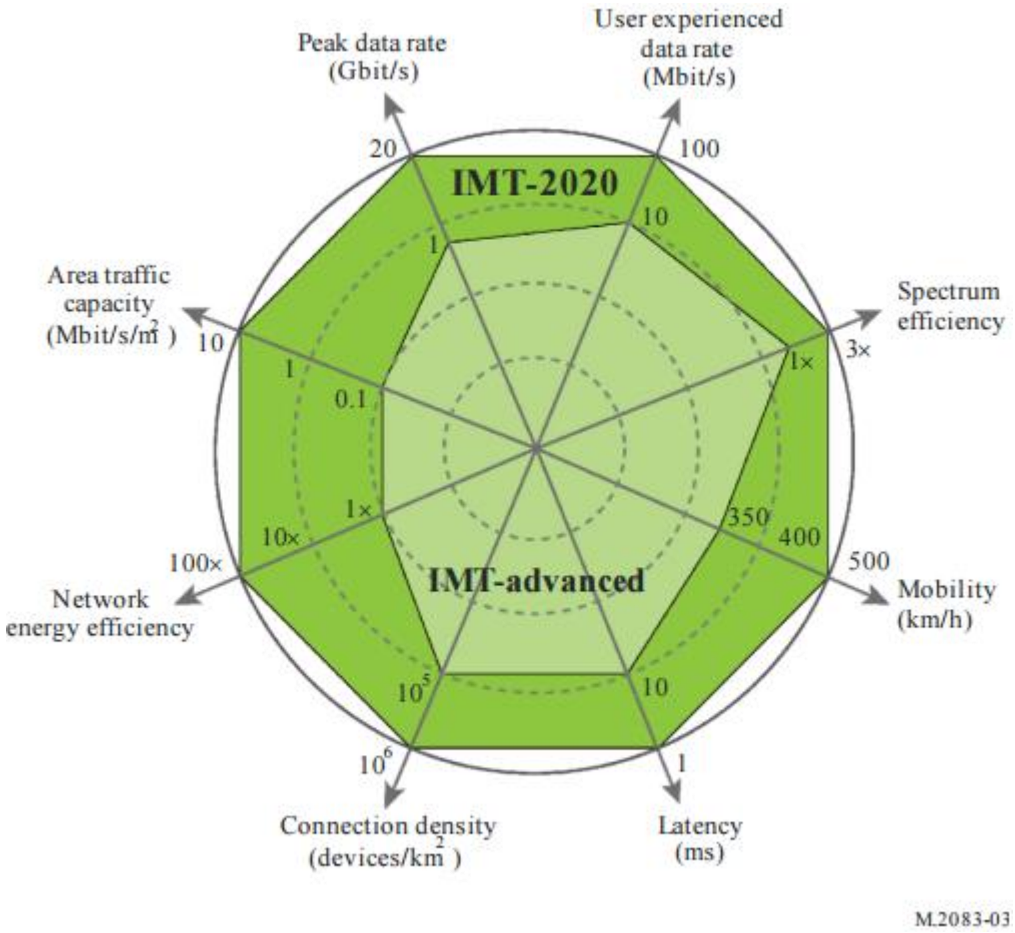

Fig. 1.4 Enhancement of key capabilities from IMT-Advanced to IMT-2020.

(Source: ITU-R, Sep. 2015)

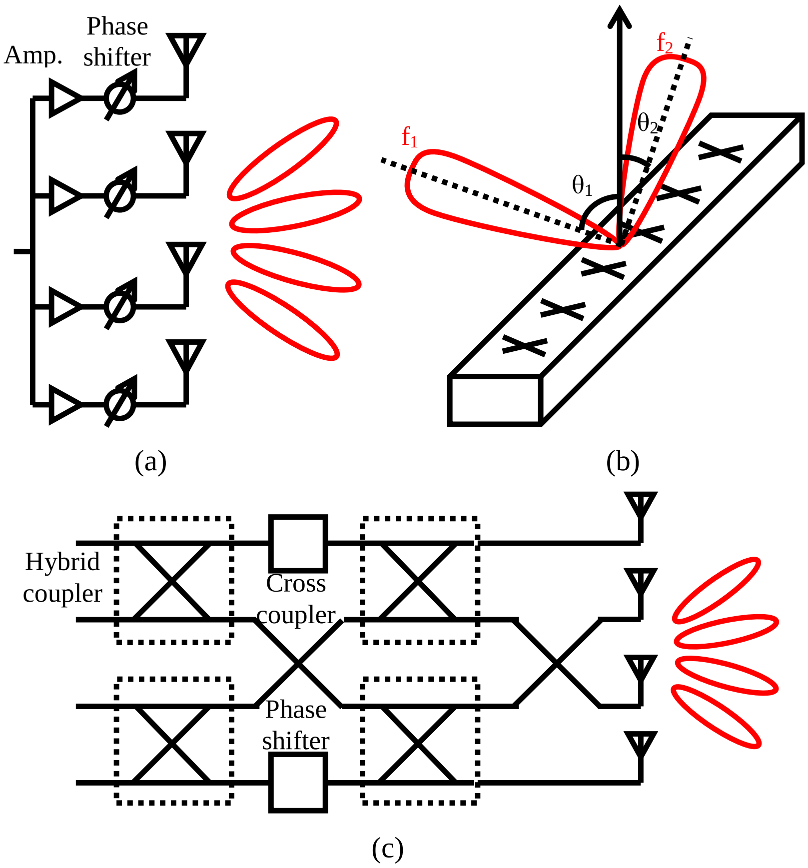

Fig. 1.5 Orthogonality of beamforming (a) Time (b) Frequency (c) Spatial.

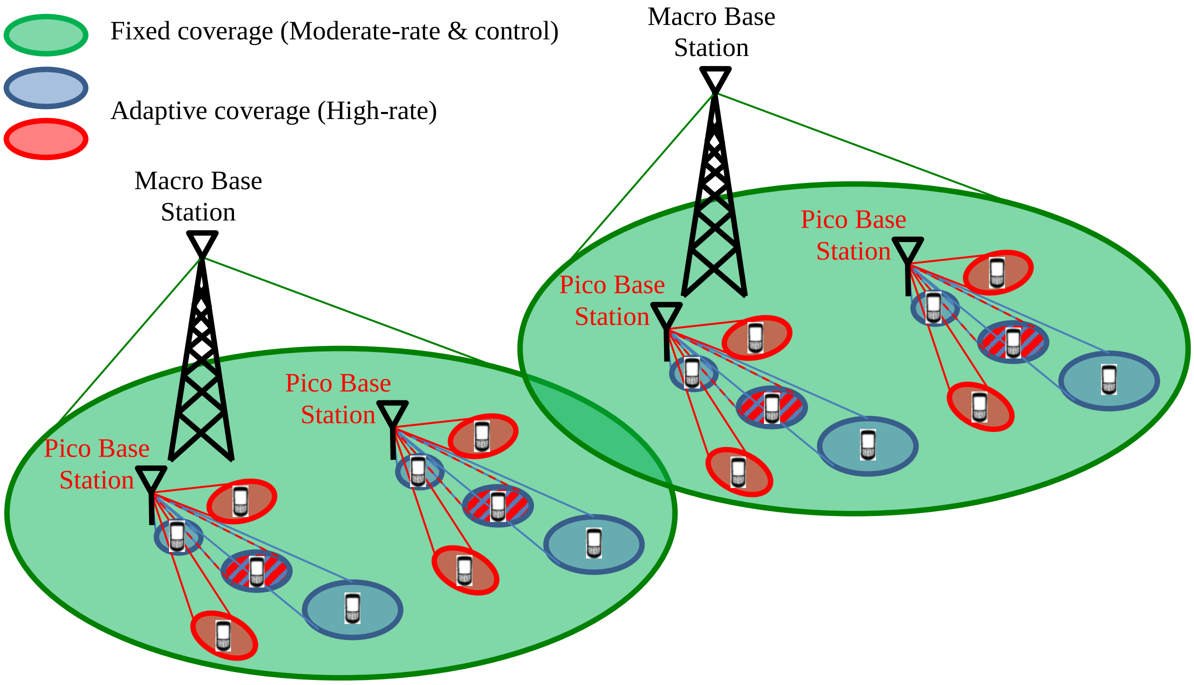

Fig. 1.6 Beamforming network for 5G (candidate).

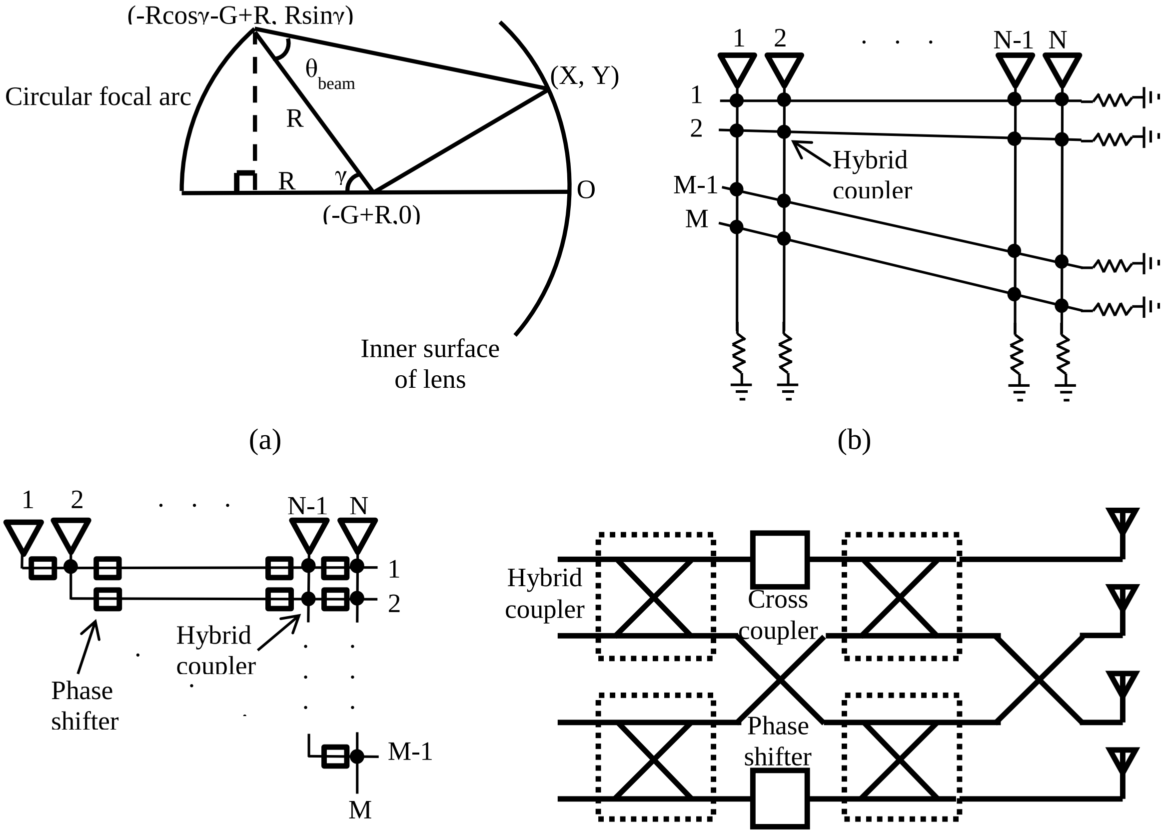

(a) (b)

(c) (d)

Fig. 1.7 Beam-switching network (a) Rotman lens (b) Blass Matrix (c) Nolen Matrix (d) Butler Matrix.

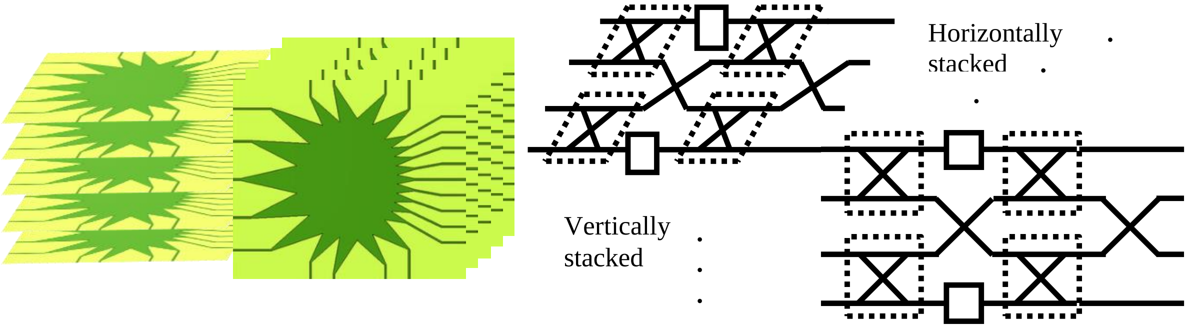

(a) (b)

Fig. 1.8 2-D beam-switching stacked network (a) Rotman lens (b) Butler matrix.

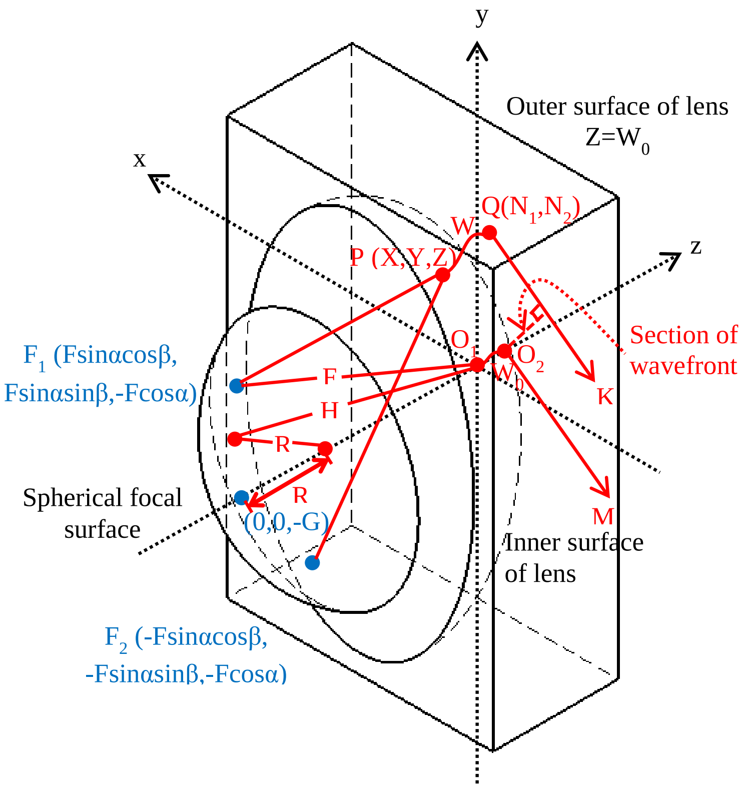

Fig. 1.9 One-body 2-D beam-switching Rotman lens.

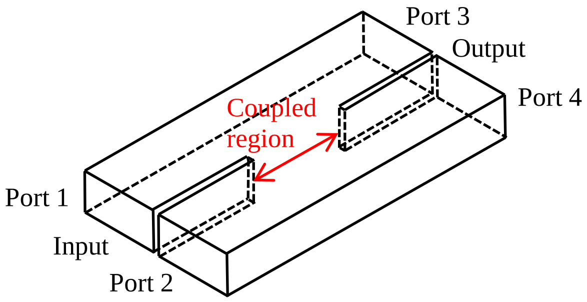

Fig. 1.10 Short-slot coupler.

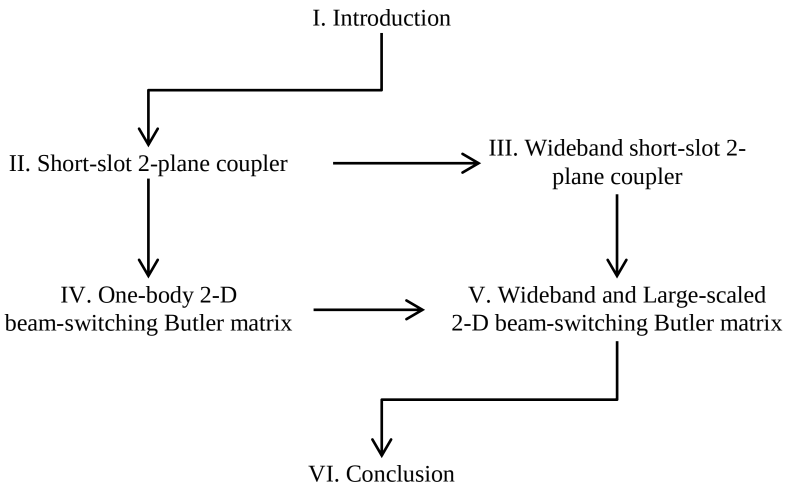

Fig. 1.11 Structure of dissertation.

Table 1.1 Summary of Per-Device Usage Growth, MB per Month. (Source: Cisco VNI Mobile, 2016)

Device Type	2015	2020
Non-smartphone	23 MB/month	116 MB/month
M2M module	164 MB/month	670 MB/month
Wearable device	153 MB/month	558 MB/month
Smartphone	929 MB/month	4,406 MB/month
Tablet	2,576 MB/month	7.079 MB/month
PC	2,679 MB/month	5,232 MB/month

Reference

[1.1] Leland I. Anderson, *Nikola Tesla On His Work With Alternating Currents and Their Application to Wireless Telegraphy, Telephony, and Transmission of Power*. Breckenridge, CO: 21st Century Books, 2002.

[1.2] 3GPP (2016, Aug.) LTE ue-Category, [Online] Available: http://www.3gpp.org/keywords-acronyms/1612-ue-category

[1.3] Cisco (2016, Feb.), Cisco VNI Mobile Forecast (2015-2020), [Online] Available: http://www.cisco.com/c/en/us/solutions/collateral/service-provider/visual-networking-index-vni/mobile-white-paper-c11-520862.html

[1.4] Dave Evans (2011, Apr.), The Internet of Things: How the Next Evolution of the Internet Is Changing Everything, Cisco IBSG.

[1.5] NHK, 8K Super Hi-Vision (8K SHV), Japan, [Online] Available: https://www.nhk.or.jp/strl/onepoint/data/8kgaiyo_e.pdf

[1.6] GSMA (2014), The Mobile Economy, [Online] Available: https://www.gsmaintelligence.com/research/?file=bb688b369d64cfd5b4e05a1ccfcbcb48&download

[1.7] Ministry of Science, ICT and Future Planning (2013, Oct.), ICT R&D mid/long term strategy (2013-2017), Korea.

[1.8] 3GPP TSG RAN WG1 Meeting #85 (2016, May), RAN1 Chairman's Notes.

[1.9] ITU-R (2015, Sep.), Recommendation ITU-R M.2083-0: IMT Vision – Framework and overall objectives of the future development of IMT for 2020 and beyond.

[1.10] Daniel N. Lapedes, *McGraw-Hill dictionary of scientific and technical terms*. New York: McGraw-Hill, 1976.

[1.11] W. Rotman and R. F. Turner, "Wide angle microwave lens for line source application," *IEEE Trans. Antennas Propag.*, vol. AP-11, pp. 623-630, Nov. 1963.

[1.12] J. Blass, , "Multidirectional antenna - A new approach to stacked beams," *IRE Int. Conf. Record*, vol. 8, 48–50, 1960.

[1.13] J. Nolen, "Synthesis of multiple beam networks for arbitrary illuminations," Ph.D. dissertation, Radio Division, Bendix Corp., Baltimore, MD, Apr. 1965.

[1.14] J. Butler and R. Lowe, "Beam-forming matrix simplifies design of electronically scanned antennas," *Electron. Des.*, vol.9, no. 8, pp. 170-173, Apr. 1961.

[1.15] W, Nester, "The fast Fourier transform and the Butler matrix," *IEEE Trans. Antennas Propag.*, vol. 16, no. 3, p. 360, 1968.

[1.16] J. W. Cooley and J. W. Tukey, "An algorithm for the machine calculation of complex fourier series," *Math. of Comput.*, 19, pp. 297-301, 1965.

[1.17] K. K. Chan and S. K. Rao, "A Rotman lens feed network for a hexagonal array of oversized radiating elements," *IEEE Intl. Symp. Antennas Propag.*, vol. 1, Salt Lake City, UT., Jul. 2000, pp. 202–205.

[1.18] B. Pattan, "The Versatile Butler Matrix," *Microw. Journal*, vol. 47, no. 11, pp. 126-138, 2004.

[1.19] W. F. Moulder, W. Khalil, and J. L. Volakis, "60-GHz two-dimensionally scanning array employing wideband planar switched beam network," *IEEE Antennas Wireless Propag. Lett.*, vol. 9, pp. 818–821, 2010.

[1.20] J. Rao, "Multifocal three-dimensional bootlace lenses," *IEEE Trans. Antennas Propag.*, vol. 30, no. 6, pp. 1050-1056, 1982.

[1.21] D.-H. Kim, J. Hirokawa, and M. Ando, “One-body 2-D Beam-switching Butler Matrix with Waveguide Short-slot 2-plane Couplers,” *IEICE Trans. Electron.*, vol. xx, no. xx, pp. xxx-xxx, xxx. 2017.

[1.22] D. M. Pozar, “Power Dividers and Directional Couplers,” in *Microwave Engineering*, 2nd Edition, New York: John Wiley & Sons, 1998, pp. 368-416.

[1.23] H. J. Riblet, “The short-slot hybrid junction,” *Proc. IRE*, vol. 40, pp. 180-184, Feb. 1952.

[1.24] J. A. Ruiz-Cruz, J. R. Montejo-Garai, and J. M. Rebollar, “Short-slot E- and H-plane waveguide couplers with an arbitrary power division ratio,” *Intl. J. of Electron.*, vol. 98, no. 1, pp. 11-24, 2011.

[1.25] L. Young, B.M. Schiffman, “Pulse Power Capacity of Short-Slot Couplers,” *IEEE Trans. Microw. Theory Techn.*, vol. 13, no. 1, pp. 133, 1965.

[1.26] G. L. Matthaei, L. Young, and E. M. T. Jones, *Microwave Filter, Impedance-Matching Networks, and Coupling Structures.*, Artech House, 1980.

[1.27] S. Yamamoto, J. Hirokawa, and M. Ando, “A Beam Switching Slot Array with a 4-Way Butler Matrix Installed in a Single Layer Post-Wall Waveguide,” *IEEE Intl. Symp. Antennas Propag.*, vol. 1, pp. 138–141, 2002.

[1.28] L. T. Hildebrand, “Results for a simple compact narrow-wall directional coupler,” *IEEE Microwave Guided Wave Lett.*, vol. 10, pp. 231–232, June 2000.

[1.29] S. Yamamoto, J. Hirokawa, and M. Ando, “A single-layer hollow-waveguide 8-way Butler matrix,” *IEEE Intl. Symp. Antennas Propag.*, vol. A1, pp. 647–650, 2005.

[1.30] S. Yamamoto, J. Hirokawa, and M. Ando, “Length reduction of short-slot directional coupler in a single layer dielectric substrate waveguide by removing dielectric near the side walls,” *IEEE Intl. Symp. Antennas Propag.*, vol. 3, pp. 2353–2356, 2004.

[1.31] U. Rosenberg and K. Beis, “Improved narrow-wall short slot coupler design exhibiting significant increased bandwidth and low cost production,” *Proc. 31st Eur. Microw. Conf.*, vol. 3, pp. 197-200, Sep. 2001.

[1.32] R. Beyer and U. Rosenberg, "Compact top-wall hybrid/coupler design for extreme broad bandwidth application," *IEEE MTT-S Intl. Symp. Dig.*, pp. 1227-1280, June 2005.

Chapter 2

Short-slot 2-plane coupler

The coupler is a key component of passive microwave circuits, especially Butler matrix. It dominates to not only the frequency performance, but also volumetric occupancy. Required characteristics of coupler and Butler matrix are focused on the loss and the volume in this dissertation. In view of the loss, the waveguide type couplers have the conduction and the dielectric loss, but the transmission line couplers include the radiation loss additionally. Among the waveguide type couplers, the short-slot coupler has simple structure to fabricate. To reduce the volume of the short-slot coupler, several techniques were applied the coupled region such as inserting metallic post, dielectric-filled waveguide with air hole, or stepped structure, etc. However those techniques have the fabrication and the performance problems. In this chapter, single coupler acquires four orthogonal outputs using the art of propagating modes. It is called the short-slot 2-plane coupler which has 2-plane modal orthogonality in the coupled region. Following sections, the operation principal, the design procedures, and the simulation and the measurement results of the short-slot coupler are presented.

2.1 Short-slot E- and H-plane couplers

2.1.1 Theory

Short-slot coupler has the waveguide structure with two input and two output ports. It is formed by connecting and removing E- or H-plane walls of two rectangular waveguides as shown in Fig. 2.1. Input and output port branches have same the aperture, and its height permits TE_{10} mode only to pass as the propagating mode. In the coupled region, its aperture has almost twice of the height (E-plane coupler) or the width (H-plane coupler) of the port branch's. In the coupled regions of short-slot E- and (H-)plane couplers, TE_{10} and TM_{11} (TE_{10} and TE_{20}) modes can exist as propagating modes. The propagation constant β_{mn} and the cutoff frequency f_{cmn} of propagating mode TE_{mn} are expressed as

$$\beta_{mn} = \sqrt{\omega^2\mu\varepsilon - \left(\left(\frac{m\pi}{a}\right)^2 + \left(\frac{n\pi}{b}\right)^2\right)} \tag{2.1}$$

$$f_{cmn} = \frac{1}{2\pi\sqrt{\mu\varepsilon}}\sqrt{\left(\frac{m\pi}{a}\right)^2 + \left(\frac{n\pi}{b}\right)^2} \tag{2.2}$$

where m and n are a positive integer included zero, ω is the angular frequency, μ is the electrical permeability, ε is the electrical permittivity, a and b are the width and the height of the coupled region, respectively.

When the input port 1 is excited with +y-direction polarized electric field component +*Ey*, the electric field distributions corresponded propagating modes in the coupled region are expressed as red arrow lines in Fig. 2.2. The polarities of electric field distribution at the boundary between the coupled region and the output port branches are symbolized as "+" and "-". These polarities of the propagating mode TE_{mn} are expressed as the elements of output vector v_{mn} with [+,+]=[1,1] and [+,-]=[1,-1]. Two propagating modes in the coupled region are orthogonal, and it is simply verified as

$$\mathrm{v}_{mode,i}\mathrm{v}_{mode,j}^{T} = \delta_{ij} \tag{2.3}$$

where v^T is transpose of v, δ_{ij} is Kronecker delta.

As a coupler, the short-slot coupler has an input, a through, a coupled, and an isolated ports. If port 1 is set an input port, port 2~4 are corresponded an isolated, a through, and a coupled ports, respectively. In the matched state, there are no transmitted powers to the input and the isolated ports. In the lossless and the reciprocal conditions of short-slot E-plane coupler, two output signals are derived from the combinations of two propagating modes as

$$E_3 = C_{TE_{10}} e^{-j\beta_{TE_{10}} l_{type}} + C_{TM_{11}} e^{-j\beta_{TM_{11}} l_{type}} \tag{2.4}$$

$$E_4 = C_{TE_{10}} e^{-j\beta_{TE_{10}} l_{type}} - C_{TM_{11}} e^{-j\beta_{TM_{11}} l_{type}} \tag{2.5}$$

$$|E_3|^2 + |E_4|^2 = 1 \tag{2.6}$$

where C_{TEmn} is a coupling coefficient of TE_{mn} mode, l_{type} is the length of the coupled region of a coupler type (*H*ybrid or *C*ross).

To work as hybrid and cross couplers, the required output signals are

$$\text{Hybrid coupler } |E_3|^2 = |E_4|^2 = \frac{1}{2} \tag{2.7}$$

$$\text{Cross coupler } |E_3|^2 = 0,\ |E_4|^2 = 1 \tag{2.8}$$

With six unknowns β_{TE10}, β_{TE11}, C_{TE10}, C_{TE11}, l_H and l_C, there are only four equations. For that reason, two unknowns are remained as functions of other unknowns. First, Eqs. (2.4) and (2.5) are inserted into Eqs. (2.7) and (2.8)

$$\left(C_{TE_{10}} \cos\beta_{TE_{10}} l_H + C_{TM_{11}} \cos\beta_{TM_{11}} l_H\right)^2 + \left(C_{TE_{10}} \sin\beta_{TE_{10}} l_H + C_{TM_{11}} \sin\beta_{TM_{11}} l_H\right)^2 = \frac{1}{2} \tag{2.9}$$

$$\left(C_{TE_{10}} \cos\beta_{TE_{10}} l_H - C_{TM_{11}} \cos\beta_{TM_{11}} l_H\right)^2 + \left(C_{TE_{10}} \sin\beta_{TE_{10}} l_H - C_{TM_{11}} \sin\beta_{TM_{11}} l_H\right)^2 = \frac{1}{2} \tag{2.10}$$

$$\left(C_{TE_{10}} \cos\beta_{TE_{10}} l_C + C_{TM_{11}} \cos\beta_{TM_{11}} l_C\right)^2 + \left(C_{TE_{10}} \sin\beta_{TE_{10}} l_C + C_{TM_{11}} \sin\beta_{TM_{11}} l_C\right)^2 = 0 \tag{2.11}$$

$$\left(C_{TE_{10}} \cos\beta_{TE_{10}} l_C - C_{TM_{11}} \cos\beta_{TM_{11}} l_C\right)^2 + \left(C_{TE_{10}} \sin\beta_{TE_{10}} l_C - C_{TM_{11}} \sin\beta_{TM_{11}} l_C\right)^2 = 1 \tag{2.12}$$

Second, considering C_{mode} a real, a positive, and a non-zero value, it can be derived from Eqs. (2.11) and (2.12)

$$C_{\mathrm{TE}_{10}} = C_{\mathrm{TM}_{11}} = \frac{1}{2} \tag{2.13}$$

Then, the remained unknowns are expressed as

$$cos\,\beta_{TE_{10}}l_H\,cos\,\beta_{TM_{11}}l_H + sin\,\beta_{TE_{10}}l_H\,sin\,\beta_{TM_{11}}l_H = cos\big(\beta_{TE_{10}}l_H - \beta_{TM_{11}}l_H\big) = 0 \quad (2.14)$$

$$cos\,\beta_{TE_{10}}l_C\,cos\,\beta_{TM_{11}}l_C + sin\,\beta_{TE_{10}}l_C\,sin\,\beta_{TM_{11}}l_C = cos\big(\beta_{TE_{10}}l_C - \beta_{TM_{11}}l_C\big) = -1 \quad (2.15)$$

$$\big(\beta_{TE_{10}} - \beta_{TM_{11}}\big)l_H = (2n+1)\frac{\pi}{2} \quad (2.16)$$

$$\big(\beta_{TE_{10}} - \beta_{TM_{11}}\big)l_C = (2n+1)\pi \quad (2.17)$$

where *n* is a positive integer included zero.

Finally, inserting derived unknowns into Eqs. (2.4) and (2.5), the output signals of the short-slot coupler are

$$E_3 = e^{-j(\beta_{TE_{10}}+\beta_{TM_{11}})l}\,cos\left(\big(\beta_{TE_{10}} - \beta_{TM_{11}}\big)\frac{l}{2}\right) \quad (2.18)$$

$$E_4 = -je^{-j(\beta_{TE_{10}}+\beta_{TM_{11}})l}\,sin\left(\big(\beta_{TE_{10}} - \beta_{TM_{11}}\big)\frac{l}{2}\right) \quad (2.19)$$

Mathematically, the short-slot coupler can be expressed as the transmission matrix.

$$\text{Hybrid coupler } \begin{bmatrix} b_3 \\ b_4 \end{bmatrix} = \frac{1}{\sqrt{2}}\begin{bmatrix} 1 & -j \\ -j & 1 \end{bmatrix}\begin{bmatrix} a_1 \\ a_2 \end{bmatrix} = \begin{bmatrix} v_{H,1} \; v_{H,2} \end{bmatrix}\begin{bmatrix} a_1 \\ a_2 \end{bmatrix} \quad (2.20)$$

$$\text{Cross coupler } \begin{bmatrix} b_3 \\ b_4 \end{bmatrix} = \begin{bmatrix} 0 & 1 \\ 1 & 0 \end{bmatrix}\begin{bmatrix} a_1 \\ a_2 \end{bmatrix} = \begin{bmatrix} v_{C,1} \; v_{C,2} \end{bmatrix}\begin{bmatrix} a_1 \\ a_2 \end{bmatrix} \quad (2.21)$$

$$\mathrm{v}_{type,i}\bar{v}_{type,j} = \delta_{ij} \quad (2.22)$$

where a_i and b_j are the coefficients of the input and the output ports, respectively, $v_{type,i}$ is a output vector corresponded to input port *i* of a coupler type (*H*ybrid or *C*ross), $\bar{v}$ is a complex conjugate of *v*, δ_{ij} is Kronecker delta.

To suppress the reflection at the excited input port, the length of the coupler region is decided to cancel-out the incident and the reflected waves in the coupled region as shown in Fig. 2.3 [2.1]. It is difficult to suppress two propagating modes at same time, TM_{11} mode is selected because of its large reflection. It can be expressed as

$$1 + \Gamma_{TM_{11}}^2 e^{-j2\beta_{TM_{11}}l} = 1 + e^{-j2\beta_{TM_{11}}l} = 0 \quad (2.23)$$

$$l = \frac{(2n+1)\pi}{2\beta_{TM_{11}}} \quad (2.24)$$

where Γ is a reflection coefficient on the boundary between the port branch and the coupled region.

When Eq. (2.24) is inserted into Eqs. (2.16) and (2.17), the propagation constant ratio between two propagating modes are

$$\frac{\beta_{TM_{11}}}{\beta_{TE_{10}}} = \begin{cases} \frac{2n+1}{2n+2}, hybrid\ coupler \\ \frac{2n+1}{2n+3}, cross\ coupler \end{cases} = \begin{cases} \frac{1}{2}, n = 0 \\ \frac{3}{5}, n = 1 \end{cases} \quad (2.25)$$

Then the length of the coupled region can be expressed by the wavelength of the propagating mode.

$$l = \begin{cases} \frac{\lambda_{TM_{11}}}{4}, hybrid\ coupler \\ \frac{3\lambda_{TM_{11}}}{4}, cross\ coupler \end{cases} \quad (2.26)$$

The operation of the short-slot H-plane coupler is also same as the short-slot E-plane coupler, change TM_{11} mode to TE_{20} mode, except the reflection suppression to TE_{10} mode.

Design procedure of the short-slot coupler is based on the previous mentioned derivations.

1. Choose the width and the height of the port branches *a* and *b* to pass TE_{10} mode only as the propagating mode in the port branch at target frequency band.
2. Set upper boundaries of the width and the height of the coupled region *a'* and *b'* to pass TE_{10} and TM_{11} (or TE_{20}) modes only as the propagating mode in the coupled region at target frequency band.
3. Adjust the mentioned design parameters with the position of the port branches to satisfy Eq. (2.13).
4. Choose the lengths of the coupled region to satisfy Eqs. (2.16) and (2.17) corresponded types of the short-slot coupler.

2.1.2 Simulation results

Using ANSYS© HFSS (High Frequency electromagnetic Field Simulation) which is FEM (Finite Element Method) based electromagnetic simulator, design and evaluate the short-slot couplers. All simulations are conducted on the lossless structure in 22 GHz band. Based on the design procedure 1 to 3, short-slot E- and H-plane couplers are designed for acquiring the coupling coefficient and the propagation constant of modes in the coupled region as shown in Fig. 2.4(a) and (b). At the center frequency 22 GHz, the propagating modes of the short-slot couplers in the coupled region are E-plane:TE_{10}, TE_{01}, TE_{11}, and TM_{11} modes, H-plane:TE_{10} and TE_{20} modes as shown in Fig. 2.4(c) and (d), respectively. The outputs of the short-slot E-plane coupler are affected by TE_{10}, TE_{11}, and TM_{11} modes, because TE_{01} mode has low coupling coefficient. And TE_{11} mode is regarded as a part of TM_{11} mode why it has same a propagation constant and polarities of electric field distribution. Amplitude of the coupling coefficient of combined TE_{11}/TM_{11} mode approaches -3 dB around the center frequency as shown in Fig. 2.4(e). In the same manner, the outputs of the short-slot H-plane coupler are affected by TE_{10} and TE_{20} modes which have -3 dB amplitudes around the center frequency as shown in Fig. 2.4(f). The flatness of output amplitudes and phases of short-slot couplers is depended on balancing the amplitude of the coupling coefficients and maintaining the difference between propagation constants of two propagating modes in the given frequency band. After the design of the coupled region, the lengths of the coupled region corresponded short-slot hybrid and cross couplers are given by the design procedure 4. Design parameters and drawings of the short-slot couplers are listed and in Table 2.1, and shown as Fig. 2.5(a), (b), (i), and (j), respectively. In the short-slot hybrid couplers, the output S31 and S41 have -3 dB amplitude and 90° phase difference between them around the center frequency as shown in Fig. 2.5(c)-(h). When the definition of the operating frequency band of the short-slot couplers is set to the output amplitudes of the short-slot hybrid coupler within -3±0.3 dB, the performances of the short-slot couplers are listed in Table 2.2, and shown as Fig. 2.5(c)-(h) and (k)-(n), respectively. In comparison with the short-slot H-plane coupler, the short-slot E-plane coupler has a narrow bandwidth. Considering the coupling coefficients and the propagation constants of propagating modes in the coupled region, those of the short-slot E-plane coupler are flatter than the short-slot H-plane coupler's. In 2.1.1, the electric field on the boundary between the coupled region and the output port branches is assumed that exists y-direction polarized only. However the actual electric field on the boundary between the coupled region and the output port branches has also x-direction polarized. Even TE_{11} and TM_{11} modes have different x-direction polarized electric fields. For that reason, the actual coupling coefficient of combined TE_{11}/TM_{11} mode is lower and less flat than assumed.

2.2 4×4-way short-slot combined coupler

2.2.1 Theory

For the design of the 3-D structure circuit such as the 2-D beam-switching matrix, there is a requirement about the component with the orthogonality. It can be expressed as

$$\mathrm{v}_i \bar{v}_j = \delta_{ij} \tag{2.27}$$

where v_i is a output matrix corresponded to input port i of a component, $\bar{v}$ is a complex conjugate of v, δ_{ij} is Kronecker delta.

The 1-D beam-switching Butler matrix has 1-D orthogonal outputs. However when the outputs of 1-D beam-switching Butler matrix are rearranged as 2-D array such as shown in Fig. 2.6(a), these 2-D rearranged output matrices have not the 2-D spatial symmetry. For example, the transmission matrix of 2-D rearranged 2×2 beam-switching Butler matrix is expressed as

$$\begin{bmatrix} b_5 \\ b_6 \\ b_7 \\ b_8 \end{bmatrix} = \frac{1}{2} \begin{bmatrix} \mathrm{e}^{-j\frac{\pi}{4}} & \mathrm{e}^{-j\frac{3\pi}{4}} & \mathrm{e}^{-j\frac{2\pi}{4}} & \mathrm{e}^{-j\frac{4\pi}{4}} \\ \mathrm{e}^{-j\frac{2\pi}{4}} & \mathrm{e}^{-j\frac{0\pi}{4}} & \mathrm{e}^{-j\frac{5\pi}{4}} & \mathrm{e}^{-j\frac{3\pi}{4}} \\ \mathrm{e}^{-j\frac{3\pi}{4}} & \mathrm{e}^{-j\frac{5\pi}{4}} & \mathrm{e}^{-j\frac{0\pi}{4}} & \mathrm{e}^{-j\frac{2\pi}{4}} \\ \mathrm{e}^{-j\frac{4\pi}{4}} & \mathrm{e}^{-j\frac{2\pi}{4}} & \mathrm{e}^{-j\frac{3\pi}{4}} & \mathrm{e}^{-j\frac{\pi}{4}} \end{bmatrix} \begin{bmatrix} a_1 \\ a_2 \\ a_3 \\ a_4 \end{bmatrix} = [v_1\ v_2\ v_3\ v_4] \begin{bmatrix} a_1 \\ a_2 \\ a_3 \\ a_4 \end{bmatrix} \tag{2.28}$$

where v_i is a output vector corresponded to input port i of 2-D rearranged 2×2 beam-switching Butler matrix.

Then the beam-direction in the spatial domain can be acquired when the array factor AF is maximized.

$$AF(\theta,\phi)=\left(\frac{1}{M}\frac{\sin\left(\frac{M}{2}\psi_x\right)}{\sin\left(\frac{\psi_x}{2}\right)}\right)\left(\frac{1}{N}\frac{\sin\left(\frac{N}{2}\psi_y\right)}{\sin\left(\frac{\psi_y}{2}\right)}\right) \tag{2.29}$$

$$\psi_x = kd_x \, sin\,\theta\, cos\,\phi + \beta_x \tag{2.30}$$

$$\psi_y = kd_y \, sin\,\theta\, sin\,\phi + \beta_y \tag{2.31}$$

where θ and ϕ are the elevation and azimuth angles of a beam-direction, M and N are the numbers of 2-D rearranged ports at x- and y-directions, k is a wavenumber, d_x and d_y are the physical distance between antenna elements at x- and y-directions, β_x and β_y are the progressive phase shift to x- and y-directions.

When d_x=d_y =0.726 λ_0, 2-D rearranged 2×2 beam-switching Butler matrix has four orthogonal beam-directions, but those have not the 2-D spatial symmetry.

$$[x_i, y_i] = [sin\,\theta_i\, cos\,\phi_i\,, sin\,\theta_i\, sin\,\phi_i] = \begin{bmatrix} (0.34{,}0.17) & (-0.34{,}0.52) \\ (0.34,-0.52) & (-0.34,-0.17) \end{bmatrix} \tag{2.32}$$

where $[x_i, y_i]$ is the position on 2-D spatial domain corresponded to input port i of 2-D rearranged 2×2 beam-switching Butler matrix. The modified 1-D beam-switching Butler matrix was proposed to solve this problem as shown in Fig. 2.6(b) [2.2]. In the waveguide structure, it is difficult to connect between the output ports of the modified 1-D beam-switching Butler matrix and the 2-D array antenna, required a large volume. For that reason, the 3-D structure component with the orthogonality is required to reduce the connection complexity and volume. Short-slot 1(E or H)-plane coupler has 1-D orthogonality determined by the configuration of its two output ports. When two output ports of a short-slot 1-plane coupler are arranged vertically, other 1-D orthogonality can be acquired by the horizontally arranged two output ports of another short-slot 1-plane coupler. The combination of these short-slot couplers have 2-D orthogonality, because these two orthogonality are independent each other. The minimum number of the ports for 2-D array antenna is four, so the combined component are required two vertically stacked short-slot 1-plane couplers and two horizontally stacked short-slot 1-plane couplers. At that time, the port branches of the short-slot couplers are settled same orientation, because there is no the requirement of twisted waveguides for connection. The drawings of stacked and short-slot combined couplers are depicted in Fig. 2.7. The transmission matrices of those couplers are expressed as

$$\begin{bmatrix} b_5 \\ b_6 \\ b_7 \\ b_8 \end{bmatrix} = \frac{1}{\sqrt{2}} \begin{bmatrix} 1 & 0 & -j & 0 \\ 0 & 1 & 0 & -j \\ -j & 0 & 1 & 0 \\ 0 & -j & 0 & 1 \end{bmatrix} \begin{bmatrix} a_1 \\ a_2 \\ a_3 \\ a_4 \end{bmatrix} = T_{H,E} \begin{bmatrix} a_1 \\ a_2 \\ a_3 \\ a_4 \end{bmatrix} \tag{2.33}$$

$$\begin{bmatrix} b_5 \\ b_6 \\ b_7 \\ b_8 \end{bmatrix} = \begin{bmatrix} 0 & 0 & 1 & 0 \\ 0 & 0 & 0 & 1 \\ 1 & 0 & 0 & 0 \\ 0 & 1 & 0 & 0 \end{bmatrix} \begin{bmatrix} \mathrm{a}_1 \\ \mathrm{a}_2 \\ \mathrm{a}_3 \\ \mathrm{a}_4 \end{bmatrix} = T_{\mathrm{C,E}} \begin{bmatrix} \mathrm{a}_1 \\ \mathrm{a}_2 \\ \mathrm{a}_3 \\ \mathrm{a}_4 \end{bmatrix} \tag{2.34}$$

$$\begin{bmatrix} b_5 \\ b_6 \\ b_7 \\ b_8 \end{bmatrix} = \frac{1}{\sqrt{2}} \begin{bmatrix} 1 & -j & 0 & 0 \\ -j & 1 & 0 & 0 \\ 0 & 0 & 1 & -j \\ 0 & 0 & -j & 1 \end{bmatrix} \begin{bmatrix} a_1 \\ a_2 \\ a_3 \\ a_4 \end{bmatrix} = T_{H,H} \begin{bmatrix} a_1 \\ a_2 \\ a_3 \\ a_4 \end{bmatrix} \tag{2.35}$$

$$\begin{bmatrix} b_5 \\ b_6 \\ b_7 \\ b_8 \end{bmatrix} = \begin{bmatrix} 0 & 1 & 0 & 0 \\ 1 & 0 & 0 & 0 \\ 0 & 0 & 0 & 1 \\ 0 & 0 & 1 & 0 \end{bmatrix} \begin{bmatrix} \mathrm{a}_1 \\ \mathrm{a}_2 \\ \mathrm{a}_3 \\ \mathrm{a}_4 \end{bmatrix} = T_{\mathrm{C,H}} \begin{bmatrix} a_1 \\ \mathrm{a}_2 \\ \mathrm{a}_3 \\ \mathrm{a}_4 \end{bmatrix} \tag{2.36}$$

$$T_{H,2} = \frac{1}{2} \begin{bmatrix} 1 & -\mathrm{j} & -\mathrm{j} & -1 \\ -\mathrm{j} & 1 & -1 & -\mathrm{j} \\ -\mathrm{j} & -1 & 1 & -\mathrm{j} \\ -1 & -\mathrm{j} & -\mathrm{j} & 1 \end{bmatrix} \tag{2.37}$$

$$T_{C,2} = \begin{bmatrix} 0 & 0 & 0 & 1 \\ 0 & 0 & 1 & 0 \\ 0 & 1 & 0 & 0 \\ 1 & 0 & 0 & 0 \end{bmatrix} \tag{2.38}$$

where a_i and b_j are the coefficients of the input and the output ports, respectively, $T_{type,plane}$ is a transmission matrix of short-slot (*E*, *H*, or *2*)-*plane* (*H*ybrid or *C*ross) *type* coupler.

Transmission matrix of the 4×4-way short-slot combined coupler is derived as products of transmission matrices of horizontally and vertically stacked short-slot 1-plane couplers. Transmission matrices of short-slot E- and H-plane couplers are commutative, because the product of symmetric matrices is symmetric (Appendix 1) [2.3].

$$T_{H,2} = T_{H,E} T_{H,H} = T_{H,H} T_{H,E} \tag{2.39}$$

$$T_{C,2} = T_{C,E} T_{C,H} = T_{C,H} T_{C,E} \tag{2.40}$$

Physical meaning of Eqs. (2.39) and (2.40) is that horizontally stacked short-slot 1-plane couplers and vertically stacked short-slot 1-plane couplers are able to switch their assembly order.

2.2.2 Simulation results

The 4×4-way short-slot combined coupler consists of horizontally stacked short-slot E-plane couplers and vertically stacked short-slot H-plane couplers designed in 2.2.1. as shown in Fig. 2.8(a) and (b). All simulations are conducted on the lossless structure in 22 GHz band. When the definition of the operating frequency band of the 4×4-way short-slot combined hybrid coupler is set to the output amplitudes within -6±0.5 dB, the performances of the 4×4-way short-slot combined couplers are listed in Table 2.3, and shown as Fig. 2.8(c)-(e), respectively. Because the characteristic of the cascaded circuit is followed by the worst performed component, the performances of the 4×4-way short-slot combined couplers are dominated by the short-slot E-plane coupler.

2.3 Short-slot 2-plane coupler

2.3.1 Theory

Although the 4×4-way short-slot combined coupler has relatively simpler structure and smaller volume than the modified 1-D beam-switching Butler matrix, there is still the requirement for reducing the volume and the complexity of the component. For that reason, author proposed the short-slot 2-plane coupler [2.3]. As shown in Fig. 2.9(a), it has the waveguide structure with 2×2 input and 2×2 output ports connected by the coupled region. Input and output port branches have same the aperture, and its height permits TE_{10} mode only to pass as the propagating mode. In the coupled region, its aperture has almost twice of the height and the width of the port branch's as shown in Fig. 2.9(b). Multiple propagating modes can exist in the coupled region of the short-slot 2-plane coupler. Within those propagating modes, at least four propagating modes with orthogonal polarities of electric field distribution should be selected to work as the 4×4-way short-slot combined coupler, because there are four orthogonal output expressed as Eqs. (2.34) and (2.35). When the input port 1 is excited with +y-direction polarized electric field component $+Ey$ and $a'>b'$, six propagating modes in the coupled region are selected, except TE_{01} (No y-direction polarity) and TE_{30} (Exceed the required number of propagating modes) modes. The electric field distributions and the polarities corresponded six propagating modes in the coupled region are expressed as red arrow lines and "+-" symbols in Fig. 2.10. These six propagating modes are classified four groups by the polarities, because TE/TM_{11} and TE/TM_{21} have each same the polarities. These polarities of the propagating mode are expressed as the elements of output vector v_{TE10}=[+,+,+,+]=[1,1,1,1], $v_{TE/TM11}$= [+,+,-,-]=[1,1,-1,-1], v_{TE20}= [+,-,+,-]=[1,-1,1,-1], and $v_{TE/TM21}$= [+,-,-,+]=[1,-1,-1,1]. Four propagating modes in the coupled region are orthogonal, and it is simply verified as

$$v_{mode,i}v_{mode,j}^{T} = \delta_{ij} \tag{2.41}$$

where v^T is transpose of v, δ_{ij} is Kronecker delta.

In the matched state, there are no transmitted powers to the input and the isolated ports. In the lossless and the reciprocal conditions of short-slot 2-plane coupler, four output signals are derived from the combinations of four propagating modes as

$$E_5 = C_1e^{-j\beta_1 l_{type}} + C_2e^{-j\beta_2 l_{type}} + C_3e^{-j\beta_3 l_{type}} + C_4e^{-j\beta_4 l_{type}} \tag{2.42}$$

$$E_6 = C_1e^{-j\beta_1 l_{type}} + C_2e^{-j\beta_2 l_{type}} - C_3e^{-j\beta_3 l_{type}} - C_4e^{-j\beta_4 l_{type}} \tag{2.43}$$

$$E_7 = C_1e^{-j\beta_1 l_{type}} - C_2e^{-j\beta_2 l_{type}} + C_3e^{-j\beta_3 l_{type}} - C_4e^{-j\beta_4 l_{type}} \tag{2.44}$$

$$E_8 = C_1e^{-j\beta_1 l_{type}} - C_2e^{-j\beta_2 l_{type}} - C_3e^{-j\beta_3 l_{type}} + C_4e^{-j\beta_4 l_{type}} \tag{2.45}$$

$$|E_5|^2 + |E_6|^2 + |E_7|^2 + |E_8|^2 = 1 \tag{2.46}$$

where C_i and β_i are a coupling coefficient and a propagation constant of mode (i=1→TE_{10}, i=2→TE/TM_{11}, i=3→TE_{20}, i=4→TE/TM_{21}), l_{type} is the length of the coupled region of a coupler type

(*H*ybrid or *C*ross).

To work as hybrid and cross couplers, the required output signals are

$$\text{Hybrid coupler}\ \ |E_5|^2 = |E_6|^2 = |E_7|^2 = |E_8|^2 = \frac{1}{4} \tag{2.47}$$

$$\text{Cross coupler}\ \ |E_5|^2 = |E_6|^2 = |E_7|^2 = 0,\ \ |E_8|^2 = 1 \tag{2.48}$$

With ten unknowns β_1, β_2, β_3, β_4, C_1, C_2, C_3, C_4, l_H and l_C, there are only eight equations. For that reason, two unknowns are remained as functions of other unknowns. First, Eqs. (2.42) to (2.45) are inserted into Eqs. (2.47) and (2.48)

$$(C_1 \cos\beta_1 l_H + C_2 \cos\beta_2 l_H + C_3 \cos\beta_3 l_H + C_4 \cos\beta_4 l_H)^2 + (C_1 \sin\beta_1 l_H + C_2 \sin\beta_2 l_H + C_3 \sin\beta_3 l_H + C_4 \sin\beta_4 l_H)^2 = \frac{1}{4} \tag{2.49}$$

$$(C_1 \cos\beta_1 l_H + C_2 \cos\beta_2 l_H - C_3 \cos\beta_3 l_H - C_4 \cos\beta_4 l_H)^2 + (C_1 \sin\beta_1 l_H + C_2 \sin\beta_2 l_H - C_3 \sin\beta_3 l_H - C_4 \sin\beta_4 l_H)^2 = \frac{1}{4} \tag{2.50}$$

$$(C_1 \cos\beta_1 l_H - C_2 \cos\beta_2 l_H + C_3 \cos\beta_3 l_H - C_4 \cos\beta_4 l_H)^2 + (C_1 \sin\beta_1 l_H - C_2 \sin\beta_2 l_H + C_3 \sin\beta_3 l_H - C_4 \sin\beta_4 l_H)^2 = \frac{1}{4} \tag{2.51}$$

$$(C_1 \cos\beta_1 l_H - C_2 \cos\beta_2 l_H - C_3 \cos\beta_3 l_H + C_4 \cos\beta_4 l_H)^2 + (C_1 \sin\beta_1 l_H - C_2 \sin\beta_2 l_H - C_3 \sin\beta_3 l_H + C_4 \sin\beta_4 l_H)^2 = \frac{1}{4} \tag{2.52}$$

$$(C_1 \cos\beta_1 l_C + C_2 \cos\beta_2 l_C + C_3 \cos\beta_3 l_C + C_4 \cos\beta_4 l_C)^2 + (C_1 \sin\beta_1 l_C + C_2 \sin\beta_2 l_C + C_3 \sin\beta_3 l_C + C_4 \sin\beta_4 l_C)^2 = 0 \tag{2.53}$$

$$(C_1 \cos\beta_1 l_C + C_2 \cos\beta_2 l_C - C_3 \cos\beta_3 l_C - C_4 \cos\beta_4 l_C)^2 + (C_1 \sin\beta_1 l_C + C_2 \sin\beta_2 l_C - C_3 \sin\beta_3 l_C - C_4 \sin\beta_4 l_C)^2 = 0 \tag{2.54}$$

$$(C_1 \cos\beta_1 l_C - C_2 \cos\beta_2 l_C + C_3 \cos\beta_3 l_C - C_4 \cos\beta_4 l_C)^2 + (C_1 \sin\beta_1 l_C - C_2 \sin\beta_2 l_C + C_3 \sin\beta_3 l_C - C_4 \sin\beta_4 l_C)^2 = 0 \tag{2.55}$$

$$(C_1 \cos\beta_1 l_C - C_2 \cos\beta_2 l_C - C_3 \cos\beta_3 l_C + C_4 \cos\beta_4 l_C)^2 + (C_1 \sin\beta_1 l_C - C_2 \sin\beta_2 l_C - C_3 \sin\beta_3 l_C + C_4 \sin\beta_4 l_C)^2 = 1 \tag{2.56}$$

Second, considering C_i is a real, a positive, and a non-zero value, it can be derived from Eqs. (2.53) and (2.56)

$$C_1 = C_2 = C_3 = C_4 = \frac{1}{4} \tag{2.57}$$

Then, the remained unknowns are expressed as

$$\cos\beta_1 l_H \cos\beta_3 l_H + \cos\beta_1 l_H \cos\beta_4 l_H + \cos\beta_2 l_H \cos\beta_3 l_H + \cos\beta_2 l_H \cos\beta_4 l_H + \sin\beta_1 l_H \sin\beta_3 l_H + \sin\beta_1 l_H \sin\beta_4 l_H + \sin\beta_2 l_H \sin\beta_3 l_H + \sin\beta_2 l_H \sin\beta_4 l_H = \cos(\beta_1 l_H - \beta_3 l_H) + \cos(\beta_1 l_H - \beta_4 l_H) + \cos(\beta_2 l_H - \beta_3 l_H) + \cos(\beta_2 l_H - \beta_4 l_H) = 0 \tag{2.58}$$

$$\cos\beta_1 l_H \cos\beta_2 l_H + \cos\beta_1 l_H \cos\beta_4 l_H + \cos\beta_2 l_H \cos\beta_3 l_H + \cos\beta_3 l_H \cos\beta_4 l_H + \sin\beta_1 l_H \sin\beta_2 l_H + \sin\beta_1 l_H \sin\beta_4 l_H + \sin\beta_2 l_H \sin\beta_3 l_H + \sin\beta_3 l_H \sin\beta_4 l_H = \cos(\beta_1 l_H -$$

$$\beta_2 l_H) + \cos(\beta_1 l_H - \beta_4 l_H) + \cos(\beta_2 l_H - \beta_3 l_H) + \cos(\beta_3 l_H - \beta_4 l_H) = 0 \tag{2.59}$$

$$\cos\beta_1 l_H \cos\beta_2 l_H + \cos\beta_1 l_H \cos\beta_3 l_H + \cos\beta_2 l_H \cos\beta_4 l_H + \cos\beta_3 l_H \cos\beta_4 l_H + \sin\beta_1 l_H \sin\beta_2 l_H + \sin\beta_1 l_H \sin\beta_3 l_H + \sin\beta_2 l_H \sin\beta_4 l_H + \sin\beta_3 l_H \sin\beta_4 l_H = \cos(\beta_1 l_H - \beta_2 l_H) + \cos(\beta_1 l_H - \beta_3 l_H) + \cos(\beta_2 l_H - \beta_4 l_H) + \cos(\beta_3 l_H - \beta_4 l_H) = 0 \tag{2.60}$$

$$\cos\beta_1 l_H \cos\beta_2 l_H - \cos\beta_1 l_H \cos\beta_3 l_H - \cos\beta_2 l_H \cos\beta_4 l_H + \cos\beta_3 l_H \cos\beta_4 l_H + \sin\beta_1 l_H \sin\beta_2 l_H - \sin\beta_1 l_H \sin\beta_3 l_H - \sin\beta_2 l_H \sin\beta_4 l_H + \sin\beta_3 l_H \sin\beta_4 l_H = \cos(\beta_1 l_H - \beta_2 l_H) - \cos(\beta_1 l_H - \beta_3 l_H) - \cos(\beta_2 l_H - \beta_4 l_H) + \cos(\beta_3 l_H - \beta_4 l_H) = 0 \tag{2.61}$$

$$\cos\beta_1 l_H \cos\beta_2 l_H - \cos\beta_1 l_H \cos\beta_4 l_H - \cos\beta_2 l_H \cos\beta_3 l_H + \cos\beta_3 l_H \cos\beta_4 l_H + \sin\beta_1 l_H \sin\beta_2 l_H - \sin\beta_1 l_H \sin\beta_4 l_H - \sin\beta_2 l_H \sin\beta_3 l_H + \sin\beta_3 l_H \sin\beta_4 l_H = \cos(\beta_1 l_H - \beta_2 l_H) - \cos(\beta_1 l_H - \beta_4 l_H) - \cos(\beta_2 l_H - \beta_3 l_H) + \cos(\beta_3 l_H - \beta_4 l_H) = 0 \tag{2.62}$$

$$\cos\beta_1 l_H \cos\beta_3 l_H - \cos\beta_1 l_H \cos\beta_4 l_H - \cos\beta_2 l_H \cos\beta_3 l_H + \cos\beta_2 l_H \cos\beta_4 l_H + \sin\beta_1 l_H \sin\beta_3 l_H - \sin\beta_1 l_H \sin\beta_4 l_H - \sin\beta_2 l_H \sin\beta_3 l_H + \sin\beta_2 l_H \sin\beta_4 l_H = \cos(\beta_1 l_H - \beta_3 l_H) - \cos(\beta_1 l_H - \beta_4 l_H) - \cos(\beta_2 l_H - \beta_3 l_H) + \cos(\beta_2 l_H - \beta_4 l_H) = 0 \tag{2.63}$$

$$\cos\beta_1 l_C \cos\beta_3 l_C + \cos\beta_1 l_C \cos\beta_4 l_C + \cos\beta_2 l_C \cos\beta_3 l_C + \cos\beta_2 l_C \cos\beta_4 l_C + \sin\beta_1 l_C \sin\beta_3 l_C + \sin\beta_1 l_C \sin\beta_4 l_C + \sin\beta_2 l_C \sin\beta_3 l_C + \sin\beta_2 l_C \sin\beta_4 l_C = \cos(\beta_1 l_C - \beta_3 l_C) + \cos(\beta_1 l_C - \beta_4 l_C) + \cos(\beta_2 l_C - \beta_3 l_C) + \cos(\beta_2 l_C - \beta_4 l_C) = 0 \tag{2.64}$$

$$\cos\beta_1 l_C \cos\beta_2 l_C + \cos\beta_1 l_C \cos\beta_4 l_C + \cos\beta_2 l_C \cos\beta_3 l_C + \cos\beta_3 l_C \cos\beta_4 l_C + \sin\beta_1 l_C \sin\beta_2 l_C + \sin\beta_1 l_C \sin\beta_4 l_C + \sin\beta_2 l_C \sin\beta_3 l_C + \sin\beta_3 l_C \sin\beta_4 l_C = \cos(\beta_1 l_C - \beta_2 l_C) + \cos(\beta_1 l_C - \beta_4 l_C) + \cos(\beta_2 l_C - \beta_3 l_C) + \cos(\beta_3 l_C - \beta_4 l_C) = 0 \tag{2.65}$$

$$\cos\beta_1 l_C \cos\beta_2 l_C + \cos\beta_1 l_C \cos\beta_3 l_C + \cos\beta_2 l_C \cos\beta_4 l_C + \cos\beta_3 l_C \cos\beta_4 l_C + \sin\beta_1 l_C \sin\beta_2 l_C + \sin\beta_1 l_C \sin\beta_3 l_C + \sin\beta_2 l_C \sin\beta_4 l_C + \sin\beta_3 l_C \sin\beta_4 l_C = \cos(\beta_1 l_C - \beta_2 l_C) + \cos(\beta_1 l_C - \beta_3 l_C) + \cos(\beta_2 l_C - \beta_4 l_C) + \cos(\beta_3 l_C - \beta_4 l_C) = -4 \tag{2.66}$$

$$\cos\beta_1 l_C \cos\beta_2 l_C - \cos\beta_1 l_C \cos\beta_3 l_C - \cos\beta_2 l_C \cos\beta_4 l_C + \cos\beta_3 l_C \cos\beta_4 l_C + \sin\beta_1 l_C \sin\beta_2 l_C - \sin\beta_1 l_C \sin\beta_3 l_C - \sin\beta_2 l_C \sin\beta_4 l_C + \sin\beta_3 l_C \sin\beta_4 l_C = \cos(\beta_1 l_C - \beta_2 l_C) - \cos(\beta_1 l_C - \beta_3 l_C) - \cos(\beta_2 l_C - \beta_4 l_C) + \cos(\beta_3 l_C - \beta_4 l_C) = 0 \tag{2.67}$$

$$\cos\beta_1 l_C \cos\beta_2 l_C - \cos\beta_1 l_C \cos\beta_4 l_C - \cos\beta_2 l_C \cos\beta_3 l_C + \cos\beta_3 l_C \cos\beta_4 l_C + \sin\beta_1 l_C \sin\beta_2 l_C - \sin\beta_1 l_C \sin\beta_4 l_C - \sin\beta_2 l_C \sin\beta_3 l_C + \sin\beta_3 l_C \sin\beta_4 l_C = \cos(\beta_1 l_C - \beta_2 l_C) - \cos(\beta_1 l_C - \beta_4 l_C) - \cos(\beta_2 l_C - \beta_3 l_C) + \cos(\beta_3 l_C - \beta_4 l_C) = -4 \tag{2.68}$$

$$\cos\beta_1 l_C \cos\beta_3 l_C - \cos\beta_1 l_C \cos\beta_4 l_C - \cos\beta_2 l_C \cos\beta_3 l_C + \cos\beta_2 l_C \cos\beta_4 l_C + \sin\beta_1 l_C \sin\beta_3 l_C - \sin\beta_1 l_C \sin\beta_4 l_C - \sin\beta_2 l_C \sin\beta_3 l_C + \sin\beta_2 l_C \sin\beta_4 l_C = \cos(\beta_1 l_C - \beta_3 l_C) - \cos(\beta_1 l_C - \beta_4 l_C) - \cos(\beta_2 l_C - \beta_3 l_C) + \cos(\beta_2 l_C - \beta_4 l_C) = -4 \tag{2.69}$$

$$\cos(\beta_1 l_H - \beta_3 l_H) + \cos(\beta_2 l_H - \beta_4 l_H) = 0 \tag{2.70}$$

$$\cos(\beta_1 l_H - \beta_2 l_H) + \cos(\beta_3 l_H - \beta_4 l_H) = 0 \tag{2.71}$$

$$\cos(\beta_1 l_H - \beta_4 l_H) + \cos(\beta_2 l_H - \beta_3 l_H) = 0 \tag{2.72}$$

$$\cos(\beta_1 l_C - \beta_3 l_C) + \cos(\beta_2 l_C - \beta_4 l_C) = -2 \tag{2.73}$$

$$cos(\beta_1 l_C - \beta_2 l_C) + cos(\beta_3 l_C - \beta_4 l_C) = -2 \tag{2.74}$$

$$cos(\beta_1 l_C - \beta_4 l_C) + cos(\beta_2 l_C - \beta_3 l_C) = 2 \tag{2.75}$$

Considering the propagation constants of the propagating modes $\beta_1>(\beta_2\lesseqgtr\beta_3)>\beta_4$, the relation between β_1, β_2, β_3, β_4, and l_C are acquired from Eqs. (2.73)-(2.75).

$$(\beta_1 - \beta_3) l_C = (2n_{13} + 1)\pi \tag{2.76}$$

$$(\beta_2 - \beta_4) l_C = (2n_{24} + 1)\pi \tag{2.77}$$

$$(\beta_1 - \beta_2) l_C = (2n_{12} + 1)\pi \tag{2.78}$$

$$(\beta_3 - \beta_4) l_C = (2n_{34} + 1)\pi \tag{2.79}$$

$$(\beta_1 - \beta_4) l_C = 2n_{14}\pi \tag{2.80}$$

$$(\beta_2 - \beta_3) l_C = 2n_{23}\pi \tag{2.81}$$

where n_{ij} is a positive integer included zero.

Minimizing l_C, set to $n_{13}= n_{24}= n_{12}= n_{34}= n_{23}=0$ and $n_{14}=1$.

$$\beta_2=\beta_3 \tag{2.82}$$

$$\beta_1+\beta_4=2\beta_2 \tag{2.83}$$

Then, the relation between β_1, β_2, β_3, β_4, and l_H are acquired from Eqs. (2.70)-(2.72).

$$(\beta_1 - \beta_3) l_H = (2n_{13} + 1)\frac{\pi}{2} \tag{2.84}$$

$$(\beta_2 - \beta_4) l_H = (2n_{24} + 1)\frac{\pi}{2} \tag{2.85}$$

$$(\beta_1 - \beta_2) l_H = (2n_{12} + 1)\frac{\pi}{2} \tag{2.86}$$

$$(\beta_3 - \beta_4) l_H = (2n_{34} + 1)\frac{\pi}{2} \tag{2.87}$$

$$(\beta_1 - \beta_4) l_H = (2n_{14} + 1)\pi \tag{2.88}$$

Minimizing l_H, set to $n_{13}= n_{24}= n_{12}= n_{34} = n_{14}=0$.

Finally, inserting derived unknowns into Eqs. (2.42)-(2.45), the output signals of the short-slot 2-plane coupler are

$$E_5 = \frac{e^{-j\frac{l}{2}(\beta_1+\beta_4)}}{2}\left(cos\frac{l}{2}(\beta_1 - \beta_4) + 1\right) \tag{2.89}$$

$$E_6 = E_7 = \frac{e^{-j\frac{l}{2}(\beta_1+\beta_4)}}{2}\left(-j\,sin\frac{l}{2}(\beta_1 - \beta_4)\right) \tag{2.90}$$

$$E_8 = \frac{e^{-j\frac{l}{2}(\beta_1+\beta_4)}}{2}\left(cos\frac{l}{2}(\beta_1 - \beta_4) - 1\right) \tag{2.91}$$

As previous mentioned in 2.1.1, the length of the coupler region is decided to cancel-out the incident and the reflected waves in the coupled region to suppress the reflection at the excited input port. It can be acquired by same manner in 2.1.1, but different thing is that TE_{10} and TM_{21} modes are suppressed because of those large reflections.

The transmission matrices of the short-slot 2-plane hybrid and cross coupler are same as of Eqs. (2.37) and (2.38). Design parameters of short-slot 2-plane couplers should be selected to satisfy Eqs. (2.57), (2.80), (2.82), (2.83), and (2.88). In the rectangular waveguide, the propagation constants of the propagating modes are expressed as

$$\beta_{TE_{10}} = \sqrt{\left(\frac{2\pi}{\lambda}\right)^2 - \left(\frac{\pi}{a'}\right)^2} \tag{2.92}$$

$$\beta_{TE/TM_{11}} = \sqrt{\left(\frac{2\pi}{\lambda}\right)^2 - \left(\frac{\pi}{a'}\right)^2 - \left(\frac{\pi}{b'}\right)^2} \tag{2.93}$$

$$\beta_{TE_{20}} = \sqrt{\left(\frac{2\pi}{\lambda}\right)^2 - \left(\frac{2\pi}{a'}\right)^2} \tag{2.94}$$

$$\beta_{TE/TM_{21}} = \sqrt{\left(\frac{2\pi}{\lambda}\right)^2 - \left(\frac{2\pi}{a'}\right)^2 - \left(\frac{\pi}{b'}\right)^2} \tag{2.95}$$

where λ is a wavelength.

Satisfying Eqs. (2.82) and (2.83), the width and the height of the coupled region are calculated as

$$b' = \frac{a'}{\sqrt{3}} \tag{2.96}$$

$$a' = \lambda\sqrt{\frac{217}{192}} \tag{2.97}$$

However, these selected parameters make TE/TM$_{21}$ mode to the evanescent mode. *a'* and *b'* should be increased to avoid this situation, but do not break the rules of Eqs. (2.82) and (2.83), and not generate TE$_{30}$ mode as a propagating mode in the coupled region.

$$a' < \frac{3}{2}\lambda \tag{2.98}$$

$$b' < a' \tag{2.99}$$

The ridge rectangular waveguide is adapted to the coupled region of the short-slot 2-plane coupler. When the width and the height of ridges are w_r and h_r, the propagation constants of the propagating modes are approximated as

$$\beta_{TE_{10}} \approx \sqrt{\left(\frac{2\pi}{\lambda}\right)^2 - \left(\frac{\pi}{a'}\right)^2} \tag{2.100}$$

$$\beta_{TE_{11}} \approx \sqrt{\left(\frac{2\pi}{\lambda}\right)^2 - \left(\frac{\pi}{a'}\right)^2 - \left(\frac{\pi}{b'+h_r}\right)^2} \tag{2.101}$$

$$\beta_{TM_{11}} \approx \sqrt{\left(\frac{2\pi}{\lambda}\right)^2 - \left(\frac{\pi}{a'}\right)^2 - \left(\frac{\pi}{b'-h_r}\right)^2} \tag{2.102}$$

$$\beta_{TE_{20}} \approx \sqrt{\left(\frac{2\pi}{\lambda}\right)^2 - \left(\frac{2\pi}{a'-w_r}\right)^2} \tag{2.103}$$

$$\beta_{TE_{21}} \approx \sqrt{\left(\frac{2\pi}{\lambda}\right)^2 - \left(\frac{2\pi}{a'-w_r}\right)^2 - \left(\frac{\pi}{b'+h_r}\right)^2} \tag{2.104}$$

$$\beta_{TM_{21}} \approx \sqrt{\left(\frac{2\pi}{\lambda}\right)^2 - \left(\frac{2\pi}{a'+w_r}\right)^2 - \left(\frac{\pi}{b'-h_r}\right)^2} \tag{2.105}$$

TE$_{ij}$ and TM$_{ij}$ modes have different the propagation constant, ones of two same order propagating modes are selected as β_2 and β_4 by considering the coupling coefficients of those propagation modes.

Because TM_{11} and TM_{21} modes have higher coupling coefficients than TE_{11} and TE_{21} modes, β_2 and β_4 are set the propagation constants of TM_{11} and TM_{21} modes, respectively. The transverse field components of TE and TM modes are [2.5]

$$E_{TE_{mn},x} = \frac{j\omega\mu n\pi}{k^2_{TE_{mn},c} b_{TE_{mn}}} A_{mn} \cos\frac{m\pi x}{a_{TE_{mn}}} \sin\frac{n\pi y}{b_{TE_{mn}}} e^{-j\beta_{TE_{mn}} z} \tag{2.106}$$

$$E_{TE_{mn},y} = -\frac{j\omega\mu m\pi}{k^2_{TE_{mn},c} a_{TE_{mn}}} A_{mn} \sin\frac{m\pi x}{a_{TE_{mn}}} \cos\frac{n\pi y}{b_{TE_{mn}}} e^{-j\beta_{TE_{mn}} z} \tag{2.107}$$

$$E_{TM_{mn},x} = -\frac{j\beta m\pi}{k^2_{TM_{mn},c} a_{TM_{mn}}} B_{mn} \cos\frac{m\pi x}{a_{TM_{mn}}} \sin\frac{n\pi y}{b_{TM_{mn}}} e^{-j\beta_{TM_{mn}} z} \tag{2.108}$$

$$E_{TM_{mn},y} = -\frac{j\beta n\pi}{k^2_{TM_{mn},c} b_{TM_{mn}}} B_{mn} \sin\frac{m\pi x}{a_{TM_{mn}}} \cos\frac{n\pi y}{b_{TM_{mn}}} e^{-j\beta_{TM_{mn}} z} \tag{2.109}$$

where A_{mn} and B_{mn} are arbitrary amplitude constants, m and n are a positive integer included zero, β_{mode} is a cutoff wavenumber of a propagation mode, a_{mode} and b_{mode} are the effective width and height of the coupled region in the given propagation mode.

Because the excited electric field is E_y component only, there is no E_x component in the coupled region. For that reason, the summation of E_x components of TM_{11} and TM_{21} modes should be zero.

$$\left|E_{TE_{mn},x}\right| = \left|E_{TM_{mn},x}\right| \tag{2.110}$$

At that time, the amplitude relation between $E_{TEmn,y}$ and $E_{TMmn,y}$ is

$$A_{mn} = \frac{\beta m k^2_{TE_{mn},c} b_{TE_{mn}}}{\omega\mu n k^2_{TM_{mn},c} a_{TM_{mn}}} B_{mn} \tag{2.111}$$

$$\frac{\left|E_{TM_{mn},y}\right|}{\left|E_{TE_{mn},y}\right|} = \frac{a_{TE_{mn}} a_{TM_{mn}} n^2}{b_{TE_{mn}} b_{TM_{mn}} m^2} \tag{2.112}$$

When (m=1, n=1) and (m=2, n=1), the amplitude of $E_{TMmn,y}$ is larger than the amplitude of $E_{TEmn,y}$. According to Eq. (2.57), four selected propagating modes in the coupled region (TE_{10}, TE_{20}, TM_{11} and TM_{21}) should have -6 dB coupling coefficients. It means that un-selected propagating modes in the coupled region (TE_{01}, TE_{11}, and TE_{21}) should be suppressed. TE_{01} mode has low coupling coefficient, because it has only x-direction polarized electric field Ex. Making TE_{21} mode to the evanescent mode, the outermost vertices of ridge waveguide structure are trimmed with the width w_t and the height h_t. These structures affect the propagation constant of TE_{21} mode in priority, less other propagation modes. In that time, the propagation constants of the affected modes are approximated as

$$\beta_{TE_{21}} \approx \sqrt{\left(\frac{2\pi}{\lambda}\right)^2 - \left(\frac{2\pi}{a' - w_r - \frac{w_t}{2}}\right)^2 - \left(\frac{\pi}{b' + h_r + \frac{h_t}{2}}\right)^2} \tag{2.113}$$

$$\beta_{TM_{21}} \approx \sqrt{\left(\frac{2\pi}{\lambda}\right)^2 - \left(\frac{2\pi}{a' + w_r + \frac{w_t}{2}}\right)^2 - \left(\frac{\pi}{b' - h_r - \frac{h_t}{2}}\right)^2} \tag{2.114}$$

$$\beta_{TE_{30}} \approx \sqrt{\left(\frac{2\pi}{\lambda}\right)^2 - \left(\frac{3\pi}{a' + w_t}\right)^2} \tag{2.115}$$

Because TE_{11} mode is located between TE_{20} and TM_{11} modes, it is impossible to change this mode to the evanescent mode. For that reason, the peak coupling coefficient of TM_{11} mode should be positioned in the center frequency. It makes that the short-slot 2-plane couplers have the four balanced output amplitudes (-6 dB) as a hybrid coupler and the single 2-D crossing output amplitude (0 dB) as a cross coupler at the center frequency. Design procedure of the short-slot 2-plane coupler is based on the previous mentioned derivations.

1. Choose the width and the height of the port branches *a* and *b* to pass TE_{10} mode only as the propagating mode in the port branch at target frequency band.
2. Set upper boundaries of the width and the height of the coupled region *a'* and *b'* to block TE_{30} mode as the evanescent mode in the coupled region at target frequency band.
3. Insert double ridges in the rectangular waveguide with the width w_r and the height h_r to satisfy Eqs. (2.82) and (2.83).
4. Trim the outermost vertices of the double ridge rectangular waveguide with the width w_t and the height h_t to make TE_{21} mode as the evanescent mode.
5. Adjust the mentioned design parameters with the position of the port branches to satisfy Eq. (2.57).
6. Choose the lengths of the coupled region to satisfy Eqs. (2.80) and (2.88) corresponded types of the short-slot 2-plane coupler.

2.3.2 Simulation results

The coupled regions of the short-slot 2-plane coupler designed in 2.3.1. are depicted in Fig. 2.11. All simulations are conducted on the lossless structure in 22 GHz band. Except a simulation for the coupling coefficient has conducting wall (C3604, specific gravity=8.5 g/cm^3, $\sigma=1.31\times10^7$ S/m) because of the convergence. In the rectangular waveguide structure, TE/TM_{11} and TE/TM_{21} modes have same the propagation constants, and TE_{30} mode is set the evanescent mode to keep the design procedure 2. as shown in Fig. 2.12(a). In the double ridge rectangular waveguide structure, TE/TM_{11} and TE/TM_{21} modes are generated the difference between the propagation constants and the design procedure 3 is satisfied as shown in Fig. 2.12(b). In the trimmed the outermost vertices of double ridge rectangular waveguide, TE_{21} mode set the evanescent mode to keep the design procedure 4. Next, the coupling coefficients of propagating modes in the coupled region can be obtained using the coupled region with four port branches (full model) or a quarter of the coupled region with single port branch as shown in Fig. 2.13(a) or (b). Full model can acquire whole propagation constants of propagating modes in the coupled region as shown in Fig. 2.13(g)-(i). TE_{10}, TE_{20}, TM_{11}, and TM_{21} modes have around -6 dB coupling coefficients at the center frequency. A quarter of full model with symmetric boundaries can alternate the full model using the image theory [2.6]. The boundary conditions given in Fig. 2.13(c)-(f) transmit single dominant modes in the coupled region which has 0 dB coupling coefficient at the center frequency as shown in Fig. 2.13(j). This simulation structure has less the computation time than the full model structure. After the design of the coupled region, the lengths of the coupled region corresponded short-slot 2-plane hybrid and cross couplers are given by the design procedure 6. Design parameters of the short-slot couplers are listed and in Table 2.4. When the definition of the operating frequency band of the short-slot 2-plane hybrid coupler is set to the output amplitudes within -6±0.5 dB, the performances of the short-slot 2-plane couplers are listed in Table 2.5, and shown as Fig. 2.13, respectively. Comparing the results of preceding researches [2.7]-[2.8], the short-slot 2-plane coupler has a narrower bandwidth than short-slot 1-plane coupler at this moment. A fundamental cause is that the coupled region of the short-slot 2-plane coupler has more the propagating modes (TE_{10}, TE_{01}, TE_{20}, TE_{11}, TM_{11}, and TM_{21} modes) than the short-slot 1-plane coupler (TE_{10}, TE_{01}, (TE_{20} or TM_{11}) modes). As mentioned in the design procedure 3 and 5, the flatness of the coupling coefficients (amplitude) and the propagation constants (phase) of the propagating modes affect the amplitudes and the phases of the outputs of the short-slot 2-plane couplers. Especially, considering the frequency dependency of the propagation constants, it is more difficult to keep the flatness in the short-slot 2-plane coupler than the short-slot 1-plane coupler. Differences between the simulation and the ideal phases of the output ports are also happened for the same reason. On the one hand, the coupled region of the short-slot 2-plane cross coupler works as a rectangular waveguide cavity [2.9], the resonant frequency is expressed as

$$f_{mno} = \frac{c}{2\pi}\sqrt{\left(\frac{m\pi}{a'}\right)^2 + \left(\frac{n\pi}{b'}\right)^2 + \left(\frac{o\pi}{l}\right)^2} \tag{2.116}$$

where *m*, *n* and *o* are a positive integer included zero, *a'* and *b'* are the effective width and height of the coupled region.

The short-slot 2-plane cross coupler has resonant frequencies around 23 GHz (TM_{211} mode) and 23.7 GHz (TE_{211} mode) as shown in Fig. 2.14(d), those frequencies restrict the upper boundary of the operating frequency band. The short-slot 2-plane coupler has a half volume of the 4×4-way short-slot combined coupler, because single coupled region of the short-slot 2-plane coupler alternates four coupled region of the short-slot 1-plane coupler. The short-slot 2-plane hybrid coupler works as 4×4 2-D beam-switching Butler matrix which generates four spatially orthogonal beams. The output port branch is able to alternate an aperture antenna as the antenna element of the antenna array. -3 dB gain patterns of the short-slot 2-plane hybrid coupler are shown in Fig. 2.15. Directivities of four beams are 11.1 dBi. The coaxial-to-waveguide transition (launcher) is required for connecting the short-slot coupler and the measurement instrument, because the size of the port branch is not a standard rectangular waveguide WR42 (10.668×4.318 mm, 17.6-26.7 GHz). The design parameters and the performances of the launcher are listed in Table 2.6, and shown as Fig. 2.16, respectively.

2.3.3 Measurement results

The center frequency is selected to 22 GHz for checking the feasibility of mm wave indirectly and securing the easiness of the fabrication and the measurement. The short-slot 2-plane couplers are fabricated by the milling with a brass (C3560P, $\sigma=1.31\times10^7$ S/m). The coaxial-to-waveguide transition is equipped the flange mount jack receptacle (M/ACOM 2752-1201-00). The measurements are conducted for S-parameters (Agilent E8361A) and far-field (anechoic chamber) data. At the simulation, the insertion loss of the fabricated short-slot 2-plane couplers is 0.1 dB. However the measurement results show that the insertion loss of the fabricated short-slot 2-plane couplers is 0.3 dB, because the insertion loss of the coaxial-to-waveguide transitions is not calibrated.

2.3.3.1 Short-slot 2-plane hybrid coupler

The fabricated short-slot 2-plane hybrid coupler consists of three parts which are two coaxial-to-waveguide transitions and single coupled region as shown in Fig. 2.17. The coupled region part has additional port branches at the output side for far-field measurement. Considering the insertion loss of the short-slot 2-plane coupler, the definition of the operating frequency band of the short-slot 2-plane hybrid coupler is set to the output amplitudes within -6.3±0.5 dB. The measured performances of the short-slot 2-plane hybrid coupler compared with the simulation results are listed in Table 2.7, and shown as Fig. 2.18, respectively. The measurement of radiation patterns of the short-slot 2-plane hybrid coupler is conducted in the anechoic chamber as shown in Fig. 2.19(c) and (d). Under the present limitation of the rotators in the measurement, which AUT (Antenna Under Test) positioner moves only in the horizontal direction, AUT looks at the specified elevation angle α corresponded to the input port as shown in Fig. 2.19(a). For the measurement of quasi E-plane in Fig. 2.19(c), the coupler rotated from x-axis to y-axis by 90 degrees with coordinators is placed with the tilting angle of $\pm\alpha_1$ in the transformed (y-z) plane and the rotator is moved in the transformed (y-z) plane. For the measurement of quasi H-plane in Fig. 2.19(d), the coupler is placed with the tilting angle of $\pm\alpha_2$ in the transformed (x-z) plane and the rotator is moved in the transformed (x-z) plane. These tilted angles and the beam directions (β_1 and β_2) on the transformed planes are calculated from the coordinate transformation (Appendix 2). It makes that beam direction is positioned at the measurement trajectory as shown in Fig. 2.19(b). The simulated and measured beam directions (β, α), realized gains, and HPBWs (Half Power BeamWidth) are listed in Table 2.8 and shown in Fig. 2.19(e)-(h).

2.3.3.2 Short-slot 2-plane cross coupler

The short-slot 2-plane cross coupler is redesigned and fabricated for the feasibility of 2-D beam-switching Butler matrix. Main difference with previous design at section 2.3.2 is that the positions of port branches move to the outer boundary of the coupled region as shown in Fig. 2.20. And the length of the coupled region is slightly changed from 22.14 mm to 21.72 mm. In the same frequency bandwidth of the short-slot 2-plane hybrid coupler, the measured performances of the short-slot 2-plane cross coupler compared with the simulation results are listed in Table 2.9, and shown as Fig. 2.21, respectively.

2.4 Summary

The short-slot 2-plane coupler is designed by the principal theory of propagating modes in the coupled region. It generates four orthogonal outputs same as the combination of short-slot two E- and two H-plane couplers's. The volume of the coupled region of the short-slot 2-plane coupler is downed to 0.7 times of the short-slot 1-plane coupler's. Considering the elimination of junctions, the volume of the short-slot 2-plane coupler can be downed to 0.5. The operating bandwidth of the short-slot 2-plane coupler is restricted by the narrow simultaneous band of four propagating modes in the coupled region and the resonance frequency of the short-slot 2-plane cross coupler.

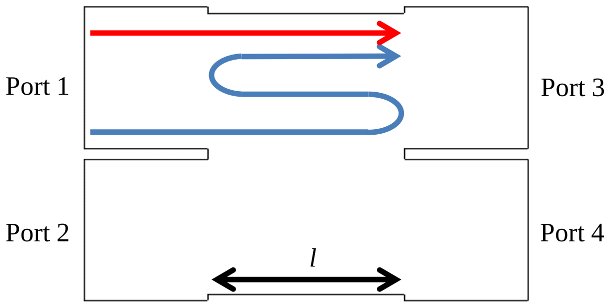

Fig. 2.1 Suppress reflection of propagating modes

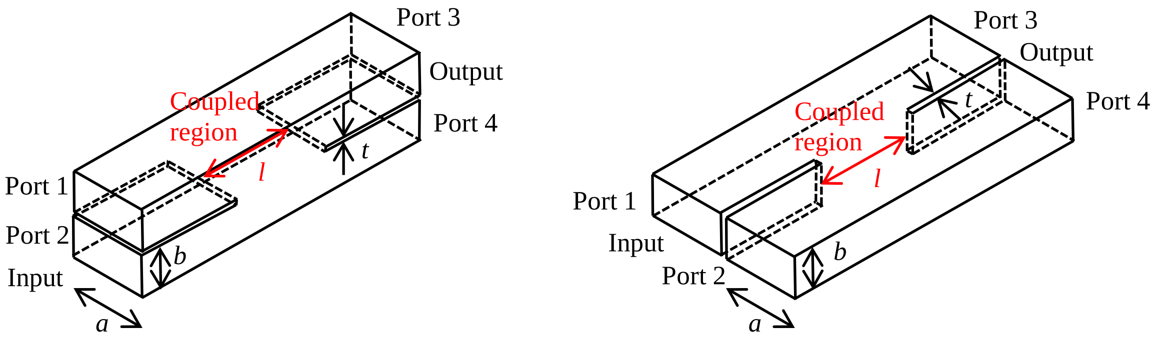

(a) (b)

Fig. 2.2 Short-slot coupler (a) E-plane (b) H-plane.

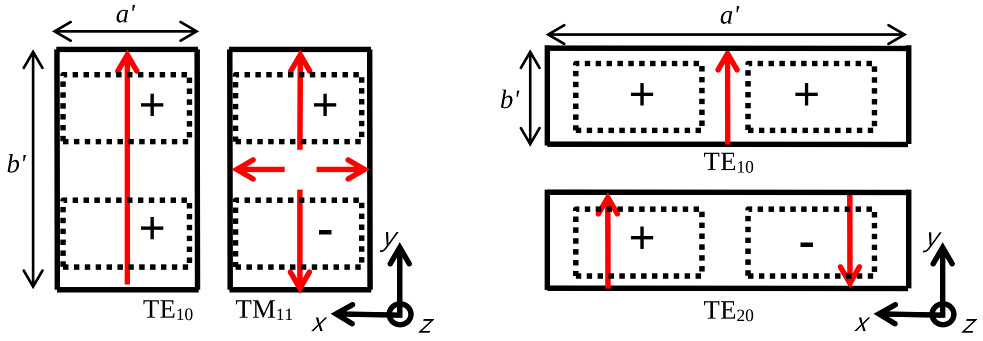

(a) (b)

Fig. 2.3 Electric field distribution and its polarities in the coupled region (a) Short-slot E-plane coupler (b) Short-slot H-plane coupler. Solid black lines: Boundary of the coupled regions, Dotted black lines: Boundary of the port branches.

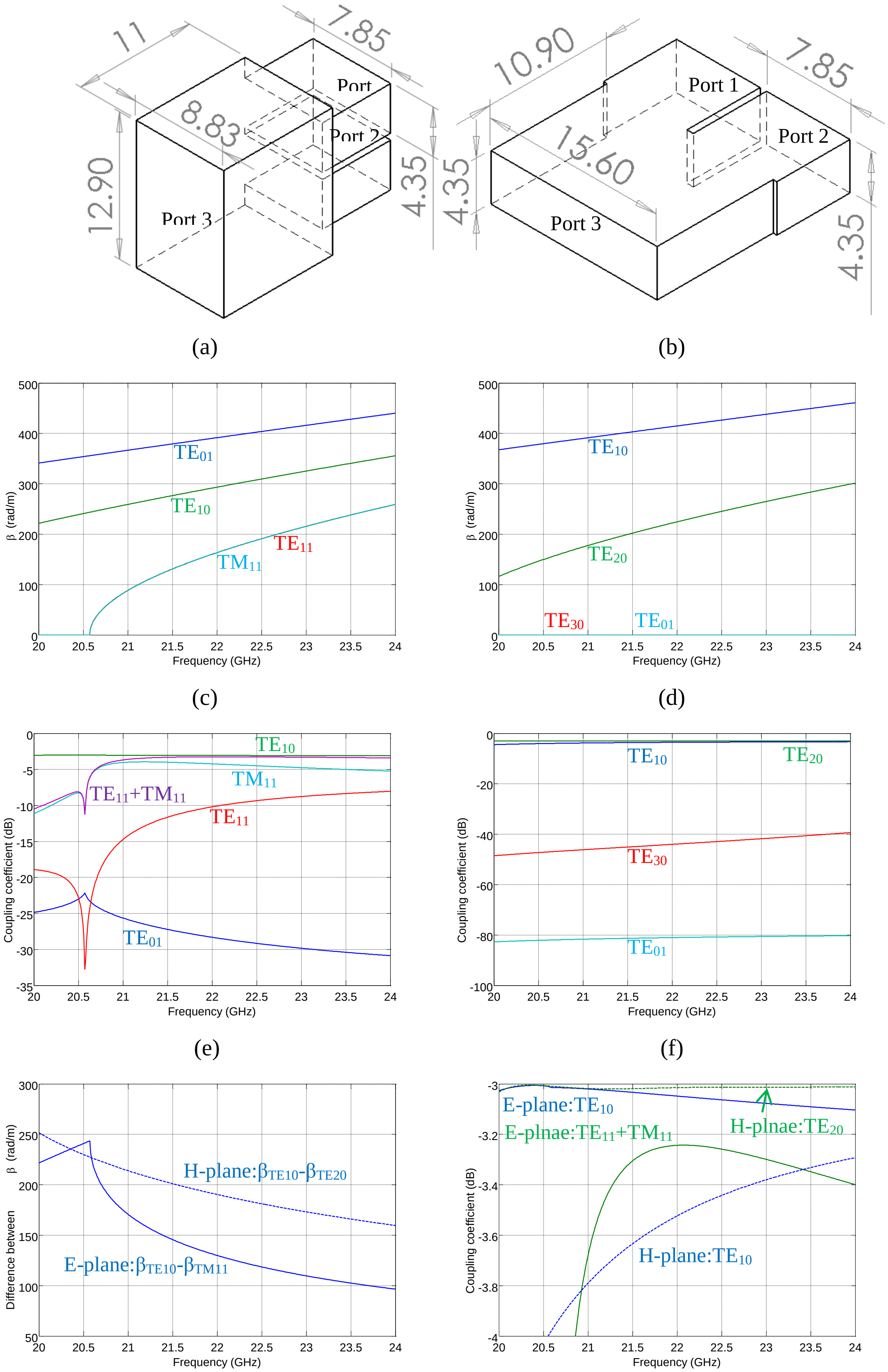
11
7.85
8.83
12.90
4.35
Port
Port 2
Port 3
10.90
15.60
7.85
4.35
4.35
Port 1
Port 2
Port 3
β (rad/m)
Frequency (GHz)
TE01
TE10
TM11
TE11
TE10
TE20
TE30
TE01
Coupling coefficient (dB)
TE10
TM11
TE11+TM11
TE11
TE01
TE10
TE20
TE30
TE01
Difference between β (rad/m)
H-plane:βTE10-βTE20
E-plane:βTE10-βTM11
E-plane:TE10
E-plnae:TE11+TM11
H-plnae:TE20
H-plane:TE10
20
20.5
21
21.5
22
22.5
23
23.5
24

(a) (b)

(c) (d)

(e) (f)

(g) (h)

Fig. 2.4 Characteristics of modes in the coupled region. For short-slot E-plane coupler (a) Drawing (c) Coupling coefficient (e) Propagation constant. For short-slot H-plane coupler (b) Drawing (d) Coupling coefficient (f) Propagation constant (g) Difference between propagation constants of two propagating modes (h) Coupling coefficient of two propagating modes. Unit: mm.

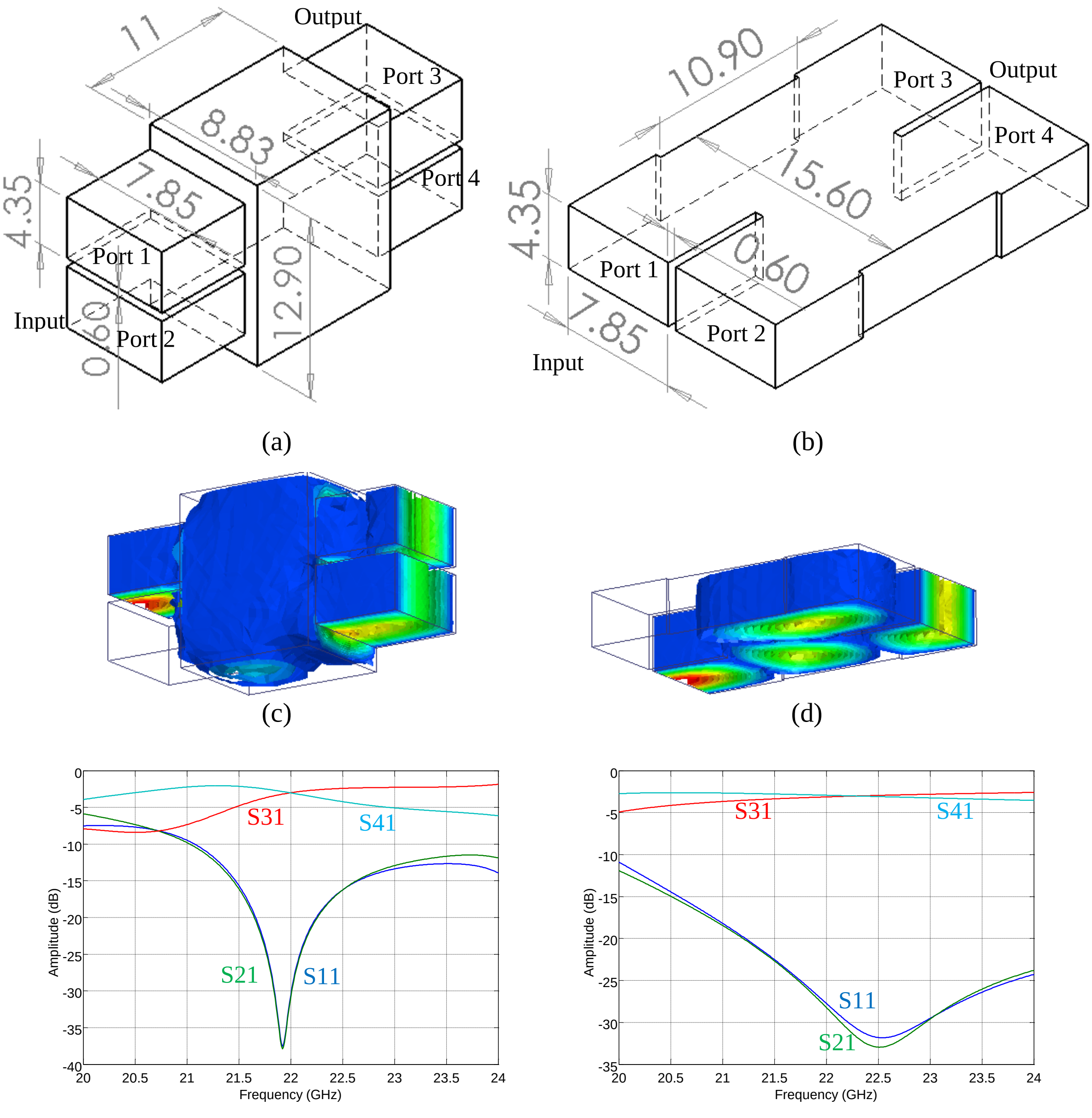

(a) (b)

(c) (d)

(e) (f)

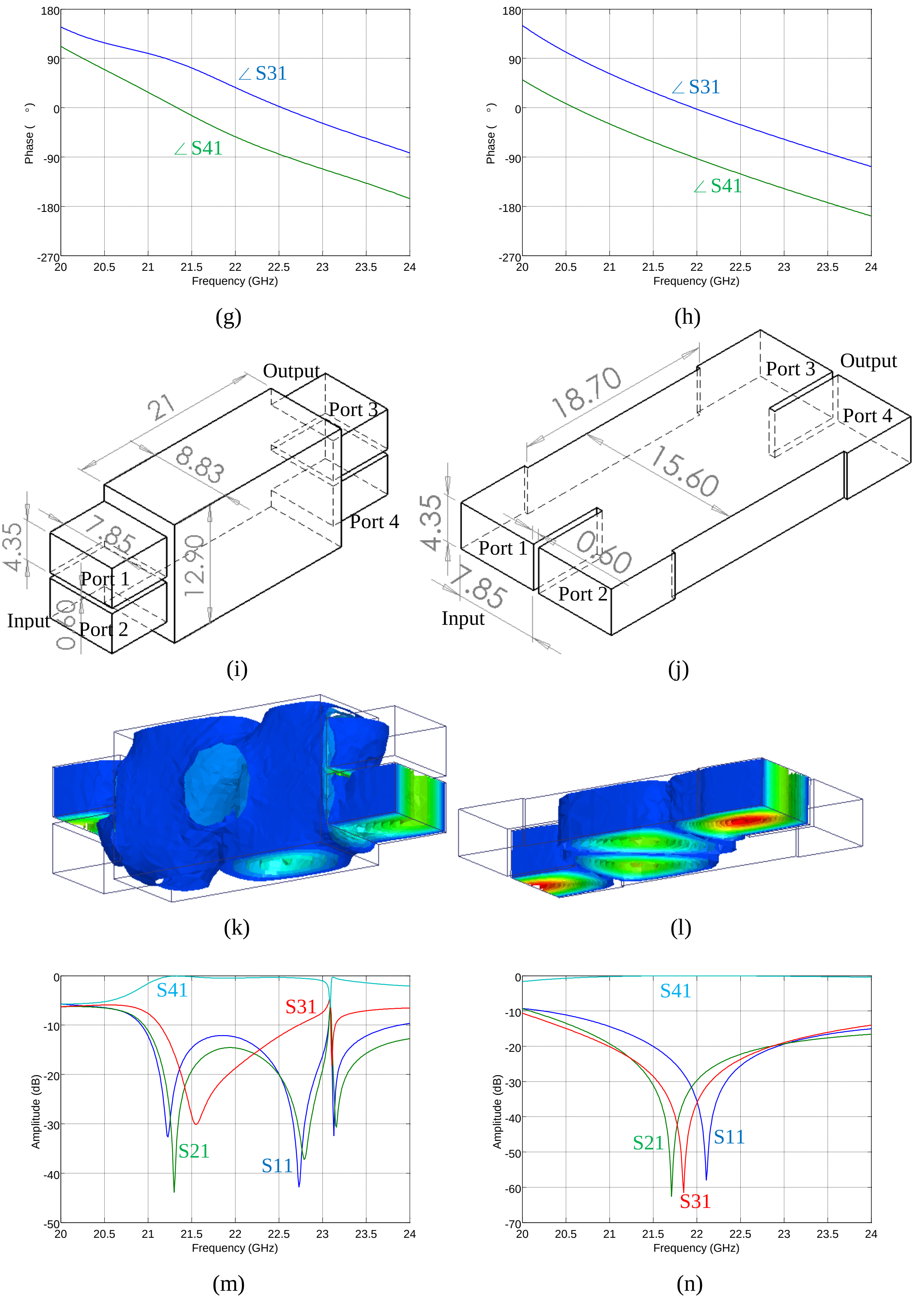

(g) (h)

(i) (j)

(k) (l)

(m) (n)

Fig. 2.5 Characteristics of short-slot coupler. E-plane hybrid coupler (a) Drawing (c) Propagation of electric field (e) Amplitude (g) Phase. H-plane hybrid coupler (b) Drawing (d)

Propagation of electric field (f) Amplitude (h) Phase. E-plane cross coupler (i) Drawing (k) Propagation of electric field (m) Amplitude. H-plane cross coupler (j) Drawing (l) Propagation of electric field (n) Amplitude. Unit: mm.

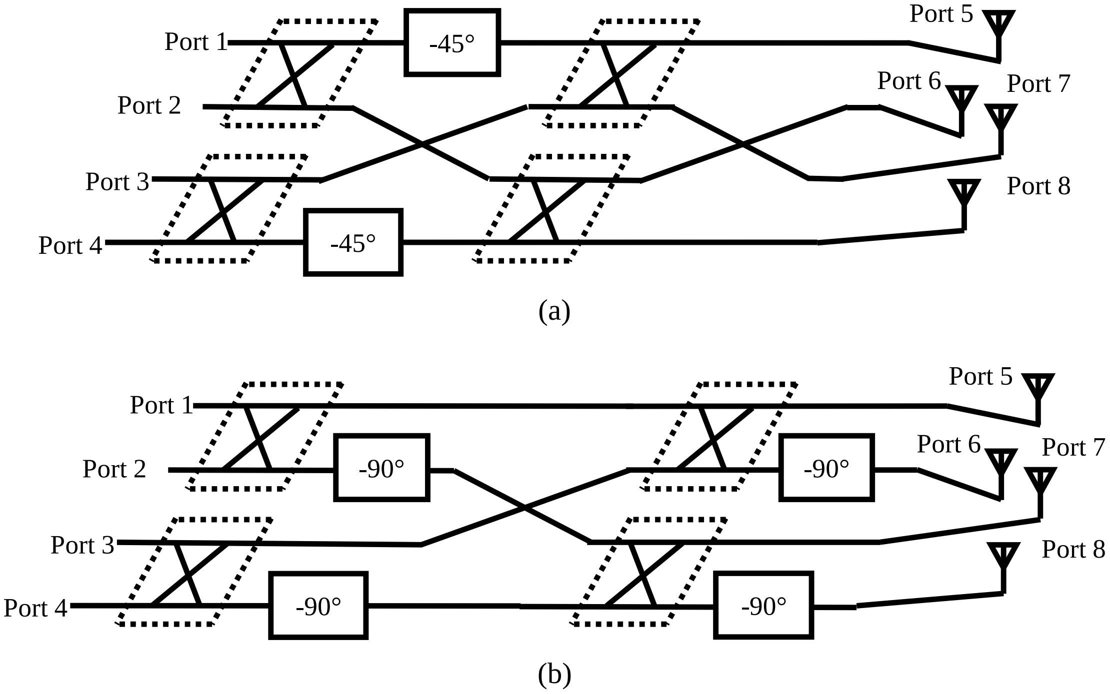

(a)

(b)

Fig. 2.6 2×2 array antenna fed by 4×4-way 1-D beam-switching Butler matrix (a) Original (b) Modified.

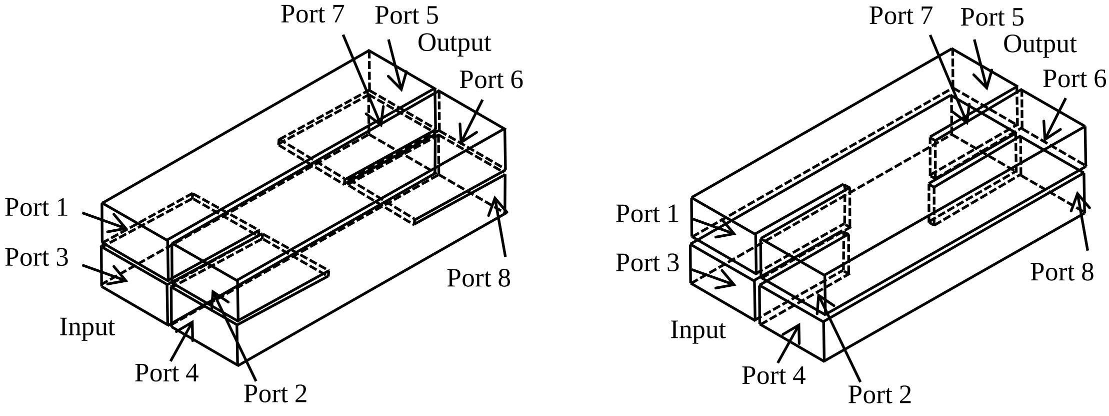

(a)

(b)

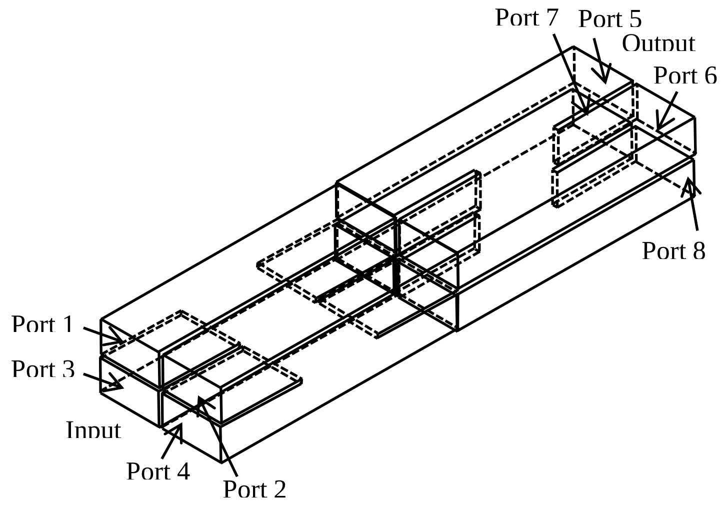

(c)

Fig. 2.7 4×4-way short-slot combined coupler (a) Horizontally stacked short-slot E-plane coupler (b) Vertically stacked short-slot H-plane coupler (c) Combination of (a) and (b)

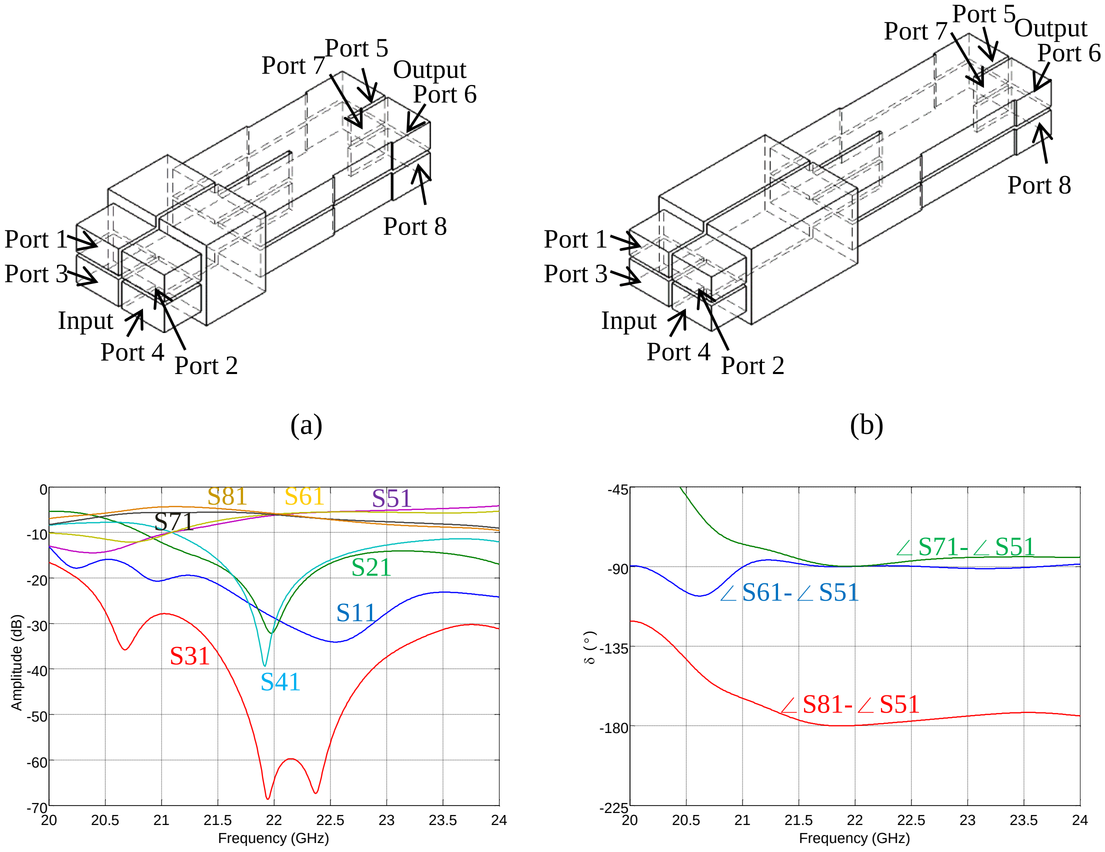

(a) (b)

(c) (d)

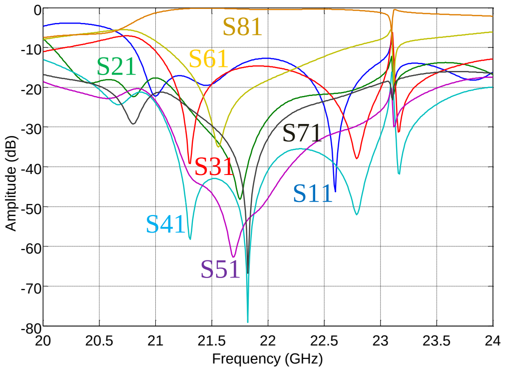

(e)

Fig. 2.8 Characteristics of 4×4-way short-slot combined coupler. Hybrid coupler (a) Drawing (c) Amplitude (d) Phase difference. Cross coupler (b) Drawing (e) Amplitude.

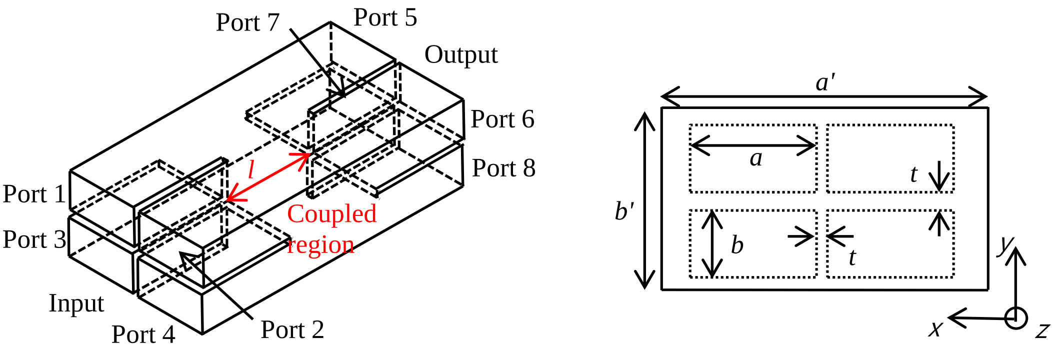

(a) (b)

Fig. 2.9 Short-slot 2-plane coupler (a) Perspective view (b) Cross-section. Solid lines: Boundary of the coupled regions, Dotted lines: Boundary of the port branches.

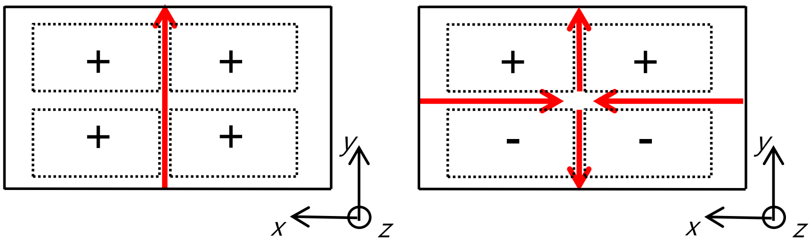

(a) (b)

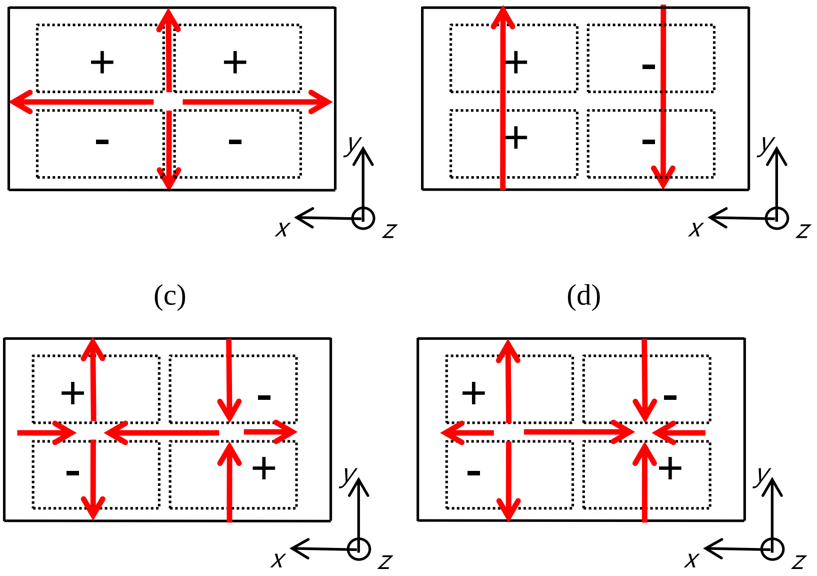

(c) (d)

(e) (f)

Fig. 2.10 Electric field distribution and its polarities in the coupled region (a) TE10 (b) TE11 (c) TM11 (d) TE20 (e) TE21 (f) TM21. Solid black lines: Boundary of the coupled regions, Dotted black lines: Boundary of the port branches.

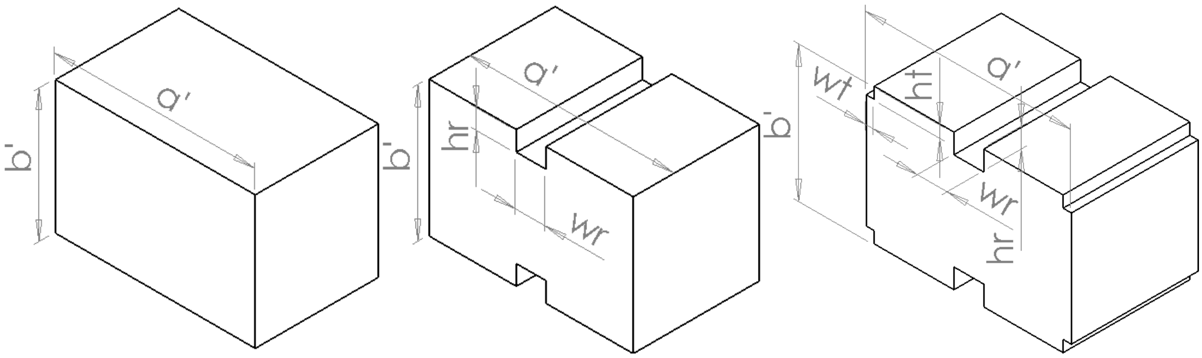

(a) (b) (c)

Fig. 2.11 The coupled region (a) Rectangular waveguide (b) Double ridge rectangular waveguide (c) Trim the outermost vertices of double ridge rectangular waveguide.

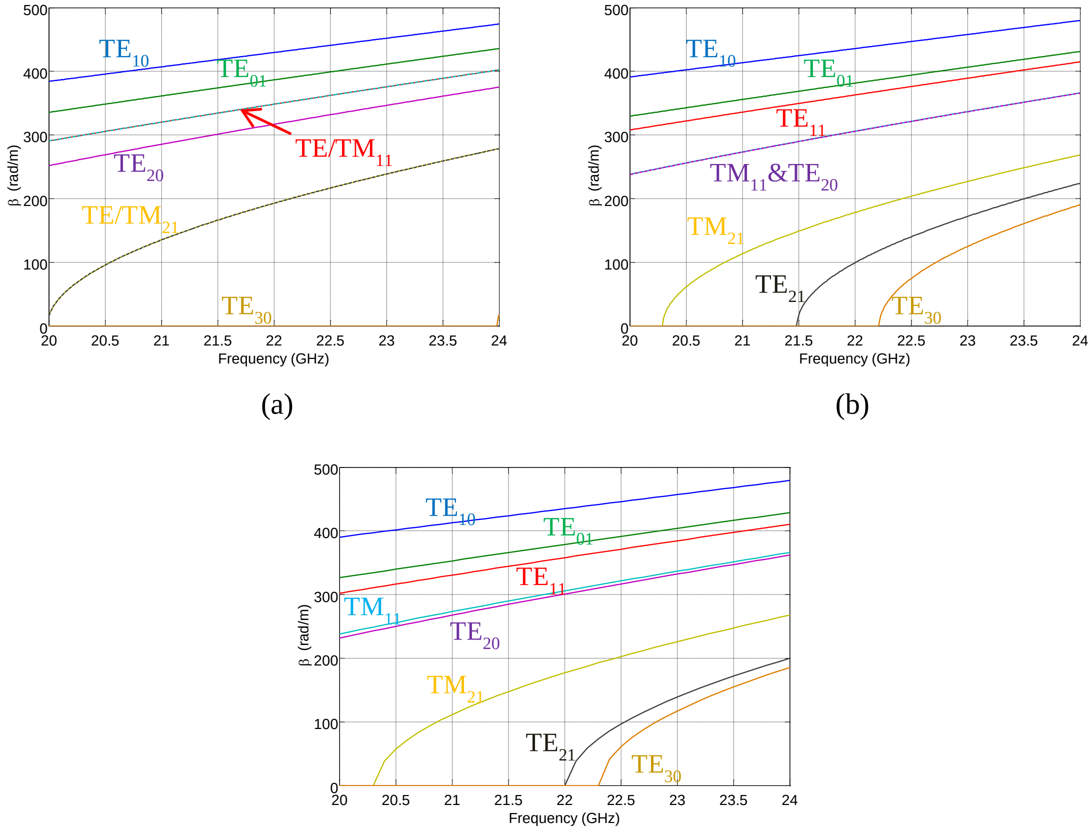

(a)

(b)

(c)

Fig. 2.12 The propagation constant of modes in the coupled region (a) Rectangular waveguide (b) Double ridge rectangular waveguide (c) Trimmed the outermost vertices of double ridge rectangular waveguide.

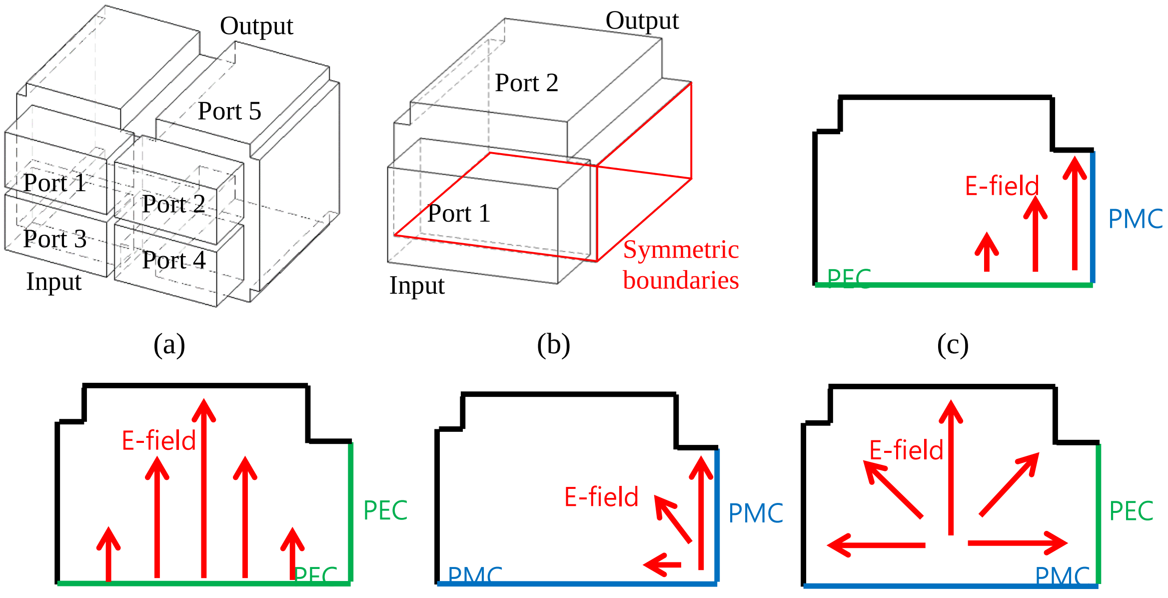

(a)

(b)

(c)

(d)

(e)

(f)

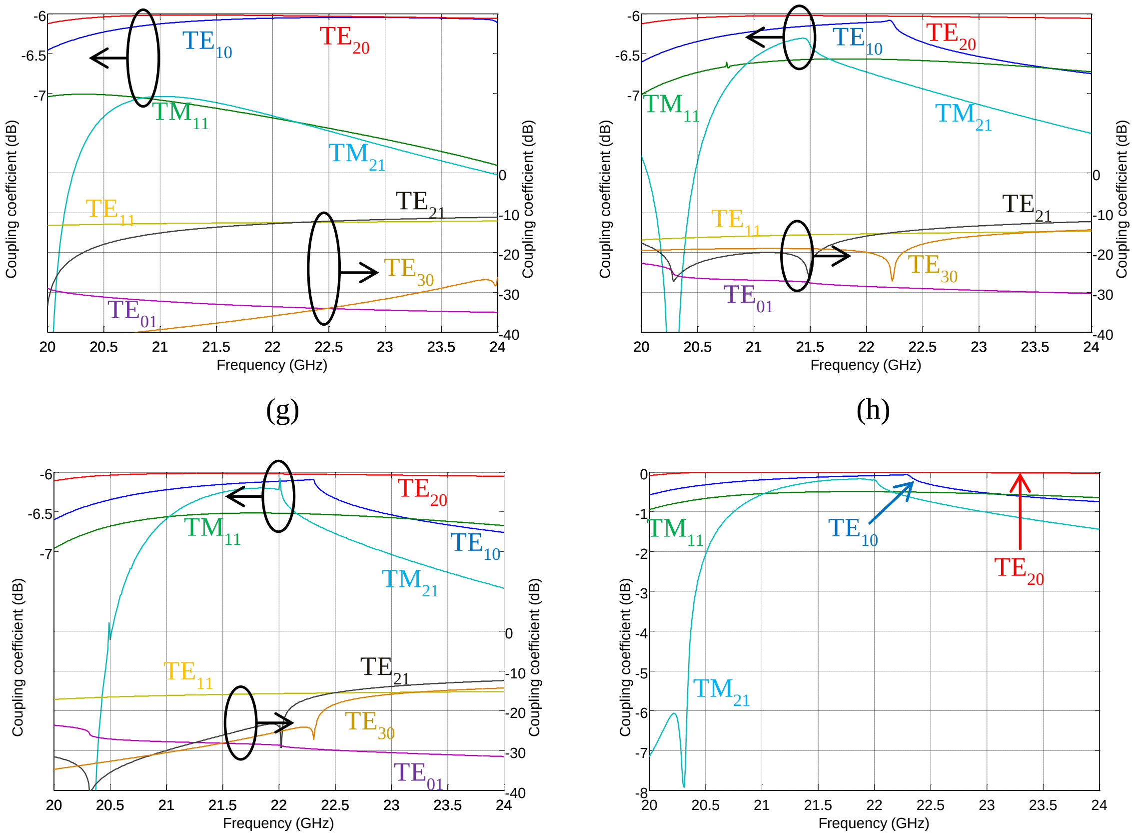

(g) (h)

(i) (j)

Fig. 2.13 Coupling coefficient of modes in the coupled region (a) Drawing of full model (b) Drawing of a quarter of full model with symmetric boundaries for (c) TE$_{10}$ mode (d) TE$_{20}$ mode (e) TM$_{11}$ mode (f) TM$_{21}$ mode. Coupling coefficients in full model for (g) Rectangular waveguide (h) Double ridge rectangular waveguide. Coupling coefficients of trimmed the outermost vertices of double ridge rectangular waveguide (j) Full model (i) A quarter of full model with symmetric boundaries.

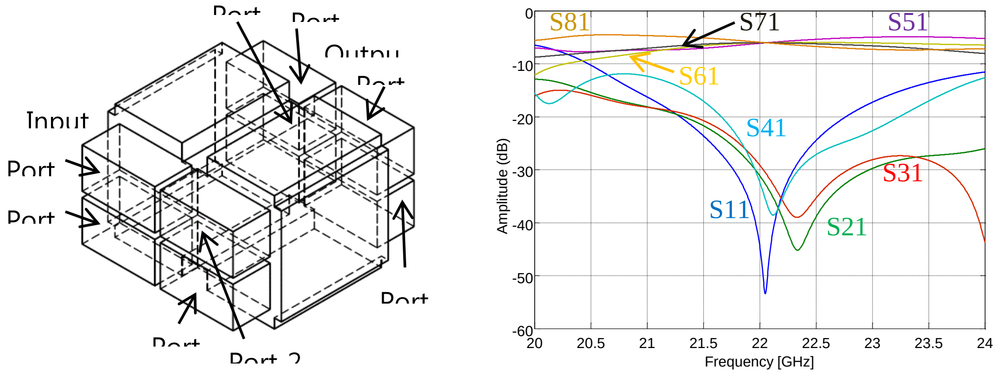

(a) (b)

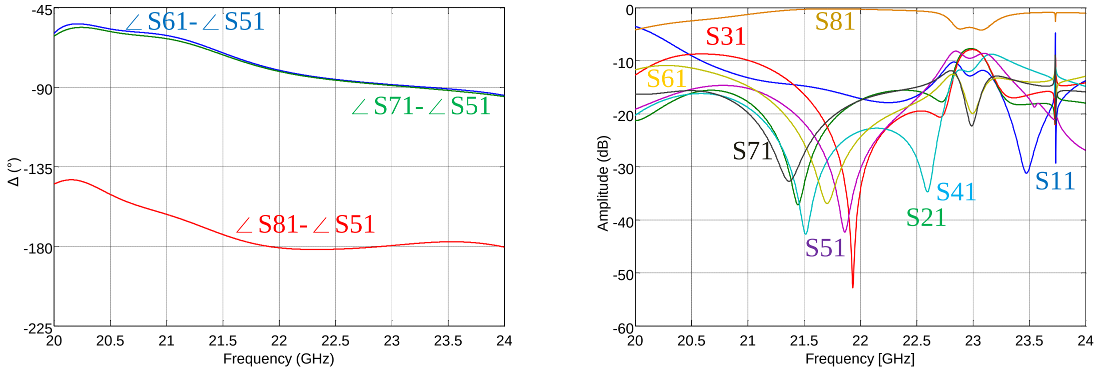

(c) (d)

Fig. 2.14 Characteristics of short-slot 2-plane coupler (a) Drawing (b) Amplitudes of hybrid coupler (c) Output phase differences of hybrid coupler (d) Amplitudes of cross coupler.

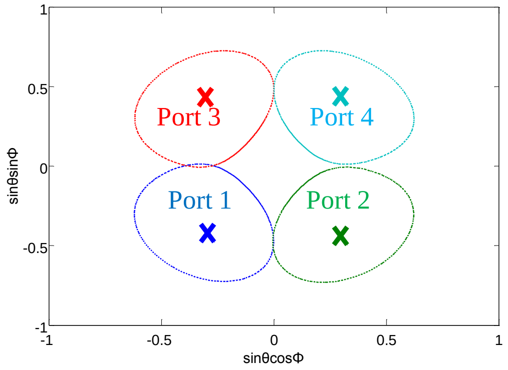

Fig. 2.15 -3 dB gain patterns of the short-slot 2-plane hybrid coupler. Symbol *X* indicates a beam direction.

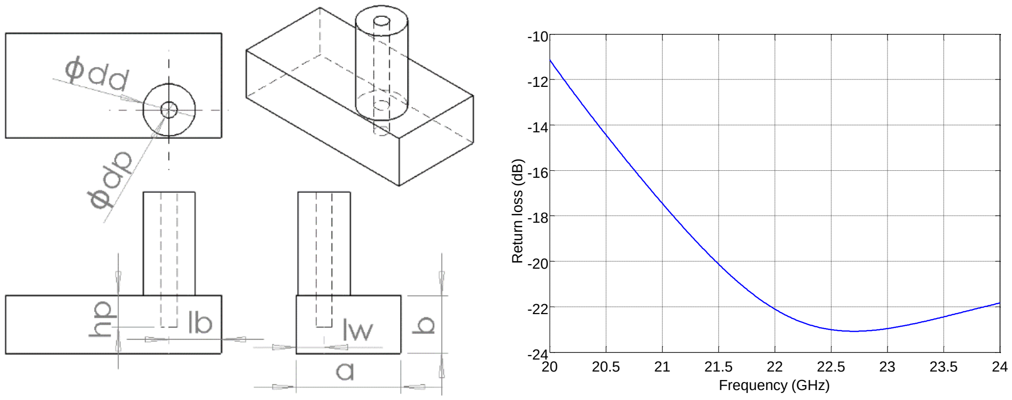

(a) (b)

Fig. 2.16 Launcher (a) Drawing (b) Return loss

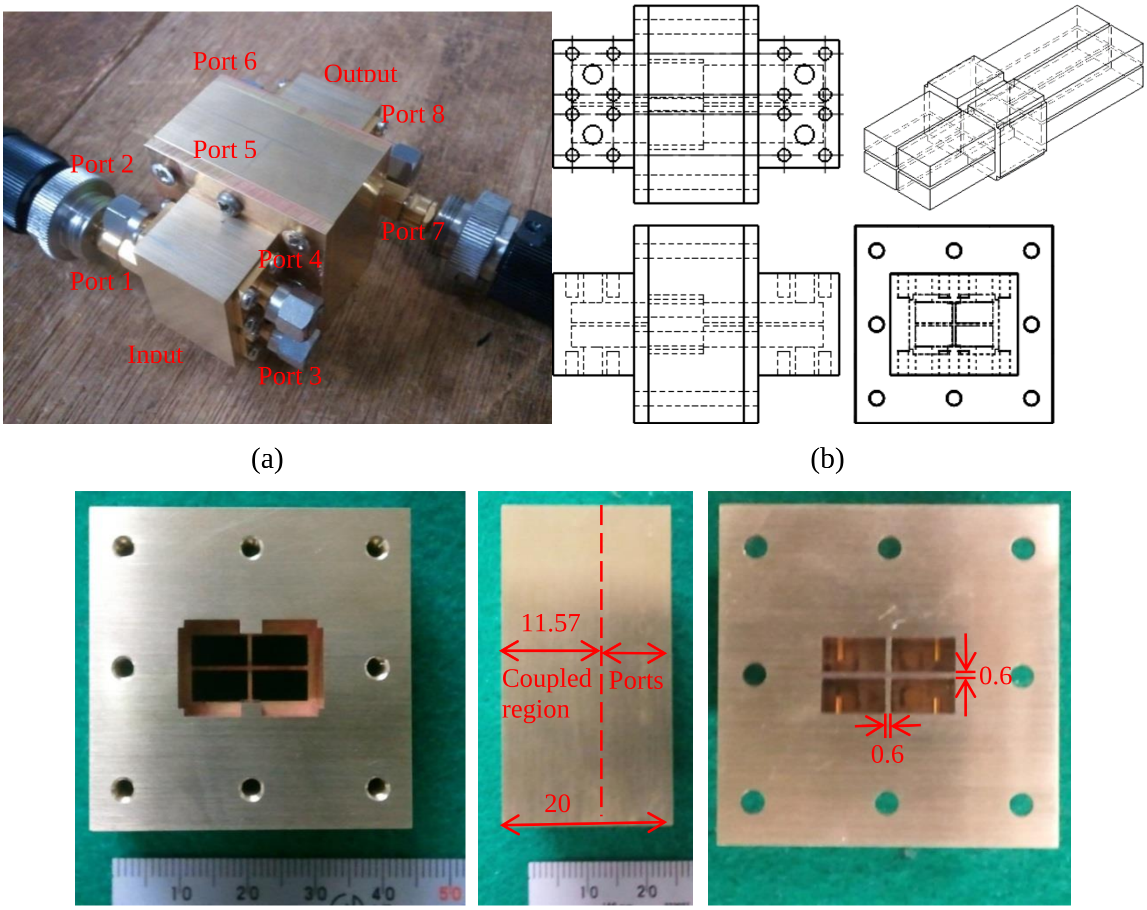

(a) (b)

(c) (d) (e)

Fig. 2.17 Fabricated short-slot 2-plane hybrid coupler (a) Measurement scene (b) Drawings (c) Frond view of the coupled region part (d) Side view of the coupled region part (e) Frond view of the coaxial-to-waveguide transition part. Unit: mm.

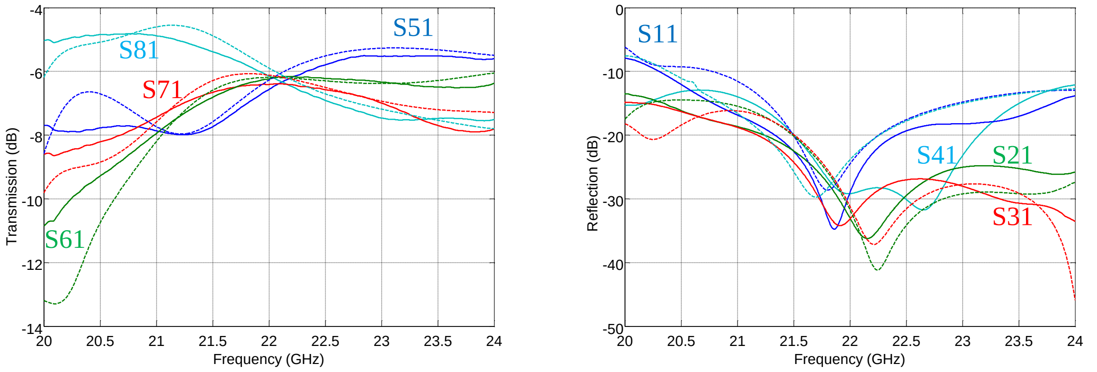

(a) (b)

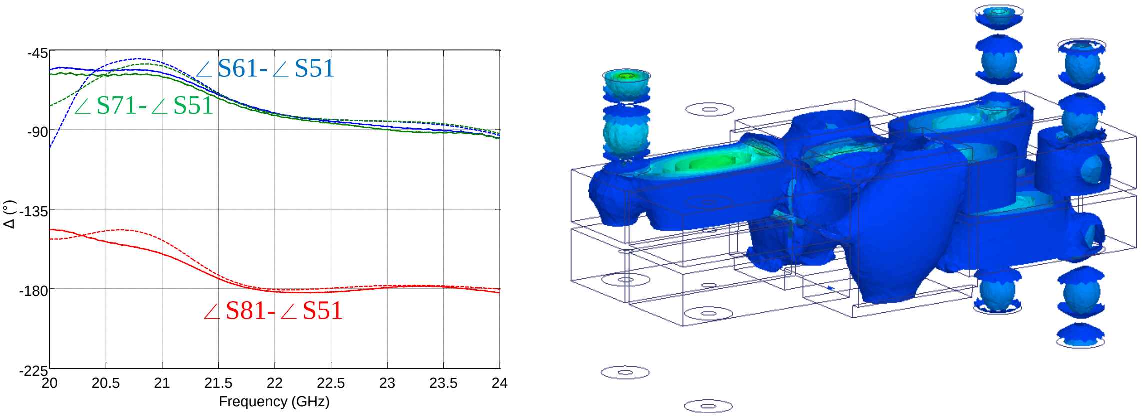

(c) (d)

Fig. 2.18 Characteristics of short-slot 2-plane hybrid coupler (a) Transmission (b) Reflection with isolations (c) Output phase difference (d) Propagation of electric field. Solid lines: measurement, Dashed lines: simulation.

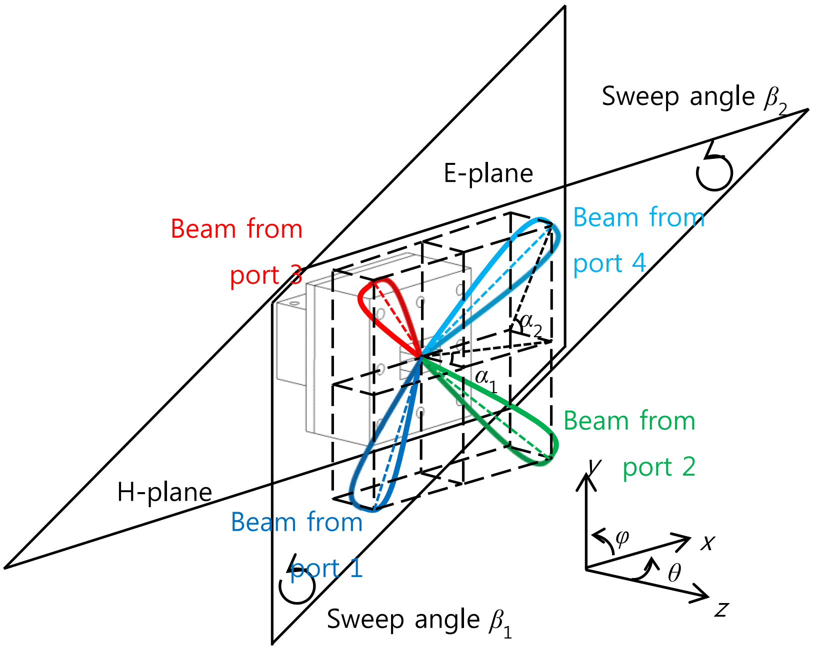

(a)

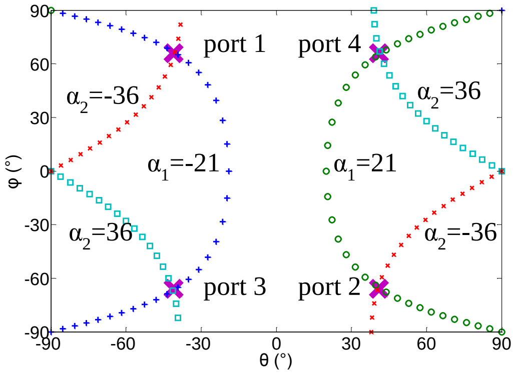

(b)

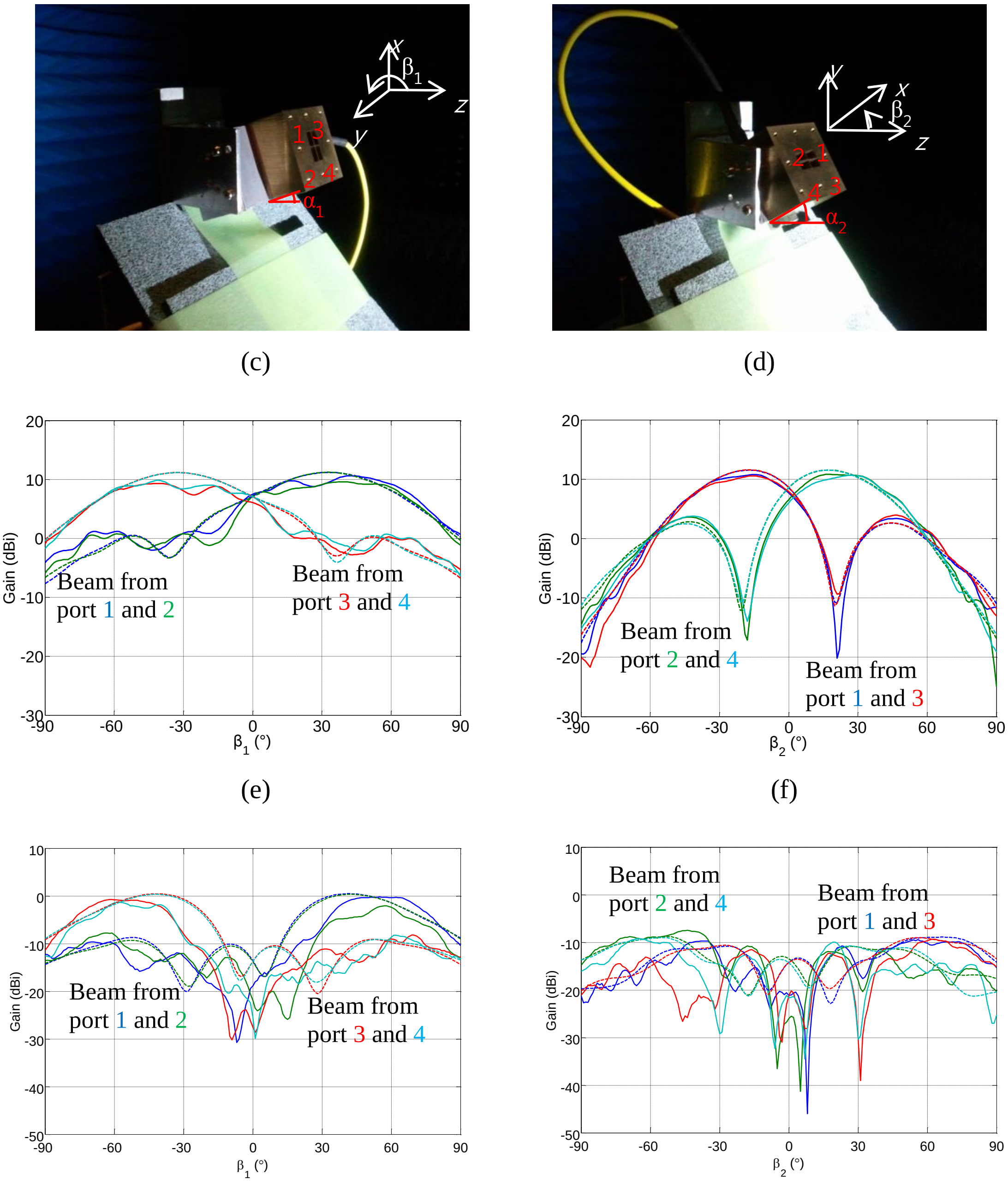

(c) (d)

(e) (f)

(g) (h)

Fig. 2.19 Radiation patterns of the short-slot 2-plane hybrid coupler (a) Configuration (b) Trajectories in the measurements and beam directions; Quasi-E plane (c) Measurement scene (e) Radiation pattern of co-polarization (g) Radiation pattern of cross-polarization; Quasi-H plane (d) Measurement scene (f) Radiation pattern co-polarization (h) Radiation pattern of cross-polarization. Solid lines: measurement, Dashed lines: simulation.

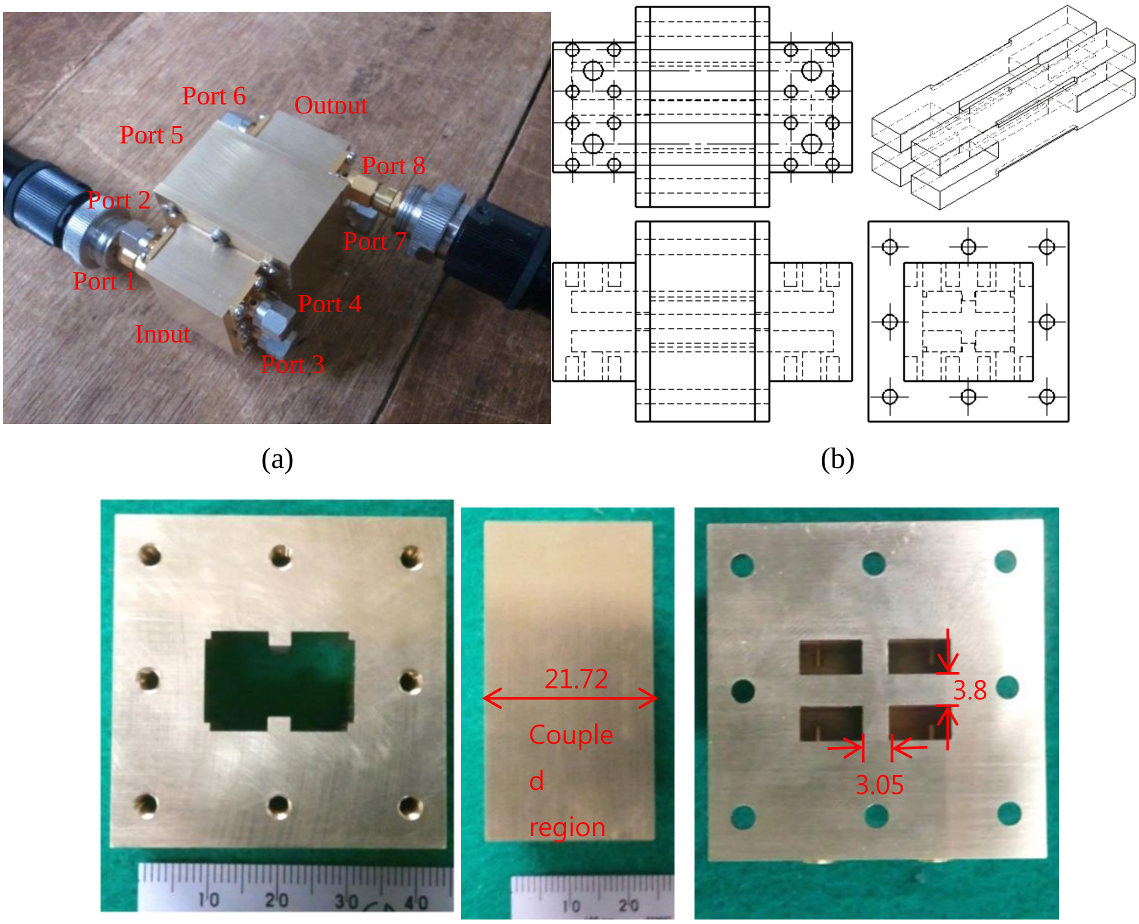

(a) (b)

(c) (d) (e)

Fig. 2.20 Fabricated short-slot 2-plane cross coupler (a) Measurement scene (b) Drawings (c) Frond view of the coupled region part (d) Side view of the coupled region part (e) Frond view of the coaxial-to-waveguide transition part. Unit: mm.

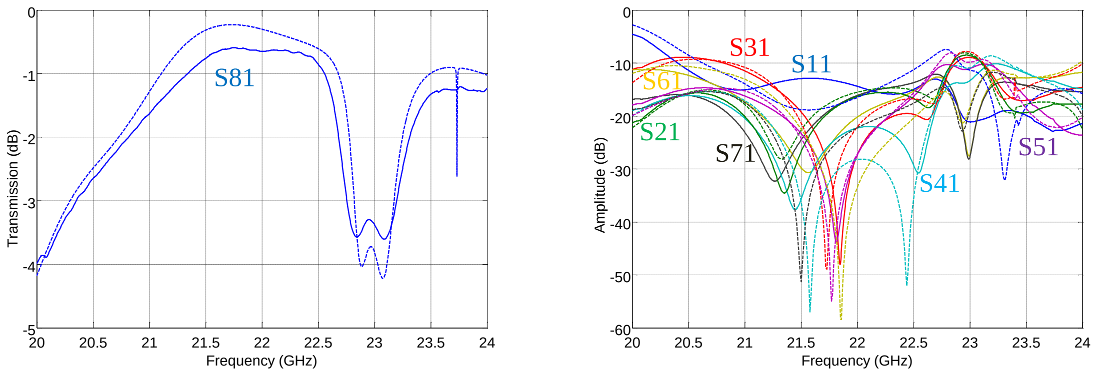

(a) (b)

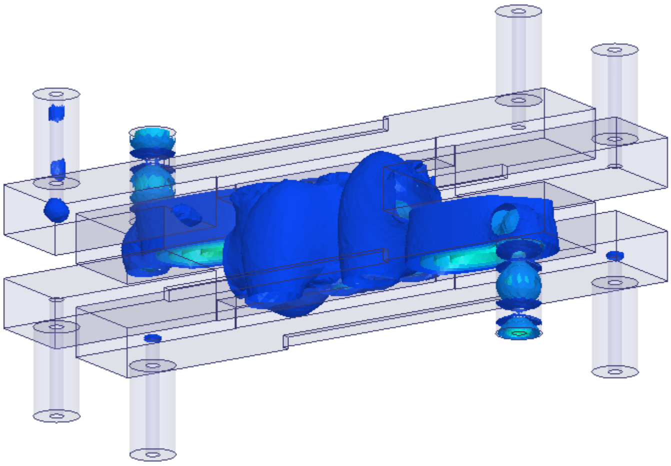

(c)

Fig. 2.21 Characteristics of short-slot 2-plane cross coupler (a) Transmission (b) Reflection with isolations (c) Propagation of electric field. Solid lines: measurement, Dashed lines: simulation.

Table 2.1 Design parameters of short-slot couplers.

Plane	E-plane (mm)		H-plane (mm)	
Type	Hybrid	Cross	Hybrid	Cross
a	7.85			
b	4.35			
a'	8.83		15.60	
b'	12.90		4.35	
l	11.00	21.00	10.90	18.70
t	0.6			

Table 2.2 Performances of short-slot couplers.

Plane	E-plane		H-plane	
Type	Hybrid	Cross	Hybrid	Cross
FBW (%)	1% (21.89~22.11 GHz)		7% (21.61~23.18 GHz)	
Transmission (dB)	-3±0.3	>-0.5	-3±0.3	>-0.2
1)Reflection (dB)	<-24.1	<-12.1	<-21.6	<-17.8
2)Phase difference (Δ°)	-90.5±0.5	-	-89.8±0.2	-

1)Include the isolation, 2)∠S41-∠S31

Table 2.3 Performances of 4×4-way short-slot combined couplers.

Type	Hybrid	Cross

FBW (%)	1.3% (21.91~22.19 GHz)	
Transmission (dB)	-6±0.5	>-0.5
1)Reflection (dB)	<-21.4	<-12.7
Phase difference (Δ°)	2)-89.5±0.5, 3)-179.5±0.5	-

1)Include the isolation, 2)∠S61-∠S51 and ∠S71-∠S51, 3)∠S81-∠S51

Table 2.4 Design parameters of short-slot 2-plane couplers. Unit: mm.

Type	a	b	a'	b'	w_r	h_r	w_t	h_t	l	t
Hybrid	7.85	4.35	18.75	12.5	2.715	1.81	0.7575	1.05	11.57	0.6
Cross									22.14	

Table 2.5 Simulated performances of short-slot 2-plane couplers.

Type	Hybrid	Cross
FBW (%)	2.4% (21.75~22.27 GHz)	
Transmission (dB)	-6±0.5	>-0.5
1)Reflection (dB)	<-23.8	<-12.7
Phase difference (Δ°)	2)-81.8±2.6, 3)-181.5±1.3	-

1)Include the isolation, 2)∠S61-∠S51 and ∠S71-∠S51, 3)∠S81-∠S51

Table 2.6 Design parameters of launcher. Unit: mm.

a	b	l_b	l_w	h_p	d_d	d_p
7.85	4.35	3.94	2.1	2.36	3.9	1.2

Table 2.7 Performances of short-slot 2-plane hybrid coupler.

Type	Measurement	Simulation
FBW (%)	2.3% (21.90~22.41 GHz)	2.3% (21.87~22.40 GHz)
Volume (mm^3)	41.4×41.4×11.57 (1)60)	
Weight (kg)	0.15	
Transmission (dB)	-6.3±0.5	-6.1±0.5
2)Reflection (dB)	<-20.0	<-18.4
Phase difference (Δ°)	3)-82.5±3.4, 4)-181.7±0.7	3)-81.5±2.4, 4)-180.1±0.5

1)Include the transitions, 2)Include the isolation, 3)∠S61-∠S51 and ∠S71-∠S51, 4)∠S81-∠S51

Table 2.8 Performances of short-slot 2-plane hybrid coupler.

	Type	Port 1	Port 1	Port 3	Port 4
Measurement	(β_1, α_1) (°)	42, -21	38, 21	-41, -21	-41, 21
	(β_2, α_2) (°)	-15, 36	18, 36	-16, 36	27, 36
	Gain (dBi)	10.8	10.8	10.6	10.7
	HPBW (°) E/H-plane	67/39	66/38	64/40	65/37
Simulation	(β_1, α_1) (°)	34, -21	34, 21	-34, -21	-34, 21
	(β_2, α_2) (°)	-17, -36	17, -36	-17, 36	17, 36
	Gain (dBi)	11.5			
	HPBW (°) E/H-plane	49/37			

Table 2.9 Performances of short-slot 2-plane cross coupler.

Type	Measurement	Simulation
FBW (%)	2.3% (21.90~22.41 GHz)	2.3% (21.87~22.40 GHz)
Volume (mm^3)	41.4×41.4×21.72 (1)61.72)	
Weight (kg)	0.28	
Transmission (dB)	>-0.7	>-0.8
2)Reflection (dB)	<-13.8	<-13.7

1)Include the transitions, 2)Include the isolation

Reference

[2.1] S. Yamamoto, J. Hirokawa, and M. Ando, “Length reduction of short-slot directional coupler in a single layer dielectric substrate waveguide by removing dielectric near the side walls,” *IEEE Intl. Symp. Antennas Propag.*, vol. 3, pp. 2353–2356, 2004.

[2.2] J. Hirokawa, “ラジアル線路用多重直交回転モード励振 1 層導波管回路の基礎検討,” *Proc. IEICE Soc. Conf.*, B-1-114, Hokkaido University, Sep. 2016.

[2.3] M. P. Drazin, "Some generalizations of matrix commutativity," *Proc. London Math. Soc.*, vol. 1, pp. 222-231, 1951.

[2.4] D.-H. Kim, J. Hirokawa, and M. Ando, “Design of Waveguide Short-slot 2-plane Couplers for One-body 2-D Beam-switching Butler Matrix Application,” *IEEE Trans. Microw. Theory Techn.*, vol. 64, no. 3, pp. 776-784, Mar. 2016.

[2.5] D. M. Pozar, “Electromagnetic Theory,” in *Microwave Engineering*, 2nd ed., New York, Wiley, 1998, p. 128.

[2.6] D. M. Pozar, “Transmissions and Waveguides,” in *Microwave Engineering*, 2nd ed., New York, Wiley, 1998, pp. 47-49.

[2.7] U. Rosenberg and K. Beis, “Improved narrow-wall short slot coupler design exhibiting significant increased bandwidth and low cost production,” *Proc. 31st Eur. Microw. Conf.*, vol. 3, pp. 197-200, Sep. 2001.

[2.8] R. Beyer and U. Rosenberg, "Compact top-wall hybrid/coupler design for extreme broad bandwidth application," *IEEE MTT-S Intl. Symp. Dig.*, pp. 1227-1280, June 2005.

[2.9] D. M. Pozar, “Microwave Resonators,” in *Microwave Engineering*, 2nd ed., New York, Wiley, 1998, pp. 313-315.

Chapter 3

Wideband short-slot 2-plane coupler

The operating bandwidth of the short-slot coupler is depended on the linearity of propagating modes in the coupled region. In the previous chapter, TE_{11} and TE_{21} modes in the coupled region are excluded, because those have small coupling coefficients and different propagation constants to TM_{11} and TM_{21} modes, respectively. In view of the law of energy of conservation, those ignored modes can improve the linearity of outputs under the specified conditions which the propagation constant difference between TE_{11} and TM_{11} (TE_{21} and TM_{21}) modes is $2\pi n$ where n is an integer. In that time, TE_{30} mode has not exact same the polarity of TE_{10} mode, it works as the complementary mode with the quasi-equal polarities of TE_{10} mode. It can also improve the linearity of TE_{10} mode. Following sections, the operation principal, the design procedures, and the simulation and the measurement results of the wideband short-slot coupler are presented.

3.1 Bandwidth boundaries of short-slot 2-plane coupler

Normally the operating bandwidth is defined by the given conditions for the purpose. In this paper, the condition of the operating bandwidth of the short-slot 2-plane coupler is the output amplitudes of a 4×4-way short-slot 2-plane hybrid coupler within -6±0.5 dB. A fundamental perspective to the operating bandwidth, the lower and the upper boundaries of that is restricted by the width of the port branch and the dimensions of the coupled region, respectively. First, when the width of the port branch is too narrow to pass the dominant mode TE_{10}, the waveguide is just an attenuator. Second, when the dimensions of the coupled region are approached the specific values those generate the resonance, it is just a resonator. Based on these restrictions, the design of wideband short-slot 2-plane couplers is conducted.

3.1.1 Theory

According to the design procedure of the short-slot 2-plane coupler in Chapter 2, four selected propagating modes in the coupled region (TE_{10}, TE_{20}, TM_{11} and TM_{21}) should have -6 dB coupling coefficients. However it is impossible because of the existence of other propagation modes (TE_{01} and TE_{11}). In view of the law of conservation of energy, the energy of a specified propagation mode transfers the complementary mode which turns from the evanescent mode to the propagating mode. In that time, a specified propagating mode and the complementary mode have equal or quasi-equal polarities of electric field distribution in the coupled region, because the combination of the energy of x- and y-direction polarized electric fields of a specified propagating mode and the complementary mode should be maintained. TE_{11} and TE_{21} modes are the complementary modes with the equal polarities of TM_{11} and TM_{21} modes. TE_{30} mode is the complementary mode with the quasi-equal polarities of TE_{10} mode. In the short-slot 2-plane coupler, TE_{mn} and TM_{mn} modes have different propagation constants. If the phase difference between a specified propagating mode and the complementary mode in the given length of the coupled region is closed a 2π multiple, these two modes can be merged with less dissipation. It makes to increase the operating bandwidth through improving the flatness of output amplitudes and phases of short-slot 2-plane couplers [3.1]. In the previous design of the short-slot 2-plane coupler, it is difficult to satisfy with Eqs. (2.76) and (2.77), simultaneously. Additionally, the inflection points of coupling coefficients of TE_{10} and TM_{21} modes exist around the center frequency as shown in Fig. 2.12(i). In these situations, the combination of coupling coefficients and propagation constants of the selected propagating modes increase the deviation of the four output amplitudes of the short-slot 2-plane hybrid coupler and the output amplitudes (except 2-D crossing output) of the short-slot 2-plane cross coupler. It makes to restrict the expansion of the operating bandwidth. So design parameters of the short-slot 2-plane coupler should be selected to satisfy not only the conditions based on the design procedures mentioned in Chapter 2, but also the flatness of the amplitudes of the coupling coefficients and the differences between the propagation constants of the propagating modes. Generally, the double ridge waveguide is used to increase the operating bandwidth toward low frequency. It means that the coupling coefficients of propagating modes are shifted to lower frequency, if the outermost of the coupled region is maintained. The height of the double ridge is increased to shift the coupling coefficients of propagating modes toward low frequency. In that time, TE_{30} and TE_{21} modes are turned from the evanescent modes to the propagating modes, and the coupling coefficients of TE_{10} and TM_{21} modes are decreased around center frequency. Then, the height of the trimmed the outermost vertices of double ridge rectangular waveguide is selected to satisfy the conditions based on the design procedures mentioned in Chapter 2 and to improve the flatness of the amplitudes of the coupling coefficients of four propagating mode groups (TE_{10}/TE_{30}, TE_{20}, TE_{11}/TM_{11}, TE_{21}/TM_{21}). In that time, the unification of the propagating mode and its complementary mode is expressed as

$$C_{cm}e^{-j\beta_{um}l_{type}} = C_{pm}e^{-j\beta_{pm}l_{type}} + C_{cm}e^{-j\beta_{cm}l_{type}} \tag{3.1}$$

where C_i and β_i are a coupling coefficient and a propagation constant of mode (*cm*→*C*ombined *M*ode, *pm*→*P*ropagating *M*ode, *cm*→*C*omplementary *M*ode), l_{type} is the length of the coupled region of a coupler type (*H*ybrid or *C*ross).

In consequence of the novel design procedures, the frequency bandwidth of the short-slot 2-plane coupler is increased under a given condition.

3.1.2 Simulation results

There are two short-slot 2-plane coupler models which are with the hollow waveguide operated in 22 GHz and with the lossy dielectric waveguide operated in 5.12 GHz. The prior model is simulated to compare the wideband short-slot 2-plane coupler with the short-slot 2-plane coupler mentioned in Chapter 2. The posterior model is simulated to check the feasibility of the waveguide filled with dielectric material for reducing a volume of the short-slot 2-plane coupler, and to verify actual performance in WiMAX application.

3.1.2.1 Hollow waveguide

When varying the widths and the heights of the double ridge and four trimmed, the width and the height of the coupled region should be changed to satisfy the novel design procedures. The cross-sections of the coupled regions of the short-slot 2-plane hybrid and cross couplers in Chapter 2 are shared same dimensions by the design procedures. In that time, the design parameters of the coupled region is focused on the short-slot 2-plane hybrid coupler. Thus the performance of the short-slot 2-plane cross coupler is not optimized, because only the length of the coupled region is variable. For that reason, the cross-sections of the coupled regions of the short-slot 2-plane cross coupler is different from the short-slot 2-plane hybrid coupler's. Design parameters of the wideband short-slot 2-plane couplers are listed in Table 3.1. Simulations are conducted on the lossless structure in 22 GHz band. Except a simulation for the coupling coefficient has conducting wall (C3560P, $\sigma=1.31\times10^7$ S/m) because of the convergence. In Fig. 3.1(a)-(b), propagation constants of modes of the coupled region of wideband short-slot 2-plane hybrid coupler are shifted to low frequency. As a result, TE_{30} and TE_{21} modes are turned from the evanescent mode to the propagating mode. In Fig. 3.1(c)-(d), propagation constants of modes of the coupled region of wideband short-slot 2-plane cross coupler have different frequency dependencies. Propagation constants of TE_{10}, TE_{01}, TE_{11}, and TE_{30} modes are shifted to low frequency, but TE_{20}, TM_{11}, TE_{21}, and TM_{21} modes are shifted to high frequency. As mentioned Eqs. (2.95) to (2.100), the variation of the design parameters of the coupled region affects the frequency dependencies of modes. Only TE_{30} mode is turned from the evanescent mode to the propagating mode. In the same way, the coupling coefficients of modes of the coupled region of wideband short-slot 2-plane couplers are shifted to the corresponded frequency directions as shown in Fig. 3.2. At Fig. 3.2(a) and (c), the coupling coefficients of TE_{10} and TM_{21} modes appear variation around center frequency. If the modes contributed the output of the short-slot 2-plane coupler are restricted only four propagating modes (TE_{10}, TE_{20}, TE_{11}, TE_{21}), the operating bandwidth is limited in the narrow boundary. Actually, four mode groups (TE_{10}/TE_{30}, TE_{20}, TE_{11}/TM_{11}, TE_{21}/TM_{21}) are contributed the output of the short-slot 2-plane coupler. The coupling coefficients of four mode groups of the short-slot 2-plane hybrid coupler achieve the flatness around the center frequency as shown in Fig. 3.3(a). On the other hand, the coupling coefficients of four mode groups of the short-slot 2-plane cross coupler have a fluctuation (TE_{10}/TE_{30}) and an inflection point (TE_{21}/TM_{21}) as shown in Fig. 3.3(b), it seems that the operating bandwidth is limited in the narrow boundary. Although the short-slot 2-plane hybrid coupler should consider the amplitude and the phase of four outputs, the short-slot 2-plane cross coupler considers only the amplitude and the phase of single output. This single output consists of two different polarity mode groups (TE_{10}/TE_{30}, TE_{21}/TM_{21}) and (TE_{20}, TE_{11}/TM_{11}). As a result, a fluctuation and an inflection point are canceled out. When the definition of the operating frequency band of the short-slot 2-plane hybrid coupler is set to the output amplitudes within -6±0.5 dB, the performances of the short-slot 2-plane couplers are listed in Table 3.2, and shown as Fig. 3.4 and 3.5, respectively. Comparing the results of Chapter 2, the short-slot 2-plane couplers based on the novel design procedures have a wide FBW (2.4%→5.5%).

3.1.2.2 Lossy dielectric waveguide

The dielectric-filled waveguide short-slot 2-plane coupler consists of dielectric material (PPS, ε_r=3.2, $\tan\delta=2.7\times10^{-3}$) covered with aluminum alloy (A6061, $\sigma=2.56\times10^{7}$ S/m). In view of electromagnetics, the design parameters of the short-slot 2-plane coupler can be rescaled by frequency ($\propto 1/f$) and electrical permittivity ($\propto 1/\sqrt{\varepsilon_r}$). In the same way, the design parameters of the dielectric-filled waveguide short-slot 2-plane coupler are listed in Table 3.3. The propagation constants of modes of the coupled region of the dielectric-filled waveguide short-slot 2-plane coupler are exactly same as the hollow waveguide short-slot 2-plane coupler's, just frequency rescaling as shown in Fig. 3.6. Although the tendency of the coupling coefficients of the dielectric-filled waveguide short-slot 2-plane coupler is same to the hollow waveguide short-slot 2-plane coupler's, the amplitude difference between coupling coefficient is not same. The loss in the dielectric-filled waveguide short-slot 2-plane coupler comes from the tangent delta of the dielectric material and the electrical conductivity of the conductor walls. The conductor and dielectric losses of the dielectric-filled waveguide short-slot 2-plane coupler are expressed as [3.2]

$$\alpha=\alpha_c+\alpha_d \tag{3.2}$$

$$\alpha_{c,\mathrm{TE}_{\mathrm{mn}}}=\frac{2R_S}{b'\eta\sqrt{1-\left(\frac{f_c}{f}\right)^2}}\left(\left(1+\frac{b'}{a'}\right)\left(\frac{f_c}{f}\right)^2+\frac{\frac{b'}{a'}\left(\frac{b'}{a'}m^2+n^2\right)}{\left(\frac{b'}{a'}m\right)^2+n^2}\left(1-\left(\frac{f_c}{f}\right)^2\right)\right) \tag{3.3}$$

$$\alpha_{c,\mathrm{TM_{mn}}} = \frac{2R_s}{b'\eta\sqrt{1-\left(\frac{f_c}{f}\right)^2}} \frac{\left(\frac{b'}{a'}\right)^3 m^2+n^2}{\left(\frac{b'}{a'}m\right)^2+n^2} \tag{3.4}$$

$$\alpha_d = \frac{k^2 \tan\delta}{\beta^2} \tag{3.5}$$

$$R_s = \sqrt{\frac{\omega\mu}{2\sigma}} \tag{3.6}$$

$$\eta = \sqrt{\frac{\mu}{\varepsilon}} \tag{3.7}$$

where α_c and α_d are attenuation constants due to conductor and dielectric losses, R_s is the wall surface resistance, *a'* and *b'* are the width and the height of the coupled region, *f* is the frequency, f_c is the cut-off, η is the intrinsic impedance, μ is the electrical permeability, σ is the electrical conductivity, ε is the electrical permittivity.

The attenuation constants due to conductor and dielectric losses are inversely proportional to the propagation constant. It means that each mode in the coupled region has a difference the attenuation constant. Especially, high order modes which have low propagation constants have more loss as shown in Fig. 3.7. It is directly reflected the coupling coefficient of propagating mode groups as shown in Fig. 3.8. These discriminated losses improve the flatness of the amplitudes of the coupling coefficients of four propagating mode groups. For that reason, the dielectric-filled waveguide short-slot 2-plane couplers based on the novel design procedures have a wider FBW (6.1%) than the hollow waveguide's. In the given design conditions, the loss is dominated by the dielectric loss. In the short-slot 2-plane hybrid coupler, the contribution portion of the loss is more than 0.2 dB from the dielectric loss and less than 0.1 dB from the conductor loss at the center frequency. The loss of the short-slot 2-plane cross coupler is almost twice of the short-slot 2-plane cross coupler's. Insertion losses of the dielectric-filled short-slot 2-plane couplers are larger than the averages of the losses included the dielectric and the conductor losses of the modes as shown in Fig. 3.11, because there are the multiple reflections in the coupled region. For the measurement, the dielectric-filled waveguide short-slot 2-plane couplers are also equipped the coaxial-to-waveguide transition (launcher). Different to the right angle launcher in Chapter 2, the end launcher is adapted for the preliminary test of the closed port formation. The design parameters and the performances of the launcher are listed in Table 3.5, and shown as Fig. 3.12, respectively.

3.1.3 Measurement results

Different to Chapter 2, following the measurement results are removed the transition effect by RLL (Reflect-Line-Line) calibration (Appendix 3) with a short plate and different length lines as shown in

Fig. 3.13. The body of the short-slot 2-plane coupler is divided into three parts as depicted in Fig. 3.14. The coupled region part has additional port branches at the output side for far-field measurement. Considering the insertion loss of the short-slot 2-plane coupler, the definition of the operating frequency band of the short-slot 2-plane hybrid coupler is set to the output amplitudes within -6.3±0.5 dB. The measured performances of the dielectric filled short-slot 2-plane coupler are listed in Table 3.6, and shown as Fig. 3.15 and 3.16, respectively. A comparison with characteristics of existing short-slot couplers is listed in Table 3.7. The wideband short-sot 2-plane coupler achieves almost same FBW of the short-slot 1-plane coupler, and reduces the volume of a combination of four short-slot 1-plane couplers to half with the same operation.

3.2 Summary

The wideband short-slot 2-plane coupler is designed by considering the combination of propagating modes in the coupled region. TE_{11}, TE_{21}, and TE_{30} modes are selected as the complimentary modes to combine TM_{11}, TM_{21}, and TE_{10} modes, respectively. Those combinations make to improve the linearity of the outputs of the short-slot coupler. In that time, the inflection points of the coupling coefficients of those combinations in the frequency domain are shifted to low frequency band. Through these processes, the bandwidth of the short-slot 2-plane coupler is increased from 2.3% to 6.1% maintaining its volume.

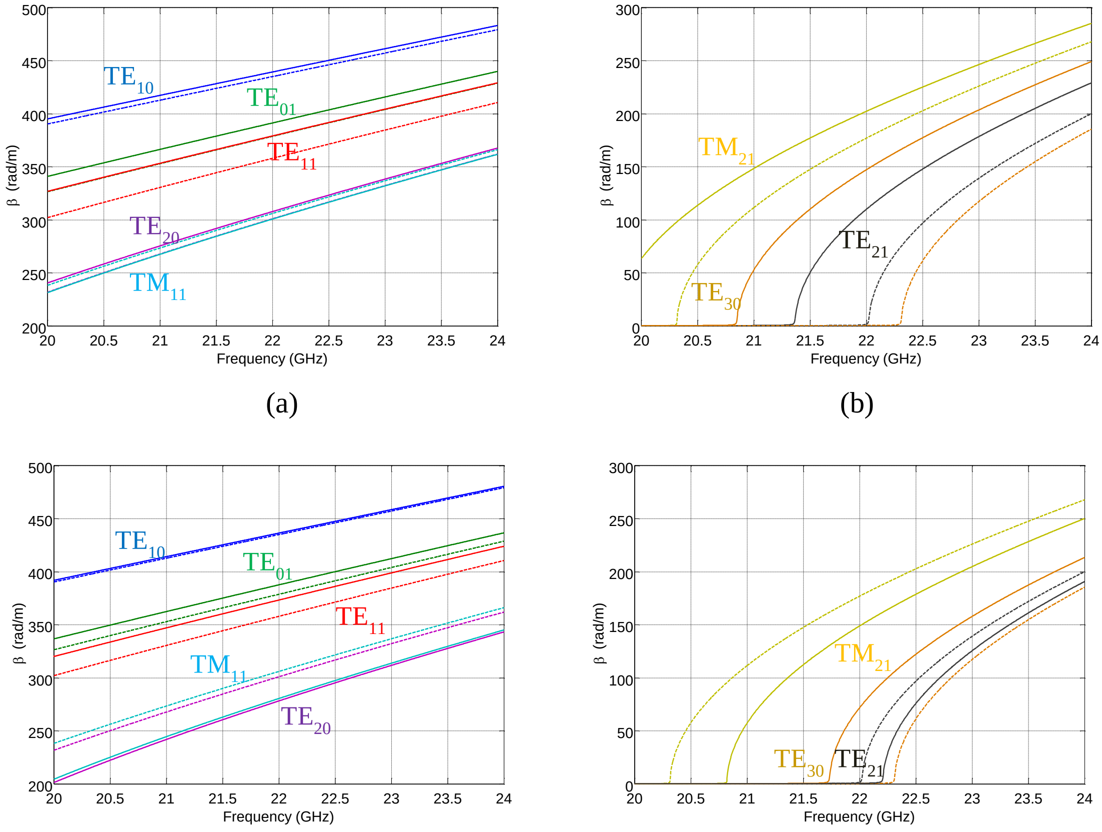

(a) (b)

(c) (d)

Fig. 3.1 The propagation constant of modes of short-slot 2-plane couplers in the coupled region (a)-(b) Hybrid coupler (c)-(d) Cross coupler. Solid lines: wideband, Dashed lines: mentioned Chapter 2.

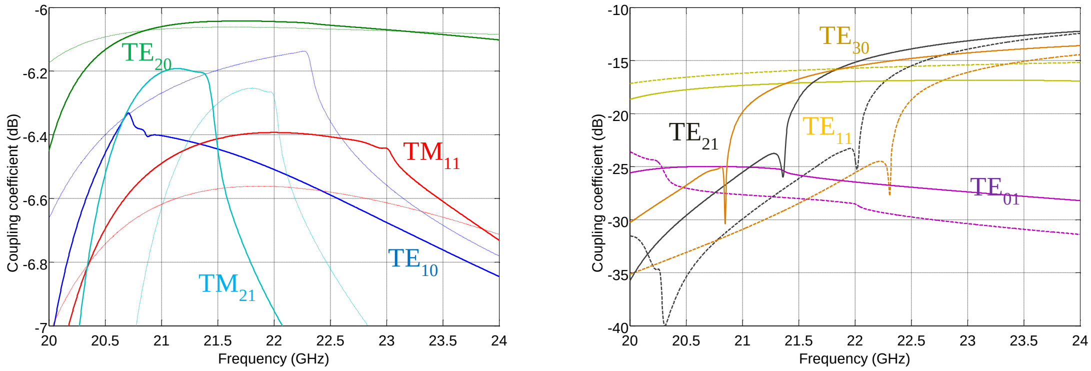

(a) (b)

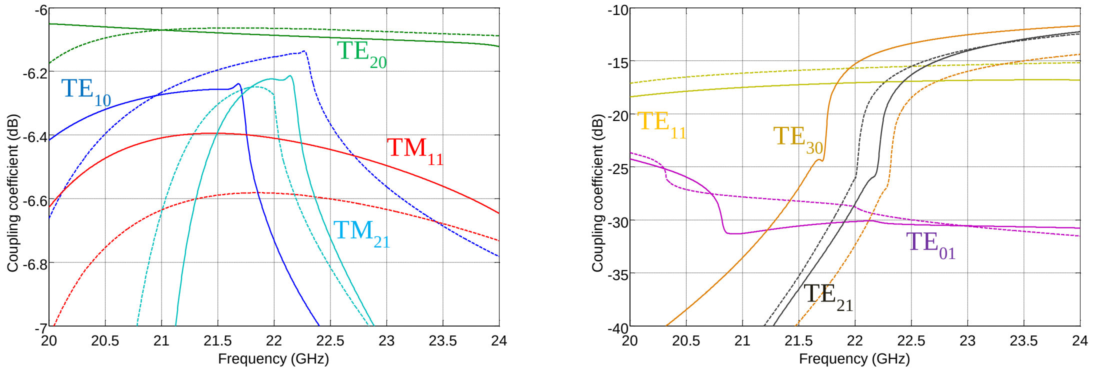

(c) (d)

Fig. 3.2 Coupling coefficient of modes in the coupled region (a)-(b) Hybrid coupler (c)-(d) Cross coupler. Solid lines: wideband, Dashed lines: mentioned Chapter 2.

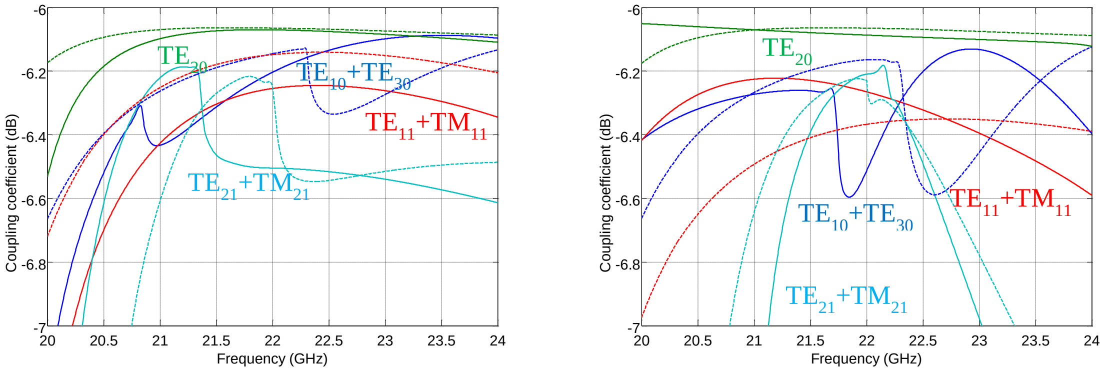

(a) (b)

Fig. 3.3 Coupling coefficient of propagating mode groups in the coupled region (a) Hybrid coupler (b) Cross coupler. Solid lines: wideband, Dashed lines: mentioned Chapter 2.

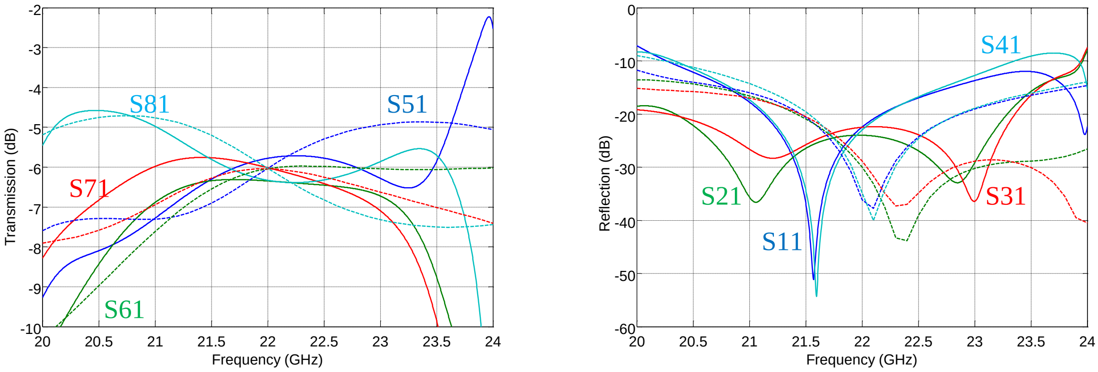

(a) (b)

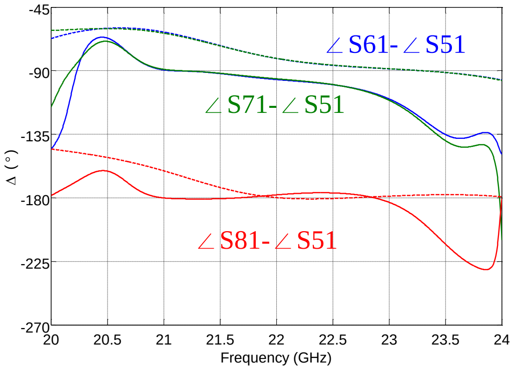

(c)

Fig. 3.4 Characteristics of short-slot 2-plane hybrid coupler (a) Transmission (b) Reflection with isolations (c) Output phase difference. Solid lines: wideband, Dashed lines: mentioned Chapter 2.

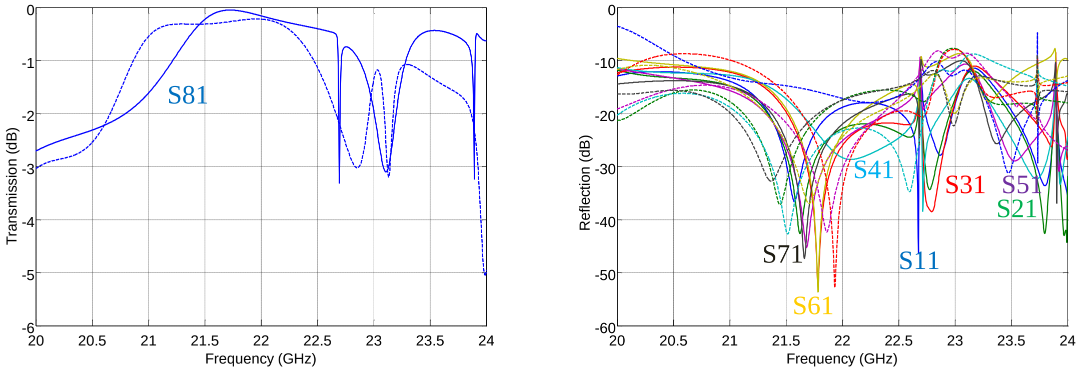

(a) (b)

Fig. 3.5 Characteristics of short-slot 2-plane cross coupler (a) Transmission (b) Reflection with isolations. Solid lines: wideband, Dashed lines: mentioned Chapter 2.

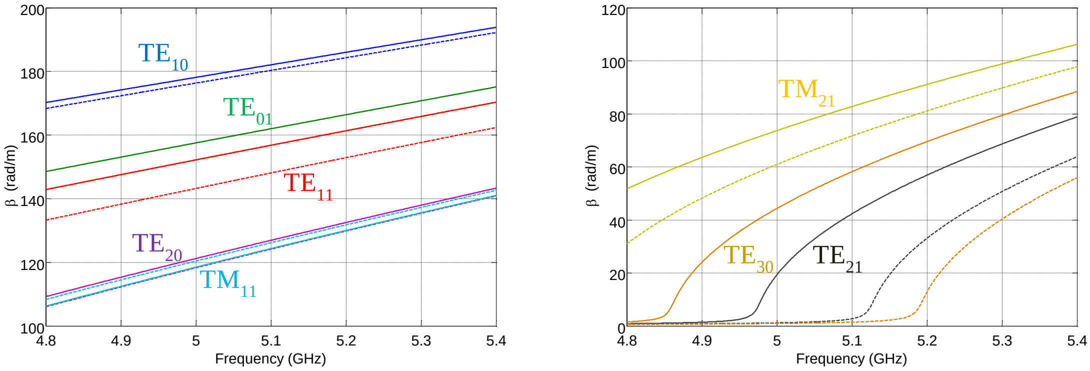

(a) (b)

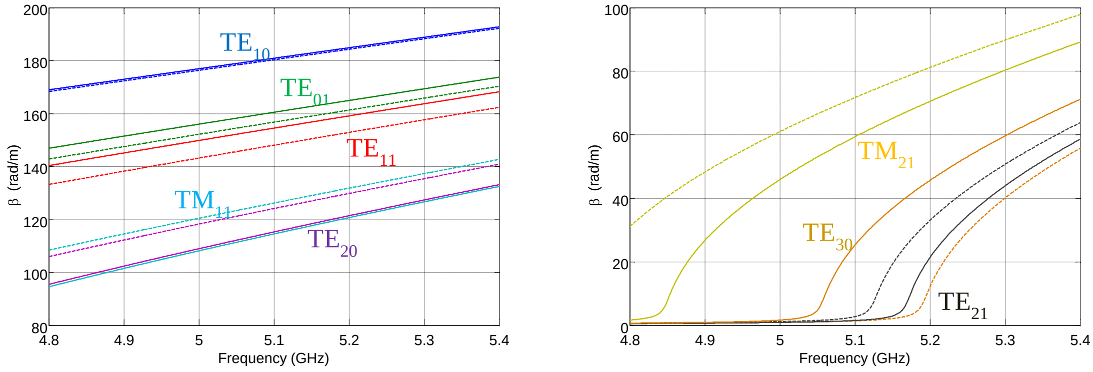

(c) (d)

Fig. 3.6 The propagation constant of modes of short-slot 2-plane couplers in the coupled region (a)-(b) Hybrid coupler (c)-(d) Cross coupler. Solid lines: wideband, Dashed lines: modified Chapter 2.

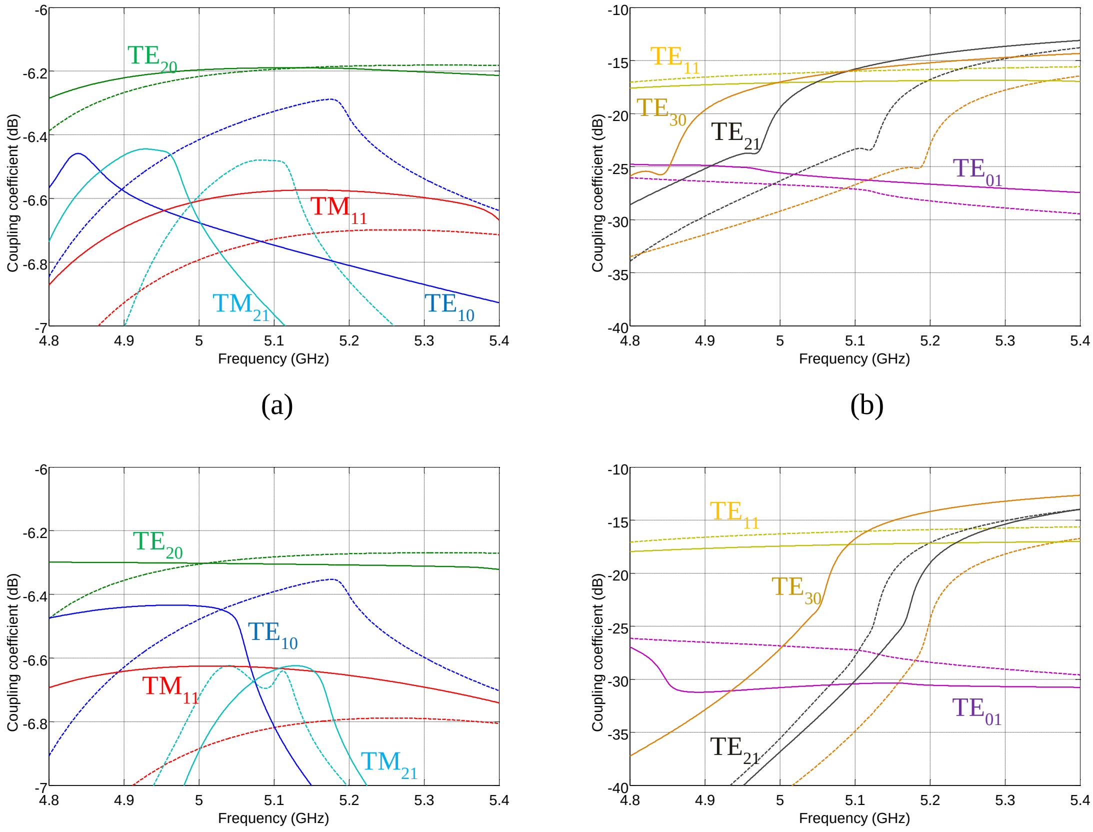

(a) (b)

(c) (d)

Fig. 3.7 Coupling coefficient of modes in the coupled region (a)-(b) Hybrid coupler (c)-(d) Cross coupler. Solid lines: wideband, Dashed lines: mentioned Chapter 2. Solid lines: wideband, Dashed lines: modified Chapter 2.

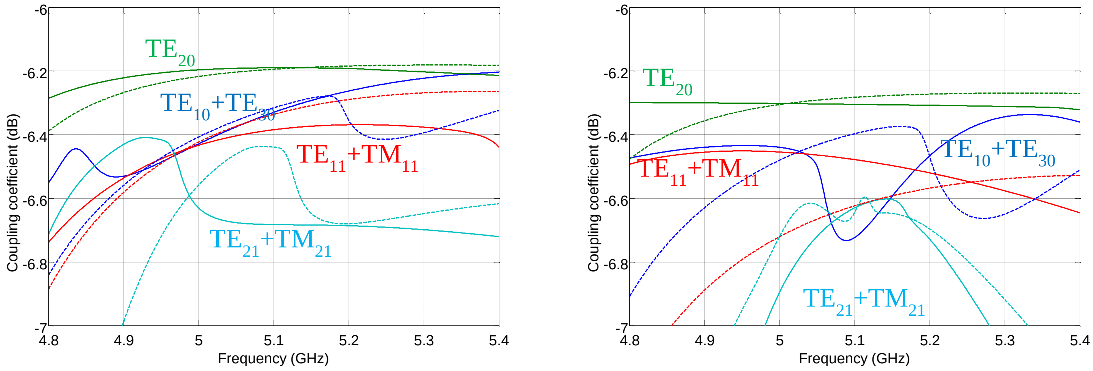

(a) (b)

Fig. 3.8 Coupling coefficient of propagating mode groups in the coupled region (a) Hybrid coupler (b) Cross coupler. Solid lines: wideband, Dashed lines: modified Chapter 2.

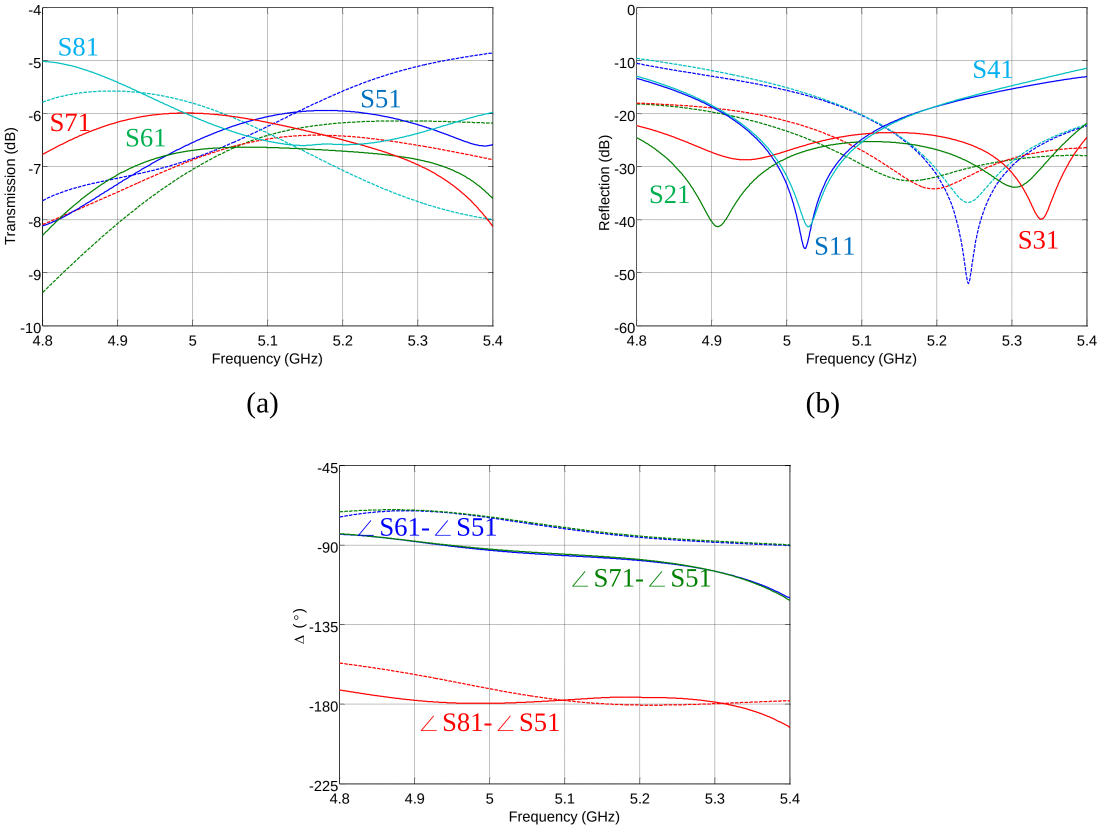

(a) (b)

(c)

Fig. 3.9 Characteristics of short-slot 2-plane hybrid coupler (a) Transmission (b) Reflection with isolations (c) Output phase difference. Solid lines: wideband, Dashed lines: modified Chapter 2.

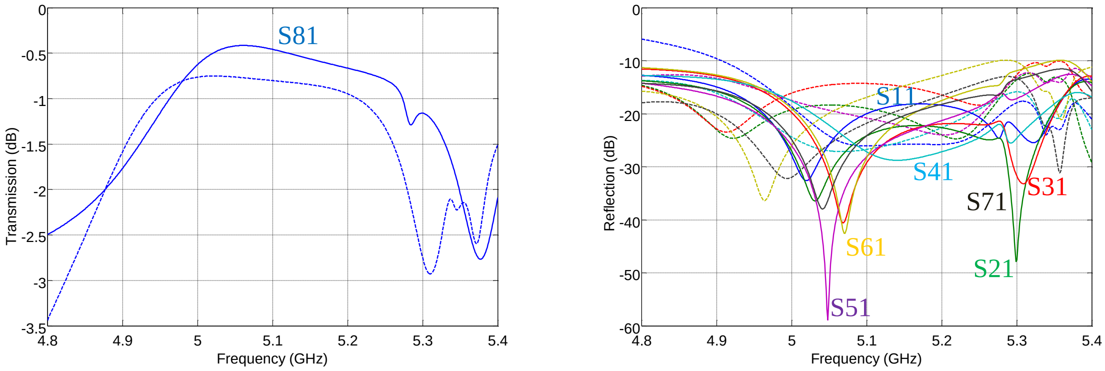

(a) (b)

Fig. 3.10 Characteristics of short-slot 2-plane cross coupler (a) Transmission (b) Reflection with isolations. Solid lines: wideband, Dashed lines: modified Chapter 2.

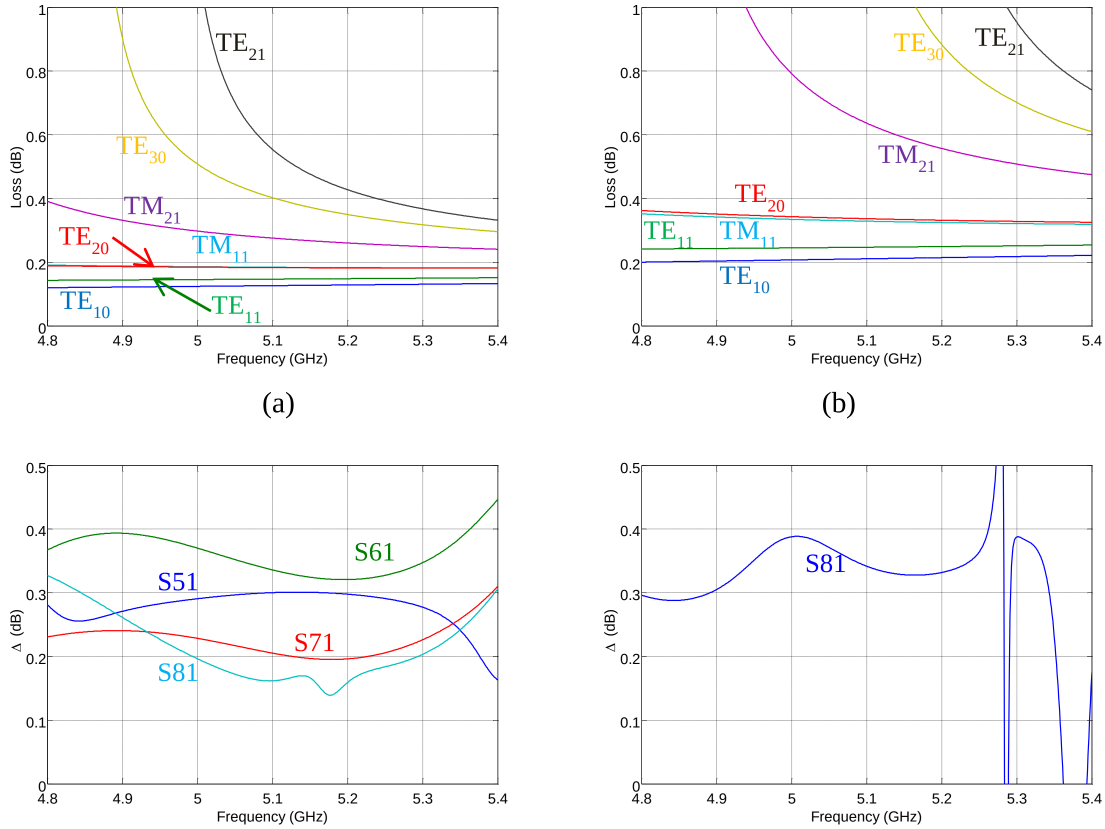

(a) (b)

(c) (d)

Fig. 3.11 Effects of the loss included the dielectric and the conductor losses of modes to the outputs of the short-slot 2-plane couplers. Hybrid (a) Modes (c) Differences of the output to the lossless case, Cross (b) Modes (d) Difference of the output to the lossless case.

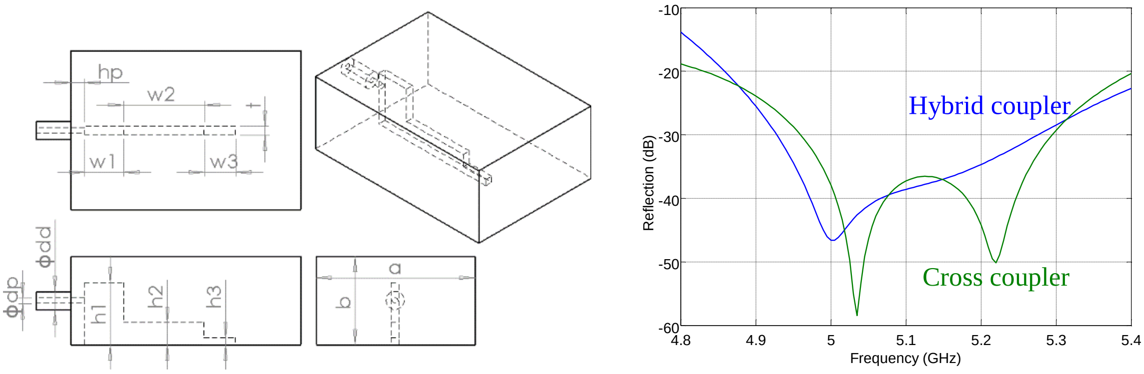

(a) (b)

Fig. 3.12 Launcher (a) Drawing (b) Return losses.

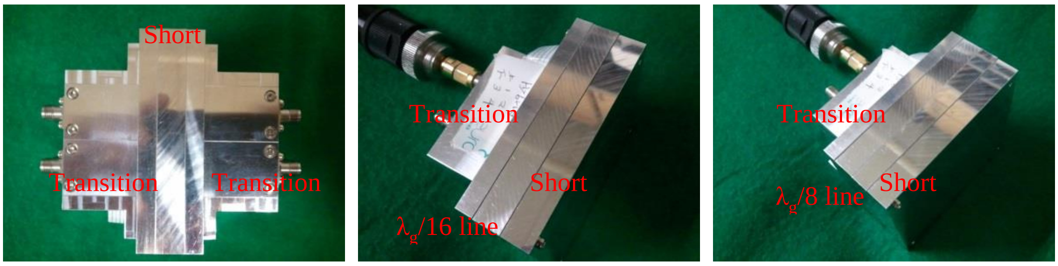

Fig. 3.13 RLL calibration (a) Reflect (b) Reflect with λ_g/16 line (c) Reflect with λ_g/8 line.

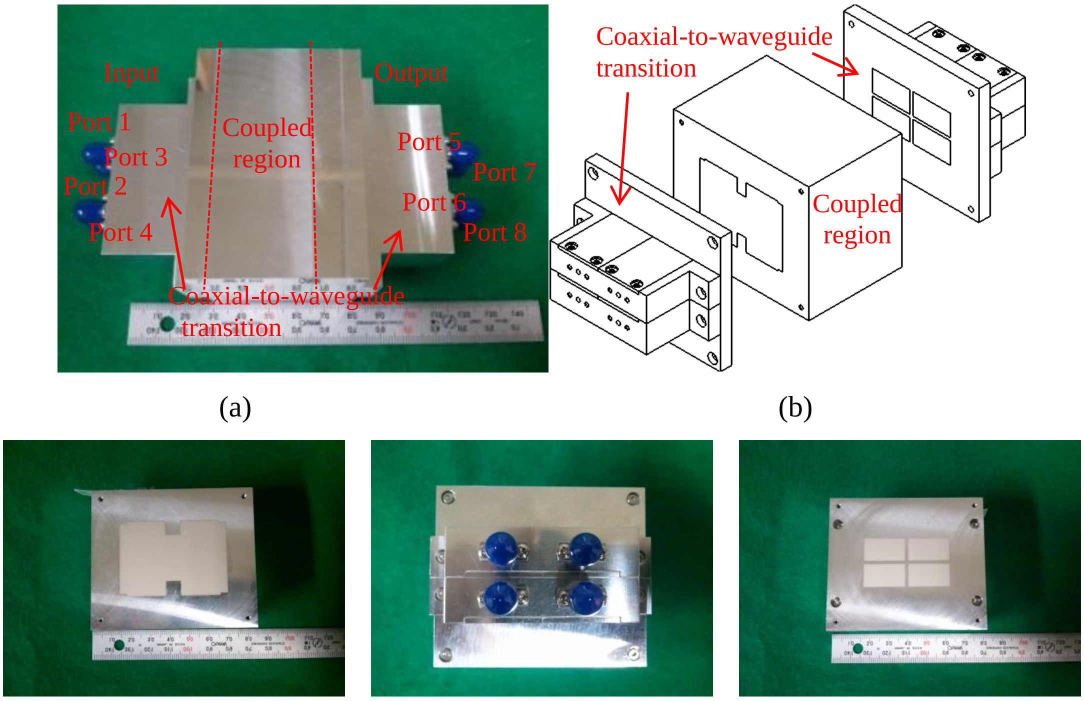

(a) (b)

(c) (d) (e)

Fig. 3.14 Fabricated short-slot 2-plane coupler (a) Assembled scene (b) Drawing (c) Frond view of the coupled region part (d) Ports of the coaxial-to-waveguide transition part (e) Waveguides of the coaxial-to-waveguide transition part. Unit: mm.

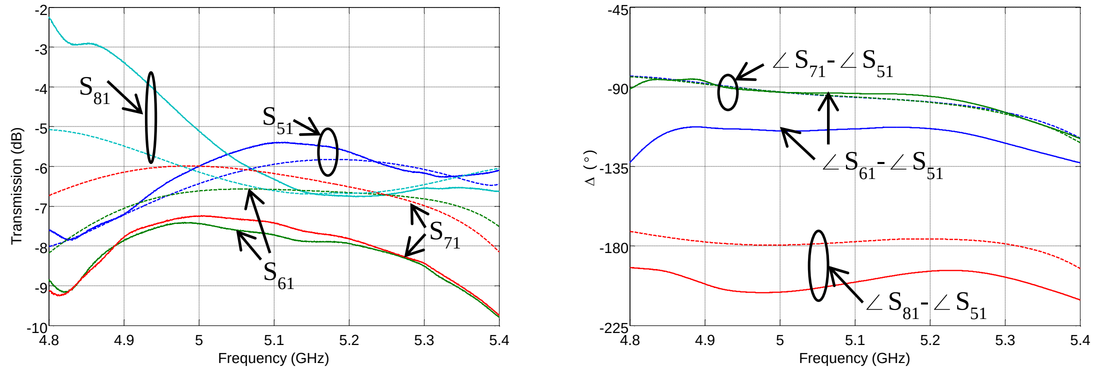

(a) (b)

Fig. 3.15 Characteristics of short-slot 2-plane hybrid coupler (a) Transmission (b) Output phase difference. Solid lines: measurement, Dashed lines: simulation.

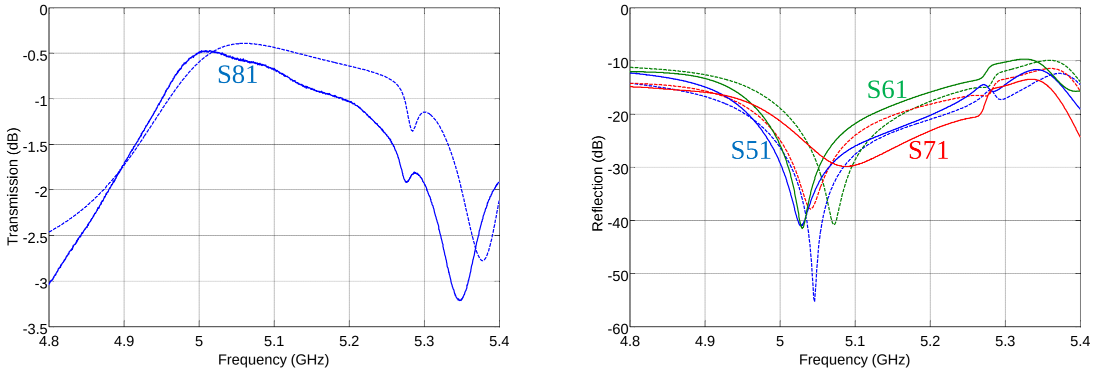

(a) (b)

Fig. 3.16 Characteristics of short-slot 2-plane cross coupler (a) Transmission (b) Reflection with isolations. Solid lines: measurement, Dashed lines: simulation.

Table 3.1 Design parameters of wideband short-slot 2-plane couplers. Unit: mm.

Type	a	b	a'	b'	w_r	h_r	w_t	h_t	l	t
Hybrid	7.66	4.27	19.1	13.43	2.66	2.59	1.33	0.39	12.09	0.6
Cross	8.1	4.57	17.77	13	1.915	2.72	0.9575	0.29	20.03	0.61

Table 3.2 Performances of wideband short-slot 2-plane couplers.

Type	Hybrid	Cross

FBW (%)	5.5% (21.39~22.59 GHz)	
Transmission (dB)	-6.0±0.5	>-0.5
1)Reflection (dB)	<-16.0	<-14.6
Phase difference (Δ°)	2)-96.0±5.0, 3)-178.6±2.2	-

1)Include the isolation, 2)∠S61-∠S51 and ∠S71-∠S51, 3)∠S81-∠S51

Table 3.3 Design parameters of wideband lossy dielectric short-slot 2-plane couplers. Unit: mm.

Type	a	b	a'	b'	w_r	h_r	w_t	h_t	l	t
Hybrid	18.4	10.26	45.88	32.26	6.39	6.22	3.195	0.94	29.04	1.44
Cross	19.46	10.98	42.68	31.23	4.6	6.53	2.3	0.7	48.11	1.47

Table 3.4 Performances of wideband lossy dielectric short-slot 2-plane couplers.

Type	Hybrid	Cross
FBW (%)	6.1% (4.96~5.27 GHz)	
Transmission (dB)	-6.3±0.5	>-1.0
1)Reflection (dB)	<-15.8	<-14.8
Phase difference (Δ°)	2)-96.6±5.9, 3)-177.9±1.8	-

1)Include the isolation, 2)∠S61-∠S51 and ∠S71-∠S51, 3)∠S81-∠S51

Table 3.5 Design parameters of launchers. Unit: mm.

Type	h_1	h_2	h_3	w_1	w_2	w_3	d_p	h_p	d_d	t
Hybrid	7.2	2.6	0.85	4.5	9.3	3.65	0.64	1.65	2.1	1
Cross	7.4	2.5		4.7				1.9		

Table 3.6 Performances of dielectric-filled waveguide short-slot 2-plane coupler.

Type	Hybrid	Cross
FBW (%)	6.1% (4.96~5.27 GHz)	
Volume (mm^3)	70×60×29.04 (1)106.34)	70×60×48.11 (1)116.43)

Weight (kg)	0.27 (1)0.66)	0.46 (1)0.77)
Transmission (dB)	-6.4±1.8	>-1.5
2)Reflection (dB)	-	<-13.7
Phase difference (Δ°)	3)-105.2±13.3, 4)-200.0±6.2	-

1)Include the transitions, 2)Include the isolation, 3)∠S61-∠S51 and ∠S71-∠S51, 4)∠S81-∠S51

Table 3.7 Comparison with characteristics of short-slot coupler.

Type	Media	$a \times b$	l	T (dB)	Γ (dB)	Δ (°)	FWB (%)@f_0	Ref.
Hybrid	Air	1.66 λ_0^2	1.52 λ_0	-3±0.2	<-30	±0.3	5@14 GHz	[3.3]
Hybrid	PTFE (ε_r=2.17)	1.46×0.40 λ_r^2	1.01 λ_r	-3.2±0.2	<-14	-	7.8@25.6 GHz	[3.4]
Cross			1.60 λ_r	>-0.7	<-13.5			
Hybrid	Air	0.72×0.58 λ_0^2	0.88 λ_0	-3.1±0.2	<-30	-	26@12 GHz	1)[3.5]
Hybrid	Air	1.38×0.82 λ_0^2	0.85 λ_0	-6.1±0.5	<-18.5	±3.7	2.3@22 GHz	2)Ch.2
Cross			1.59 λ_0	>-0.7	<-12.8	-		
Hybrid	PPS (ε_r=3.2)	1.40×0.98 λ_r^2	0.89 λ_r	-6.4±1.8	-	±13.3	@5.12 GHz	2)Ch.3
Cross		1.31×0.95 λ_r^2	1.47 λ_r	>-1.5	<-13.7	-		

1)Not included the length of transformer sections, 2)2-plane

Reference

[3.1] L.W. Hendrick, R. Levy; “Design of Waveguide Narrow-Wall Short-Slot Couplers,” *IEEE Trans. Microw. Theory Techn,*. vol. 48, no. 10, pp. 1771-1774, Oct. 2000.

[3.2] M. Sadiku, “Waveguides,” in *Elements of Electromagnetics*, 3rd ed., New York, Oxford University Press Inc., 2001, pp. 565-569.

[3.3] L. T. Hildebrand, “Results for a simple compact narrow-wall directional coupler,” *IEEE Microwave Guided Wave Lett.*, vol. 10, pp. 231–232, June 2000.

[3.4] S. Yamamoto, J. Hirokawa, and M. Ando, "A Half-Sized Post-Wall Short-Slot Directional Coupler with Hollow Rectangular Holes in a Dielectric Substrate," *IEICE Trans. Electron.*, vol. E88-C, no .7, pp. 1387-1394, Jul. 2005.

[3.5] R. Beyer and U. Rosenberg, "Compact top-wall hybrid/coupler design for extreme broad bandwidth application," *IEEE MTT-S Intl. Symp. Dig.*, pp. 1227-1280, June 2005.

Chapter 4

One-body 2-D beam-switching Butler matrix

Butler matrix is one of beam-switching circuits which have spatial orthogonality corresponded input ports. In the communication and the radar system, it provides high channel capacity and simultaneous wide scanning area with high resolution, because its channels (or beams) can share the antenna aperture, simultaneously. Despite that advantage, it has a longer profile than other beam-switching circuits. To reduce the length of Butler matrix, several minimized short-slot 1-plane couplers were inserted into the Butler matrix. In this chapter, the units are rearranged by those commutativity, and overlapped by the short-slot 2-plane couplers. At that time, the product is called the one-body 2-D beam-switching Butler matrix. Following sections, the operation principal, the design procedures, and the simulation and the measurement results of the one-body 2-D beam-switching Butler matrix are presented.

4.1 Theory

4.1.1 1-D beam-switching Butler matrix

The Butler matrix is a multi-port symmetric network for beam-switching [4.1]. The conventional Butler matrix consists of 2×2-way hybrid couplers, 2×2-way cross couplers, and phase shifters as shown in Fig. 4.1. The structure of the Butler matrix is same as Cooley-Tukey algorithm [4.2]. The outputs of 4×4-way beam-switching Butler matrix have same amplitude, but different phase delays expressed as the products of the transmission matrices of the units composited of the same components such as hybrid couplers, cross couplers, and phase shifters.

$$T_H = \frac{1}{\sqrt{2}}\begin{bmatrix} 1 & e^{-j\frac{\pi}{2}} & \multicolumn{2}{c}{0} \\ e^{-j\frac{\pi}{2}} & 1 & & \\ \multicolumn{2}{c}{0} & 1 & e^{-j\frac{\pi}{2}} \\ & & e^{-j\frac{\pi}{2}} & 1 \end{bmatrix} \tag{4.1}$$

$$T_C = \begin{bmatrix} 1 & 0 & 0 & 0 \\ 0 & 0 & 1 & 0 \\ 0 & 1 & 0 & 0 \\ 0 & 0 & 0 & 1 \end{bmatrix} \tag{4.2}$$

$$T_P = \begin{bmatrix} \begin{matrix} e^{-j\frac{\pi}{4}} & 0 \\ 0 & 1 \end{matrix} & 0 \\ 0 & \begin{matrix} 1 & 0 \\ 0 & e^{-j\frac{\pi}{4}} \end{matrix} \end{bmatrix} \tag{4.3}$$

$$\begin{bmatrix} b_1 \\ b_2 \\ b_3 \\ b_4 \end{bmatrix} = T_C T_H T_P T_C T_H \begin{bmatrix} a_1 \\ a_2 \\ a_3 \\ a_4 \end{bmatrix} = \frac{1}{2} \begin{bmatrix} e^{-j\frac{\pi}{4}} & e^{-j\frac{3\pi}{4}} & e^{-j\frac{\pi}{2}} & e^{-j\pi} \\ e^{-j\frac{\pi}{2}} & 1 & e^{j\frac{3\pi}{4}} & e^{-j\frac{3\pi}{4}} \\ e^{-j\frac{3\pi}{4}} & e^{j\frac{3\pi}{4}} & 1 & e^{-j\frac{\pi}{2}} \\ e^{-j\pi} & e^{-j\frac{\pi}{2}} & e^{-j\frac{3\pi}{4}} & e^{-j\frac{\pi}{4}} \end{bmatrix} \begin{bmatrix} a_1 \\ a_2 \\ a_3 \\ a_4 \end{bmatrix} = \begin{bmatrix} v_1 & v_2 & v_3 & v_4 \end{bmatrix} \begin{bmatrix} a_1 \\ a_2 \\ a_3 \\ a_4 \end{bmatrix} \tag{4.4}$$

$$v_i \bar{v}_j = \delta_{ij} \tag{4.5}$$

Where S_{type} is a transmission matrix of *type* (H: hybrid coupler, C: cross coupler, P: phase shifter) unit, a_i is ith input port, b_i is ith output port, v is a column vector of the transmission matrix of a Butler matrix, $\bar{v}$ is a complex conjugate of v, δ_{ij} is Kronecker delta.

Eq. (4.5) means that the outputs corresponded the input ports are numerically orthogonal, and those generated beams are spatially orthogonal. The number of the beams by the phase tapers at the output ports correspond to the number of the input ports given as 2^n where n is an integer. The beam-directions are decided the amount of phase increment or decrement between the output ports and the interval between the antenna elements. If the antenna elements fed by a Butler matrix are same antennas and separated with same interval, the radiation pattern of the 1-D antenna array fed by a Butler matrix is expressed as [4.3]

$$D_{array}(\theta, \phi) = AF(\theta) \times D_{ant}(\theta, \phi) \tag{4.6}$$

$$AF(\theta) = \frac{1}{M} \frac{\sin\frac{M}{2}\psi}{\sin\frac{\psi}{2}} \tag{4.7}$$

$$\psi = kd\sin\theta + \beta \tag{4.8}$$

where θ and ϕ are the azimuth and the elevation angles, D_{array} is the directivity of antenna array, AF is the array factor, D_{ant} is the directivity of an antenna element, M is the number of antenna element, k is the wavenumber, d is the physical interval length, β is the progressive phase shift.

In the specified frequency, the radiation pattern of antenna array is depended on the progressive phase shift. The numbers of the units and the elements of the hybrid and cross couplers and the phase shifters are listed in Table 4.1.

4.1.2 Conventional 2-D beam-switching Butler matrix

A 2-D beam-switching by a cascade of 1-D beam-switching Butler matrices horizontally and vertically stacked was proposed to generate 2-D multiple beams as shown in Fig. 4.2 [4.4], with each array of the 1-D beam-switching Butler matrix having functionality to steer the beam direction orthogonally to the stacked direction. In this structure, twisted waveguides or different (E- and H-)

plane based Butler matrices in waveguide and wirings in the planar structures were required for the connections. The outputs of $4^2 \times 4^2$-way 2-D beam-switching Butler matrix are expressed as the products of the transmission matrices of the 2-D units.

$$T_{H,h} = \frac{1}{\sqrt{2}} \begin{bmatrix} \begin{matrix} I_4 & -jI_4 \\ -jI_4 & I_4 \end{matrix} & 0_8 \\ 0_8 & \begin{matrix} I_4 & -jI_4 \\ -jI_4 & I_4 \end{matrix} \end{bmatrix} \tag{4.9}$$

$$T_{H,v} = \frac{1}{\sqrt{2}} \begin{bmatrix} \begin{matrix} A & 0_4 \\ 0_4 & A \end{matrix} & 0_8 \\ 0_8 & \begin{matrix} A & 0_4 \\ 0_4 & A \end{matrix} \end{bmatrix} \tag{4.10}$$

$$T_{C,h} = \begin{bmatrix} I_4 & 0_4 & 0_4 & 0_4 \\ 0_4 & 0_4 & I_4 & 0_4 \\ 0_4 & I_4 & 0_4 & 0_4 \\ 0_4 & 0_4 & 0_4 & I_4 \end{bmatrix} \tag{4.11}$$

$$T_{C,v} = \begin{bmatrix} \begin{matrix} B & 0_4 \\ 0_4 & B \end{matrix} & 0_8 \\ 0_8 & \begin{matrix} B & 0_4 \\ 0_4 & B \end{matrix} \end{bmatrix} \tag{4.12}$$

$$T_{P,h} = \begin{bmatrix} \begin{matrix} C & 0_4 \\ 0_4 & C \end{matrix} & 0_8 \\ 0_8 & \begin{matrix} C & 0_4 \\ 0_4 & C \end{matrix} \end{bmatrix} \tag{4.13}$$

$$T_{P,v} = \begin{bmatrix} \begin{matrix} D & 0_4 \\ 0_4 & I_4 \end{matrix} & 0_8 \\ 0_8 & \begin{matrix} I_4 & 0_4 \\ 0_4 & D \end{matrix} \end{bmatrix} \tag{4.14}$$

$$A = \begin{bmatrix} \begin{matrix} 1 & e^{-j\frac{\pi}{2}} \\ e^{-j\frac{\pi}{2}} & 1 \end{matrix} & 0_2 \\ 0_2 & \begin{matrix} 1 & e^{-j\frac{\pi}{2}} \\ e^{-j\frac{\pi}{2}} & 1 \end{matrix} \end{bmatrix} \tag{4.15}$$

$$B = \begin{bmatrix} 1 & 0 & 0 & 0 \\ 0 & 0 & 1 & 0 \\ 0 & 1 & 0 & 0 \\ 0 & 0 & 0 & 1 \end{bmatrix} \tag{4.16}$$

$$C = \begin{bmatrix} \begin{matrix} e^{-j\frac{\pi}{4}} & 0 \\ 0 & 1 \end{matrix} & 0_2 \\ 0_2 & \begin{matrix} 1 & 0 \\ 0 & e^{-j\frac{\pi}{4}} \end{matrix} \end{bmatrix} \tag{4.17}$$

$$D = e^{-j\frac{\pi}{4}} I_4 \tag{4.18}$$

$$\begin{bmatrix} b_1 \\ \vdots \\ b_{16} \end{bmatrix} = T_{2-D} \begin{bmatrix} a_1 \\ \vdots \\ a_{16} \end{bmatrix} = T_{1-D,v} T_{1-D,h} \begin{bmatrix} a_1 \\ \vdots \\ a_{16} \end{bmatrix} = \left(T_{C,v} T_{H,v} T_{P,v} T_{C,v} T_{H,v}\right)\left(T_{C,h} T_{H,h} T_{P,h} T_{C,h} T_{H,h}\right) \begin{bmatrix} a_1 \\ \vdots \\ a_{16} \end{bmatrix} =$$

$$\frac{1}{4}\begin{bmatrix} e_1 & e_3 & e_2 & e_4 \\ e_2 & e_5 & e_6 & e_3 \\ e_3 & e_6 & e_5 & e_2 \\ e_4 & e_2 & e_3 & e_1 \end{bmatrix}\begin{bmatrix} a_1 \\ \vdots \\ a_{16} \end{bmatrix} = [v_1 \quad \cdots \quad v_{16}]\begin{bmatrix} a_1 \\ \vdots \\ a_{16} \end{bmatrix} \tag{4.19}$$

$$e_1 = \begin{bmatrix} 1 & e^{-j\frac{\pi}{2}} & e^{-j\frac{3\pi}{4}} & e^{j\frac{3\pi}{4}} \\ e^{-j\frac{3\pi}{4}} & e^{-j\frac{\pi}{4}} & e^{-j\pi} & e^{-j\frac{\pi}{2}} \\ e^{-j\frac{\pi}{2}} & e^{-j\pi} & e^{-j\frac{\pi}{4}} & e^{-j\frac{3\pi}{4}} \\ e^{j\frac{3\pi}{4}} & e^{-j\frac{3\pi}{4}} & e^{-j\frac{\pi}{2}} & 1 \end{bmatrix} \tag{4.20}$$

$$e_2 = \begin{bmatrix} e^{-j\frac{3\pi}{4}} & e^{j\frac{3\pi}{4}} & e^{j\frac{\pi}{2}} & 1 \\ e^{j\frac{\pi}{2}} & e^{-j\pi} & e^{j\frac{\pi}{4}} & e^{j\frac{3\pi}{4}} \\ e^{j\frac{3\pi}{4}} & e^{j\frac{\pi}{4}} & e^{-j\pi} & e^{j\frac{\pi}{2}} \\ 1 & e^{j\frac{\pi}{2}} & e^{j\frac{3\pi}{4}} & e^{-j\frac{3\pi}{4}} \end{bmatrix} \tag{4.21}$$

$$e_3 = \begin{bmatrix} e^{-j\frac{\pi}{2}} & e^{-j\pi} & e^{j\frac{3\pi}{4}} & e^{j\frac{\pi}{4}} \\ e^{j\frac{3\pi}{4}} & e^{-j\frac{3\pi}{4}} & e^{j\frac{\pi}{2}} & e^{-j\pi} \\ e^{-j\pi} & e^{j\frac{\pi}{2}} & e^{-j\frac{3\pi}{4}} & e^{j\frac{3\pi}{4}} \\ e^{j\frac{\pi}{4}} & e^{j\frac{3\pi}{4}} & e^{-j\pi} & e^{-j\frac{\pi}{2}} \end{bmatrix} \tag{4.22}$$

$$e_4 = \begin{bmatrix} e^{j\frac{3\pi}{4}} & e^{j\frac{\pi}{4}} & 0 & e^{-j\frac{\pi}{2}} \\ 1 & e^{j\frac{\pi}{2}} & e^{-j\frac{\pi}{4}} & e^{j\frac{\pi}{4}} \\ e^{j\frac{\pi}{4}} & e^{-j\frac{\pi}{4}} & e^{j\frac{\pi}{2}} & 1 \\ e^{-j\frac{\pi}{2}} & 1 & e^{j\frac{\pi}{4}} & e^{j\frac{3\pi}{4}} \end{bmatrix} \tag{4.23}$$

$$e_5 = \begin{bmatrix} e^{-j\frac{\pi}{4}} & e^{-j\frac{3\pi}{4}} & e^{-j\pi} & e^{j\frac{\pi}{2}} \\ e^{-j\pi} & e^{-j\frac{\pi}{2}} & e^{j\frac{3\pi}{4}} & e^{-j\frac{3\pi}{4}} \\ e^{-j\frac{3\pi}{4}} & e^{j\frac{3\pi}{4}} & e^{-j\frac{\pi}{2}} & e^{-j\pi} \\ e^{j\frac{\pi}{2}} & e^{-j\pi} & e^{-j\frac{3\pi}{4}} & e^{-j\frac{\pi}{4}} \end{bmatrix} \tag{4.24}$$

$$e_6 = \begin{bmatrix} e^{-j\pi} & e^{j\frac{\pi}{2}} & e^{j\frac{\pi}{4}} & e^{-j\frac{\pi}{4}} \\ e^{j\frac{\pi}{4}} & e^{j\frac{3\pi}{4}} & 1 & e^{j\frac{\pi}{2}} \\ e^{j\frac{\pi}{2}} & 1 & e^{j\frac{3\pi}{4}} & e^{j\frac{\pi}{4}} \\ e^{-j\frac{\pi}{4}} & e^{j\frac{\pi}{4}} & e^{j\frac{\pi}{2}} & e^{-j\pi} \end{bmatrix} \tag{4.25}$$

$$\nu_i\bar{\nu}_j = \delta_{ij} \tag{4.26}$$

where $T_{type,stacked}$ is a transmission matrix of *h*orizontally and *v*ertically *stacked type* (*H*: hybrid coupler, *C*: cross coupler, *P*: phase shifter, *1-D*: 1-D beam-switching Butler matrix, *2-D*: 1-D beam-switching Butler matrix) unit, a_i is i^{th} input port, b_i is i^{th} output port, v is a column vector of the transmission matrix of a Butler matrix, $\bar{v}$ is a complex conjugate of v, δ_{ij} is Kronecker delta.

The radiation pattern of the 2-D antenna array fed by a Butler matrix is expressed as [4.5]

$$D_{array}(\theta, \phi) = AF(\theta, \phi) \times D_{ant}(\theta, \phi) \tag{4.27}$$

$$AF(\theta, \phi) = \frac{1}{M}\frac{sin\left(\frac{M}{2}\psi_x\right)}{sin\left(\frac{\psi_x}{2}\right)}\frac{1}{N}\frac{sin\left(\frac{N}{2}\psi_y\right)}{sin\left(\frac{\psi_y}{2}\right)} \tag{4.28}$$

$$\psi_x = kd_x \sin\theta \cos\phi + \beta_x \tag{4.29}$$

$$\psi_y = kd_y \sin\theta \sin\phi + \beta_y \tag{4.30}$$

where θ and ϕ are the azimuth and the elevation angle, D_{array} is the directivity of antenna array, AF is the array factor, D_{ant} is the directivity of an antenna element, M and N are the numbers of antenna elements arranged x and y directions, k is the wavenumber, d_i is the physical interval length between antenna elements arranged i direction, β_i is the progressive phase shift of i direction.

The numbers of the units and the elements of the hybrid and cross couplers and the phase shifters are listed in Table 4.2. Comparing with 1-D beam-switching Butler matrix, the numbers of the cross coupler and the phase shifter units are reduced. Especially, when n_1=n_2 case, the number of the cross coupler units is reduced from $\Theta(3\times2^{n-1})$ to $\Theta(3\times2^{n/2})$.

4.1.3 One-body 2-D beam-switching Butler matrix

The volume of the Butler matrix depends on the size of a unit and the number of units. Many methodologies have been proposed to reduce the size of the Butler matrix concentrating only on reduction in the size of the components such as the hybrid and cross couplers, and the phase shifter in rectangular waveguides [4.6], microstrip lines [4.7]-[4.10], striplines [4.11]-[4.12], and substrate integrated waveguides (SIW) [4.13] maintaining the schematic outline of the Butler matrix. Author proposed the one-body 2-D beam-switching Butler matrix using the commutativity and the overlapping of units. It is first approach to reduce the volume of the Butler matrix using the reduction of the number of units. As previously mentioned in Section 2.1.1, a product between the orthogonally-stacked units is a symmetric matrix, because the output values of one-dimensional unit are inserted into the inputs of other-dimensional unit independently. The transmission matrices of the orthogonally-stacked units are commutative, because the product of symmetric matrices is symmetric. It means that orthogonally-stacked units can be switched those assembly orders. On the other hand, a product between the parallel-stacked units is an asymmetric matrix. The parallel-stacked units are not able to switch each position. In Eqs. (4.31)-(4.33), the products of the transmission matrices of the stacked coupler units verify the relationship between the commutativity and the orthogonality.

$$T_{i,h}T_{j,v}=T_{j,v}T_{i,h} \tag{4.31}$$

$$T_{i,h}T_{j,h}\neq T_{j,h}T_{i,h} \tag{4.32}$$

$$T_{i,v}T_{j,v}\neq T_{j,v}T_{i,v} \tag{4.33}$$

where subscript i and j are types of units.

By the commutativity of the units, the transmission matrix of the conventional $4^2\times4^2$-way 2-D beam-switching Butler matrix can be rearranged

$$T_{2\text{-}D}=(T_{C,v}T_{C,h})(T_{H,v}T_{H,h})(T_{P,v}T_{P,h})(T_{C,v}T_{C,h})(T_{H,v}T_{H,h}) \tag{4.34}$$

Neighbored two orthogonally-stacked same type units are numerically overlapped as shown in Fig. 4.3. The overlapped two E-plane and two H-plane couplers are substituted a 2-plane coupler, but an un-overlapped E-plane or H-plane coupler is remained their own forms. There are only 2-plane hybrid couplers in the hybrid coupler unit of the one-body 2-D beam-switching Butler matrix, because E- and H-plane hybrid couplers are overlapped coincidentally. On the other hand, the cross coupler unit of the one-body 2-D beam-switching Butler matrix consists of E-, H-, and 2-plane cross couplers, because the E- and H-plane cross couplers are partly overlapped. It makes the output phase difference. Phase shifters are just added those delays. The transmission matrix of the one-body $4^2 \times 4^2$-way 2-D Butler matrix is

$$T_{2\text{-}D}=T_{C,2}T_{H,2}T_{P,2}T_{C,2}T_{H,2} \tag{4.35}$$

where subscript 2 indicates that the unit is overlapped two orthogonally-stacked same type units.

The structure of $4^2 \times 4^2$-way one-body 2-D beam-switching Butler matrix using the commutativity of orthogonally-stacked units and the overlapping two same types, but orthogonally-stacked units is shown in Fig. 4.4. The numbers of the units and the elements of the hybrid and cross couplers and the phase shifters are listed in Table 4.3. Comparing with conventional 2-D beam-switching Butler matrix, the numbers of the cross coupler and the phase shifter units are reduced. Especially, when $n_1=n_2$ case, the number of the cross coupler units is reduced to half.

4.2 Simulation results

Different to previous mentioned the beam-switching Butler matrices, the one-body 2-D beam-switching Butler matrix has the design considerations. First, it is required the phase compensation between the components in the cross coupler unit. The hybrid coupler unit has same outputs corresponded input port, because it consists of only 2-plane hybrid coupler. On the other hand, the cross coupler unit has different outputs corresponded input port, because it consists of E-, H-, and 2-plane cross couplers. The E-plane, the H-plane, and the 2-plane couplers have different cross-section sizes of the coupled region, and these results in the differences in terms of the output phases are expressed as

$$\angle S_{E,41} = -\left(\beta_{E,TE_{10}} + \beta_{E,TM_{11}}\right)\frac{l_E}{2} - \frac{\pi}{2} \tag{4.36}$$

$$\angle S_{H,41} = -\left(\beta_{H,TE_{10}} + \beta_{H,TE_{20}}\right)\frac{l_H}{2} - \frac{\pi}{2} \tag{4.37}$$

$$\angle S_{2,81} = -\beta_{2,TM_{11}} l_2 - \pi \tag{4.38}$$

$$l_E = \frac{\pi}{\beta_{E,TE_{10}} - \beta_{E,TM_{11}}} \tag{4.39}$$

$$l_H = \frac{\pi}{\beta_{H,TE_{10}} - \beta_{H,TE_{20}}} \tag{4.40}$$

$$l_2 = \frac{\pi}{\beta_{2,TE_{10}} - \beta_{2,TE_{20}}} \tag{4.41}$$

$$\frac{\beta_{E,TE_{10}} + \beta_{E,TM_{11}}}{2} < \frac{\beta_{H,TE_{10}} + \beta_{H,TE_{20}}}{2} < \beta_{2,TM_{11}} \tag{4.42}$$

$$\left|\angle S_{E,41}\right| < \left|\angle S_{H,41}\right| < \left|\angle S_{2,81}\right| \tag{4.43}$$

where $\angle S_{type,ij}$ is an *j*th output angle of *type*-plane cross coupler when the input port *i* excited.

Considering the propagation constants of the short-slot cross couplers in Chapter 2, the lengths of the coupled region l_e, l_h, and l_2 are almost same. In Eq. 4.43, however those short-slot cross couplers have different output phases. Compensating for this difference, an additional phase shifter unit is attached to the front or the back of the cross coupler unit, increasing the length of the Butler matrix here. The propagation paths in the cross coupler unit have a one-to-one correspondence relationship, and the compensated phase values of the propagation paths are also independent. This allows a phase compensator to be arranged by the pattern of a neighboring cross coupler unit to exchange position with a neighboring cross coupler unit. Except for the last cross coupler unit (near the output side), each cross coupler unit is neighboring a phase shifter unit. Additional phase shifter units and phase shifter unit are able to overlap, and to be the single phase shifter unit. In Fig. 4.4, the second cross coupler unit (near the output side) has a phase compensator to ensure coincidence of output phases. On the other hands, the first cross coupler unit (near the input side) can be merged with a phase shift unit and a phase compensator. This reduces the increase of the length of 2-D beam-switching Butler matrix. In the phase shifter design like Fig. 4.5, the specified phase shift value can be expressed by the variation of a width and a length of a hollow waveguide as

$$\Delta\phi = l_{step}\left(\sqrt{k^2 + \left(\frac{\pi}{a}\right)^2} - \sqrt{k^2 + \left(\frac{\pi}{a+\Delta \mathrm{a}}\right)^2}\right) \tag{4.36}$$

where l_{step} is the length of an inductive step, k is a wavenumber, a is a width of waveguide, and Δa is a variation of the width of an inductive step.

When Δa has a (±) sign, $\Delta\phi$ has a (±) value which indicates an additional increment or decrement of the compensators. Second is the connection (waveguide junction) between the units for reducing insertion loss. In an ideal Butler matrix, the output values have the same amplitude and sequenced phases. However in the actual design, it is difficult to achieve balance in the output values because of the imbalance of the output phases of the short-slot couplers. Each of the outputs travel through different paths formed by a combination of the hybrid and cross couplers, and the phase shifters. Here, the frequency characteristics of the hybrid and cross couplers, and the phase shifter are different in the transmission and the reflection coefficients, and as a result the output values are different from the ideal ones. The insertion loss is inversely proportional to the deviation of the output phases.

$$IL_j(\mathrm{dB}) = -10\log_{10}\sum_{i=N+1}^{2N}\left|S_{type,ij}\right|^2 \tag{4.37}$$

$$\sigma_j = \sqrt{\frac{1}{N}\sum_{i=N+1}^{2N}\left(x_{ij} - \mu_j\right)^2} \tag{4.38}$$

$$x_{ij} = \angle S_{S,ij} - \angle S_{I,ij} \tag{4.39}$$

$$\mu_j = \frac{1}{N}\sum_{i=N+1}^{2N} x_{ij} \tag{4.40}$$

where IL_j is an insertion loss of input port j, N is the number of output ports. $S_{type,ij}$ is a S-parameter of *type* (*S*imulation or *I*deal), σ_j is a deviation of phase difference between the simulation and the ideal. The deviation of the output phases is less effective to the deviation of the beam directions than the deviation of the output powers. For that reason, the junction design concentrates on an increase in the efficiency of the Butler matrix. Except the phase shifter unit, all the units have the input and the output junctions.

4.2.1 Hollow waveguide one-body $4^2\times4^2$-way 2-D beam-switching Butler matrix

The hollow waveguide one-body $4^2\times4^2$-way 2-D beam-switching Butler matrix with brass (C3560P, σ=1.31×10^7 S/m) wall is consisted of the short-slot 2-plane couplers mentioned in Chapter 2 and operated in 22 GHz. The design parameters of the phase compensators are listed in Table 4.4 and the relative phases of the cross couplers show differenct variations in the frequency domain in Fig. 4.6. These freqeuncy dependency of the cross coupler components affect the deviations of transmission output phases, restrict the frequency bandwidth of the one-body 2-D beam-switching Butler matrix. The junctions inserted to connect the units work as an impedance matching network by changing the length of the junctions for the second hybrid coupler unit as shown in Fig. 4.7 when the length of other junctions of hybrid and cross coupler units sets 4 mm. The lengths of the junctions attached to the second hybrid coupler unit are selected as $l_{H2,i}$ (the input side, 7.5 mm) and $l_{H2,o}$ (the output side, 4.4 mm) as shown in Fig. 4.4. When the input port 1 is excited, S-parameters of the main body (excluded transitions in Fig. 4.4) of the hollow waveguide one-body $4^2\times4^2$-way 2-D beam-switching Butler matrix are shown in Fig. 4.8 and 4.9, and listed in Table 4.5. The frequency bandwidth is selected under the insertion loss, because other parameters such as the deviation of S-parameter (the amplitude and the phase) difference between the simulation and the ideal [4.14] are less affected the radiation pattern and the gain. The expressions of the processed simulation results such as the insertion loss, the deviation of the phase difference between the simulation and the ideal shown in Fig. 4.10 are based on four input ports (cf. Quadrant I: port 1, 2, 5, and 6) which can be seen to represent all input ports, because the structure of the 2-D beam-switching Butler matrix is symmetrical, two dimensionally. Acquiring the radiation pattern and the gain pattern, the waveguide output ports are separated at regular intervals for generating the equiangular beams. However the interval of the waveguide output ports of the main body is not equidistance, because the deployment of the waveguide output ports of the main body are followed by the short-slot 2-plane hybrid coupler’s for minimizing the length of the main body. Considering the fabrication (the size of the receptacle, HPC1440-02) and the measurement (large beam-coverage), selected the regular interval is 9.9 mm (0.73 λ_0) to x- and y-axes. The radiation patterns are acquired the y-polarized E-field and its Ludwig’s third definition of cross polarization [4.15] considered the limitation of the rotators in the measurement in the quasi E- and H-planes as shown in Fig. 4.11. To compare with the measurement results, the simulation results of the radiation patterns are expressed by Ludwig’s third definition of cross polarization. A half of input ports can substitute others such as the quasi E-plane (Quadrant I and III) and the quasi H-plane (Quadrant I and II). Realized gain with types of conducting wall, beam-direction compared with the ideal, and HPBW (Half Power BeamWidth) are listed in Table 4.6 to 4.8, respectively. The gain pattern is depicted 3.9 dB-down contour and the peak corresponded the input port as shown in Fig. 4.12. The coverage which is an area of 3.9 dB-down contour acquired by L'Huilier's theorem (Appendix 4) [4.16] is listed in Table 4.9. Each 3.9 dB-down contour is spatially orthogonal to other and the summation of the coverages is 1.94 sr (30.9% of a hemisphere).

4.2.2 Transition for one-body 2-D beam-switching Butler matrix

When the design parameters of the launcher can be varied with the ratio, its frequency characteristics are just shifted. Unfortunately, the receptacle is applied same type to one-body 2-D beam-switching Butler matrices, the optimized design parameters on the specific one-body 2-D beam-switching Butler matrix cannot reuse to other one-body 2-D beam-switching Butler matrices with different the operating frequencies and the materials. The design parameters and the performances of the coaxial-to-waveguide transitions for Section 4.2.1 are listed in Table 4.10, and shown as Fig. 4.13, respectively.

4.3 Measurement results

Three hollow waveguide one-body $4^2\times4^2$-way 2-D beam-switching Butler matrices covered with the different conducting wall materials which are brass (C3560P), copper plated ABS-like, and aluminum alloy (A6061) are fabricated and evaluated. Those center frequencies are 22 GHz (brass, copper plated ABS-like) and 19.55 GHz (aluminum alloy). Each material is selected for the durability (brass), the loss (aluminum alloy), and the weight (ABS-like). Physical and electrical characteristics of the materials are listed in Table 4.11. Because of the difficulty of the fabrication of the coaxial-to-waveguide with the stepped stubs, these hollow waveguide one-body 2-D beam-switching Butler matrices consist of main-body divided into five blocks along the broad walls of the waveguides arrayed in the horizontal plane, the input and the output transitions, and the input and the output plates as shown in Fig. 4.14. Fabricated by milling, some of the corner edges in the structure are rounded to a 0.5 mm radius by a cutting drill, but it affects the performances scarcely. All the blocks are screwed together for a tight snug contact. Soldering connection between the inner conductor of coaxial cable and the stepped stub is difficult because of those sizes and structures. It makes to reduce the reproducibility of the measurement, and to increase the deviation of the performances between the input ports. These measurement uncertainties are calibrated by TRL (Thru-Reflect-Line) (Appendix A.5) with a short plate and a transmission line as shown in Fig. 4.15 [4.17]. The definition of the operating frequency band of the one-body 2-D beam-switching Butler matrices is set to under 0.97 dB of the insertion loss. The calibrated performances compared with the simulation and the measured (raw data) results are listed in Table 4.12 and 13, and shown as Fig. 4.16 to 18, respectively. In that time, the isolation is not measured because of the limitation of the space between ports. Comparing the calibrated results with the raw data, the amplitude performances are improved, but the phase performances not. The differences between the calibrated results and the simulation results are happened by the fabrication processing. Although the calibrated results corresponded most of input ports approach to the simulation results, the calibrated results corresponded few input ports deviate from the simulation results. It is caused by a problem of soldering connection between the inner conductor of coaxial cable and the stepped stub because of those sizes and structures. Because the copper plated ABS-like body made by 3-D printing, the roughness of the surface of the body is large compare to copper itself, the oxidation is partly happened on the copper plating which has 15 um thickness, and the electrical contact is poor. For those reasons, the hollow waveguide one-body 2-D beam-switching Butler matrix covered with copper plated ABS-like is not worked as the beam-switching circuit. The output ports of the one-body 2-D beam-switching Butler matrix are able to work as a 4^2 aperture array antenna, with apertures of 7.85×4.35 mm in 22GHz and 8.83×4.89 mm in 19.55 GHz, and the aperture spacing 9.9 mm (0.73 λ_0 in 22 GHz, 0.65 λ_0 in 19.55 GHz). The measurement of radiation patterns of the hollow waveguide one-body 2-D beam-switching Butler matrices is conducted in the anechoic chamber as shown in Fig. 4.19(b) and (c). In that time, the covered with brass is conducted for all input ports, but the covered with aluminum alloy is conducted for four input ports (1, 2, 5, 6), because its 2-D symmetricity is already checked by the results of the covered with brass. As same reason in Section 2.3.3.1, AUT positioner moves only in the horizontal direction, AUT looks at the specified elevation angle α corresponded to the input port. For the measurement of quasi E-plane in Fig. 4.19(a), the Butler matrix rotated from x-axis to y-axis by 90 degrees with coordinators is placed with the tilting angle of $\pm\alpha_1$ in the transformed (y-z) plane and the rotator is moved in the transformed (y-z) plane. For the measurement of quasi H-plane in Fig. 4.9(a), the Butler matrix is placed with the tilting angle of ±α_2 in the transformed (x-z) plane and the rotator is moved in the transformed (x-z) plane. The simulated and measured beam directions (β, α), realized gains, and HPBWs are listed in Table 4.14 to 16 and shown in Fig. 4.19(d)-(m). The measured gains from some input ports are lower than the simulated gain because of the lower transmission power and the larger phase deviation caused by the fabrication flaw of the coaxial-to-waveguide transitions. The beam-coverages listed in Table 4.17 are acquired by NFFFT (Near-Field to Far-Field Transformation, Appendix 6) [4.18], the electric field distribution of the hemisphere is derived from the near-field measured results (by Anritsu 37269D) as shown in Fig. 4.20. In that time, the covered with brass and the covered with aluminum alloy are conducted for all input ports. This ensures that the beam direction is in the measurement plane.

4.4 Summary

The one-body 2-D beam-switching Butler matrix is designed by the commutativity and the overlapping of units. It makes to reduce the length of the one-body 2-D beam-switching Butler matrix to half, minimally. In that time, the phase difference is happened in the cross coupler unit, because the different types of the short-slot cross coupler have different output phases. It can be compensated by additional phase shifter called the phase compensator, and then only the length of single phase shifter unit is increased. Frequency characteristics of the one-body 2-D beam-switching Butler matrix are followed the short-slot 2-plane coupler’s.

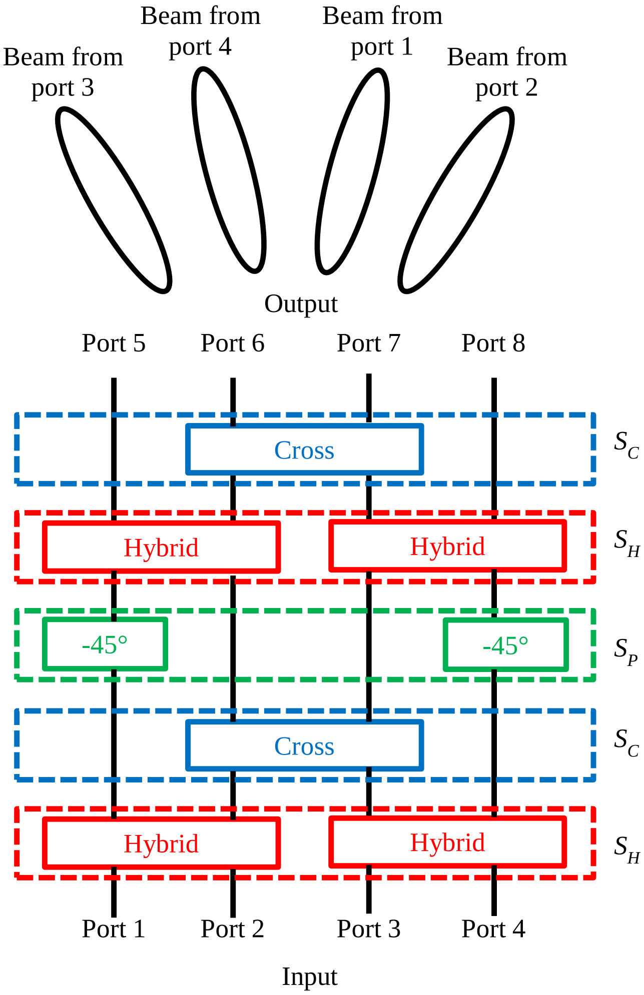

Fig. 4.1 4×4-way beam-switching Butler matrix

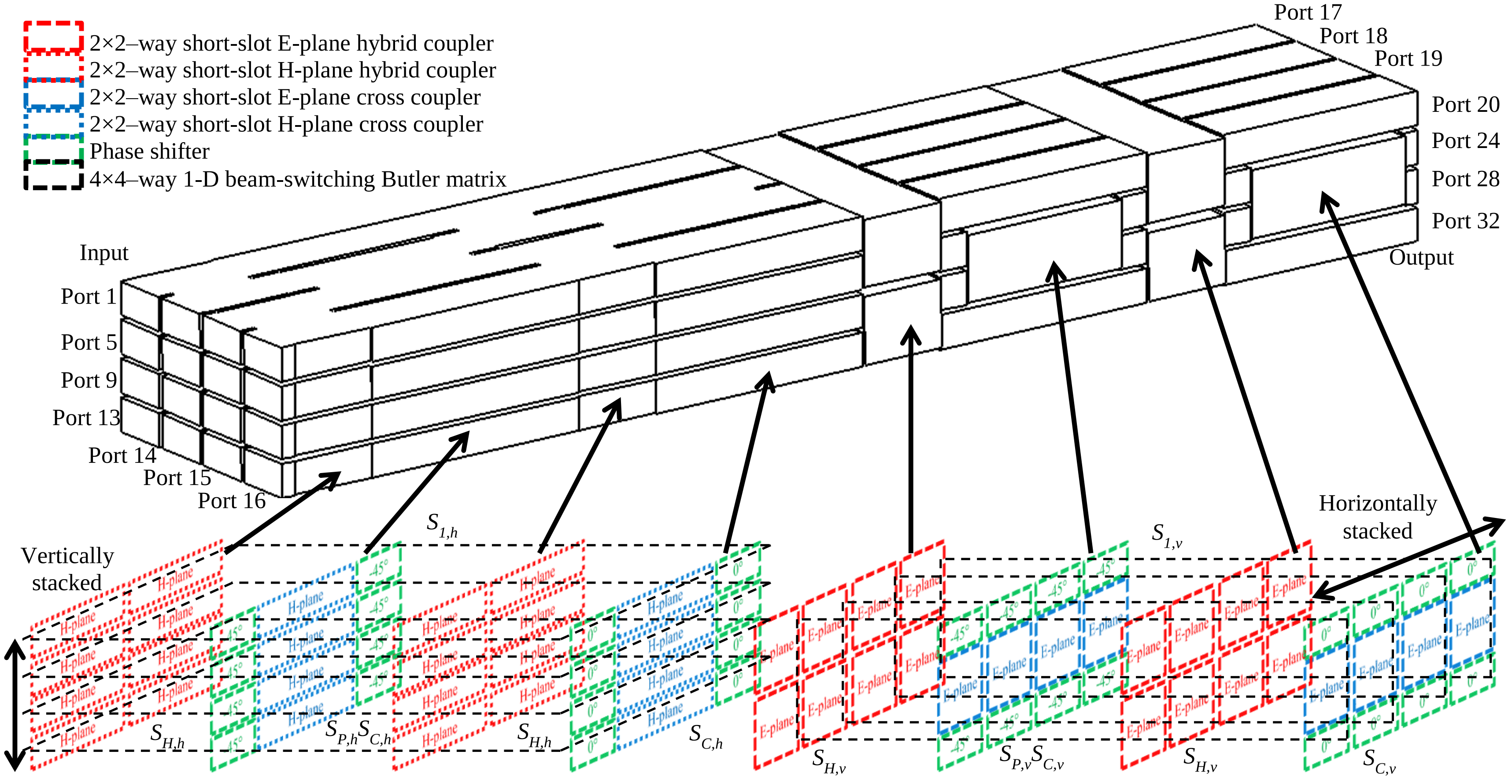

Fig. 4.2 Conventional 4^2×4^2-way 2-D beam-switching Butler matrix.

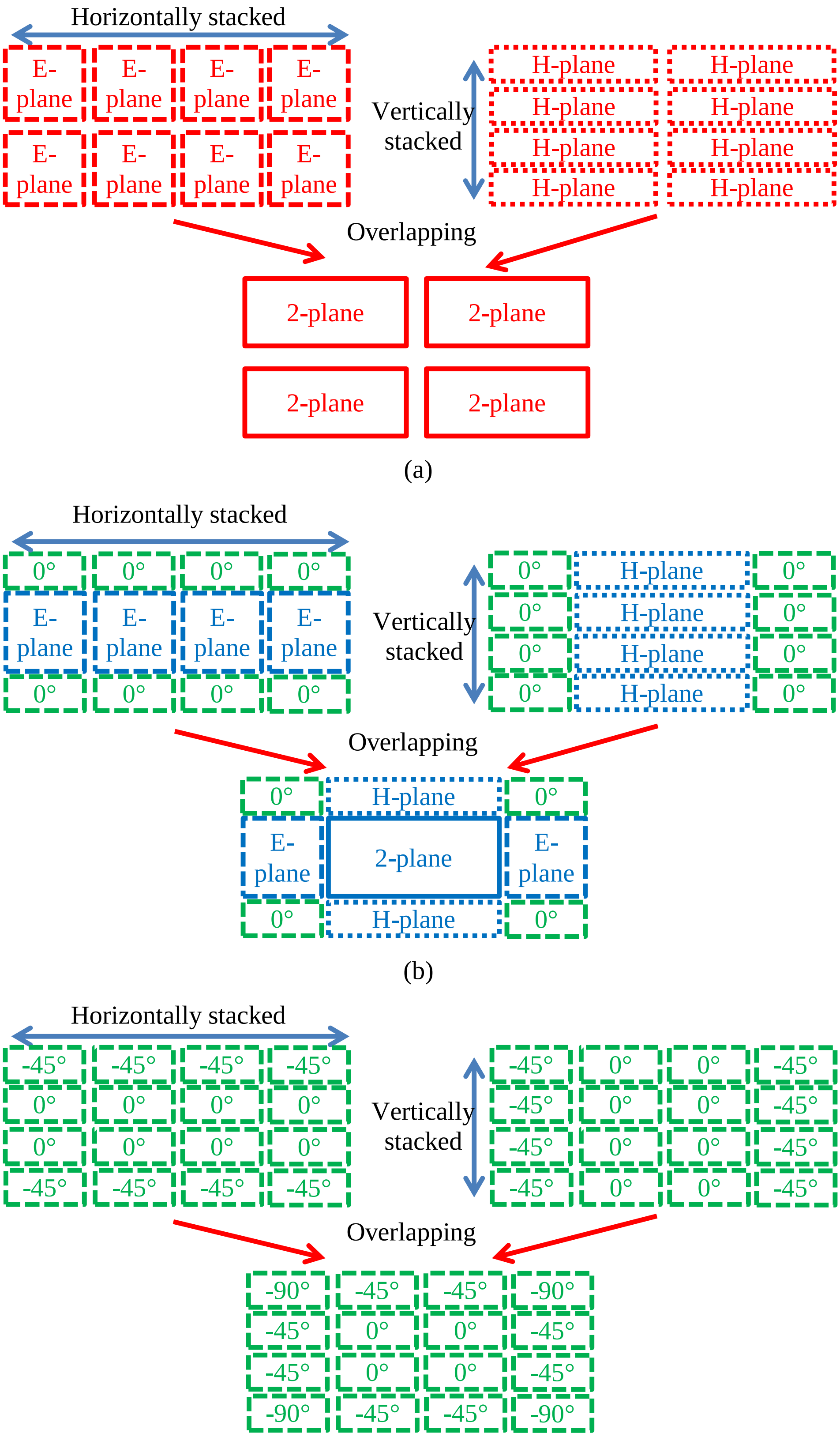

(a)

(b)

(c)

Fig. 4.3 Overlapping of units of $4^2 \times 4^2$-way 2-D beam-switching Butler matrix (a) Hybrid coupler (b) Cross coupler (c) Phase shifter.

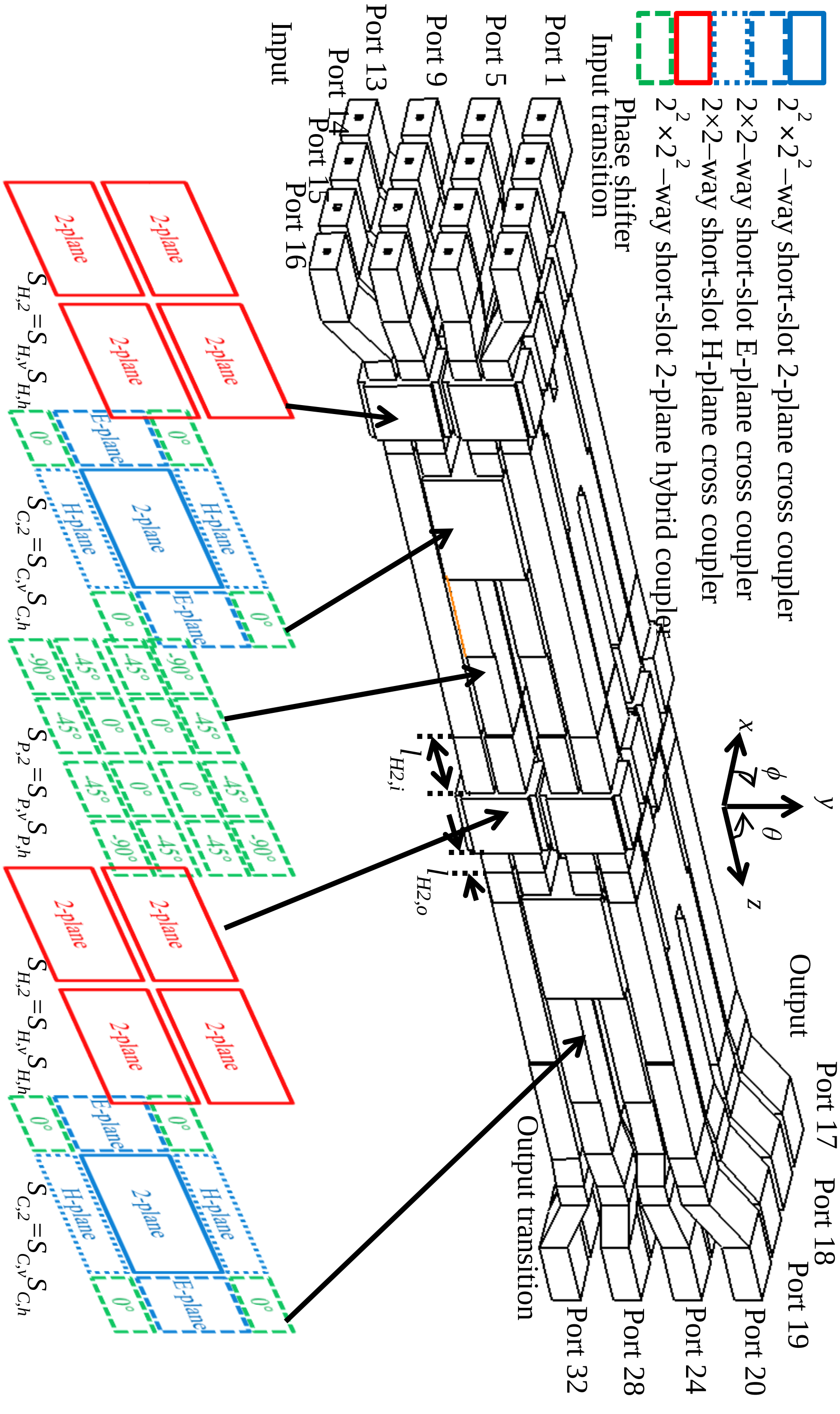

Fig. 4.4 One-body $4^2\times4^2$-way 2-D beam-switching Butler matrix.

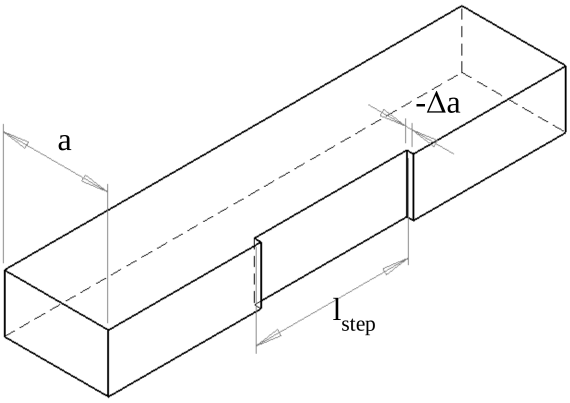

Fig. 4.5 Drawing of phase compensator.

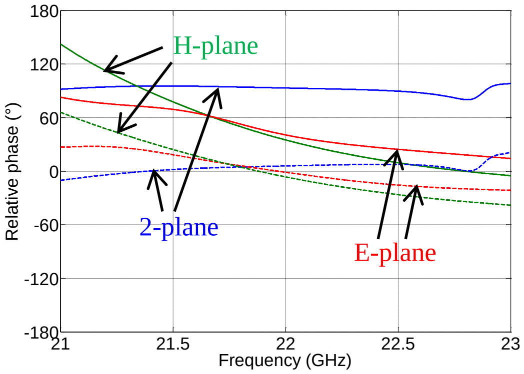

Fig. 4.6 Relative output phases of components of cross coupler unit compensated by output phase of 0° phase shifter. Without phase compensator - Solid lines. With phase compensator - Dashed lines.

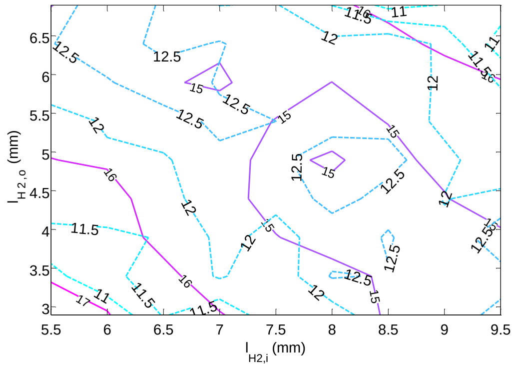

Fig. 4.7 Impedance matching by varying the lengths of input and output branches of the second hybrid coupler unit of one-body $4^2 \times 4^2$-way 2-D beam-switching Butler matrix. Un-transmitted power to output ports - Solid lines and units is %. Deviation between simulation and ideal output phases - Dashed lines and units is degrees.

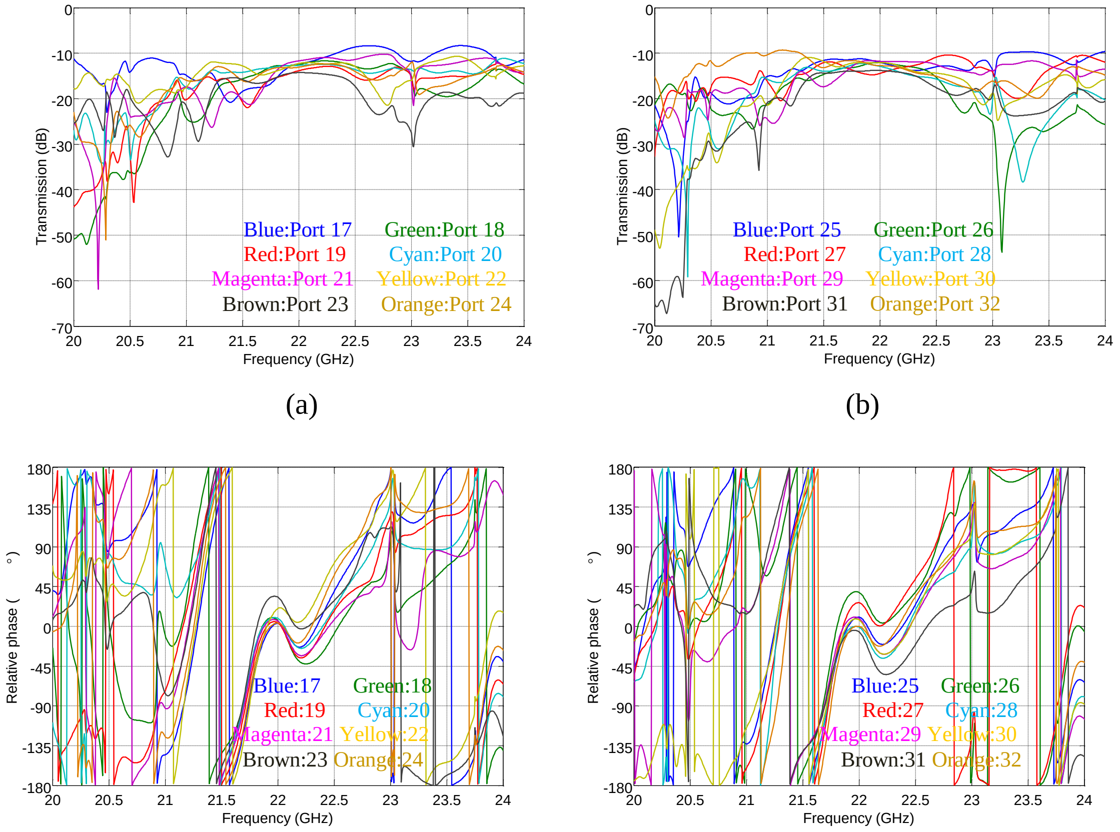

(a) (b)

(c) (d)

Fig. 4.8 S-parameters of one-body $4^2 \times 4^2$-way 2-D beam-switching Butler matrix when input port 1 is excited. Transmission coefficients (a) port 17-24 (b) port 25-32, Relative phases to ideals (c) port 17-24 (d) port 25-32.

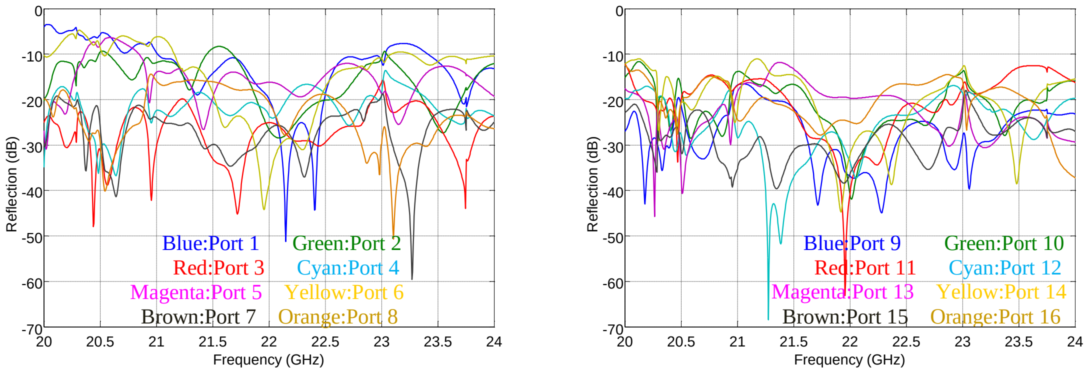

(a) (b)

Fig. 4.9 S-parameters of one-body $4^2 \times 4^2$-way 2-D beam-switching Butler matrix when input port 1 is excited. Reflection and isolations (a) port 17-24 (b) port 25-32

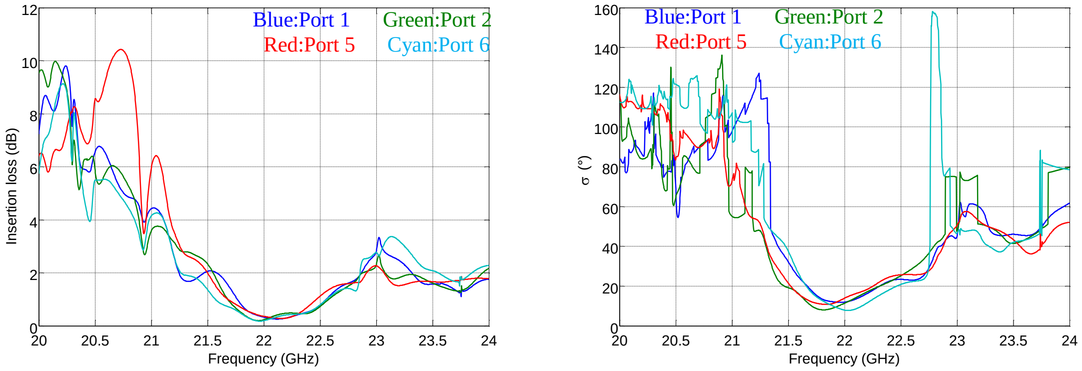

(a) (b)

Fig. 4.10 Processed parameters (a) Insertion loss (b) Deviation of the phase difference between the simulation and the ideal.

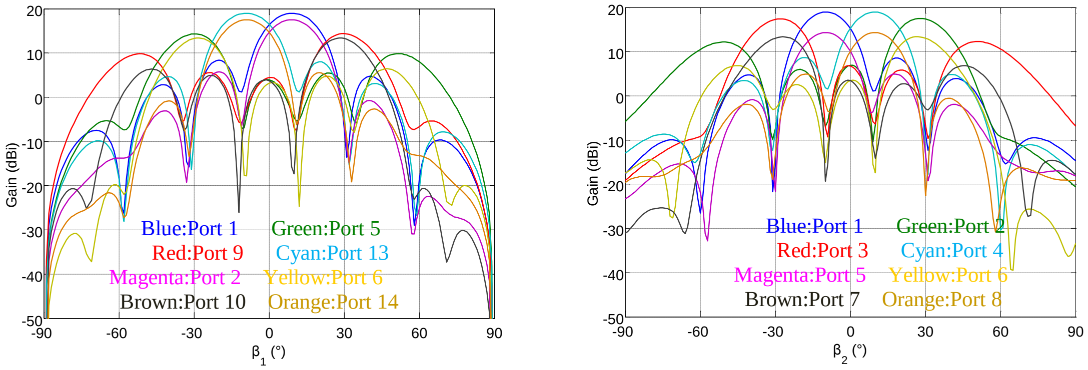

(a) (b)

Fig. 4.11 Radiation patterns (a) Quasi E-plane (b) Quasi H-plane.

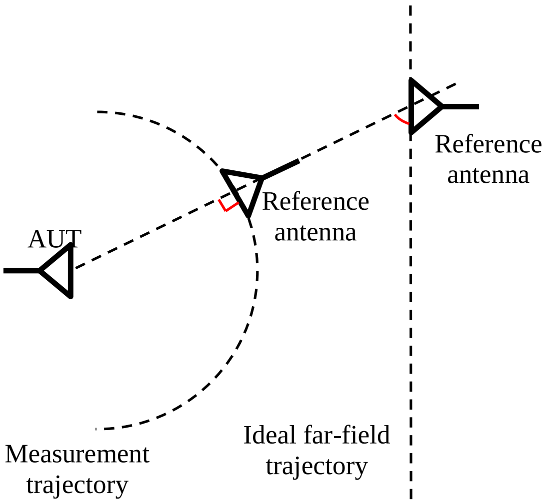

(a)

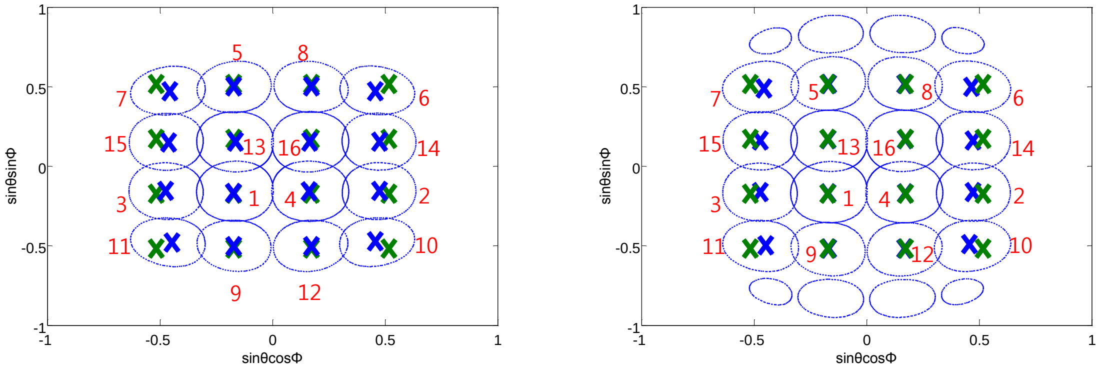

(a) (b)

Fig. 4.12 3.9 dB-down contour gain patterns. The numbers and the symbol Xes indicate the input port number and the position of peak gain (a) Drawing of simulation scenes (b) Ey (c) Ludwig's third definition of cross polarization. Blue - Simulations, Green - Ideals.

8

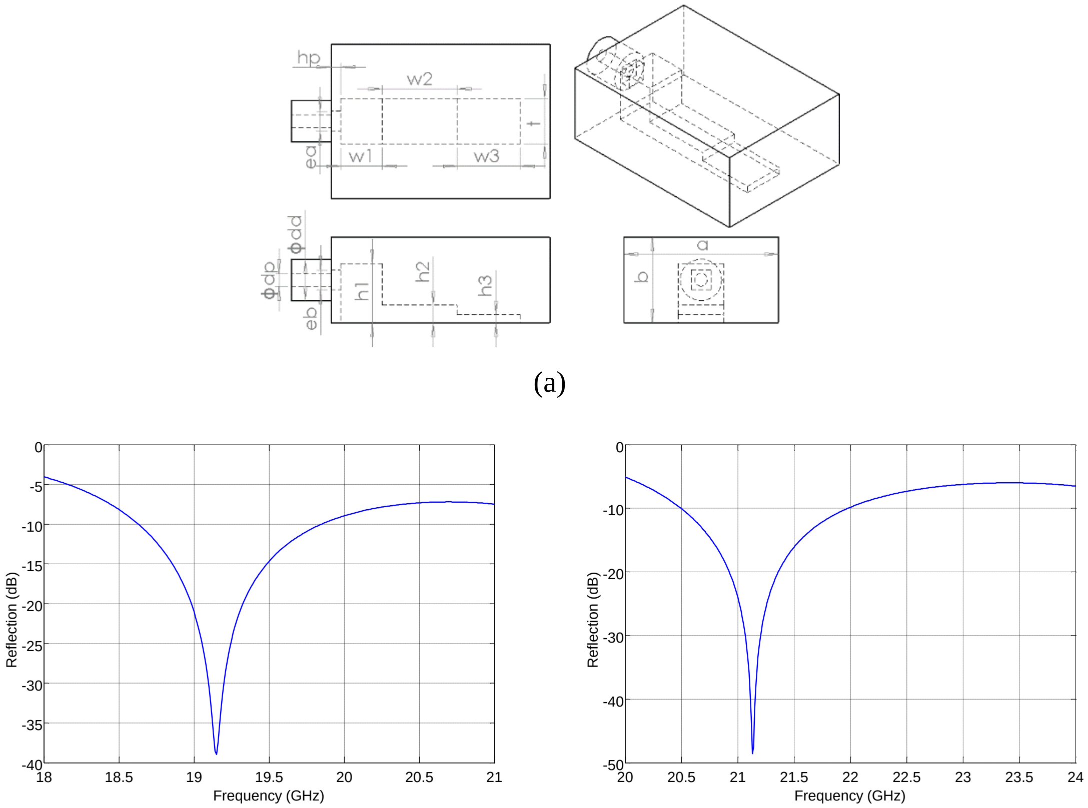

(a)

(b) (c)

Fig. 4.13 Launcher (a) Drawing (b) 19.55 GHz (c) 22 GHz.

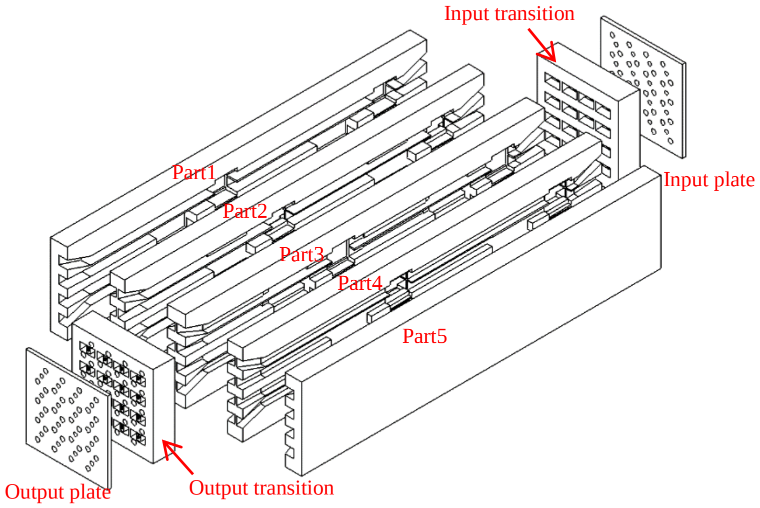

Fig. 4.14 Assembly view of hollow waveguide one-body $4^2 \times 4^2$-way 2-D beam-switching Butler matrix.

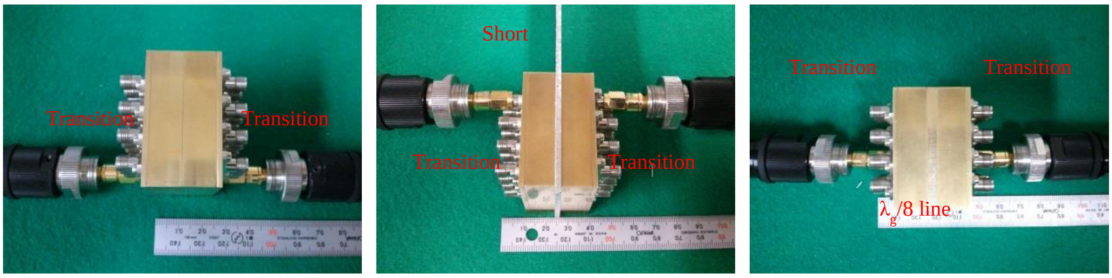

Fig. 4.15 TRL calibration (a) Thru (b) Reflect (c) λ_g/8 line.

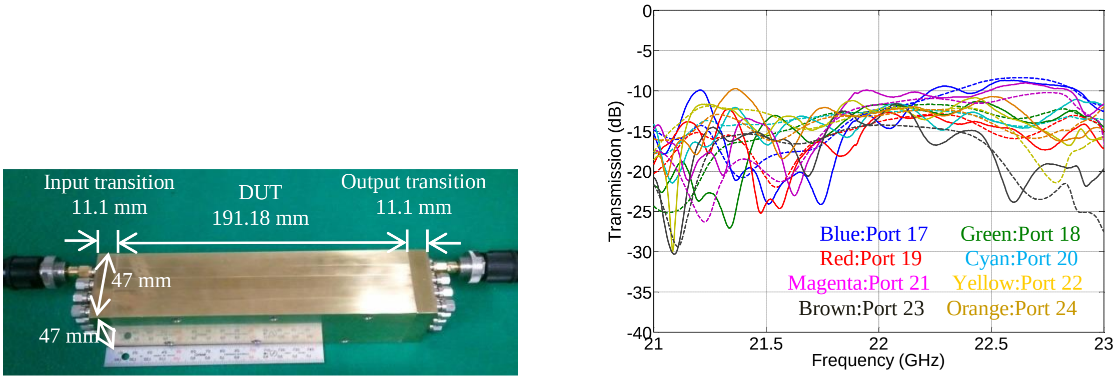

(a) (b)

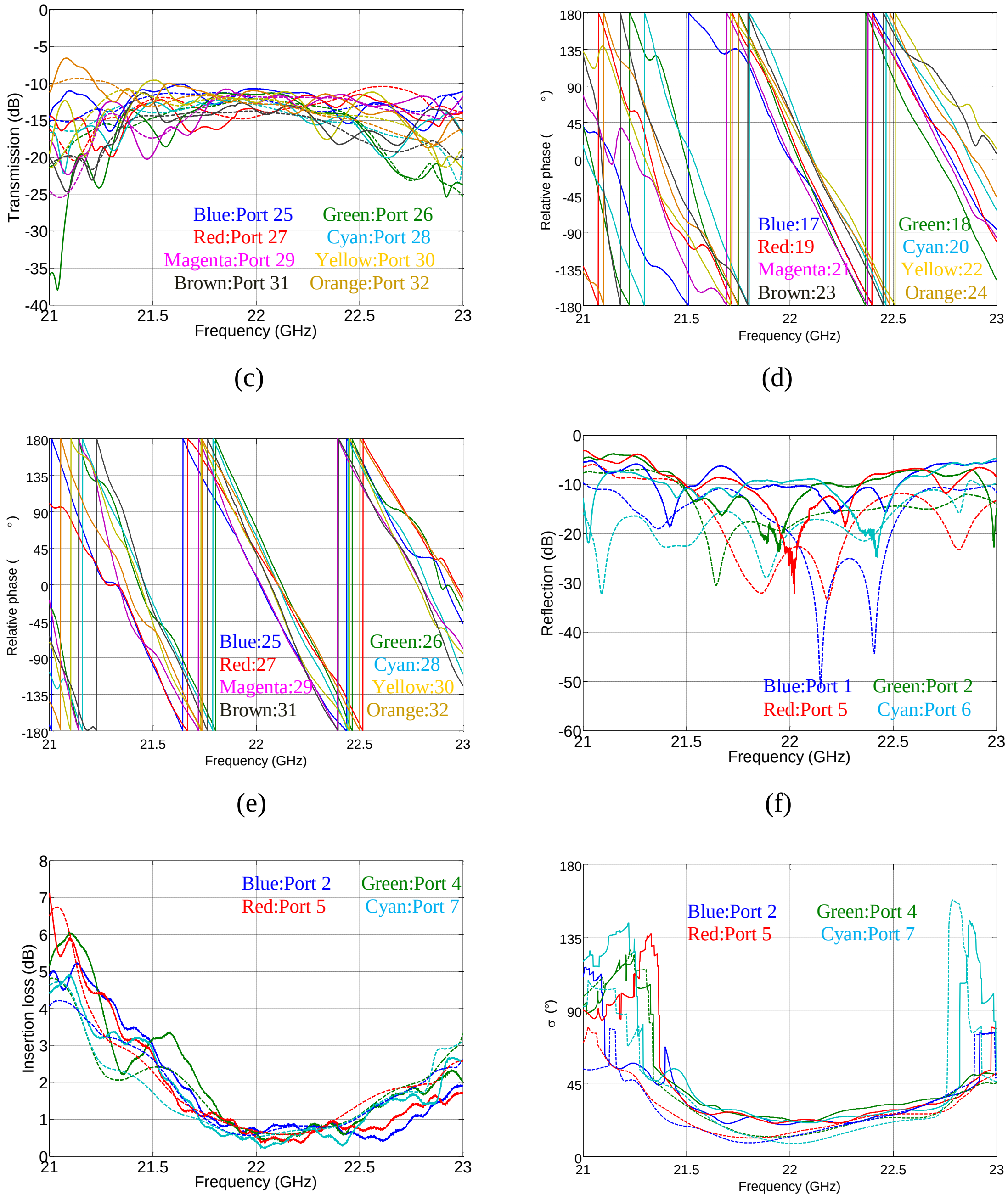

(c) (d)

(e) (f)

(g) (h)

Fig. 4.16 Characteristics of one-body $4^2 \times 4^2$-way 2-D beam-switching Butler matrix covered brass (a) Measurement scene. When port 1 excited, transmission coefficients (b) port 17-24 (c) port 25-32, relative phases to ideals (d) port 17-24 (e) port 25-32 (f) Return loss (g) Insertion loss (h) Deviation of the phase difference between the measurement and the ideal . Solid lines: measurement, Dashed lines: simulation.

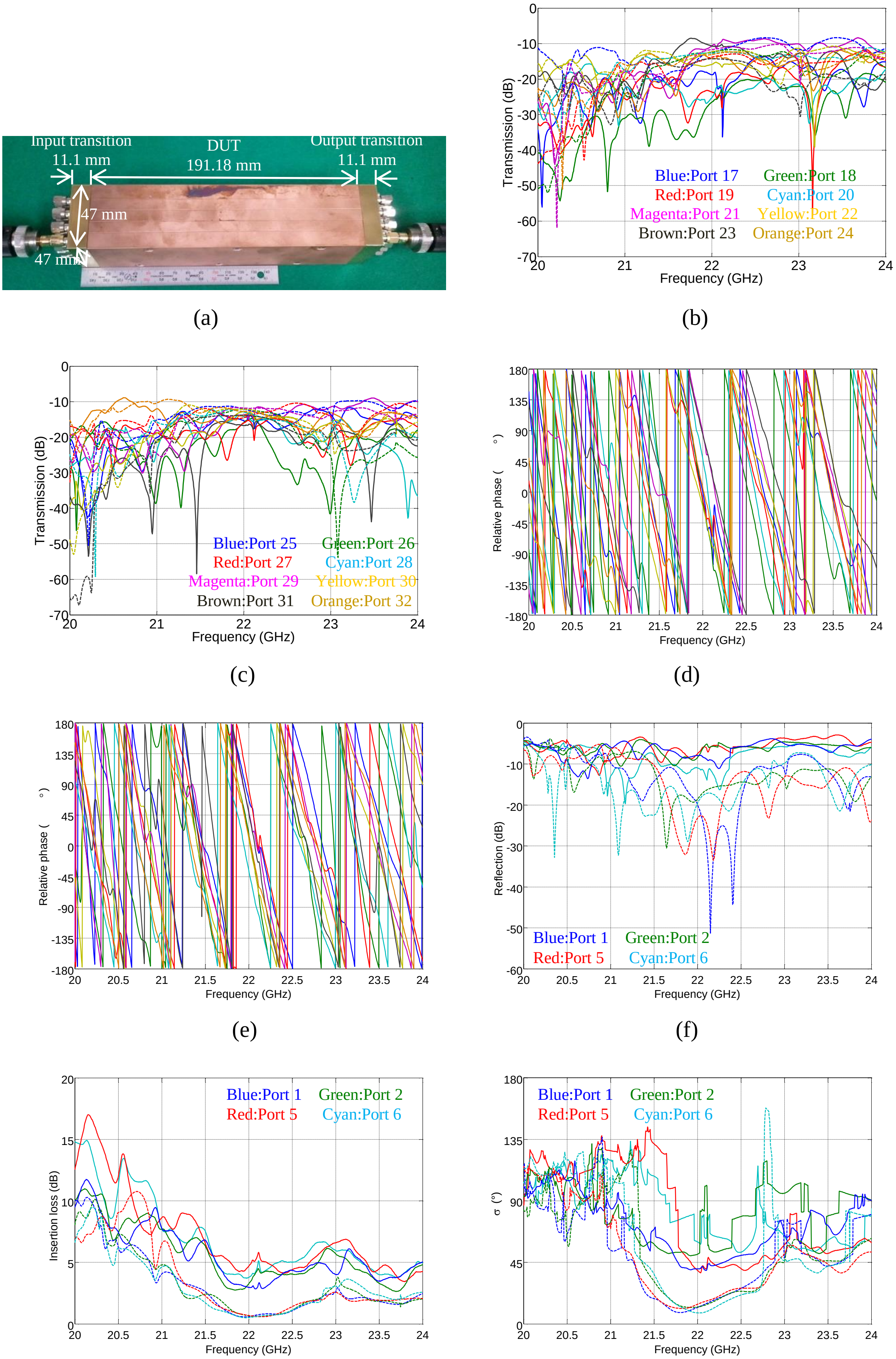

Input transition
11.1 mm
DUT
191.18 mm
Output transition
11.1 mm
47 mm
47 mm
Transmission (dB)
Frequency (GHz)
Blue:Port 17
Green:Port 18
Red:Port 19
Cyan:Port 20
Magenta:Port 21
Yellow:Port 22
Brown:Port 23
Orange:Port 24
Blue:Port 25
Green:Port 26
Red:Port 27
Cyan:Port 28
Magenta:Port 29
Yellow:Port 30
Brown:Port 31
Orange:Port 32
Relative phase (°)
Reflection (dB)
Blue:Port 1
Green:Port 2
Red:Port 5
Cyan:Port 6
Insertion loss (dB)
σ (°)

(a)

(b)

(c)

(d)

(e)

(f)

(g) (h)

Fig. 4.17 Characteristics of one-body $4^2\times4^2$-way 2-D beam-switching Butler matrix covered copper plated ABS-like (a) Measurement scene. When port 1 excited, transmission coefficients (b) port 17-24 (c) port 25-32, relative phases to ideals (d) port 17-24 (e) port 25-32 (f) Return loss (g) Insertion loss (h) Deviation of the phase difference between the measurement and the ideal . Solid lines: measurement, Dashed lines: simulation.

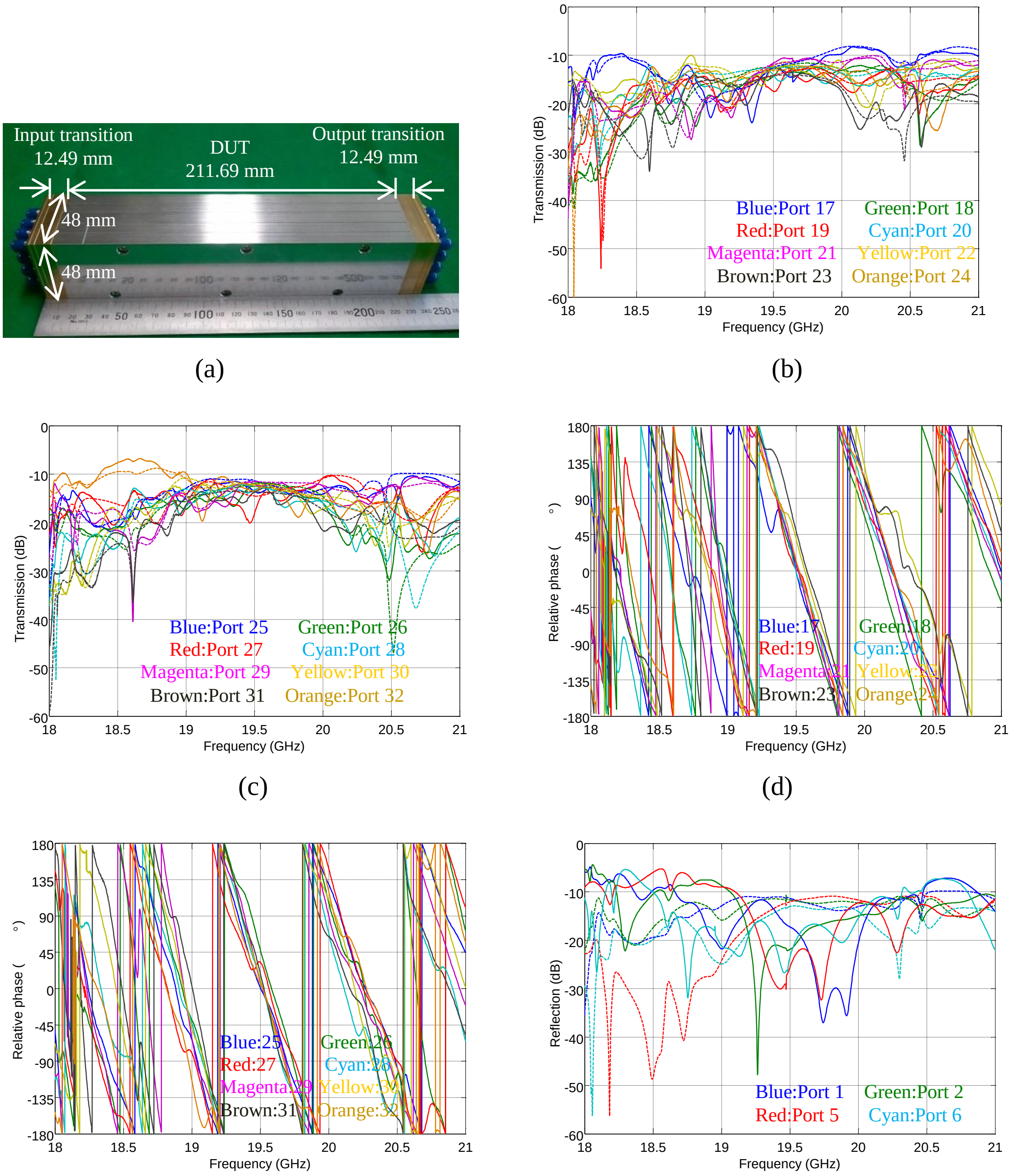

(a) (b)

(c) (d)

(e) (f)

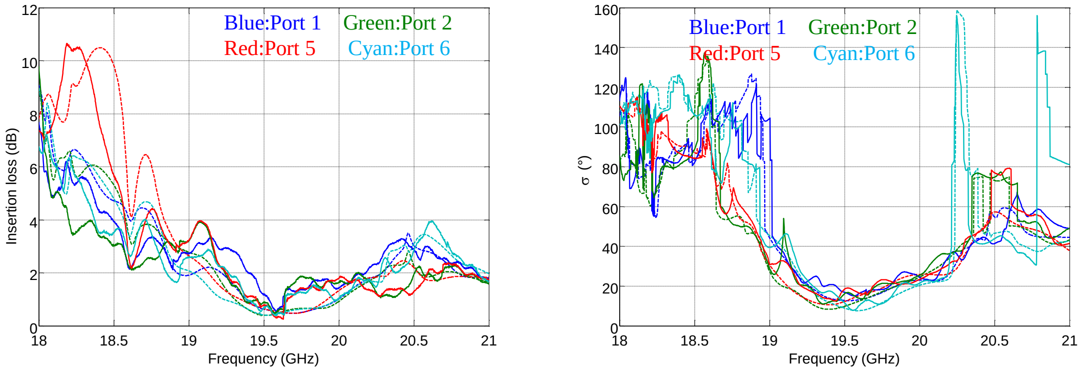

(g) (h)

Fig. 4.18 Characteristics of one-body $4^2 \times 4^2$-way 2-D beam-switching Butler matrix covered aluminum alloy (a) Measurement scene. When port 1 excited, transmission coefficients (b) port 17-24 (c) port 25-32, relative phases to ideals (d) port 17-24 (e) port 25-32 (f) Return loss (g) Insertion loss (h) Deviation of the phase difference between the measurement and the ideal . Solid lines: measurement, Dashed lines: simulation.

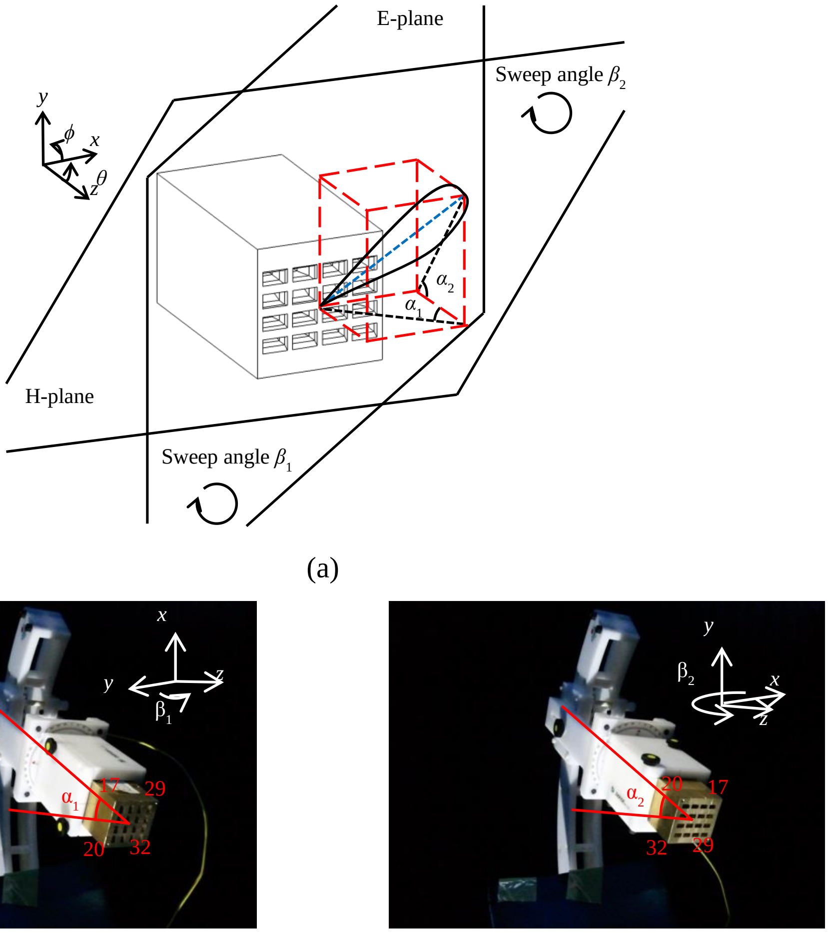

(a)

(b) (c)

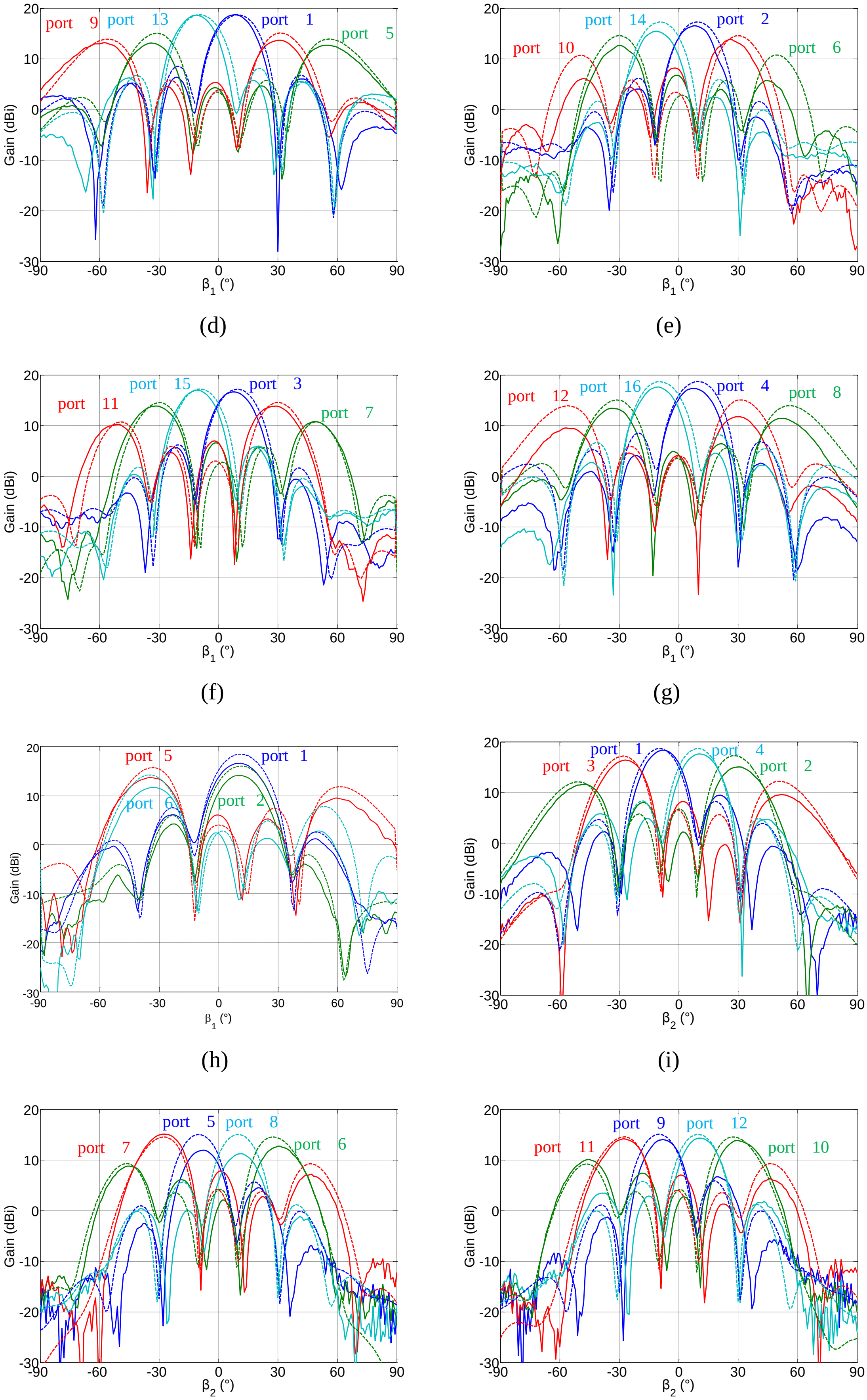
port 9
port 13
port 1
port 5
port 14
port 2
port 10
port 6
port 15
port 3
port 11
port 7
port 12
port 16
port 4
port 8
port 5
port 1
port 6
port 2
port 1
port 4
port 3
port 2
port 5
port 8
port 7
port 6
port 9
port 12
port 11
port 10
Gain (dBi)
β_1 (°)
β_2 (°)
20
10
0
-10
-20
-30
-90
-60
-30
0
30
60
90

(d) (e)

(f) (g)

(h) (i)

(j) (k)

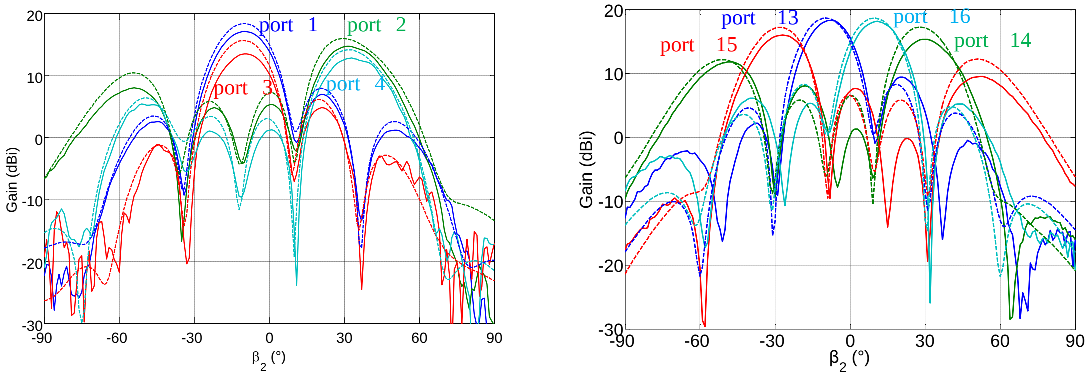

(l) (m)

Fig. 4.19 Radiation patterns of one-body $4^2 \times 4^2$-way 2-D beam-switching Butler matrix. (a) Configuration. Quasi E-plane, AUT looks at α_1 in the x-z plane (b) Measurement scene (d)-(g) Results covered brass at 22 GHz (h) Result covered aluminum alloy at 19.55 GHz. Quasi H-plane, AUT looks at α_2 in the y-z plane (c) Measurement scene (i)-(l) Results covered brass at 22 GHz (m) Result covered aluminum alloy at 19.55 GHz.

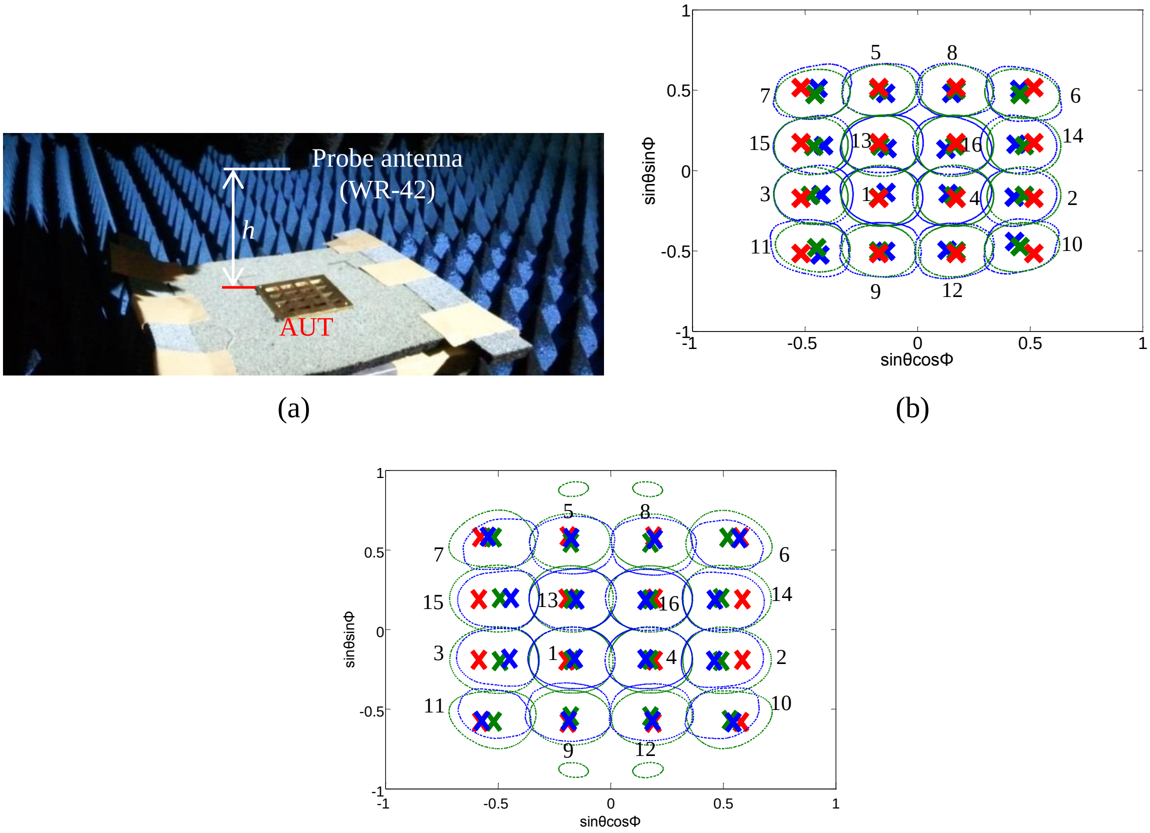

(a) (b)

(c)

Fig. 4.20 Near-field to far-field transformation of one-body $4^2 \times 4^2$-way 2-D beam-switching Butler matrix covered brass at 22 GHz where h=82 mm. (a) Measurement scene (b) 3.9 dB-down contour gain patterns. Covered aluminum alloy at 19.55 GHz where h=92 mm (c) 3.9 dB-down contour gain patterns. The numbers and the symbol Xes indicate the input port number and the position of peak gain. Blue - Measurements, Green - Simulations, and Red - Ideal.

Table 4.1 The numbers of units and elements of 1-D beam-switching Butler matrix

Type	Units	Elements per unit	Total components
Hybrid	n	$N/2$	$nN/2$
Cross	a_n	-	b_n
Phase shifter	n-1	$N/2$	$N(n-1)/2$

$$\mathrm{n} = \log_2 N,\ a_n = 2^{n-1} - 1 + \sum_{i=1}^{n-1}(2^i - 1),\ b_n = \sum_{i=0}^{\frac{N}{2}-1} i + \sum_{i=1}^{n-1}\left[(2^i - 1)2^{n-1} - 2^{n-3+i}\right]$$

Table 4.2 The numbers of units and elements of conventional 2-D beam-switching Butler matrix.

Type	Units	Total components
Hybrid	n	$nN/2$
Cross	$a_{n_1} + a_{n_2}$	$2^{n_2} b_{n_1} + 2^{n_1} b_{n_2}$
Phase shifter	n-2	$N(n-2)/2$

$n=n_1+n_2$

Table 4.3 The numbers of units and elements of one-body 2-D beam-switching Butler matrix.

Type	Units (un-overlapped/overlapped)	Total components
Hybrid	n_1-n_2 / n_2	$N(n_1-n_2)/2+Nn_2/4$
Cross	$a_{n_1} - a_{n_2}$ / a_{n_2}	1)-
Phase shifter	n_1-n_2 / n_2-1	$N(n_1-n_2)/2+3N(n_2-1)/4$

1)Can't express the series of the number of 2-plane cross coupler

Table 4.4 Dimensions and output phase values of the phase compensators in 22 GHz.

Connected component	Side-wall stubs of 1)waveguide					
	Phase compensator alone			With phase shifter unit		
	Length (mm)	2)Width (mm)	3)Δφ (°)	Length (mm)	Width (mm)	Δφ (°)

E-plane	11.5	-0.5	81.7	17.2	-0.6	124.0
H-plane	31.3	-0.5	145.2	32.2	-0.6	185.5
2-plane	31.5	+1.2	-89.0	31.5	+0.4	-1.0
0° phase shifter	20	+0.5	0.0	21	+0.6	0.0

1)Size of apertures is 7.85 (width)×4.35 (height) mm

2)(+) and (-) indicate the extrusion from and the intrusion into the side-wall

3)Phase differences between 0° phase shifter and the others

Table 4.5 Performances of hollow waveguide one-body $4^2\times4^2$-way 2-D beam-switching Butler matrix in 22 GHz.

Conducting wall	PEC	Brass
Volume (mm^3)	38.10×34.05×191.18	
FBW (%)	2.4% (21.84~22.37 GHz)	
Transmission (dB)	-13.3±3.3	-13.6±3.2
1)Reflection (dB)	<-13.5	<-13.7
IL (dB)	<0.68	<0.97
2)$\Delta\varphi$ (°)	<24.4	<24.8

1)Include the isolation, 2)Deviation of phase difference between the simulation and the ideal

Table 4.6 Realized gains of hollow waveguide one-body $4^2\times4^2$-way 2-D beam-switching Butler matrix in 22 GHz.

Conducting wall	PEC (dBi)	Brass (dBi)
Port 1	19.0	18.6
Port 2	17.5	17.2
Port 3	17.4	17.2
Port 4	19.0	18.6
Port 5	14.3	13.8
Port 6	13.4	12.9
Port 7	13.4	12.9

Port 8	14.3	13.8
Port 9	14.4	13.8
Port 10	13.4	12.9
Port 11	13.4	12.9
Port 12	14.3	13.8
Port 13	19.0	18.6
Port 14	17.5	17.2
Port 15	17.5	17.2
Port 16	19.0	18.6

Table 4.7 Beam-directions of hollow waveguide one-body $4^2 \times 4^2$-way 2-D beam-switching Butler matrix in 22 GHz.

Input port	1)Ideal (°)				Simulation (°)			
	E-plane		H-plane		E-plane		H-plane	
	β_1	α_1	β_2	α_2	β_1	α_1	β_2	α_2
1	10	-9	-9	-9	10	-10	-10	-9
2	10	32	32	-11	9	39	29	-10
3	10	-31	-31	-11	9	-38	-28	-10
4	10	10	10	-9	9	10	10	-9
5	-31	-11	-9	32	-30	-11	-9	31
6	-31	38	32	38	-28	32	28	33
7	-31	-37	-31	38	-28	-31	-27	33
8	-31	-9	10	32	-30	12	10	31
9	32	32	-9	-31	31	-11	-9	-30
10	32	-31	32	-37	29	32	28	-32
11	32	10	-31	-37	29	-30	-26	-32
12	32	-11	10	-31	31	12	10	-30

13	-9	38	-9	10	-8	-9	-9	9
14	-9	-37	32	12	-8	29	29	11
15	-9	-9	-31	12	-8	-27	-27	10
16	-9	32	10	10	-8	10	10	9

[1]Peak direction of array factor with ideal phase

Table 4.8 HPBWs of hollow waveguide one-body $4^2 \times 4^2$-way 2-D beam-switching Butler matrix in 22 GHz.

Input port	E-plane (°)	H-plane (°)
1	19	17
2	18	18
3	18	18
4	19	17
5	18	17
6	17	18
7	17	18
8	18	17
9	18	17
10	17	18
11	17	18
12	18	17
13	19	17
14	18	18
15	18	18
16	19	17

Table 4.9 Coverages of hollow waveguide one-body $4^2 \times 4^2$-way 2-D beam-switching Butler matrix in 22 GHz.

Input port	Coverage (sr)
1	0.11
2	0.11
3	0.11
4	0.11
5	0.11
6	0.12
7	0.12
8	0.11
9	0.11
10	0.12
11	0.12
12	0.11
13	0.11
14	0.11
15	0.11
16	0.11

Table 4.10 Design parameters of launchers. Unit: mm.

Type	h_1	h_2	h_3	w_1	w_2	w_3	d_p	h_p	d_d	t	e_a	e_b
19.55 GHz	2	3.2	1	2.5	4.8	0.9	0.64	1.13	2.1	0.6	1	1
22 GHz	3	0.9	0.4	2.1	3.8	3.2		1		2.3	1	1

Table 4.11 Physical and electrical characteristics of the materials

Material	Brass	Copper plated ABS-like	Aluminum alloy
Specific gravity (g/cm^3)	8.5	1.11	2.7
Tensile strength (N/mm^2)	408~432	36~64	245~250

Electric conductivity (S/m)	1.31×10^7	5.8×10^7	2.56×10^7

Table 4.12 Performances of hollow waveguide one-body $4^2\times4^2$-way 2-D beam-switching Butler matrix covered with brass or copper plated ABS-like in 22 GHz.

Material	Brass			Copper plated ABS-like	
Type	Simulation	Raw data	Calibrated	Raw data	Calibrated
Volume (mm^3)	47×47×191.18 (1)213.38)				
Weight (kg)	2.57 (1)2.99)			0.34 (1)0.76)	
FBW (%)	2.4% (21.84~22.37 GHz)				
Transmission (dB)	-13.6±3.2	-16.3±5.5	-14.4±5.6	-26.2±16.6	-24.6±16.8
2)Reflection (dB)	<-13.7	<-7.2	<-7.7	<-4.8	<-3.0
IL (dB)	<0.97	<3.80	<2.09	<6.50	<4.83
3)Δφ (°)	<24.8	<32.1	<31.0	<113.8	<99.6

1)Include the transitions, 2)Include the isolation, 3)Deviation of phase difference between the simulation and the ideal

Table 4.13 Performances of hollow waveguide one-body $4^2\times4^2$-way 2-D beam-switching Butler matrix covered with aluminum alloy in 19.55 GHz.

Material	Aluminum alloy		
Type	Simulation	Raw data	Calibrated
Volume (mm^3)	48×48×211.69 (1)236.67)		
Weight (kg)	0.85 (1)1.26)		
FBW (%)	2.5% (19.39~19.88 GHz)		
Transmission (dB)	-13.0±2.9	-19.9±9.7	-19.0±9.6
2)Reflection (dB)	<-13.6	<-5.4	<-5.8
IL (dB)	<0.96	<3.69	<2.70
3)Δφ (°)	<23.8	<28.0	<29.3

1)Include the transitions, 2)Include the isolation, 3)Deviation of phase difference between the simulation and the ideal

Table 4.14 Realized gains and XPDs of one-body $4^2 \times 4^2$-way 2-D beam-switching Butler matrix covered with brass in 22 GHz and aluminum alloy in 19.55 GHz.

Input port	Brass in 22 GHz		Aluminum alloy in 19.55 GHz
	Gain (dBi)	XPD (dB)	Gain (dBi)
1	18.7	37.7	17.1
2	16.5	28.4	14.7
3	16.6	28.4	-
4	17.4	38.0	-
5	13.1	28.6	13.6
6	12.7	13.9	12.8
7	13.9	14.1	-
8	13.4	28.6	-
9	13.7	27.8	-
10	13.9	14.1	-
11	13.9	14.3	-
12	11.8	28.5	-
13	18.6	38.0	-
14	15.5	28.5	-
15	17.0	28.5	-
16	17.6	38.5	-

Table 4.15 Beam-directions of one-body $4^2 \times 4^2$-way 2-D beam-switching Butler matrix covered with brass in 22 GHz and aluminum alloy in 19.55 GHz.

Input port	Brass in 22 GHz				Aluminum alloy in 19.55 GHz			
	E-plane		H-plane		E-plane		H-plane	
	β_1	α_1	β_2	α_2	β_1	α_1	β_2	α_2

1	8	-10	-8	-9	11	-10	-10	-11
2	8	39	30	-10	11	30	29	-13
3	7	-38	-27	-10	-	-	-	-
4	8	10	11	-9	-	-	-	-
5	-34	-11	-8	31	-33	-12	-10	34
6	-30	32	31	33	-35	38	31	43
7	-32	-31	-27	33	-	-	-	-
8	-34	12	11	31	-	-	-	-
9	31	-11	-8	-30	-	-	-	-
10	26	32	29	-32	-	-	-	-
11	29	-30	-28	-32	-	-	-	-
12	30	12	11	-30	-	-	-	-
13	-11	-9	-8	9	-	-	-	-
14	-11	29	30	11	-	-	-	-
15	-11	-27	-27	10	-	-	-	-
16	-10	10	11	9	-	-	-	-

Table 4.16 HPBWs of one-body $4^2 \times 4^2$-way 2-D beam-switching Butler matrix covered with brass in 22 GHz and aluminum alloy in 19.55 GHz.

Input port	Brass in 22 GHz		Aluminum alloy in 19.55 GHz	
	E-plane (°)	H-plane (°)	E-plane (°)	H-plane (°)
1	19	17	21	19
2	17	20	20	22
3	18	19	-	-
4	18	17	-	-
5	20	16	23	18
6	18	19	22	21

7	22	19	-	-
8	20	16	-	-
9	20	16	-	-
10	18	19	-	-
11	20	18	-	-
12	19	17	-	-
13	18	17	-	-
14	17	20	-	-
15	17	19	-	-
16	18	17	-	-

Table 4.17 Coverages of one-body $4^2 \times 4^2$-way 2-D beam-switching Butler matrices covered with brass in 22 GHz and aluminum alloy in 19.55 GHz.

Input port	Coverage (sr)	
	0.73 λ_0@22 GHz	0.65 λ_0@19.55 GHz
1	0.13	0.14
2	0.12	0.13
3	0.12	0.13
4	0.11	0.16
5	0.12	0.14
6	0.14	0.12
7	0.13	0.13
8	0.11	0.14
9	0.12	0.14
10	0.13	0.13
11	0.14	0.12
12	0.12	0.13

13	0.14	0.15
14	0.12	0.13
15	0.12	0.13
16	0.11	0.15

Reference

[4.1] J. Butler and R. Lowe, “Beam-forming matrix simplifies design of electronically scanned antennas,” *Electron. Des.*, vol. 9, no. 8, pp. 170-173, Apr. 1961.

[4.2] J. W. Cooley and J. W. Tukey, “An algorithm for the machine calculation of complex fourier series,” *Math. of Comput.*, vol. 19, no. 90, pp. 297-301, 1965.

[4.3] C. Balanis, “Array: Linear, Planar, and Circular,” in *Antenna Theory: Analysis and Design*, 2nd ed., NJ, John Wiley & Sons, Inc., 1997, pp. 257-261.

[4.4] B. Pattan, "The Versatile Butler Matrix," *Microw. Journal*, vol. 47, no. 11, pp. 126-138, 2004.

[4.5] C. Balanis, “Array: Linear, Planar, and Circular,” in *Antenna Theory: Analysis and Design*, 2nd ed., NJ, John Wiley & Sons, Inc., 1997, pp. 309-314.

[4.6] S. Yamamoto, J. Hirokawa, and M. Ando, “Length reduction of short-slot directional coupler in a single section dielectric substrate waveguide by removing dielectric near the side walls,” *IEEE Intl. Symp. Antennas Propag.*, vol. 3, pp. 2353–2356, 2004.

[4.7] G. T. K. Kwang and P. Gardner, “4×4 Butler matrix beam forming network using novel reduced size branchline coupler,” *31st Eur. Microw. Conf.*, pp. 1-4, Sep. 2001.

[4.8] C. W. Wang, T. G. Ma, and C. F. Yang, “A new planar artificial transmission line and its applications to a miniaturized Butler matrix,” *IEEE Trans. Microw. Theory Techn.*, vol. 55, no. 12, pp. 2792–2801, Dec. 2007.

[4.9] Y. S. Jeong and T.W. Kim, “Design and analysis of swapped port coupler and its application in a miniaturized Butler matrix,” *IEEE Trans. Microw. Theory Techn.*, vol. 58, no. 4, pp. 764-770, Apr. 2010.

[4.10] D. Titz, F. Ferrero, R. Pilard, C. Laporte, S. Jan, H. Ezzeddine, F. Gianesello, D. Gloria, C. Luxey, and G. Jacquemod, “New wideband integrated miniature branchline coupler for beamforming applications,” *IEEE MTT-S Intl. Symp.*, pp. 1-3, Jun. 2012.

[4.11] M. Bona, L. Manholm, J. P. Starski, and B. Svensson, “Low-loss compact Butler matrix for a microstrip antenna,” *IEEE Trans. Microw. Theory Techn.*, vol. 50, no. 9, pp. 2069-2075, Sep. 2002.

[4.12] G. Tudosie, H. Barth, and R. Vahldieck, “A compact LTCC Butler matrix realization for phased array applications,” *IEEE MTT-S Intl. Symp. Dig.*, pp. 441-444, Jun. 2006.

[4.13] A. Ali, N. J. G. Fonseca, F. Concetti, and H. Aubert, “Design and implementation of two-section compact wideband Butler matrices in SIW technology for Ku-band applications,” *IEEE Trans. Antennas Propag.*, vol. 59, no. 2, pp. 503-512, Feb. 2011.

[4.14] M. Schühler, “On Evaluation of Beamforming Networks,” *IEEE Antennas Wireless Propag. Lett.*, vol. 13, 2014.

[4.15] Arthur C. Ludwig, The Definition of Cross Polarization, *IEEE Trans. Antennas Propag.*, vol. AP-21 no. 1, pp. 116 -119, Jan. 1973.

[4.16] D. Zwillinger (Ed.), *CRC Standard Mathematical Tables and Formulae*. Boca Raton, FL: CRC Press, p. 469, 1995.

[4.17] G. F. Engen and C. A. Hoer, “Thru-reflect-line: An improved technique for calibrating the dual six-port automatic network analyzer," *IEEE Trans. Microw. Theory Techn.*, vol. 27, no. 12, pp. 987-993, Dec. 1979.

[4.18] C. Balanis, “Antenna Measurements,” in *Antenna Theory: Analysis and Design*, 2nd ed., NJ, John Wiley & Sons, Inc., 1997, pp. 852-858.

Chapter 5

Wideband and large-scaled 2-D beam-switching Butler matrix

5.1 Wideband one-body $4^2\times4^2$-way 2-D beam-switching Butler matrix

5.1.1. Hollow waveguide

Because the performances of one-body 2-D beam-switching Butler matrix are depended on the short-slot 2-plane coupler's, the hollow waveguide one-body $4^2\times4^2$-way 2-D beam-switching Butler matrix with the short-slot 2-plane coupler in Chapter 3 shown in Fig. 5.1 succeeds the performances of the components. These performances are shown in Fig. 5.2 to 5.4 and listed in Table 5.1 and 5.2. As improving the linearity of the output amplitudes and phases, the frequency bandwidth is increased from 2.4% to 5.8%. In that time, E- and H-plane angled junctions are inserted to connect the components, it leads to increase the length of the Butler matrix. Considering the variation of the components and the junctions, the design parameters of the phase compensators are listed in Table 5.3. The radiation and gain patterns in 22 GHz are same as shown in Fig. 5.5(a), because the interval between the antenna elements is same. And in the frequency bandwidth, the gain pattern maintains its form as shown in Fig. 5.5(b).

5.1.2. Dielectric-filled waveguide

The dielectric-filled (PPS, ε_r=3.2, tanδ=2.7×10^{-3}) waveguide one-body $4^2\times4^2$-way 2-D beam-switching Butler matrix with aluminum (A6061, σ=2.56×10^{7} S/m) wall is consisted of the dielectric-filled short-slot 2-plane couplers in Chapter 3 and operated in 5.12 GHz. As previously mentioned in Section 3.1.2.2, the performance of the dielectric-filled waveguide Butler matrix scaled by the center frequency and the electrical permittivity of the dielectric material is different to the hollow waveguide Butler matrix because of the attenuation difference of the propagating modes in the coupled region of the short-slot 2-plane coupler. Those are shown in Fig. 5.6 to 5.8 and listed in Table 5.4. Different the hollow waveguide Butler matrix, the dielectric-filled waveguide Butler matrix has the reflection on the boundary between the antenna aperture (Dielectric material) and the propagation media (Air). Solving that problem, the quarter-wave transformer is attached to the waveguide output as shown in

Fig. 5.9(a)-(b). The dimension and the electrical permittivity of the quarter-wave transformer are derived from

$$\mathrm{Z_{tran}} = \sqrt{\mathrm{Z_{ant}Z_{air}}} \tag{5.1}$$

$$Z_i = k_i\eta_i/\beta_i \tag{5.2}$$

$$\varepsilon_{\mathrm{tran}} = \sqrt{\varepsilon_{\mathrm{ant}}\varepsilon_{\mathrm{air}}} \tag{5.3}$$

$$\lambda_{tran} = 2\pi/\beta_{tran} \tag{5.4}$$

where Z_i is the characteristic impedance of i (*trans*former, *ant*enna, *air*), k is a wavenumber, η is an intrinsic impedance, β is a propagation constant, ε is an electrical permittivity, λ is a wavelength. Calculated parameters are 24.6×13.72×32.15 mm and ε_r=1.79. Considering the fabrication, parameters are selected 23.2×18.5×24.1 mm and PTFE (ε_r=2.1). It makes to improve the impedance matching as shown in Fig. 5.4(c) and the realized gain is listed in Table 5.5. In that time, the radiation and the gain patterns of dielectric-filled waveguide one-body $4^2\times4^2$-way 2-D beam-switching Butler matrix with the interval between the antenna elements is 0.6 λ_0 are shown in Fig. 5.10. The beam-direction compared with the ideal, HPBW, and the coverage are listed in Table 5.6 to 5.8, respectively. The sixteen coverages can be covered 2.81 sr (44.7% of a hemisphere). The coaxial-to-waveguide transitions are same previously mentioned as Chapter 3.

5.2 Large-scaled one-body 2-D beam-switching Butler matrix

Based on the previous mentioned contents in Chapter 4, design procedures of the $N\times N$-way one-body 2-D beam-switching Butler matrix are

1. Prepare diagrams of $2^{n_1}\times 2^{n_1}$-way and $2^{n_2}\times 2^{n_2}$-way 1-D beam-switching Butler matrices where $N = 2^{n_1+n_2}$.
2. Keeping the law of the commutativity, overlap orthogonally stacked same type units of $2^{n_1}\times 2^{n_1}$-way and $2^{n_2}\times 2^{n_2}$-way 1-D beam-switching Butler matrices.
3. Compensate phase difference between the short-slot cross couplers of the cross coupler unit.
4. If the phase compensator unit neighbors the phase shifter unit, those are merged.

In that time, several design considerations should be applied to the large-scaled one-body 2-D beam-switching Butler matrix, additionally. If $n_1>n_2$, overlapped hybrid coupler and phase shifter units have same the distribution of the components. On the other hand, the distributions of the components of the overlapped cross coupler units are depended on the selected unit and stage which consists of neighbored cross coupler units. For example, three overlapped cross couplers shown in Fig. 5.11 are occupied same volume, but the composition of the components is different. The overlapped cross coupler unit in Fig. 5.11(c) has the least short-slot 2-plane coupler than others, it makes to reduce the insertion loss of the unit in the operating frequency. Another is the connection of the cross coupler units in the same stage. As previously mentioned in Section 5.1.1, the angled junctions are required when the positions of the port branches are different between the connected units. In the small-scaled one-body 2-D beam-switching Butler matrix, the angled junctions contribute little to increase the length of the one-body 2-D beam-switching Butler matrix and bring out the performance of components maximally. However in the large-scaled one-body 2-D beam-switching Butler matrix, the length of the angled junctions cannot be ignored, and difficult to maintain the performance of components maximally from the multiple reflections at the discontinuity. For those reasons, the short-slot E-, H-, and 2-plane cross couplers should be designed two different versions which have different positions of port branches as shown in Fig. 5.12. As feasibility study of large-scaled one-body 2-D beam-switching Butler matrix, the dielectric-filled waveguide one-body $8^2 \times 8^2$-way 2-D beam-switching Butler matrix is design as shown in Fig. 5.13. In that time, the coaxial cross coupler is adopted to substitute the short-slot E-plane coupler, because it cannot shrink to limited space maintaining required performance. The operating frequency in the simulation is set to 19.55 GHz, and the dielectric material and the conducting wall are same as Section 5.1. The performance of the dielectric-filled waveguide one-body $8^2 \times 8^2$-way 2-D beam-switching Butler matrix is depicted as Fig. 5.14 and 15, and listed in Table 5.9 to 5.13. Comparing with dielectric-filled waveguide one-body $4^2 \times 4^2$-way 2-D beam-switching Butler matrix in Section 5.1, the insertion loss is increased linearly in the frequency band, because the dielectric and the conduction losses are proportional to the distance of the propagating path. On the other hand, the deviation of phase difference to the ideal is maintained around the center frequency, because N orthogonal propagating paths passed same number ($n/2$) of the hybrid coupler units. Comparing with Section 5.1, the radiation and the gain patterns have narrow beam-widths and beam-coverages, because the interval between the antenna elements and the summation of the coverages are same, but the number of the input port is more. The design parameters and the performances of the coaxial-to-waveguide transitions for Section 5.2 are listed in Table 5.14, and shown as Fig. 5.16, respectively.

5.3 Comparison with other beam-switching networks

A comparison with other beam-switching networks, it should have information about the number of ports, the volume (expressed as wavelength unit), the insertion loss, and the FBW. To the best of author’s knowledge, there is no comparison equipped whole information in the 2-D beam-switching networks. In that reason, estimate performances of the 2-D beam-switching networks from the 1-D beam-switching networks [5.1]-[5.20]. Then these estimated 2-D beam-switching networks are compared with one-body 2-D beam-switching Butler matrices as shown in Fig. 5.18 and listed in Table 5.15 and 16. There are two typical beam-switching networks which are Butler matrix and Rotman lens. Butler matrix has better performances in all aspects except FBW because of the difference in the propagation way. Within Butler matrices, the one-body type is outclassed in the volume and the FBW. However it has the lowest insertion loss, and can deal with high power. So it is most pertinent to high power and low loss applications.

5.3 Summary

Adapting the wideband short-slot 2-plane coupler to the one-body 2-D beam-switching Butler matrix, FWB is increased from 2.4% to 5.1%. In the cross coupler stage which has multiple units of the large-scaled one-body 2-D beam-switching Butler matrix, six cross couplers are designed for removing angled connections. Even the number of the unit connections is increased in the large-scaled one-body 2-D beam-switching Butler matrix, it maintains the spatial orthogonality in given frequency band.

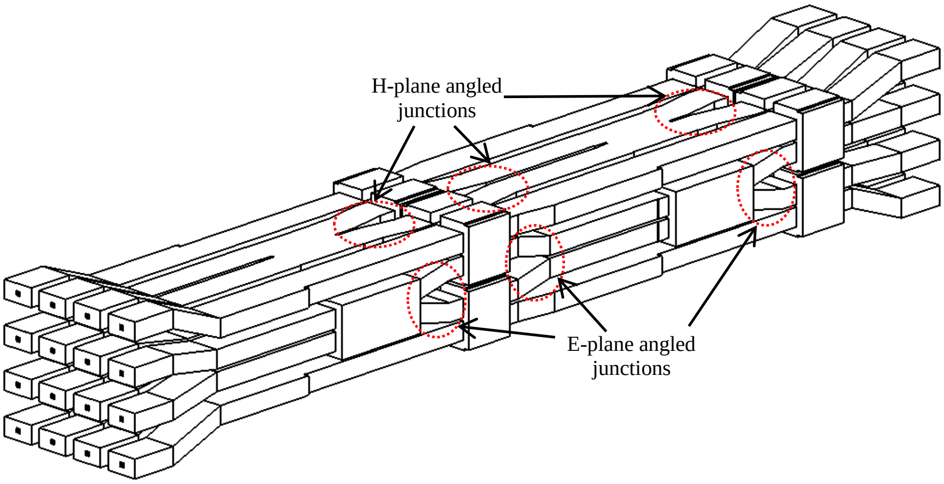

Fig. 5.1 Drawing of One-body $4^2 \times 4^2$-way 2-D beam-switching Butler matrix with couplers in chapter 3.

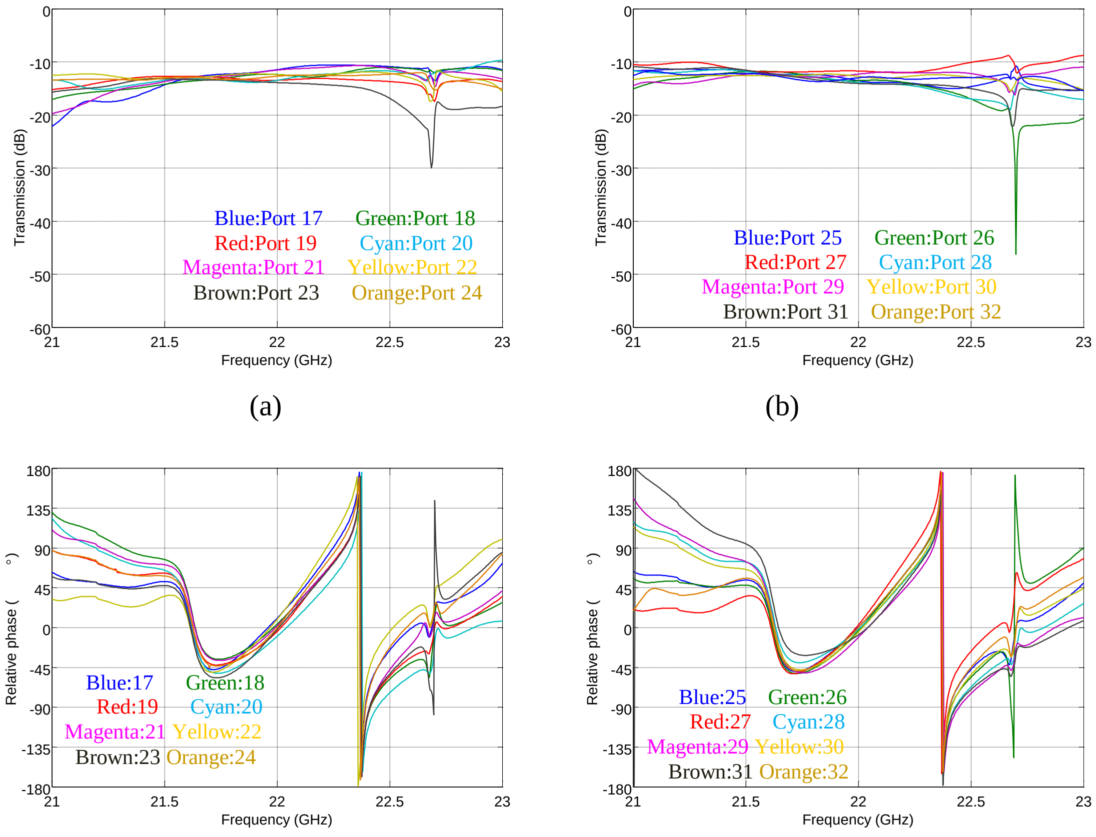

(a) (b)

(c) (d)

Fig. 5.2 S-parameters of one-body $4^2 \times 4^2$-way 2-D beam-switching Butler matrix with couplers in chapter 3 when input port 1 is excited. Transmission coefficients (a) port 17-24 (b) port 25-32, Relative phases to ideals (c) port 17-24 (d) port 25-32.

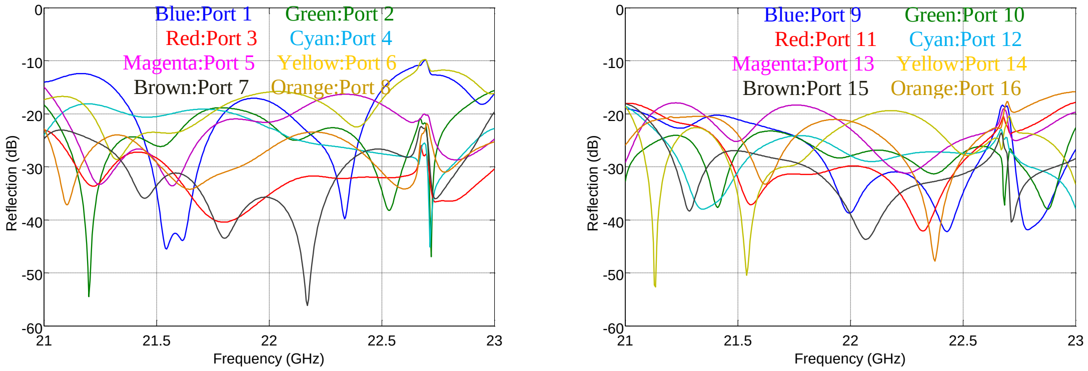

(a) (b)

Fig. 5.3 S-parameters of one-body $4^2 \times 4^2$-way 2-D beam-switching Butler matrix with couplers in chapter 3 when input port 1 is excited. Reflection and isolations (a) port 17-24 (b) port 25-32

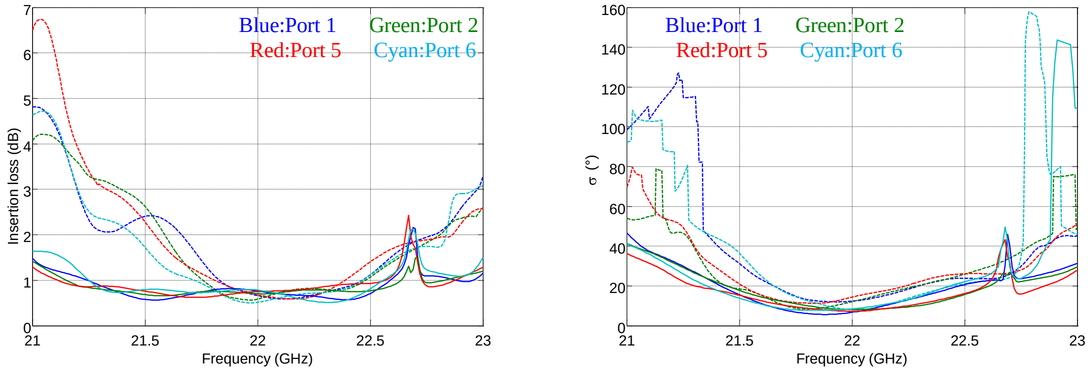

(a) (b)

Fig. 5.4 Processed parameters (a) Insertion loss (b) Deviation of the phase difference between the simulation and the ideal. With couplers in chapter 3 - Solid lines. With couplers in chapter 2 - Dashed lines.

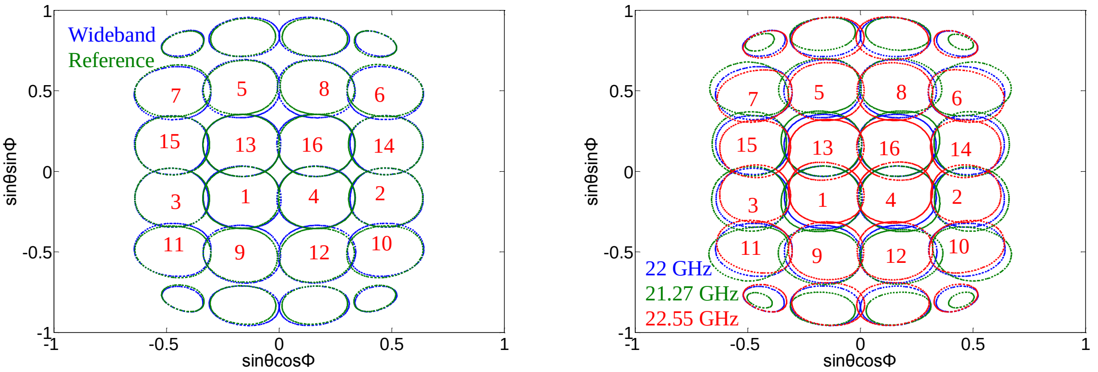

(a) (b)

Fig. 5.5 Comparison between 3.9 dB-down contour gain patterns (a) Different structure in 22 GHz (b)

Wideband with frequencies.

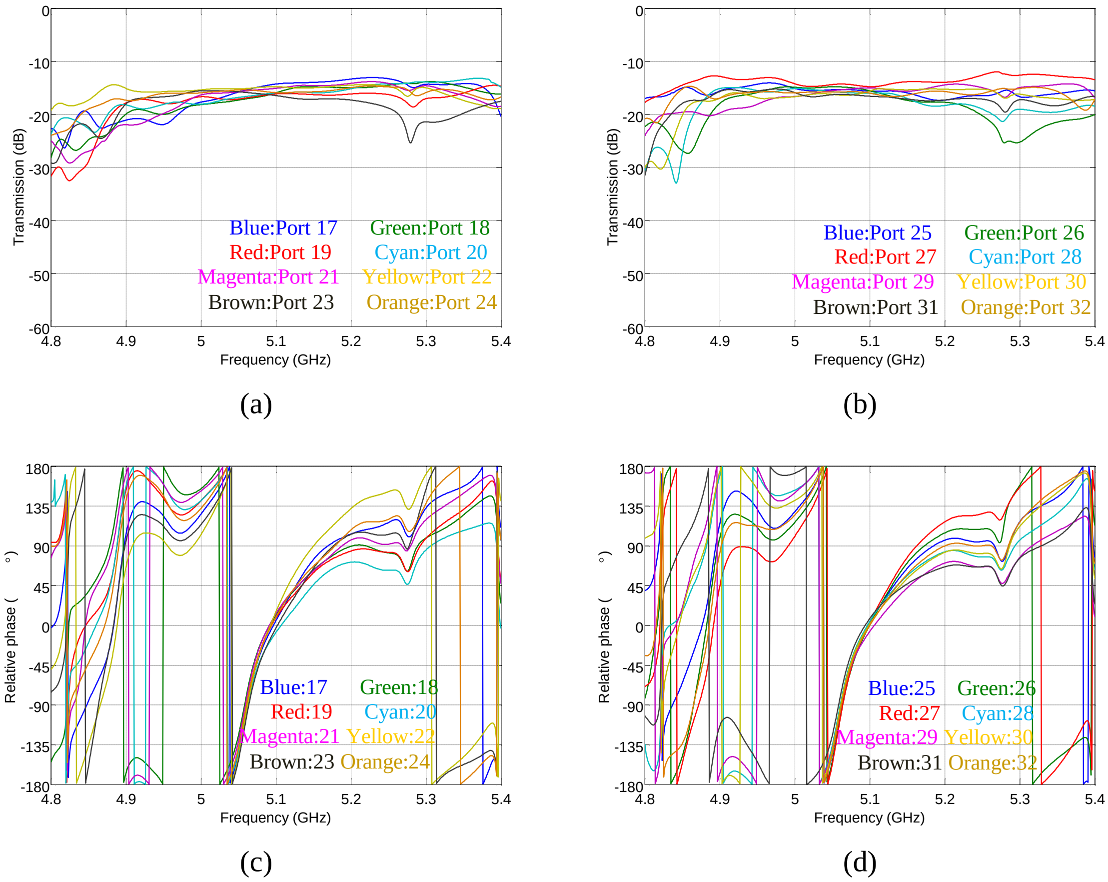

Fig. 5.6 S-parameters of dielectric-filled one-body $4^2 \times 4^2$-way 2-D beam-switching Butler matrix with couplers in chapter 3 when input port 1 is excited. Transmission coefficients (a) port 17-24 (b) port 25-32, Relative phases to ideals (c) port 17-24 (d) port 25-32.

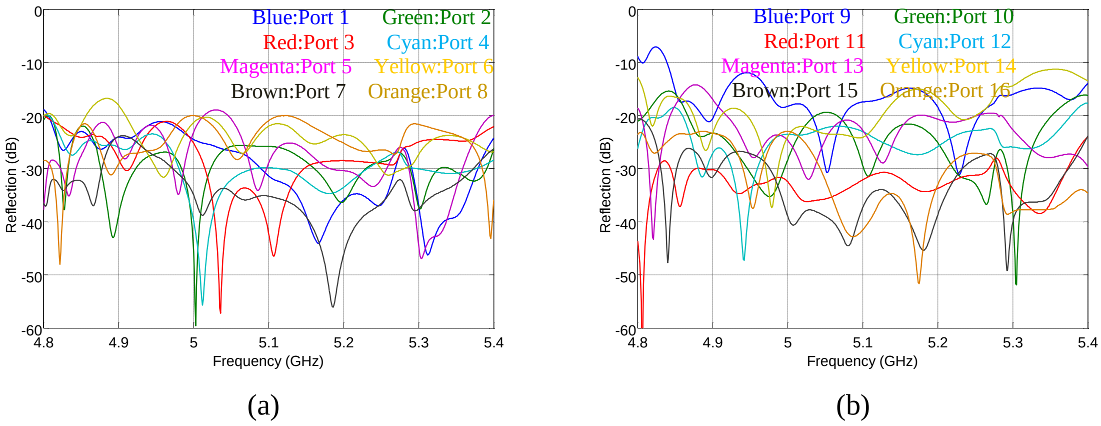

Fig. 5.7 S-parameters of dielectric-filled one-body $4^2 \times 4^2$-way 2-D beam-switching Butler matrix with couplers in chapter 3 when input port 1 is excited. Reflection and isolations (a) port 17-24 (b)

port 25-32

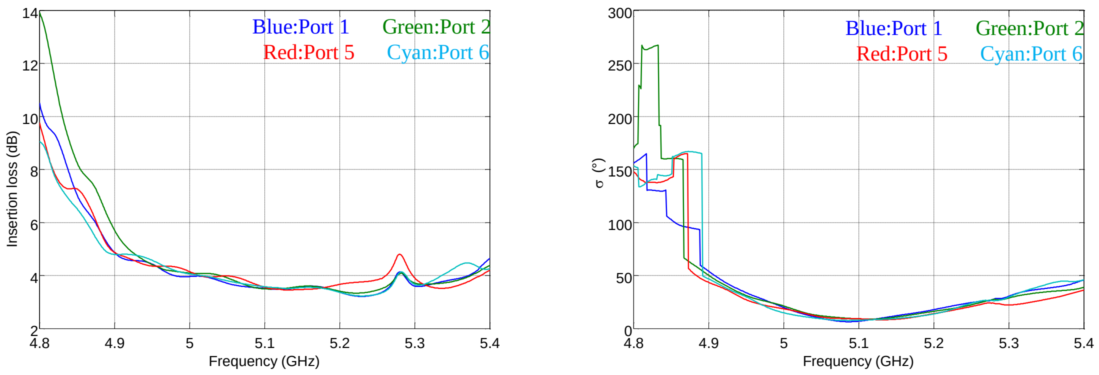

(a) (b)

Fig. 5.8 Processed parameters of dielectric-filled one-body $4^2 \times 4^2$-way 2-D beam-switching Butler matrix with couplers in chapter 3 (a) Insertion loss (b) Deviation of the phase difference between the simulation and the ideal.

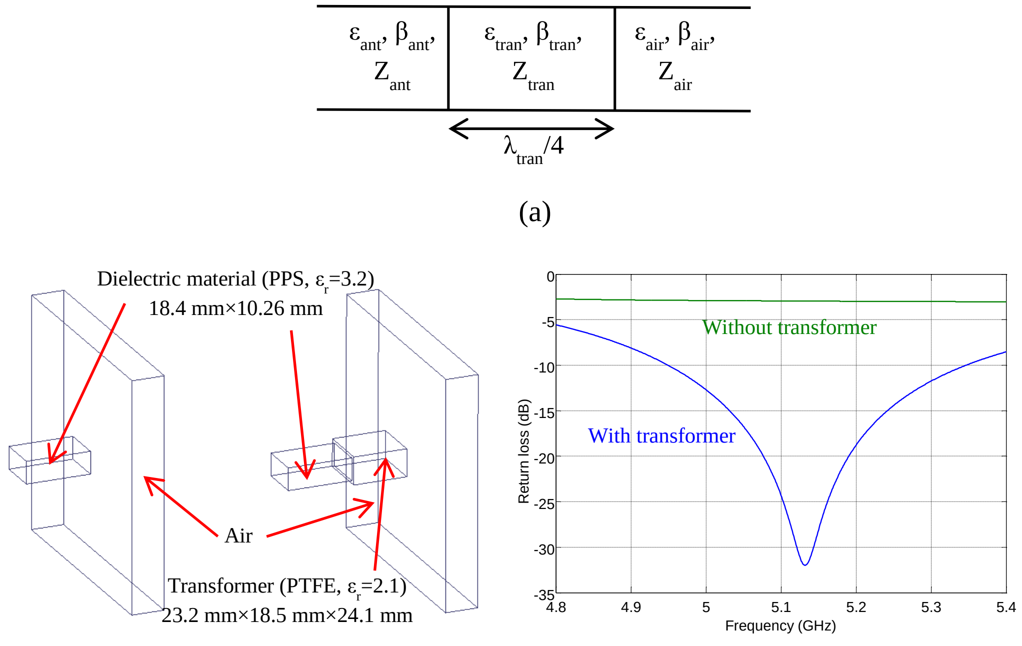

(a)

(b) (c)

Fig. 5.9 Transformer for the impedance matching (a) Schematic diagram (b) Configuration (c) Return loss.

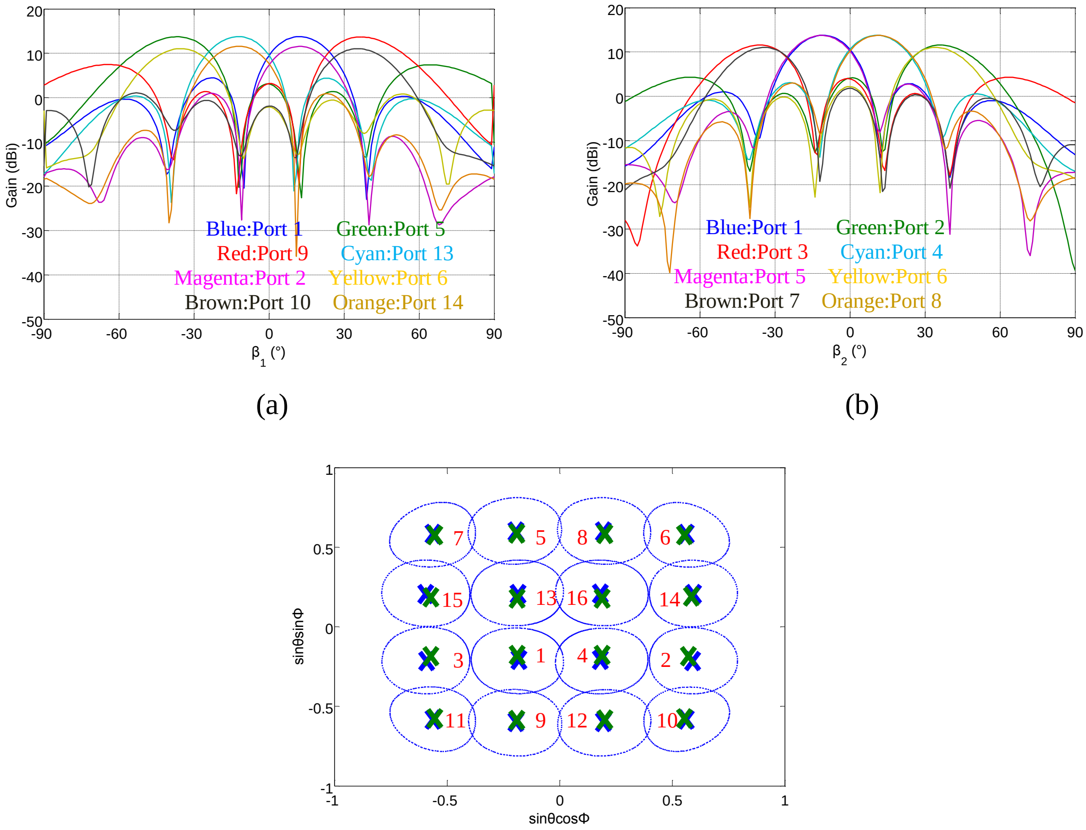

(a) (b)

(c)

Fig. 5.10 Radiation and gain patterns of dielectric-filled one-body $4^2\times4^2$-way 2-D beam-switching Butler matrix with couplers in chapter 3 (a) Quasi E-plane (b) Quasi H-plane (c) 3.9 dB-down contour gain patterns. The numbers and the symbol Xes indicate the input port number and the position of peak gain. Blue - Simulations, Green - Ideals.

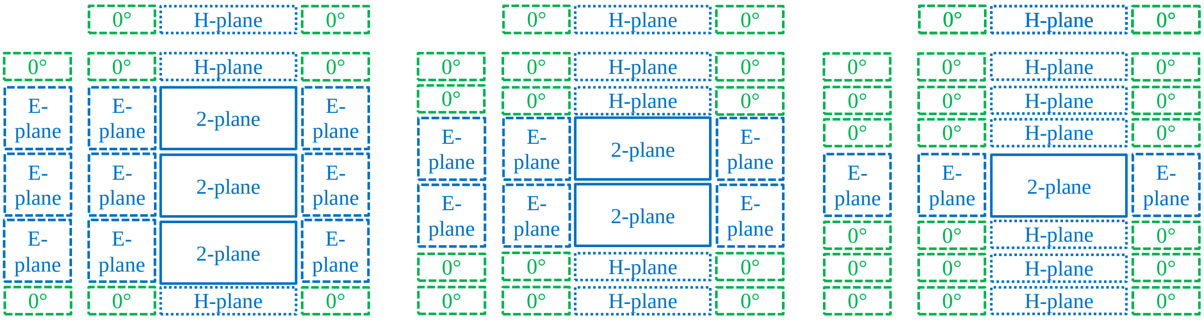

(a) (b) (c)

Fig. 5.11 Overlapped of cross coupler units of $8^2\times4^2$-way 2-D beam-switching Butler matrix. Unit of 4×4-way 1-D beam-switching Butler matrix with (a) 1st unit of 3rd stage (b) 2nd unit of 3rd stage (c) 3rd unit of 3rd stage of 8×8-way 1-D beam-switching Butler matrix.

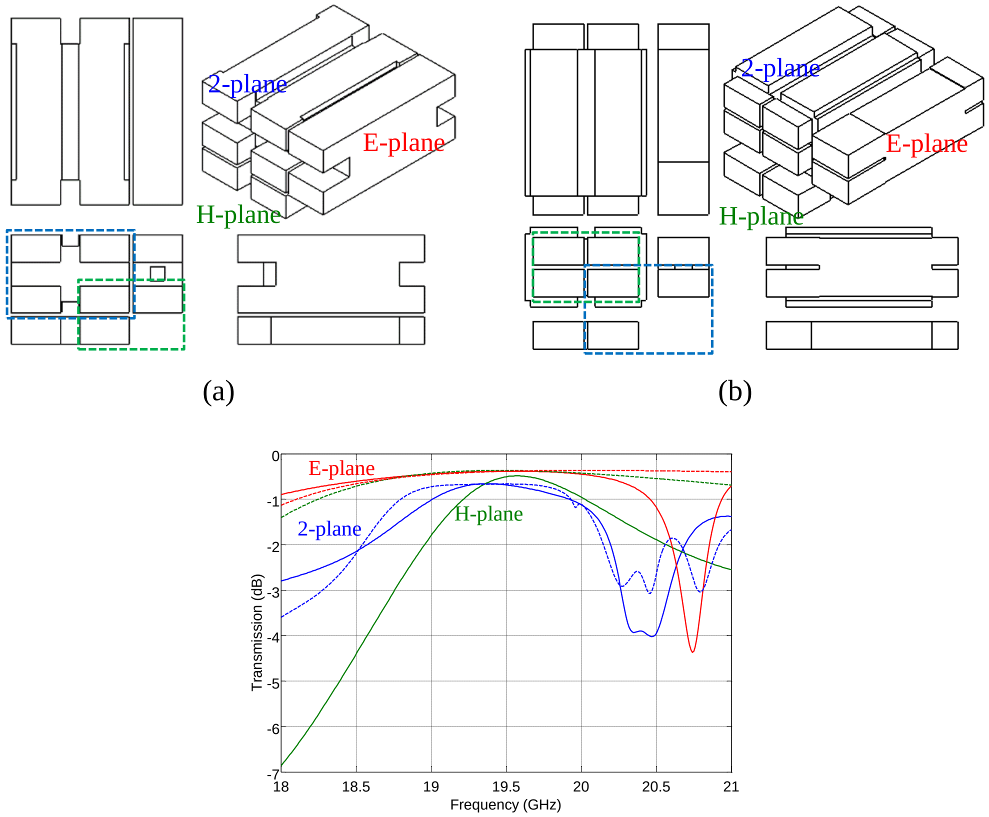

(a) (b)

(c)

Fig. 5.12 Cross couplers for large-scaled one-body 2-D beam-switching Butler matrix (a) ports separated far (b) ports separated near (c) Transmission coefficient. Solid lines: (a), Dashed lines: (b).

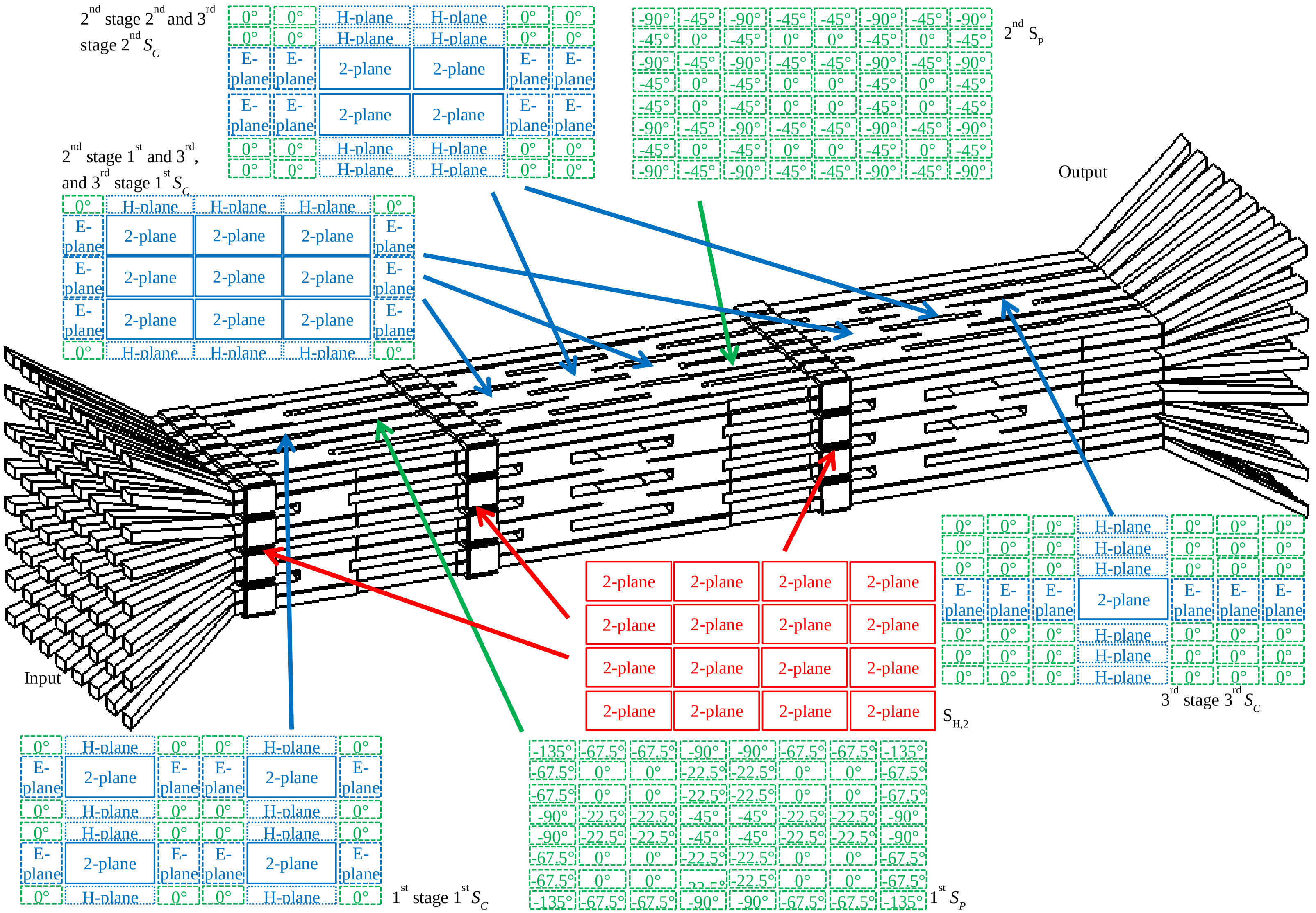

Fig. 5.13 One-body $8^2 \times 8^2$-way 2-D beam-switching Butler matrix.

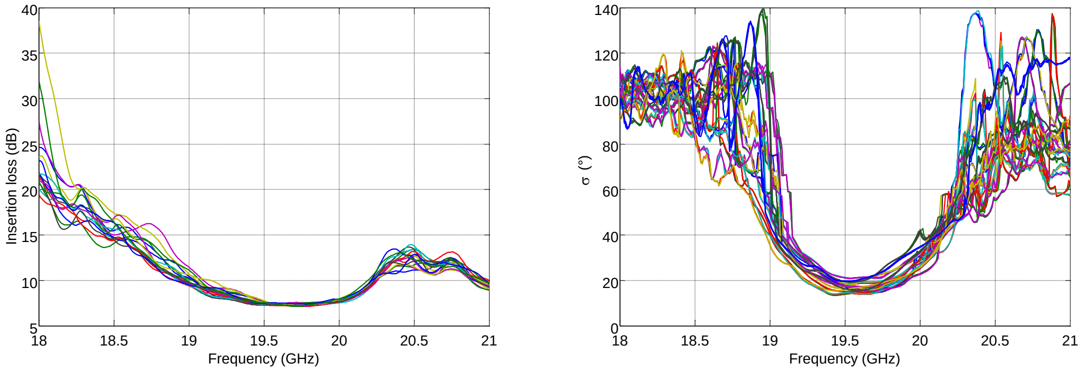

(a) (b)

Fig. 5.14 Processed parameters of dielectric-filled one-body $8^2\times8^2$-way 2-D beam-switching Butler matrix (a) Insertion loss (b) Deviation of the phase difference between the simulation and the ideal.

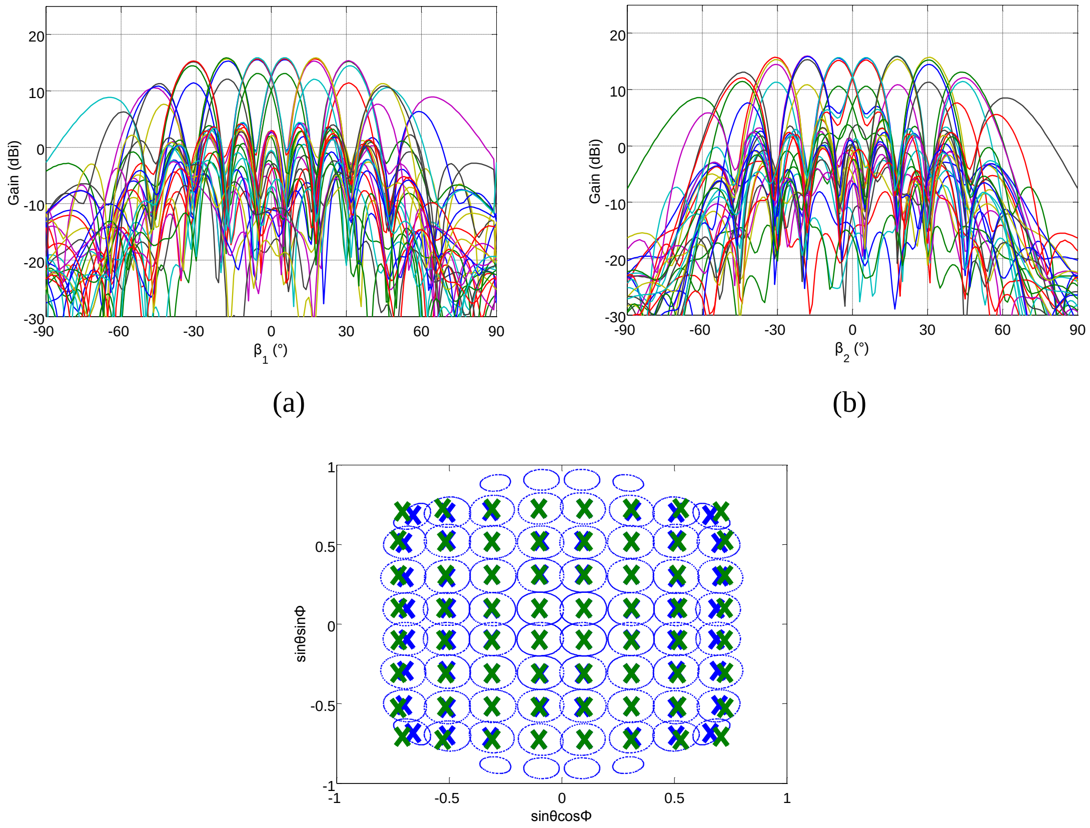

(a) (b)

(c)

Fig. 5.15 Radiation and gain patterns (a) Quasi E-plane (b) Quasi H-plane (c) 3.9 dB-down contour gain patterns. The numbers and the symbol Xes indicate the input port number and the position of peak gain. Blue - Simulations, Green - Ideals.

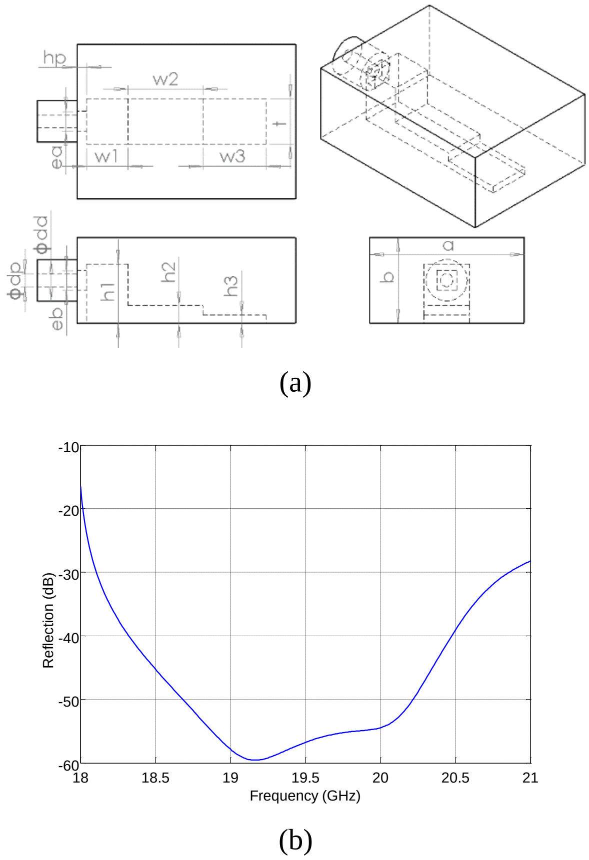

Fig. 5.16 Launcher (a) Drawing (b) Return loss.

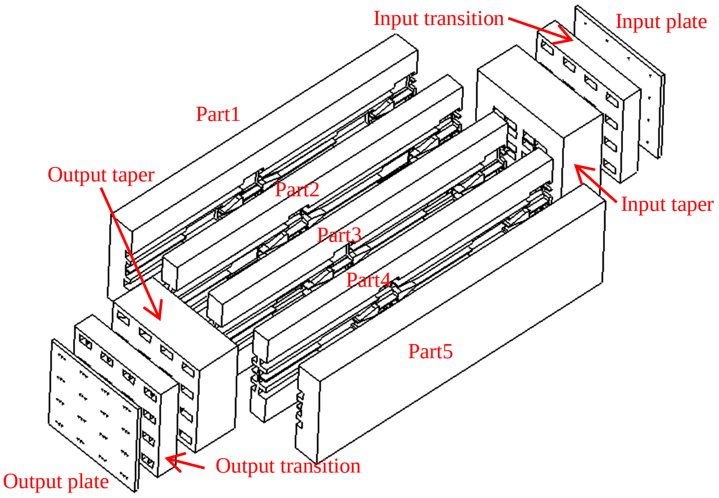

(a)

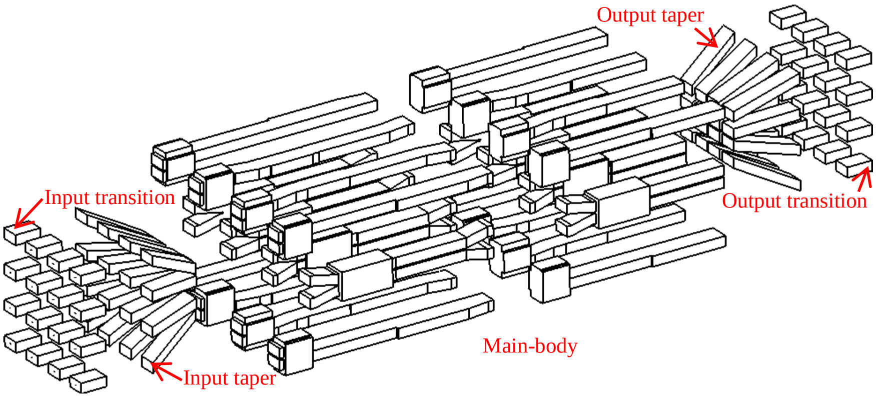

(b)

Fig. 5.17 Assembly view of dielectric-filled one-body $4^2 \times 4^2$-way 2-D beam-switching Butler matrix (a) Molding metal parts (b) Dielectric parts.

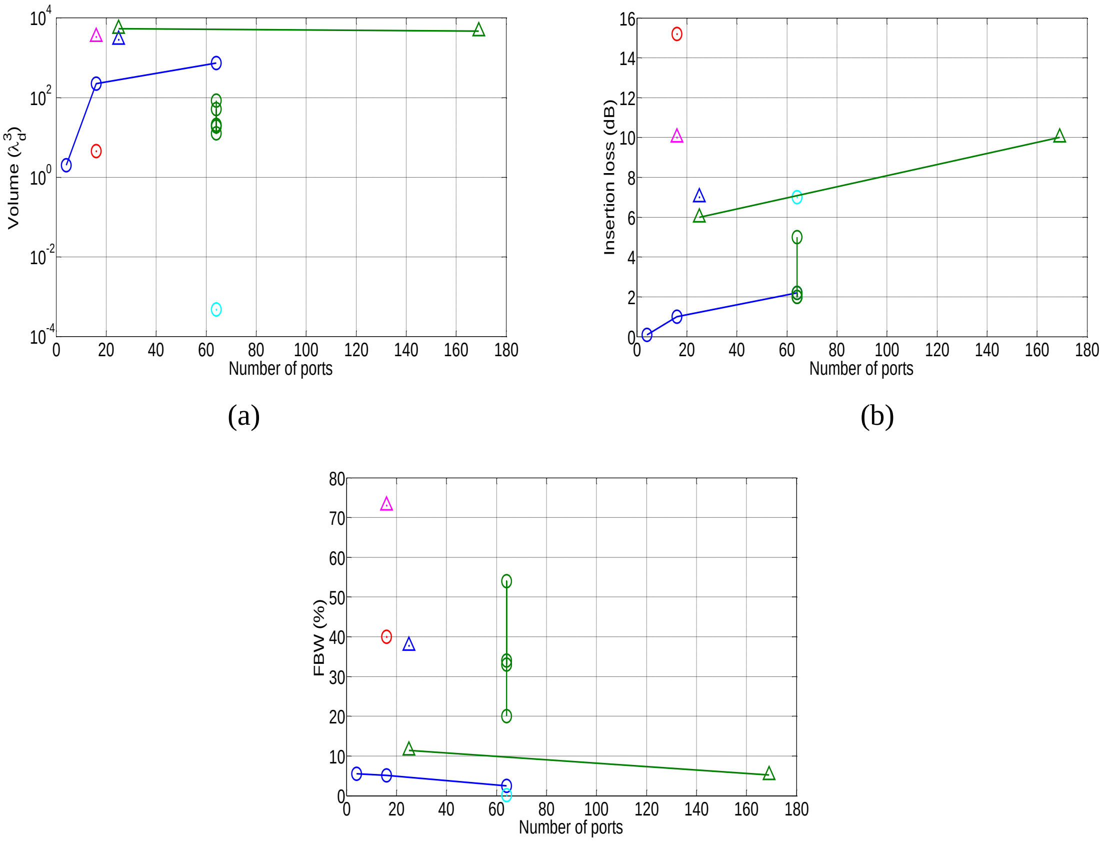

(a)

(b)

(c)

Fig. 5.18 Characteristics comparison between 2-D beam-switching circuits (a) Volume (b) Insertion loss (c) Fracture bandwidth. Circle: Butler matrix, Triangle: Rotman lens, Blue: hollow waveguide, Green: microstrip and stripline, Red: coplanar waveguide, Cyan: CMOS, Magenta: Surface micro-machining.

Table 5.1 Performances of hollow waveguide one-body $4^2 \times 4^2$-way 2-D beam-switching Butler matrix in 22 GHz.

Conducting wall	Brass
Volume (mm^3)	39.76×33.97×212.31
FBW (%)	5.8% (21.27~22.55 GHz)
Transmission (dB)	-13.7±4.6
1)Reflection (dB)	<-11.7
IL (dB)	<0.97
2)$\Delta\varphi$ (°)	<28.5

1)Include the isolation, 2)Deviation of phase difference between the simulation and the ideal

Table 5.2 Realized gains of hollow waveguide one-body $4^2 \times 4^2$-way 2-D beam-switching Butler matrix in 22 GHz.

Conducting wall	Brass
Port 1	18.6
Port 2	17.1
Port 3	17.1
Port 4	18.6
Port 5	15.3
Port 6	14.3
Port 7	14.4
Port 8	15.3
Port 9	15.4
Port 10	14.4
Port 11	14.4
Port 12	15.4
Port 13	18.5

Port 14	17.1
Port 15	17.1
Port 16	18.6

Table 5.3 Dimensions and output phase values of the phase compensators with the short-slot 2-plane coupler in Chapter 3 in 22 GHz.

Connected component	Side-wall stubs of 1)waveguide					
	Phase compensator alone			With phase shifter unit		
	Length (mm)	2)Width (mm)	3)Δφ (°)	Length (mm)	Width (mm)	Δφ (°)
E-plane	-	-	-213.4	31.5	-0.14	-167.9
H-plane	31.5	-0.17	-171.0		-0.24	-126.2
2-plane		+1.14	-13.2		+0.5	77.1
0° phase shifter	26	+1	0.0		+1.14	0.0

1)Size of apertures is 7.66×4.27 mm, except 8.10×4.57 mm for 2-plane

2)(+) and (-) indicate the extrusion from and the intrusion into the side-wall

3)Phase differences between 0° phase shifter and the others

Table 5.4 Performances of dielectric-filled waveguide one-body $4^2\times4^2$-way 2-D beam-switching Butler matrix in 5.12 GHz.

Dielectric loss / Conducting wall	Lossless / PEC	Lossy / Aluminum alloy
Volume (mm^3)	123.88×115.74×543.17	
FBW (%)	5.1% (5.00~5.26 GHz)	
Transmission (dB)	-14.2±3.2	-16.7±4.7
1)Reflection (dB)	<-8.8	<-10.3
IL (dB)	<1.03	<4.17
2)Δφ (°)	<27.8	<25.4

1)Include the isolation, 2)Deviation of phase difference between the simulation and the ideal

Table 5.5 Realized gains of dielectric-filled waveguide one-body $4^2\times4^2$-way 2-D beam-switching Butler matrix in 5.12 GHz.

Input port	Un-transformed (dBi)		Transformed (dBi)	
	Lossless	1)Lossy	Lossless	Lossy
1	13.8	10.6	17.2	14.3
2	11.6	8.4	15.0	12.1
3	11.6	8.4	15.0	12.1
4	13.8	10.6	17.2	14.3
5	13.7	10.6	15.7	12.8
6	11.0	7.8	13.3	10.5
7	11.0	7.8	13.3	10.5
8	13.7	10.6	15.7	12.8
9	13.7	10.6	15.7	12.8
10	11.0	7.8	13.3	10.5
11	11.0	7.8	13.3	10.5
12	13.7	10.6	15.7	12.8
13	13.8	10.6	17.2	14.3
14	11.6	8/4	15.0	12.2
15	11.6	8.4	15.0	12.2
16	13.8	10.6	17.2	14.3

1)Dielectric material with aluminum alloy conducting wall

Table 5.6 Beam-directions of dielectric-filled waveguide one-body $4^2\times4^2$-way 2-D beam-switching Butler matrix in 5.12 GHz.

Input port	1)Ideal (°)				Simulation (°)			
	E-plane		H-plane		E-plane		H-plane	
	β_1	α_1	β_2	α_2	β_1	α_1	β_2	α_2
1	12	-12	-12	-12	11	-11	-11	-11
2	12	40	39	-15	10	35	34	-13

3	12	-40	-39	-15	10	-35	-34	-13
4	12	12	12	-12	11	11	11	-11
5	-39	-15	-12	40	-35	-13	-11	36
6	-39	53	39	53	-34	41	33	42
7	-39	-53	-39	53	-34	-41	-33	42
8	-39	15	12	40	-35	13	11	36
9	39	-15	-12	-40	35	-13	-11	-36
10	39	53	39	-53	34	41	33	-42
11	39	-53	-39	-53	34	-41	-33	-42
12	39	15	12	-40	35	13	11	-36
13	-12	-12	-12	12	-11	-11	-11	11
14	-12	40	39	15	-10	35	34	13
15	-12	-40	-39	15	-10	-35	-34	13
16	-12	12	12	12	-11	11	11	11

1)Peak direction of array factor with ideal phase

Table 5.7 HPBWs of dielectric-filled waveguide one-body $4^2\times4^2$-way 2-D beam-switching Butler matrix in 5.12 GHz.

Input port	E-plane (°)	H-plane (°)
1	21	21
2	21	23
3	21	23
4	21	21
5	27	21
6	23	22
7	23	22
8	27	21

9	27	21
10	23	23
11	23	23
12	27	21
13	21	21
14	21	22
15	21	22
16	21	21

Table 5.8 Coverages of dielectric-filled waveguide one-body $4^2\times4^2$-way 2-D beam-switching Butler matrix in 5.12 GHz.

Input port	Coverage (sr)
1	0.17
2	0.17
3	0.17
4	0.17
5	0.17
6	0.20
7	0.20
8	0.17
9	0.17
10	0.20
11	0.20
12	0.17
13	0.17
14	0.17
15	0.17

16	0.17

Table 5.9 Performances of dielectric-filled waveguide one-body $8^2\times8^2$-way 2-D beam-switching Butler matrix in 19.55 GHz.

Dielectric loss / Conducting wall	Lossless / PEC	Lossy / aluminum alloy
Volume (mm^3)	69.41×67.21×291.78	
FBW (%)	2.6% (19.27~19.77GHz)	
Transmission (dB)	-26.1±13.1	-29.9±10.1
1)Reflection (dB)	<-8.9	<-10.7
IL (dB)	<2.31	<9.12
2)$\Delta\varphi$ (°)	<32.0	<30.0

1)Include the isolation, 2)Deviation of phase difference between the simulation and the ideal

Table 5.10 Realized gains of dielectric-filled waveguide one-body $8^2\times8^2$-way 2-D beam-switching Butler matrix in 19.55 GHz.

Input port	Lossy / aluminum alloy (dBi)
1, 8, 57, 64	15.6
2, 7, 58, 63	13.1
3, 6, 59, 62	15.7
4, 5, 60, 61	15.9
9, 16, 49, 56	10.6
10, 15, 50, 55	7.6
11, 14, 51, 54	11.3
12, 13, 52, 53	10.9
17, 24, 41, 48	15.2
18, 23, 42, 47	11.4
19, 22, 43, 46	14.5
20, 21, 44, 45	15.3

25, 32, 33, 40	15.7
26, 31, 34, 39	12.1
27, 30, 35, 38	15.3
28, 29, 36, 37	15.9

Table 5.11 Beam-directions of dielectric-filled waveguide one-body $8^2 \times 8^2$-way 2-D beam-switching Butler matrix in 19.55 GHz.

Input port	1)Ideal (°)				Simulation (°)			
	E-plane		H-plane		E-plane		H-plane	
	β_1	α_1	β_2	α_2	β_1	α_1	β_2	α_2
1	6	-6	-6	-6	6	-6	-6	-6
2	6	47	46	-8	6	44	43	-8
3	6	-32	-31	-7	6	-31	-30	-7
4	6	18	18	-6	5	18	18	-6
9	-46	-8	-6	47	-46	-8	-6	47
10	-45	90	45	90	-43	65	41	66
11	-47	-50	-32	59	-44	-46	-31	54
12	-46	27	18	50	-45	27	18	48
17	31	-7	-6	-32	31	-6	-5	-32
18	32	59	47	-50	31	54	44	-46
19	31	-37	-31	-37	32	-37	-31	-38
20	31	21	18	-33	31	21	18	-33
25	-18	-6	-6	18	-18	-6	-5	18
26	-18	50	46	27	-17	48	45	25
27	-18	-33	-31	21	-17	-32	-31	20
28	-18	19	18	19	-18	19	18	19

1)Peak direction of array factor with ideal phase

Table 5.12 HPBWs of dielectric-filled waveguide one-body $8^2 \times 8^2$-way 2-D beam-switching Butler matrix in 19.55 GHz.

Input port	E-plane (°)	H-plane (°)
1, 8, 57, 64	10	11
2, 7, 58, 63	10	13
3, 6, 59, 62	10	12
4, 5, 60, 61	10	11
9, 16, 49, 56	14	10
10, 15, 50, 55	9	10
11, 14, 51, 54	11	11
12, 13, 52, 53	13	10
17, 24, 41, 48	11	11
18, 23, 42, 47	11	12
19, 22, 43, 46	11	11
20, 21, 44, 45	11	11
25, 32, 33, 40	10	11
26, 31, 34, 39	10	13
27, 30, 35, 38	11	11
28, 29, 36, 37	10	11

Table 5.13 Coverages of dielectric-filled waveguide one-body $8^2 \times 8^2$-way 2-D beam-switching Butler matrix in 19.55 GHz.

Input port	Coverage (csr)
1, 8, 57, 64	3.51
2, 7, 58, 63	4.64
3, 6, 59, 62	4.05

4, 5, 60, 61	3.64
9, 16, 49, 56	4.66
10, 15, 50, 55	6.75
11, 14, 51, 54	6.57
12, 13, 52, 53	5.05
17, 24, 41, 48	4.00
18, 23, 42, 47	6.37
19, 22, 43, 46	5.06
20, 21, 44, 45	4.31
25, 32, 33, 40	3.70
26, 31, 34, 39	5.29
27, 30, 35, 38	4.32
28, 29, 36, 37	3.86

Table 5.14 Design parameters of launchers. Unit: mm.

Type	h_1	h_2	h_3	w_1	w_2	w_3	d_p	h_p	d_d	t	e_a	e_b
19.55 GHz	1.7	0.62	0.3	0.57	2.42	1.48	0.64	1	2.1	1	-	-

Table 5.15 Comparison between Butler matrices

Type	a×b×c	IL (dB)	T (dB)	Γ (dB)	Δ (°)	FBW (%)@f_0	Ref.
1)HW 4×4	1.38×0.92×1.44 λ_0^3	<0.1	-6.1±0.5	<-18.4	±2.4	2.3@22.1 GHz	Ch.2
HW 4×4	1.40×0.98×1.48 λ_0^3	<0.1	-6.1±0.5	<-16.0	±5	5.5@22 GHz	Ch.3
HW 16×16	3.45×3.45×14.02 λ_0^3	<1.0	-13.0±2.9	<-13.6	<23.8	2.5@19.6 GHz	Ch.4
DW 16×16	3.79×3.54×16.62 λ_r^3	<4.2	-16.7±4.7	<-10.3	<25.4	5.1@5.1 GHz	Ch.5
HW 64×64	5.09×5.63×25.83 λ_0^3	<2.2	-33.7±21.0	<-7.5	<43.4	2.5@19.6 GHz	Ch.5
2)SIW 4×4	-	7)<1.4	-7.2±0.6	<-20	±5.0	5.0@59.5 GHz	[5.1]
SIW 4×4	-	<0.7	-	<-20	±7	11.8@76.5 GHz	[5.2]
3)CPW 4×4	1.36×1.24 λ_r^2	<7.6	±1.6	-	±13.6	40@2.5 GHz	[5.3]

4)MS 4×4	-	<0.5	-	<-17	-	13.3@60 GHz	[5.4]
MS 8×8	3.47×3.47 λ_r^2	<2.5	±1.5	<-10	±12	20@4.2 GHz	[5.5]
MS 8×8	2.41×1.65 λ_r^2	<1	±0.5	<-15	±7.5	34@1.9 GHz	[5.6]
5)SL 8×8	2.16×1.35 λ_r^2	<1.1	±1.5	-	±31	54@2.2 GHz	[5.7]
SL 8×8	216×216 mm^2	<7	±1.5	<-8.5	±16	160@10 GHz	[5.8]
SL 8×8	2.39×1.84 λ_r^2	<1	±0.45	<-20	±7.5	33@3 GHz	[5.9]
SL 8×8	3.13×2.67 λ_r^2	<1	±0.5	<-20	±10	33@3 GHz	[5.10]
6)CMOS 8×8	0.93×1.45 mm^2	<3.1	±2.5	<-14	±22	16.6@60 GHz	[5.11]
CMOS 8×8	0.068×0.052 λ_r^2	<3.5	-	<-10	-	0.18@5.5 GHz	[5.12]
CMOS 4×4	0.024×0.037 λ_r^2	<9.0	-	<-16.7	±6.4	8.3@2.4 GHz	[5.13]
CMOS 4×4	1.21×1.25 mm^2	<4.5	±1.5	<-20	±4	8.3@2.4 GHz	[5.14]

1)Hollow waveguide, 2)Substrate Integrated Waveguide, 3)Co-Planar Waveguide, 4)Microstrip Line, 5)StripLine, 6)Complimentary Metal Oxide Semiconductor, 7)59.2 GHz

Table 5.16 Comparison between Rotman lenses

Type	*a*×*b*	IL (dB)	FBW (%)@f₀	Ref.
1)HW 2)5×3)6	12×10 λ_0^2	<3.5	37.8@92.5 GHz	[5.15]
4)LTCC 3×5	10.6×5.8 λ_r^2	7)<1.7	6.7@60 GHz	[5.16]
5)MS 5×7	14.0×13.7 λ_r^2	<3	11.4@61.5 GHz	[5.17]
MS 3×5	4×3 λ_0^2	<5@60 GHz	16.7@60 GHz	[5.18]
MS 13×9	13.3×13.3 λ_r^2	<5	5.2@76.5 GHz	[5.19]
6)SMM 4×5	13.14×9.7 λ_0^2	<5	73.1@102.5 GHz	[5.20]

1)Hollow waveguide, 2)Beam ports, 3)Array ports, 4)Low Temperature Co-fired Ceramic, 5)Microstrip, 6)Surface Micro-machining, 7)Delay line only

Reference

[5.1] F. F. He, K. Wu, W. Hong, L. Han, X. P. Chen, "Low-cost 60-GHz smart antenna receiver subsystem based on substrate integrated waveguide technology", *IEEE Trans. Microw. Theory Tech.*, vol. 60, no. 4, pp. 1156-1164, Apr. 2012.

[5.2] T. Djerafi and K. Wu, "A Low-Cost Wideband 77-GHz Planar Butler Matrix in SIW Technology," *IEEE Trans. Antennas Propag.*, vol. 60, no. 10, pp. 4949-4954, Oct. 2012.

[5.3] W. Y. Chen, Y. R. Hsieh, C. C. Tsai, Y. M. Chen, C. C. Chang and S. F. Chang, "A compact two-dimensional phased array using grounded coplanar-waveguides butler matrices," *2012 42nd European Microwave Conference*, Amsterdam, 2012, pp. 747-750.

[5.4] C. E. Patterson, W. T. Khan, G. E. Ponchak, G. S. May and J. Papapolymerou, "A 60-GHz Active Receiving Switched-Beam Antenna Array With Integrated Butler Matrix and GaAs Amplifiers," *IEEE Trans. Microw. Theory Techn.*, vol. 60, no. 11, pp. 3599-3607, Nov. 2012.

[5.5] K. Ding, F. He, X. Ying, and J. Guan, “A compact 8 ×8 Butler matrix based on double-layer structure,” in *Proc. IEEE 5th Int. Symp. Microw., Antenna, Propag. EMC Technol. Wireless Commun. (MAPE),* Oct. 2013, pp. 650–653.

[5.6] R. D. Cerna and M. A. Yarlequé, “Design and implementation of a wideband 8×8 Butler matrix for AWS and PCS 1900 MHz beamforming networks,” in *Proc. IEEE Int. Wireless Symp. (IWS)*, Mar./Apr. 2015, pp. 1–4.

[5.7] C.-C. Chang, R.-H. Lee, and T.-Y. Shih, “Design of a beam switching/steering Butler matrix for phased array system,” *IEEE Trans. Antennas Propag.*, vol. 58, no. 2, pp. 367–374, Feb. 2010.

[5.8] R. A. De Lillo, “A high performance 8-input, 8-output Butler matrix beamforming network for ultra-broadband applications,” in *IEEE Antennas Propag. Int. Symp. Dig.*, vol. 1, Jun. 1993, pp. 474–477.

[5.9] K. Wincza, S. Gruszczynski, and K. Sachse, “Broadband planar fully integrated 8 × 8 Butler matrix using coupled-line directional couplers,” *IEEE Trans. Microw. Theory Techn.*, vol. 59, no. 10, pp. 2441–2446, Oct. 2011.

[5.10] K. Wincza and S. Gruszczynski, “Broadband Integrated 8 × 8 Butler Matrix Utilizing Quadrature Couplers and Schiffman Phase Shifters for Multibeam Antennas With Broadside Beam,” *IEEE Trans. Microw. Theory Techn.*, vol. 64, no. 8, pp. 2596–2604, Aug. 2016.

[5.11] T.-Y. Chin, J.-C. Wu, S.-F. Chang, and C.-C. Chang, “A V-band 8×8 CMOS Butler matrix MMIC,” *IEEE Trans. Microw. Theory Techn.*, vol. 58, no. 12, pp. 3538–3546, Dec. 2010.

[5.12] B. Cetinoneri, Y. A. Atesal, and G. M. Rebeiz, “An 8×8 Butler matrix in 0.13-μm CMOS for 5–6-GHz multibeam applications,” *IEEE Trans. Microw. Theory Techn.*, vol. 59, no. 2, pp. 295–301, Feb. 2011.

[5.13] W. T. Fang and Y. S. Lin, "Highly Integrated Switched Beamformer Module for 2.4-GHz Wireless Transceiver Application," *IEEE Trans. Microw. Theory Techn.*, vol. 64, no. 9, pp. 2933-2942, Sept. 2016.

[5.14] C. C. Chang, T. Y. Chin, J. C. Wu and S. F. Chang, "Novel Design of a 2.5-GHz Fully Integrated CMOS Butler Matrix for Smart-Antenna Systems," *IEEE Trans. Microw. Theory Techn.*, vol. 56, no. 8, pp. 1757-1763, Aug. 2008.

[5.15] H. H. Fuchs and D. Nubler, “A Rotman lens at W-band,” *Frequenz*, vol. 56, no. 11, pp. 244–248, Nov. 2002.

[5.16] I. S. Song et al., “60 GHz Rotman lens and new compact low loss delay line using LTCC technology,” in *Proc. IEEE Radio Wireless Symp.*, Jan. 2009, pp. 663–666.

[5.17] W. Lee, J. Kim, C. S. Cho, and Y. J. Yoon, “Beamforming lens antenna on a high resistivity silicon wafer for 60 GHz WPAN,” *IEEE Trans. Antennas Propag.*, vol. 58, no. 3, pp. 706–713, Mar. 2010.

[5.18] J. Lee et al., “Development of a V band Rotman lens using thin-film dielectric,” in *Proc. IEEE APS Int. Symp.*, Jun. 2007, pp. 2670–2673.

[5.19] J. Dong and A. I. Zaghloul, “Extremely high-frequency beam steerable lens-fed antenna for vehicular sensor applications,” *IET Microw. Antennas Propag.*, vol. 4, no. 10, pp. 1549–1558, Oct. 2010.

[5.20] N. Jastram, D. S. Filipovic, "Design of a wideband millimeter wave micromachined Rotman lens", *IEEE Trans. Antennas Propag.*, vol. 63, no. 6, pp. 2790-2796, Jun. 2015.

Chapter 6

Conclusion

6.1 Summary of preceding chapters

One-body 2-D beam-switching Butler matrices and its main components, short-slot 2-plane couplers, are proposed.

Chapter 1 has discussed the fundamental background and the outline of 2-D beam-switching circuit.

Chapter 2 has presented the theory of the short-slot 2-plane coupler and the considerations of its design and fabrication. The following results are investigated and acquired.

5. Four modes (TE_{10}, TE_{20}, TM_{11}, and TM_{21}) are chosen as the selected propagating modes which have two-dimensionally orthogonal polarities of electric field distribution each other in the coupled region of the short-slot 2-plane coupler.
6. To acquire four orthogonal outputs (=eigenvectors), the four selected propagating modes have same the coupling coefficient and the different propagation constants which satisfy $\beta_{\mathrm{TE}_{20}} = \beta_{\mathrm{TM}_{11}} = \frac{\beta_{\mathrm{TE}_{10}}+\beta_{\mathrm{TM}_{21}}}{2}$.
7. The width of the rectangular waveguide is selected to make TE_{30} mode as evanescent mode.
8. Double ridge is inserted into the rectangular waveguide, and its width and height are selected to satisfy ‘2.’
9. The outermost vertices of the double ridge rectangular waveguide are trimmed and its width and height are selected to make TE_{21} mode as evanescent modes.
10. Select the length of the coupled region to work the short-slot 2-plane coupler as hybrid (four outputs have same amplitude, but different phases) and cross (single output which is two-dimensionally across the excited input port only) coupler.
11. The size and the position of input and output port branches are selected to optimize the balance of the outputs.
12. Single short-slot (hybrid or cross) 2-plane coupler substitutes a 4×4-way short-slot combined coupler which consists of short-slot two E- and two H-plane (hybrid or cross) couplers. Especially, the short-slot 2-plane hybrid coupler works as $2^2 \times 2^2$-way 2-D beam-switching Butler matrix. The volume of the coupled region of the short-slot 2-plane coupler is a half of 4×4-way short-slot combined coupler’s.
13. The operating frequency band of the short-slot 2-plane coupler is restricted by the

frequency characteristic of the four selected propagating modes. In that reason, it has narrow operating frequency band in comparison with the short-slot E- and H-plane couplers.

14. The short-slot 2-plane hybrid and cross couplers made of brass is simulated, fabricated, and evaluated.

Chapter 3 has proposed the wideband short-slot 2-plane coupler and the considerations of its design and fabrication. The following results are investigated and acquired.

1. Among the propagating modes excluded the selected propagating modes, TE_{11}, TE_{21}, and TE_{30} modes (called the complementary modes) which have same (TE_{11}/TM_{11}, TE_{21}/TM_{21}) and quasi (TE_{10}/TE_{30}) polarities of electric field distribution affect the output of the short-slot 2-plane coupler.
2. The propagating modes which possess same or quasi polarities can be merged as the combined mode.
3. The flatness of the coupling coefficients and the phases of the propagating and the combined modes affect the operating frequency band. Although the outputs of the short-slot 2-plane coupler in Chapter 2 converge to a balanced amplitude (-6 dB) at center frequency, the deviation of its outputs is increased because of the inflection points of the coupling coefficients of the propagating and the combined modes.
4. Design parameters of the coupled region are selected to shift the inflection points of the coupling coefficients of the propagating and the combined modes toward low frequency. Its operating frequency band is increased more than twice than Chapter 2’s without unnecessary volume increment.
5. The loss in the short-slot 2-plane coupler affects differently the coupling coefficients of the propagating modes in the frequency. Considering the electrical characteristics of the existing conductors and dielectric materials, the main parameter is the loss tangent.
6. The dielectric-filled short-slot 2-plane hybrid and cross couplers made of PPS covered with aluminum alloy are simulated, fabricated, and evaluated.

Chapter 4 has proposed the one-body 2-D beam-switching Butler matrix and the considerations of its design and fabrication. The following results are investigated and acquired.

1. Orthogonally (horizontally and vertically) stacked hybrid, cross, and phase shifter units are commutative. It indicates that the arrangement of two neighbored orthogonally stacked units can be switched, physically.
2. Two orthogonally stacked same type units are overlapped to single unit. Overlapped short-slot two E- and two H-plane (hybrid or cross) coupler components are substituted a short-slot 2-plane (hybrid or cross) coupler. Un-overlapped short-slot E- and H-plane

(hybrid or cross) coupler components are maintained their own things.

3. The cross coupler unit of the one-body 2-D beam-switching Butler matrix consists of 0° phase shifter, short-slot E-, H-, and 2-plane cross coupler components. Because those components have different output phases in the same length, the phase compensator unit should be attached to remove these phase differences. The phase compensator unit can be merged to neighbored phase shifter unit, except last phase compensator unit. Thus additional volume increment caused by the phase compensator is restricted single unit.
4. The number of units of Butler matrix is proportional to the length of Butler matrix. Compare one-body 2-D beam-switching Butler matrix with conventional thing, its length can be reduced a half of conventional thing, minimally. In view of the volume of the 2-D beam-switching Butler matrix, it is also exactly same its length relationship.
5. The one-body $4^2 \times 4^2$-way 2-D beam-switching Butler matrices made of brass, aluminum ally, and copper plated ABS-like are simulated, fabricated, and evaluated.

Chapter 5 has proposed the wideband and the large-scaled one-body 2-D beam-switching Butler matrices and the considerations of those design and fabrication. The following results are investigated and acquired.

1. One-body 2-D beam-switching Butler matrix is inherited the frequency characteristics from the wideband short-slot 2-plane coupler's.
2. When the input and output ports of the large-scaled one-body 2-D beam-switching Butler matrix are not arranged a square ($n_1 \neq n_2$), several overlapping unit options are given to reduce the imbalance of the outputs.
3. The one-body $4^2 \times 4^2$-way and $8^2 \times 8^2$-way 2-D beam-switching Butler matrices made of PPS covered with aluminum alloy are simulated and evaluated.

6.2 Remarks for future studies

The remarks for future investigation are listed below.

1. Comparison the short-slot 2-plane coupler with short-slot E- and H-plane couplers, its weakness is its narrow operating frequency band. The linearity of amplitudes and phases of propagating modes in the coupled region of the short-slot 2-plane coupler can be improved by additional geometric parameters such as corrugated stub or wall.
2. Dominant volume occupancy of the one-body 2-D beam-switching Butler matrix is the cross coupler stages. Considering the purpose of the cross coupler stages which shuffle and connect 4^{i-1} ith hybrid coupler unit outputs to 4^i i+1th hybrid coupler unit inputs,

those are just one-to-one correspondence. If the volume of a transmission line can be alternated such as a coaxial line, the required volume for those connections is drastically reduced in the large-scaled one-body 2-D beam-switching Butler matrix.

3. In the high power purpose such as radar and base station, the hollow waveguide structure is required. The weight of the one-body 2-D beam-switching Butler matrix is proportional to its volume and the specific gravity of conductor material. Best solution to minimize the weight is light-weight dielectric material covered with metal plating. However the surface roughness of hollow waveguide structure fabricated by existing 3-D printing is too large and the plating metal is easily oxidized (make the leakage and lower electrical conductivity), the insertion loss is larger than the simulation result. In the future, the fabrication method and materials should be investigated to satisfy low surface roughness and specific gravity, high electrical and thermal conductivity.
4. If the selected application is not required to deal with high power and low loss, dielectric-filled waveguide is a good solution to reduce the volume of the one-body 2-D beam-switching Butler matrix. However existing plating techniques cannot plate narrow surface into the inside of the complex structure, the dielectric structure should be divided into several parts, and then be separately plated. It generates the multiple reflections between connected dielectric parts, and increases the insertion loss. In the future, the fabrication method and materials should be investigated to fabricate single-body structure with metal plating.
5. Most powerful function of beam-switching Butler matrix is the spatial orthogonality to the input and the output. In communication and radar, it can be worked as $N \times M$ MIMO system and N-sector monitoring system, respectively. Basic premise of those works is keeping orthogonality between Tx and Rx signals (full duplex) during the operation, but it is required additional signal process units. Using passive components such as the isolator, the combiner and the divider, the system burden can be reduced.

Appendix

A.1 Matrix commutativity

The simultaneously diagonalizable multiple matrices are always commutative.

$$AB = U\Lambda_A U^{-1} U\Lambda_B U^{-1} = U\Lambda_A\Lambda_B U^{-1} = U\Lambda_B\Lambda_A U^{-1} = U\Lambda_B U^{-1} U\Lambda_A U^{-1} = BA \quad \text{(A.1.1)}$$

where U is a matrix that columns are the basis of eigenvectors, Λ_i is a diagonal matrix of i.

Even if one of matrices is not simultaneously diagonalizable, its product is always not commutative.

$$A\Lambda_C B = U\Lambda_A U^{-1}\Lambda_C U\Lambda_B U^{-1} = U\Lambda_A C\Lambda_B U^{-1} \quad \text{(A.1.2)}$$

$$\Lambda_A C\Lambda_B \neq C\Lambda_A\Lambda_B \neq \Lambda_A\Lambda_B C \quad \text{(A.1.3)}$$

A.2 Coordinate transformation

Considering the configuration of far-field measurement as shown in Fig. 2.18(a), the beam-direction expressed by spherical coordinates can be transformed the modified planes for quasi E-plane (x-z plane) and quasi H-plane (y-z plane).

$$x = r\sin\theta\cos\phi \quad \text{(A.2.4)}$$

$$y = r\sin\theta\sin\phi \quad \text{(A.2.5)}$$

$$z = r\cos\theta \quad \text{(A.2.6)}$$

$$\alpha_1 = \tan^{-1}\frac{x}{z} \quad \text{(A.2.4)}$$

$$\beta_1 = \tan^{-1}\frac{-y}{\sqrt{x^2+z^2}} \quad \text{(A.2.8)}$$

$$\alpha_2 = \tan^{-1}\frac{y}{z} \quad \text{(A.2.9)}$$

$$\beta_2 = \tan^{-1}\frac{x}{\sqrt{y^2+z^2}} \quad \text{(A.2.10)}$$

A.3 RLL (Reflect-Line-Line) calibration

RLL calibration is one of one-port calibration and is required three equations for three unknowns (I_{11}, I_{12}, and I_{22}) when the de-embedded device is reciprocal (I_{12}=I_{21}) as shown in Fig. A.3.1. Measured S-parameters for *R*eflect (short)-*RL*ine (short with l_1)-*RLL*ine (short with l_2) are expressed as

$$S_{11,type} = I_{11} + \frac{I_{12}^2\Gamma_{type}}{1-I_{22}\Gamma_{type}} \quad \text{(A.3.1)}$$

where *type* is *R*, *RL*, or *RLL*, Γ is a reflection coefficient.

Using three equations, S-parameters of the transition are derived as

$$I_{12}^2 = \frac{S_{11,R}-I_{11}}{\Gamma_R} + I_{22}\left(I_{11} - S_{11,R}\right) \tag{A.3.2}$$

$$I_{22} = \frac{\Gamma_{LR}\left(I_{11}-S_{11,R}\right)-\Gamma_R\left(I_{11}-S_{11,LR}\right)}{\Gamma_R\Gamma_{LR}\left(S_{11,LR}-S_{11,R}\right)} \tag{A.3.3}$$

$$I_{11} = \frac{\Gamma_R S_{11,LLR}-\Gamma_{LLR}S_{11,R}+\frac{\Gamma_{LLR}\left(S_{11,LLR}-S_{11,R}\right)}{\Gamma_{LR}\left(S_{11,LR}-S_{11,R}\right)}\left(\Gamma_{LR}S_{11,R}-\Gamma_R S_{11,LR}\right)}{\Gamma_R-\Gamma_{LLR}+\frac{\Gamma_{LLR}\left(S_{11,LLR}-S_{11,R}\right)}{\Gamma_{LR}\left(S_{11,LR}-S_{11,R}\right)}\left(\Gamma_{LR}-\Gamma_R\right)} \tag{A.3.4}$$

The characteristic of two transitions connected to the short-slot 2-plane coupler is able to de-embed.

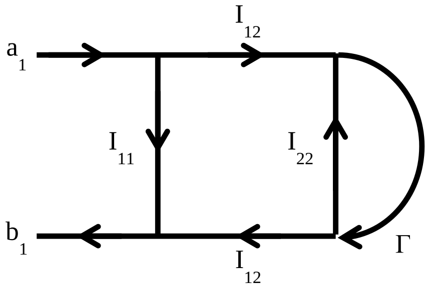

Fig. A.3.1 Signal flow graph of RLL.

A.4 L'Huilier's theorem

For calculating the area of arbitrary surface on the sphere, the arbitrary surface is divided into multiple spherical triangles which share a vertex as shown in Fig. A.4.1.

L'Huilier's Theorem gives the spherical excess E_{ij} of spherical triangle in terms of its three sides a_{ij}, b_{ij}, and c_{ij} where subscripts i and j indicate jth triangle of ith input port.

$$tan\left(\frac{E_{ij}}{4}\right) = \sqrt{tan\left(\frac{s_{ij}}{2}\right)tan\left(\frac{s_{ij}-a_{ij}}{2}\right)tan\left(\frac{s_{ij}-b_{ij}}{2}\right)tan\left(\frac{s_{ij}-c_{ij}}{2}\right)} \tag{A.4.1}$$

$$a_{ij} = cos^{-1}\frac{\overrightarrow{r_o}\cdot\overrightarrow{r_{ij}}}{|\overrightarrow{r_o}||\overrightarrow{r_{ij}}|} \tag{A.4.2}$$

$$b_{ij} = cos^{-1}\frac{\overrightarrow{r_o}\cdot\overrightarrow{r_{ij+1}}}{|\overrightarrow{r_o}||\overrightarrow{r_{ij+1}}|} \tag{A.4.3}$$

$$c_{ij} = cos^{-1}\frac{\overrightarrow{r_{ij}}\cdot\overrightarrow{r_{ij+1}}}{|\overrightarrow{r_{ij}}||\overrightarrow{r_{ij+1}}|} \tag{A.4.4}$$

$$s_{ij} = \frac{a_{ij}+b_{ij}+c_{ij}}{2} \tag{A.4.5}$$

$$R = |\overrightarrow{r_o}| = \left|\overrightarrow{r_{ij}}\right| = \left|\overrightarrow{r_{ij+1}}\right| \tag{A.4.6}$$

$$A_{ij}=E_{ij}R^2 \tag{A.4.7}$$

$$A = \sum_{j=1}^{N}\sum_{i=1}^{N_j}A_{ij} \tag{A.4.8}$$

$$\Omega = \frac{A}{R^2} = E \tag{A.4.9}$$

where R is a radius of the sphere, Ω is a solid angle of an arbitrary surface on the sphere.

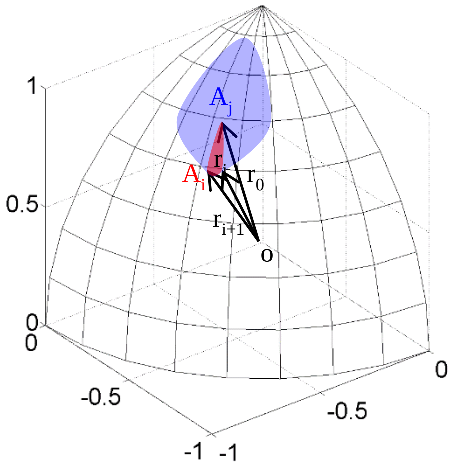

Fig. A.4.1 An arbitrary surface on the sphere.

A.5 TRL (Thru-Reflect-Line) calibration

TRL calibration is one of two-port calibration and is required eight equations for eight unknowns (I_{11}, I_{12}, I_{22}, O_{11}, O_{12}, O_{22}, Γ, and X) when the de-embedded device is reciprocal (I_{12}=I_{21}, O_{12}=O_{21}) as shown in Fig. A.5.1. Measured S-parameters are expressed as

$$S_{11,T} = I_{11} + \frac{O_{22}I_{12}^2}{1-I_{22}O_{22}} \tag{A.5.1}$$

$$S_{22,T} = O_{11} + \frac{I_{22}O_{12}^2}{1-I_{22}O_{22}} \tag{A.5.2}$$

$$S_{21,T} = S_{12,T} = \frac{I_{12}O_{12}}{1-I_{22}O_{22}} \tag{A.5.3}$$

$$S_{11,R} = I_{11} + \frac{I_{12}^2\Gamma}{1-I_{22}\Gamma} \tag{A.5.4}$$

$$S_{22,R} = O_{11} + \frac{O_{12}^2\Gamma}{1-O_{22}\Gamma} \tag{A.5.5}$$

$$S_{11,L} = I_{11} + \frac{O_{22}I_{12}^2X^2}{1-I_{22}O_{22}X^2} \tag{A.5.6}$$

$$S_{22,L} = O_{11} + \frac{I_{22}O_{12}^2X^2}{1-I_{22}O_{22}X^2} \tag{A.5.7}$$

$$S_{21,L} = S_{12,L} = \frac{I_{12}O_{12}X}{1-I_{22}O_{22}X^2} \tag{A.5.8}$$

where Γ is a reflection coefficient, X is a phase delay by the line.

First, Γ and X are derived as

$$b = S_{12,T}^2 + S_{12,L}^2 - \left(S_{11,T} - S_{11,L}\right)\left(S_{22,T} - S_{22,L}\right) \tag{A.5.9}$$

$$X = \frac{b \pm \sqrt{b^2 - 4S_{12,T}^2 S_{12,L}^2}}{2S_{12,T}S_{12,L}} \tag{A.5.10}$$

$$\frac{S_{11,T} - S_{11,L}}{S_{12,T} - S_{12,L}X} = C_1 \tag{A.5.11}$$

$$\frac{S_{22,T} - S_{22,L}}{S_{12,T} - S_{12,L}X} = C_2 \tag{A.5.12}$$

$$C_3 = C_1 C_2 \tag{A.5.13}$$

$$\frac{S_{11,T} - S_{11,R}}{S_{22,T} - S_{22,R}} = C_4 \tag{A.5.14}$$

$$V = \frac{C_1(S_{22,R} - S_{22,T})}{S_{12,T}(1 - C_3)} + \frac{C_3}{1 - C_3} \tag{A.5.15}$$

$$W = \frac{C_2(S_{11,R} - S_{11,T})}{S_{12,T}(1 - C_3)} + \frac{C_3}{1 - C_3} \tag{A.5.16}$$

$$\Gamma = \pm\sqrt{\frac{VW}{(V+1)(W+1)C_3}} \tag{A.5.17}$$

Remained S-parameters of the transition are derived as

$$\Gamma(C_1^2 - C_4) = D_1 \tag{A.5.18}$$

$$(\Gamma^2 + 1)(C_3 C_4 - C_1^2) = D_2 \tag{A.5.19}$$

$$\Gamma(C_1^2 - C_3^2 C_4) = D_3 \tag{A.5.20}$$

$$O_{22} = \frac{-D_2 + \sqrt{D_2^2 - 4D_1 D_3}}{2D_1} \tag{A.5.21}$$

$$I_{22} = \frac{C_2}{O_{22}} \tag{A.5.22}$$

$$I_{12} = \pm\sqrt{\frac{S_{11,T} - S_{11,R}}{\left(\frac{O_{22}}{1 - C_2} - \frac{\Gamma}{1 - \Gamma I_{22}}\right)}} \tag{A.5.23}$$

$$O_{12} = \pm\sqrt{\frac{S_{22,T} - S_{22,R}}{\left(\frac{I_{22}}{1 - C_2} - \frac{\Gamma}{1 - \Gamma O_{22}}\right)}} \tag{A.5.24}$$

$$I_{11} = S_{11,R} - \frac{\Gamma I_{12}^2}{1 - \Gamma I_{22}} \tag*{(A.5.24)}$$

$$O_{11} = S_{22,R} - \frac{\Gamma O_{12}^2}{1 - \Gamma O_{22}} \tag*{(A.5.24)}$$

The characteristic of two transitions connected to the one-body 2-D beam-switching Butler matrix is able to de-embed.

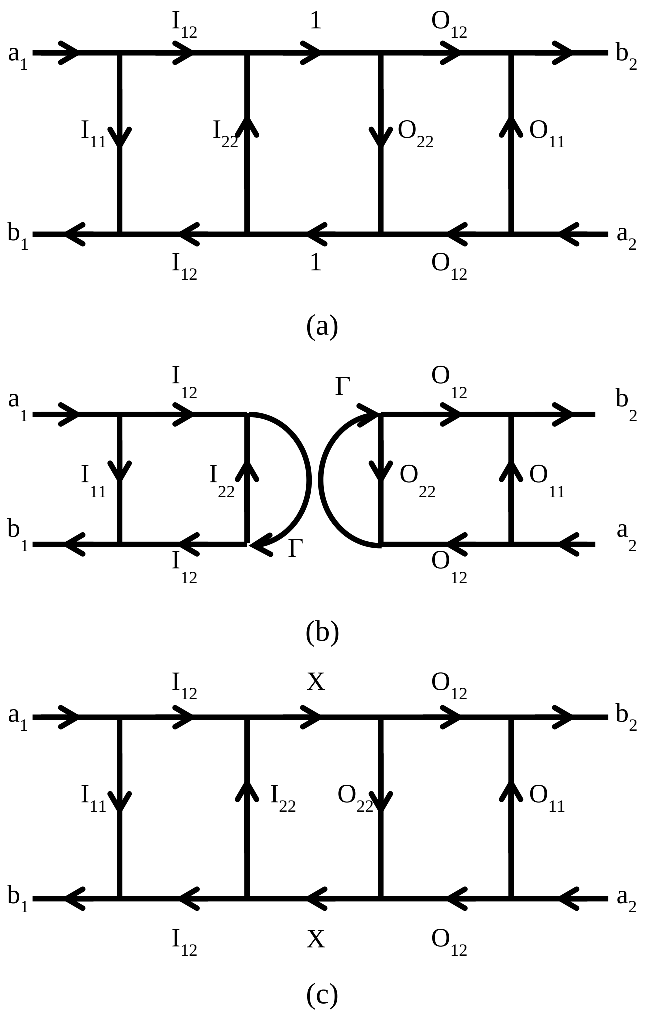

(a)

(b)

(c)

Fig. A.5.1 Signal flow graph of TRL (a) Thru (b) Reflect (c) Line.

A.6 NFFFT (Near-Field to Far-Field Transformation)

Acquiring the radiation power distribution in the far-field region for the evaluation of the 2-D beam-switching circuit, a bi-axial positioner is required. Most anechoic chamber facility, the automatic bi-axial positioner is not equipped because of its expensive cost and limited flexibility. It is not impossible to measure the radiation power distribution using a manual bi-axial positioner, but it takes long time. NFFFT is one of solution to these restricted measurement circumstance. In this case, near-field data are acquired in the x-y planar system. First, the plane wave spectrum of the field $\boldsymbol{A}$ is derived from measured near-zone $\boldsymbol{E}$-field.

$$\mathrm{A_x}(\mathrm{k_x}, \mathrm{k_y}; \mathrm{z} = \mathrm{z_0}) = \mathrm{F}^{-1}(\mathrm{E_x}(\mathrm{x}, \mathrm{y}, \mathrm{z} = \mathrm{z_0})) = \int_{-\infty}^{\infty}\int_{-\infty}^{\infty} \mathrm{E_x}(\mathrm{x}, \mathrm{y}, \mathrm{z} = \mathrm{z_0}) e^{i(\mathrm{k_x}x + \mathrm{k_y}y)} dxdy \quad \text{(A.6.1)}$$

$$\mathrm{A_y}(\mathrm{k_x}, \mathrm{k_y}; \mathrm{z} = \mathrm{z_0}) = \mathrm{F}^{-1}\left(\mathrm{E}_y(\mathrm{x}, \mathrm{y}, \mathrm{z} = \mathrm{z_0})\right) = \int_{-\infty}^{\infty}\int_{-\infty}^{\infty} \mathrm{E}_y(\mathrm{x}, \mathrm{y}, \mathrm{z} = \mathrm{z_0}) e^{i(\mathrm{k_x}x + \mathrm{k_y}y)} dxdy \quad \text{(A.6.2)}$$

Then the far-field pattern of the antenna is expressed as in terms of $\boldsymbol{A}$.

$$E_\theta(r,\theta,\phi) \approx \frac{ik_0 e^{-ik_0 r}}{2\pi r} e^{jk_z z_0}\left(A_x\left(k_x,k_y;z=z_0\right)\cos\phi + A_y\left(k_x,k_y;z=z_0\right)\sin\phi\right) \quad \text{(A.6.3)}$$

$$E_\phi(r,\theta,\phi) \approx \frac{ik_0 e^{-ik_0 r}}{2\pi r} e^{jk_z z_0}\cos\theta\left(-A_x\left(k_x,k_y;z=z_0\right)\sin\phi + A_y\left(k_x,k_y;z=z_0\right)\cos\phi\right) \quad \text{(A.6.4)}$$

Finally, the gain pattern is expressed as

$$U(\theta,\phi) \approx \frac{1}{2\eta}\left(|E_\theta(r,\theta,\phi)|^2 + \left|E_\phi(r,\theta,\phi)\right|^2\right) \quad \text{(A.6.5)}$$

$$P_{rad} = \oiint_\Omega U(\theta,\phi)d\Omega = \int_0^{2\pi}\int_0^{\pi} U(\theta,\phi)\sin\theta\, d\theta d\phi \quad \text{(A.6.6)}$$

$$G(\theta,\phi) = e_{cd} 4\pi \frac{U(\theta,\phi)}{P_{rad}} \quad \text{(A.6.7)}$$

U is a radiation intensity, P_{rad} is a total radiated power, e_{cd} is an antenna radiation efficiency.

List of publications

Journal papers

[1] D.-H. Kim, J. Hirokawa, and M. Ando, “Design of Waveguide Short-slot 2-plane Couplers for One-body 2-D Beam-switching Butler Matrix Application,” *IEEE Trans. Microw. Theory Techn.*, vol. 64, no. 3, pp. 776-784, Mar. 2016.

[2] D.-H. Kim, J. Hirokawa, and M. Ando, “One-body 2-D Beam-switching Butler Matrix with Waveguide Short-slot 2-plane Couplers,” submitted to *IEICE Trans. Electron.*

Conference papers (International)

[1] D.-H. Kim, J. Hirokawa, and M. Ando, “Design of Short-Slot 2-plane Waveguide Couplers,” *Proc. of International Symposium on Antennas and Propagation (ISAP)*, S3.11, Hobart, Australia, Nov. 9-12, 2015.

[2] D.-H. Kim, J. Hirokawa, and M. Ando, “Design and Application of Short-slot 2-plane Coupler,” *2015 Korea-Japan EMT/EMC/BE Joint Conf.*, P-01, Sendai, Japan, Nov. 23-24, 2015.

[3] D.-H. Kim, J. Hirokawa, M. Zhang, and M. Ando, “Design of a Novel 2-D Beam-switching Waveguide Butler Matrix,” *IEEE Intl. Symp. Antennas Propag.*, WEP-UA.2P.7, Fajardo, Puerto Rico, Jun. 26-Jul. 1, 2016.

[4] D.-H. Kim, J. Hirokawa, K. Tekkouk, M. Ando, R. Sauleau, “Comparison between One-body 2-D Beam-switching Butler Matrix and 2-D Beam-switching Rotman Lens,” *Proc. of International Symposium on Antennas and Propagation (ISAP)*, POS1-8, Okinawa, Japan, Oct. 24-28, 2016.

[5] D.-H. Kim, J. Hirokawa, and K. Nishimori, “Design of one-body 64×64-way 2-D beam-switching Butler matrix,” *IEEE Intl. Symp. Antennas Propag.*, San Diego, USA, Jul. 9-14, 2017.

Conference papers (Domestic)

[1] D.-H. Kim, J. Hirokawa, and M. Ando, "Design of a Two-Plane-Dividing Short-Slot Waveguide Coupler," *Proc. of the IEICE General Conf.*, B-1-49, Kusatsu, Japan, Mar. 2015.

[2] D.-H. Kim, J. Hirokawa, and M. Ando, "Design of Two-dimensional Beam-switching Butler Matrix using Short-Slot Two-plane Couplers," *IEICE Technical Report*, vol.115, no.12, AP2015-4, pp.13-16, Apr. 2015.

[3] D.-H. Kim, J. Hirokawa, and M. Ando, "Compact Design of Cross Coupler Part in 2-D Beam-Switching Butler Matrix," *Proc. of IEICE Society Conf.*, B-1-54, Sendai, Japan, Sep. 2015.

[4] D.-H. Kim, J. Hirokawa, and M. Ando, “Evaluation of 16×16-way One-body 2-D Beam-switching Butler Matrix,” *IEICE Technical Report*, vol.116, no.82, AP2016-33, pp.9-12, Jun. 2016.

[5] D.-H. Kim, J. Hirokawa, and K. Nishimori, "Wideband 2-plane Short-slot Coupler Using Frequency Shift of Propagating Modes," *Proc. of the IEICE General Conf.*, B-1-84, Nagoya, Japan, Mar. 2017.

Acknowledgement

I wish to express my gratitude to Prof. Jiro Hirokawa for providing me a chance of the research work and useful suggestions. I also wish to express my gratitude to thank Dr. Makoto Ando, Vice president, Tokyo Institute of Technology, for giving me an instructive suggestion for the thesis construction.

I would like to thank Prof. Tetsuya Mizumoto, Prof. Kei Sakaguchi, Assoc. Prof. Atsuhiro Nishikata, Assoc. Prof. Takahiro Aoyagi, School of Engineering, Tokyo Institute of Technology, and Yoshihiko Konishi, Faculty of Engineering, Hiroshima Institute of Technology, for giving me a correct suggestion for the thesis content.

I express my deep appreciation to laboratory staffs, Mr. Kimio Sakurai for experimental helps, and Assistant Prof. Takashi Tomura and Mrs. Nagao Keiko for their helps in my laboratory life. I would like to thank laboratory members, Dr. Karim Tekkouk, Mr. Xin Xu, Mr. Mikihiro Aruga, Mr. Ryotaro Ohashi, Mr. Akihide Nagamine, Mr. Tatsuya Nagayama, Mr. Masahiro Wakasa, Mr. Tuchjuta Ruckkwaen, Ms. Haruka Arakawa, Mr. Yuta Saito, Mr. Moto Maruyama, Mr. Shuki Wai, Mr. Soichi Sakurai, Mr. Yuki Sunaguchi, Mr. Kentaro Wada. All of them make my academic life fun a lot. During my stay in Hirokawa (included Ando-Hirokawa) laboratory, many people came and left. All of them gave me good advice and excitation. I also would like to thank them.

I would like to thank Emeritus Prof. Kiyomichi Araki, Prof. Fumio Watanabe, School of Engineering, Tokyo Institute of Technology, and Prof. Kentaro Nishimori, Faculty of Engineering, Niigata University, for their helps in this study.

I would like to thank KIST IMRC former members, Dr. Se-Yun Kim, Dr. Sang-Wook Kim, Prof. Seung-Yeup Hyun, Dr. Ji-Hyun Jung, Dr. Jea-Hyoung Cho, and LG Electronics Inc. PLS former members, Dr. Hyun-jung Kim, Dr. Byeong-ju Park, Consulting Prof. Jung-won Kang, and Prof. Motoyuki Sato, CNEAS, Tohoku University. All of them help to enhance my engineering experience.

This work has been supported in part by the Strategic Information and Communications R&D Promotion Programme, the Ministry of Internal Affairs and Communications.

I would like to thank my parents and brother for exuberant support and love.